Volume 40 No. 1 | JNSChE Mar/April, 2025 | ISSN 0794-6759

DOI: 10.51975/EFSD2591

# JOURNAL OF THE NIGERIAN SOCIETY OF CHEMICAL ENGINEERS



.

*Published by,*
THE NIGERIAN SOCIETY OF CHEMICAL ENGINEERS
National Secretariat: Infinite Grace Hocuse, Plot 4, Oyetubo Street,
Off Obafemi Awolowo Way, Ikeja, Lagos State, Nigeria.
E-mail: nationalhqtrs@nsche.org, nsche_headquarters@yahoo.com
Website: https://www.nsche.org.ng; Journal URL: https://journal.nsche.org.ng
Submission of Manuscripts: nschejournal@yahoo.com and copy: stevmomoh@yahoo.com
The journal is indexed in International Scientific Indexing (ISI). The URL for journal in the ISI server is https://isindexing.com/isi/journaldetails.php?id=16333

**JOURNAL OF THE NIGERIAN SOCIETY OF CHEMICAL ENGINEERS**
**A Publication on the Science and Technology of Chemical Engineering**

10.51975/25400101.som
Journal of the Nigerian Society of Chemical Engineers, 40(1), 2025

# REMOVAL OF LEAD FROM TEXTILE WASTE WATER USING CHITOSAN PRODUCED FROM SNAIL SHELL

**Oyedeko K F K., Akinyanju A S., Lasisi-Amokun M K.**
*Department of Chemical Engineering, Lagos State University, Epe, Nigeria*
*Department of Chemical Engineering, University of Lagos, Lagos, Nigeria*
*Email of the Corresponding author: mlasisi@unilag.edu.ng(+234-7055047648)*

**ABSTRACT**
*The sorption process of lead (II) ions from textile effluent was investigated using chitosan obtained from a snail shell (SSC). The effects of various experimental parameters on Pb (II) ions adsorption were studied, and optimal conditions were determined. The equilibrium data were analyzed with Langmuir, Freundlich, Temkin, Elovich, Florry Huggins, Jovanovic, Harkin Jura, and Dubinin–Radushkevich (DRK) adsorption models. The high correlation factor of Langmuir isotherm indicates the monolayer coverage of the adsorbent. Freundlich isotherm fitted the adsorption data excellently. The adsorption intensity (n) is 1.68. This means the suitability of the adsorption process. The adsorption process is beneficial when the adsorption intensity is between 1 and 10. Adsorption kinetics data for sorption of $Pb^{2+}$ ion unto chitosan were analyzed using the pseudo-first order, pseudo-second order, and intraparticle diffusion models. The results indicated that the pseudo-second-order model best described the adsorption kinetic data. For the thermodynamic studies, the enthalpy change, ΔH°, and the entropy change, ΔS°, for the adsorption processes are -18.10 kJ/mol and -0.0652 KJ/mol K respectively. The free energy, ΔG° for the process are 2186.39 J/mol, 3071.761 J/mol, 3689.615J/mol, and 4153.032 J/mol at 303K, 313K, and 323K respectively. The thermodynamic parameters showed that the adsorption of lead into SSC was exothermic and non-spontaneous.*
***Keywords**: Adsorption, sorption, chitosan, isotherm, kinetic models, intra-particle diffusion.*

## 1. INTRODUCTION

Water pollution by the discharge of harmful heavy metals has been one of the problems threatening the human health and ecological system. These heavy metals may be released naturally into the environment or through anthropogenic activities like mining and smelting processes, battery and machinery manufacturing, and electroplating plants,( Zhang et al, 2020). Pb(II) is highly toxic and forms complexes in the liver and kidney, resulting in endocrine disorders, and cancer ( Ghorbani et al, 2020, Zhu et al, 2021).

Lead is one of the highly toxic heavy metals, that even at a low concentration, can cause serious health hazards to man and aquatic animals. Thus, there is a growing demand for the elimination of toxic metals from polluted areas such as water streams and wastewater to avert their hazardous impacts. (Zhu et al, 2021)

Several methods such as ion exchange (Li. et al, 2021), membrane technology (El-Batouti et al, 2021), precipitation (Qasem et al, 2021), ion exchange (Hussain et, al, 2021), coagulation (Sylwan et al, 2021), co-precipitation (Zhao et al, 2021), electrolysis (Kumar, et al, 2021), and adsorption are being used to remove heavy metals from textile waste. The adsorption technique can be considered useful for removing dissolved heavy metals from liquid wastes. It is also more effective and economical for removing heavy metals from industrial wastewater than other conventional wastewater treatment methods. (Iconaru et al, 2016) The adsorption method is effective in removing from wastewater low concentrations of heavy metal ions and is also used at the industrial level (Khazael, et al 2016 Oliveira, et al 2011). Of all the low-cost adsorbents, chitosan has the highest sorption capacity for several metal ions. (Babel and Kurniawan, 2004; Nomanbhay and Palanisamy, 2005).

The waste derived from snails constitutes environmental challenges after removing the inner part, which greatly benefits human health. Waste generated from the shells of snails is the main precursor for the production of chitosan. Chitosan is one of the low-cost adsorbents with high sorption capacity for metals removal. It is widely used in diverse fields, ranging from waste management to food processing, medicine, and biotechnology (Kalut, 2008). In agriculture, it is used to improve the yield of rice and orchid production (Kim, 2010).

Chitosan is the most common derivative of chitin formed based on chitin partial N-deacetylation through variations of chemical processes with more than one soluble analog. As a result of numerous benefits (non-toxicity, biocompatibility, biodegradability, and non-antigenicity) attributed to chitin and chitosan, they have continued to attract interest worldwide (Daniel and James, 2019). The Chitosan produced through chitin deacetylation is a high molecular weight molecule with a biodegradable polymer and consists of-(14)-2-amino, 2-deoxy- Dglucopyranose (Islam et al., 2017).

Heavy metals discharged into water from various industries are toxic and carcinogenic. They cause severe problems for humans and aquatic ecosystems. Thus, the removal of heavy metals from wastewater is a serious

concern. Both commercial adsorbents and bio-adsorbents are used for the removal of heavy metals from wastewater, with high removal capacity. The challenge in heavy metal removal from wastewater is that it may require large amounts of bio-adsorbents and extra chemicals to maintain a pH that provides suitable conditions for adsorption.

This study aimed to remove $Pb^{2+}$ in the wastewater by adsorption using chitosan. The chitosan used for adsorbent was obtained from a snail shell (SSC).

## 2. MATERIALS AND METHODS

All the chemical reagents used for this research work were of analytical grade and were supplied by Foray Enterprises Ltd, Lagos State. The raw material used for chitosan production is *Archachatina marginata* (African giant). The reagents are hydrochloric acid and sodium hydroxide. Deionized water used for this research was obtained from the Chemistry Department, University of Lagos, Akoka, Yaba, Lagos.

### 2.1 PREPARATION OF CHITIN

There are four basic stages involved in the production of chitosan. The stages are Demineralization, deproteinization, depigmentation or decolorization, and deacetylation.

The first stage in Chitosan production is the Demineralization stage. The methods employed for the production of chitin from snail shells were as described by Moosa et al. (2016). 500 g of the sieved sample was weighed and put into a beaker. 2500 ml of 3.2525 M of HCl solution was added (1:5w/v). The mixture was stirred using a griffin shaker at 30 $^{o}$C, for 2 hours to avoid effervescence and to remove carbonate and phosphate content. The resulting solution was washed with distilled water and filtered with Whatman filter paper. The residue was scraped into a petri dish and dried in an oven at 105 $^{o}$C for 2 hours. In the deproteinization process, the demineralized chitin was soaked in 870 ml of 2.39M of sodium hydroxide (NaOH) solution (1:5w/v). The mixture was stirred and boiled in a water bath at 70 $^{o}$C for 2 hours. The resulting solution was filtered with Whatman filter paper and washed with distilled water until the pH of the filtrate was neutral. After washing (as shown in plate 3), the mixture was filtered and the residue was put in an oven at 105 $^{o}$C for 2hrs to dry.

### 2.2 PREPARATION OF CHITOSAN.

The obtained chitin was soaked in 750 mL of 50 wt /wt% NaOH, heated at 85 $^{o}$C for 2 hours, 30 mins in a water bath, and cooled for 30 min at room temperature. The mixture was placed on a magnetic stirrer at 30$^{o}$C for 4 hours. The mixture was washed and the pH of the filtrate was constantly checked until it was neutral. Thereafter, the mixture was filtered using Whatman filter paper to retain the solid matter. The chitosan thus produced was dried in an oven at 105 $^{o}$C for 2 hours. This process is known as Deacetylation.

## 3.0. CHARACTERIZATION OF CHITOSAN

### 3.1 DEGREE OF DEACETYLATION

The degree of deacetylation (DD) of chitosan is an important parameter to be noted as it affects the solubility, chemical reactivity, and biodegradability of chitosan. DD may range from 30% to 95% (Martino et al., 2005), depending on the available source and procedure.100% DD is very scarcely obtained, with commercial chitosan with various DD in the range of 75-85%. IR technique was used for determining the degree of deacetylation, DD, of chitosan, according to the methods described by (Ghimire et al., 2011): The degree of Deacetylation (DDA) of the refined chitosan from snail shells was calculated using the equation given

$$DD = \left(100 - \frac{A_{1320}}{A_{1420}} \times \frac{1}{0.03133}\right)$$

$A_{1320}$ and $A_{1420}$ are the absorbance values at the wavelengths 1320 and 1420 $cm^{-1}$ respectively. the FTIR analysis of chitosan, the % transmittance of the wavelength 1320 and 1420 $cm^{-1}$ was obtained as 21.5 % and 25.1 % respectively. This was then converted to absorbance [A=2- log (% T), where T is transmittance. The degree of deacetylation of the chitosan sample was obtained to be 64.50%.

### 3.2 DETERMINATION OF ASH CONTENT

A 2g sample of the sample was weighed into an empty crucible that had previously been heated, cooled, and weighed. This was then kept in the furnace at 600$^{o}$C for 5 hrs. and later allowed to cool to about 200$^{o}$C. The crucible was transferred directly into a desiccator to cool to room temperature and weighed immediately. The percentage (%) ash content was calculated as follows (Baby R. et al. 2021)

$$\frac{(\textbf{\textit{Mass of crucible+ash}})-(\textbf{\textit{Mass of empty crucible}})}{\textbf{\textit{Mass of sample used}}} \times \mathbf{100}$$

### 3.3 DETERMINATION OF MOISTURE CONTENT

A clean crucible was dried in an oven at 105 $^{o}$C for 1 hr. cooled in a desiccator, and the mass of the crucible was weighed as $W_o$. A 5 g sample of the bio sorbent was placed in an oven at 105 $^{o}$C for 2hrs, cooled in a desiccator, and weighed. The same procedure was conducted severally until a constant weight was observed. The moisture content of the sample was then calculated (Ajala, LO et al. 2012):

$$\frac{W1-\boldsymbol{W2}}{W1-Wo} \times \mathbf{100}$$

Where the mass of the empty crucible is $W_o$; that mass of the sample and crucible before heating = $W_1$ and the mass of the sample and crucible after heating =$W_2$

### 3.4 SOLUBILITY

Chitosan dissolution was carried out by dissolving 1 gram of chitosan in 100 ml of 2% acetic acid. The solution is stirred until homogeneous or vortex for 10 seconds. The solution was then centrifuged for 15 minutes and then filtered to get residue on filter paper. The filter paper was

then in the oven at 100-105ºC for 2 hours, the process was repeated until a constant weight was obtained.
Solubility is obtained by inserting into the formula (Shon et al, 2011):

Insolubility (%) = $\frac{Final\ weight\ (g)}{Initial\ weight\ (g)} x\ 100\%$

Solubility (%) = 100% - Insolubility

**4.0 BATCH EXPERIMENTS**

Batch adsorption was carried out to study how various factors affect the removal of lead ($Pb^{+}$) from wastewater using locally produced chitosan. The factors considered are pH, adsorbent dosage, contact time, and temperature. 50 mL of known lead solution was put into a 250 mL Erlenmeyer flask at specific conditions. The effects of pH were studied by varying the pH of wastewater using 0.1 M HCl and 0.1 M NaOH. The effect of time was within 130 mins at a fixed mass of 0.1g chitosan and at room temperature of 30 ±1 ºC. Also, a thermodynamics study was carried out with temperature ranges from 30 to 50 ºC at a fixed mass adsorbent of 1g.

**4.1 ADSORPTION KINETICS**

Adsorption kinetics describes the rate at which solute is adsorbed at the solid–solution interface. This helps to understand the sorption process to design a proper wastewater treatment plant. The kinetic parameters assist in predicting the rate of adsorption and as well as equilibrium time. (Sivarajasekar and Baskat, 2014). Adsorption kinetics is a major issue in the design of a treatment system using adsorbent. Adsorption kinetics provides information that assists industry operators and planners to effectively treat contaminated wastewater. (Olafadehan et. al. 2021). The adsorption kinetics examined in this study as illustrated below.

**4.1.1 PSEUDO-FIRST ORDER MODEL**

The pseudo-first-order kinetic model, shown in equation 1 below, has been widely used to predict the metal adsorption kinetics. The metal adsorption kinetics following the pseudo-first-order
model is given by (Ho and McKay 2000, Sivaraj 2001)

$$\frac{dq_t}{dt} = K_{e_1}(q_e - q_t) \qquad 1$$

Where

$K_{e_1}$ =equilibrium rate constant of pseudo-first order sorption ($min^{-1}$)

$q_t$ = Integrating equation with the conditions

$q_t = 0 \quad at \quad t = 0$ ;

$q_t = q_t \quad at \quad t = t$

Integrating and applying the boundary conditions give:

$$In(q_e - q_t) = Inq_e - Ke_1 t$$

Therefore, a straight line should be obtained from the plot of (qe-qt) against t, which is adequate to determine $ke_1$.

**4.1.2 PSEUDO-SECOND ORDER MODEL**

The pseudo-second-order kinetic model assumes the adsorption of solutes onto adsorbents follows the second-order mechanism and is expressed as:

$$\frac{dq_t}{dt} = K_{e_2}(q_e - q_t)^2 \qquad 2$$

Integrating and substituting equation conditions.

$q_t = 0\, at\, t = 0;$

$q_t = q_t\, at\, t = t$

$$\frac{1}{(q_e - q_t)} = Ke_2 t + C \qquad 3$$

$q_t = 0 \quad t = 0$

$$C = \frac{1}{q_e}$$

Substituting C into equation 3 above and re-arranging the equation gives

$$\frac{1}{Ke_2 q_e^{\,2}} + \frac{t}{q_e} = \frac{t}{q_t} \qquad 4$$

The plot of $\frac{t}{q_t}$ versus $t$ should give a straight line if pseudo-second-order kinetics are applicable and the values of $q_e$ and $k_{e2}$ can be determined from the slope and intercept respectively.

$h = k_{e2}\, q_e^{\,2}$.

**4.1.3 INTRAPARTICLE DIFFUSION (IPD)**

One of the most widely used techniques for identifying the mechanism involved in
the adsorption process is an intraparticle diffusion model. The intra-particle diffusion equation is expressed as follows:

$$q_e = k_d t^{1/2} + C \qquad 5$$

where $k_d$ Is the intraparticle diffusion rate constant ($mg/gmin^{1/2}$) and $C$ Is the intercept (mg/g).

The plot of $q_t$ versus $t^{1/2}$ gives a straight line from which the slope of the graph $K_d$ and the intercept C which gives

information about the thickness of the boundary layer can be calculated.

**4.1.4 ELOVICH RATE EQUATION**

Elovich rate equation is used to describe second-order kinetic, with the assumption that the actual solid surfaces are energetically heterogeneous, (E. Malkoc *et al.*2007). It is given as follows:

$$\frac{dq_t}{dt} = a\exp(-bq_t) \quad 6$$

Integrating and substituting equation conditions and subsequently linearizing the result yields

$$\frac{1}{ab\exp(-bqt)} = t + \frac{1}{ab}.$$

$$bq_t = In(ab) + In(t + t_o)$$

$$q_t = \frac{1}{b}In(ab) + \frac{1}{b}In(t + t_0) \quad 7$$

Where $a$ and $b$ are the parameters of the Elovich rate equation indicating the initial adsorption rate $(mg/g.\min)$ and the desorption constant (g/ mg) respectively. This can further be simplified (Rajeshwari Sivaraj *et al.*, 2010).

$$q_t = \frac{1}{b}In(ab) + \frac{1}{b}Int \quad 8$$

**4.1.5 AVRAMI KINETIC MODEL**

The Avrami kinetic model assumes arbitrary nucleation locations across the reaction surface of the adsorbent. It evaluates changes in kinetic parameters as a function of reaction time and temperature. The linear form of the expression is given (Ahmad et al., 2014; Yoro et al., 2017):

$$\ln[\ln(\frac{q_m}{q_{m-q_t}})] = n_{av}lnk_{av} + n_{av}\,lnt \quad 9$$

Where $K_{Av}$ is the Avrami adsorption kinetic constant and $n_{Av}$ is another constant, which is related to the adsorption mechanism changes. The slopes and intersections values of this equation provide the $n_{Av}$ and $lnK_{Av}$ values, respectively.

**4.2 THERMODYNAMIC STUDY:**

For the determination of thermodynamic parameters, the following were used:

$$K_c = \frac{C_{Ads}}{C_e} \quad 10$$

$$\ln K_e = \frac{\Delta S^0}{R} - \frac{\Delta H^0}{RT} \quad 11$$

$$\Delta G^o = \Delta H^o - T\Delta S^0 \quad 12$$

where Kc: Equilibrium constant Cad: Adsorbed heavy metals concentration

Ce: Equilibrium concentration of metal in solution (mg $L^{-1}$)

G: Change in standard Gibbs free energy (kJ $mol^{-1}$)

H : Change in enthalpy (kJ $mol^{-1}$)

S: Change in entropy (J $mol^{-1}$ $K^{-1}$)

T: Temperature

**4.3 ADSORPTION ISOTHERMS**

The Freundlich, Langmuir, Temkin, Jovanovic, Harkins-Jura, Flory-Huggins, and Dubinin-Radushkevich isotherms were used to investigate sorption processes. They are expressed in Eq. (13) to Eq. (19) as follows:

A linear form of the Freundlich expression is:

$$Log\,q_e = LogK_f + \frac{1}{n}LogC_e \quad 13$$

The linear form of Langmuir Isotherm is given as:

$$\frac{C_e}{q_e} = \frac{1}{KQ_m} + \frac{C_e}{Q_m} \quad 14$$

The linearized Dubinin-Radushkevich Isotherm is expressed as:

$$lnq_e = lnq_s - \beta\varepsilon^2 \quad 15$$

The linearized Temkin Isotherm is expressed as:

$$q_e = B\ln A_T + B\,lnC_e \quad 16$$

$A_T$ = Temkin isotherm equilibrium binding constant (L/g)

$b_T$ = Temkin isotherm constant

R = universal gas constant (8.314 J/mol/K)

T = Temperature at 298 K

B = constant related to heat of sorption (J/mol)

The plot of $q_e$ against $lnC_e$ is required to fit the model (Rajeshwari Sivaraj et al., 2010)

The linear form of Harkins- Jura Adsorption Isotherm is given as:

$$\frac{1}{q_e^{\,2}} = \left(\frac{B}{A}\right) - \left[\left(\frac{1}{A}\right)(Log\,C_e)\right] \quad 17$$

$C_e$ Is the equilibrium concentration ( $mg/l$ ) and $q_e$ Is the amount adsorbed onto the adsorbent ( $mg/g$ )

Where $A$ and $B$ are constants. The plot of 1/qe against Log Ce gives the required fit for the model (Rajeshwari Sivaraj*et al.*, 2010).

The linearized form Jovanovic Isotherm is expressed as:

$$\ln q_e = lnq_{max} - K_J C_e \quad 18$$

The linearized form of Flory- Huggins Isotherm is expressed as:

$$\ln\frac{\theta}{C_o} = logK_{FH} + \alpha_{FH} ln(1-\theta) \quad 19$$

where: $\theta = 1 - \frac{C_e}{C_o}$

The values of $K_{FH}$ and $\alpha_{FH}$ are determined from the intercept and the slope of the plot of $\ln\frac{\theta}{C_o}$ versus ln(1-θ) (Hossain et al, 2016)

## 5. RESULTS AND DISCUSSION

The experimental data were fitted into different adsorption isotherms: Langmuir, Freundlich, Temkin isotherm, Toth adsorption isotherm, Dubinin-Radushkevich (DRK), Harkins-Jura Adsorption Isotherm, Jovanovic Isotherm, and Flory-Huggins adsorption isotherm. The linear plot of Ce/qe versus Ce suggests the applicability of the Langmuir isotherm (Fig. 1 a) The maximum monolayer coverage ($Q_m$) from the Langmuir isotherm model was found to be 50.51mg/g, $K_L$ (Langmuir isotherm constant) is 0.00374L/mg, $R_L$ (the separation factor) is 0.217 indicating that the equilibrium sorption was favorable. The coefficient of correlation for Freundlich Isotherm was 0.991. (Fig 1 b). The values $K_f$ and n are constants that show factors affecting the adsorption capacity and the intensity of adsorption. The intensity of adsorption is a suggestion for the bond energies between $Pb^{2+}$ and chitosan. The value of 1.68 for the adsorption intensity showed that the adsorption is more favorable. The heat of the sorption process was estimated from the Temkin isotherm model (Fig. 1 e) to be 9.92 J/mol and the mean free energy was determined from DRK isotherm (Fig. 1g) as 50 KJ/mol. This shows that the adsorption experiment followed a physical process. The Coefficient of correlation, $R^2$ values were used for fitting the experimental data to these isotherms. As shown in Fig 1, all eight (8) isotherms fitted to the experimental data. Table 1 shows isotherm parameters and their correlation coefficients

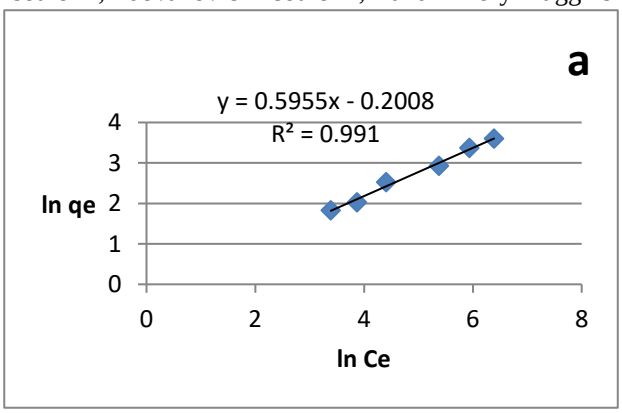


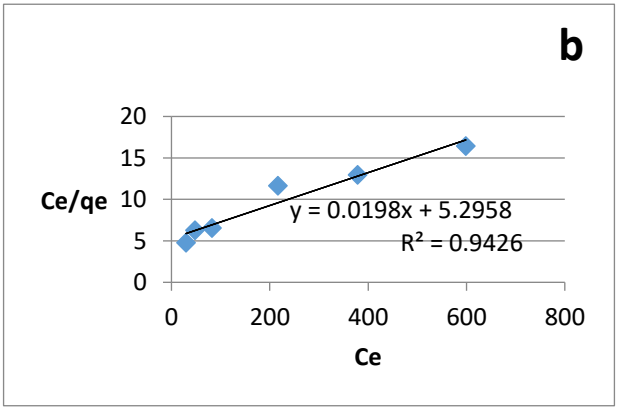


.

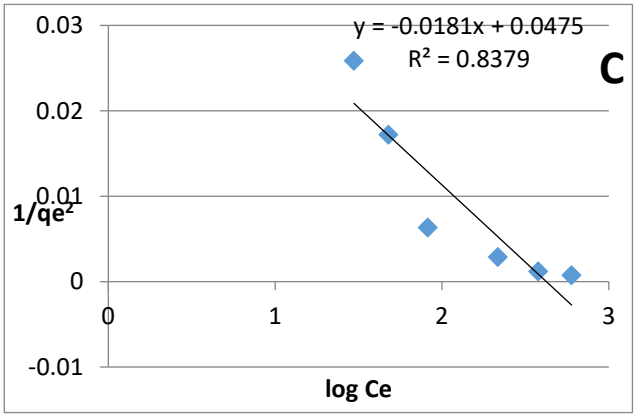


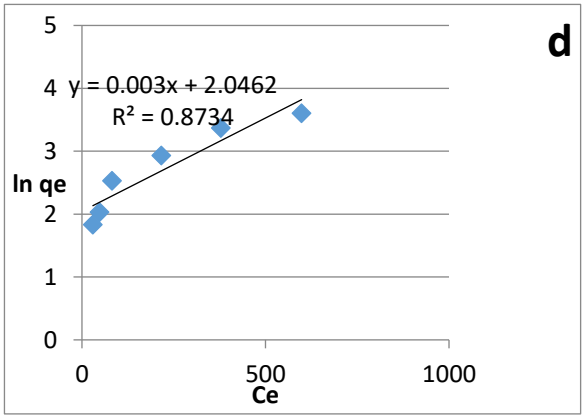

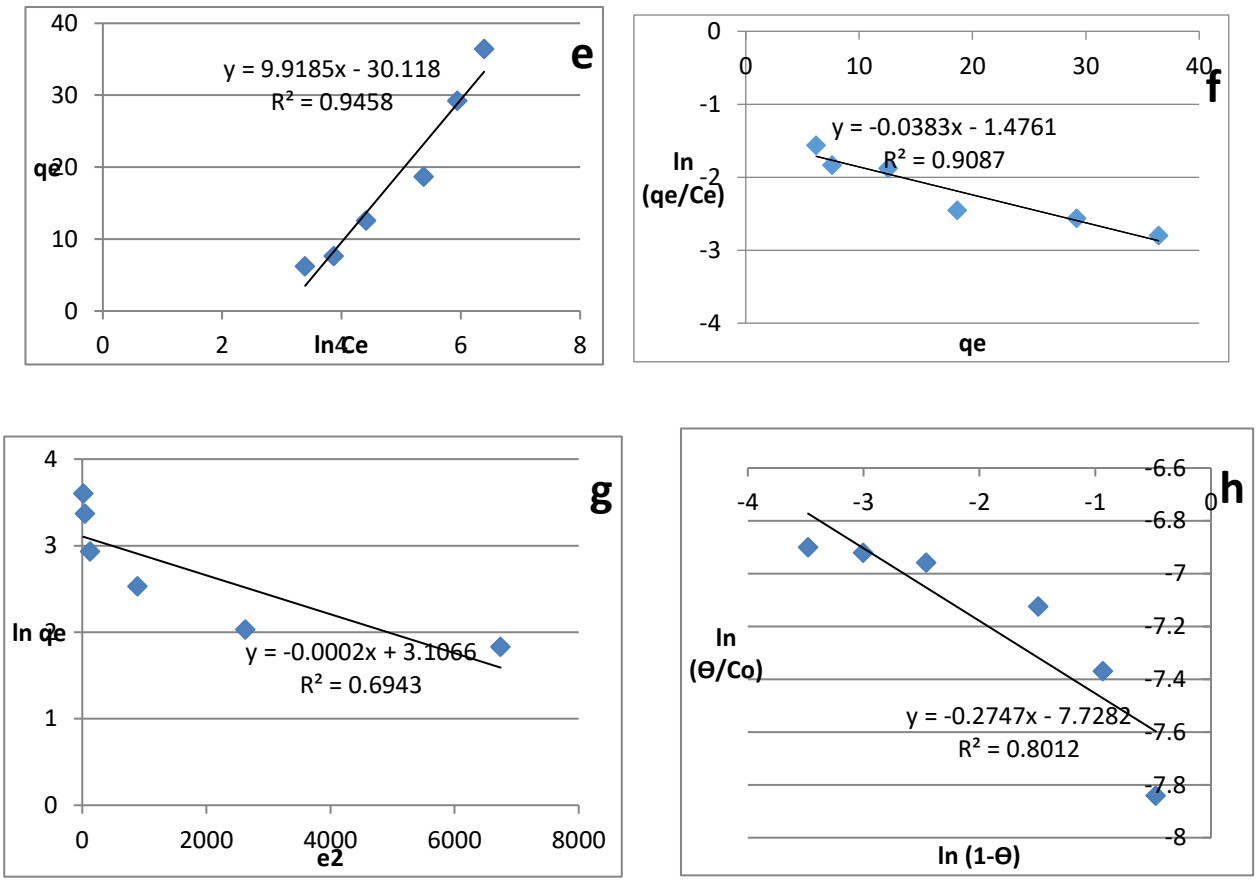


**Fig 1(a) Freundlich adsorption Isotherm (b) Langmuir adsorption Isotherm (c) Harkin-Jura adsorption Isotherm (d) Jovanovic adsorption Isotherm (e) Temkin adsorption Isotherm (f) Elovich adsorption Isotherm (g) Dubinin- Radushkevich adsor(DRK) Isotherm (h) Florry- Hugguins adsorption Isotherm**

**Table 1: Isotherm Constants for Pb2+ ions into Chitosan.**

| Isotherm Model | Isotherm parameters | Coefficient of Correlation ($R^2$) |
|---|---|---|
| **Langmuir** | Qm = 50.51(mg/g)<br>$K_L$ = 0.00374 (L/mg)<br>$R_L$ = 0.217 | 0.943 |
| **Freundlich** | 1/n =0.596<br>n =1.68<br>$K_f$ = 0.818 (mg/g) | 0.991 |
| **Harkin -Jura** | B =2.74<br>A= 63.69 | 0.816 |
| **Jovanovic** | $K_J$ = 0.873<br>$q_{max}$ = 0.774 (mg/g) | 0.873 |
| **Temkin** | $A_T$ = 0.048 (L/mg)<br>$B_T$ = 249.79<br>B = 9.92 (J/mol | 0.946 |
| **Elovich** | $K_e$ = 0.945<br>$q_m$ = 26.11 | 0.909 |
| **DRK** | $Q_m$ =22.34<br>β = 0.0002<br>E = 50 (KJ/mol) | 0.694 |
| **Florry-Hugguins** | $\alpha_{FH}$ = 0.275<br>$K_{FH}$ =0.531 | 0.801 |

**Kinetics of Adsorption of $Pb^{2+}$ unto SSC**

The kinetics of lead (II) ions adsorption unto chitosan was analyzed using pseudo-first order, pseudo-second order, Elovich, Fractional Power model, Bangham's model (pore diffusion model), Avrami kinetic model, and Intraparticle diffusion models. The kinetic modeling of Pb (II) ions adsorption showed that the pseudo-second-order kinetic model gave the best fit among the investigated kinetic models.

As shown in Fig 2, the experimental kinetic data fitted perfectly into all the kinetic models. The $R^2$ values of all the models are close to unity. The linear plot of the intraparticle diffusion model (Fig.2) did not pass through the origin. This showed that the Intraparticle kinetic model was not the rate-controlling step in the adsorption of $Pb^{2+}$ into SSC. It means that there is some degree of boundary layer diffusion. The sorption can be approximated more by the pseudo-second-order kinetic model than by the first order kinetic model.

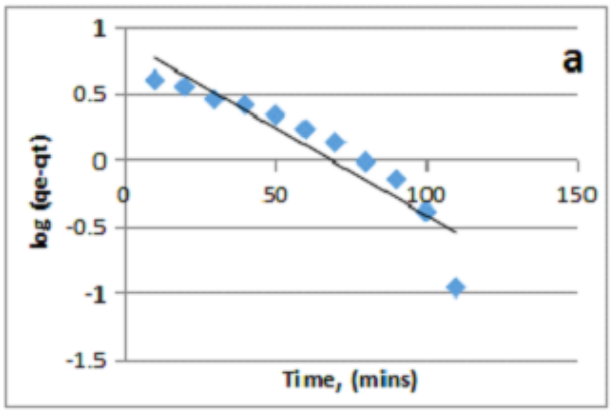


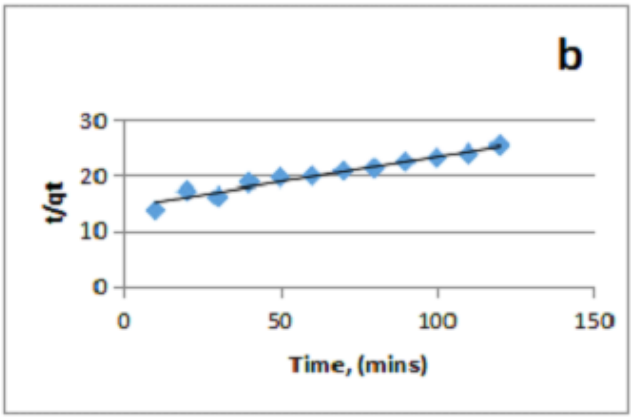


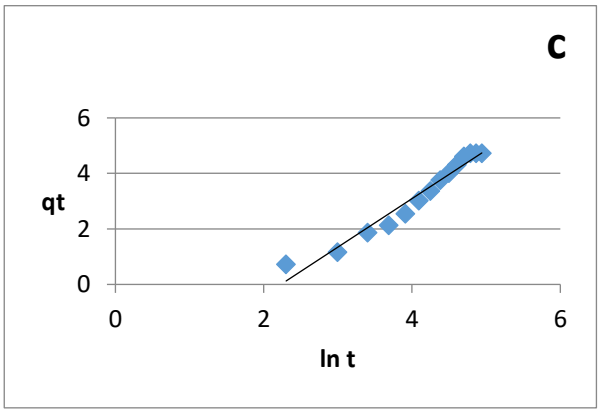


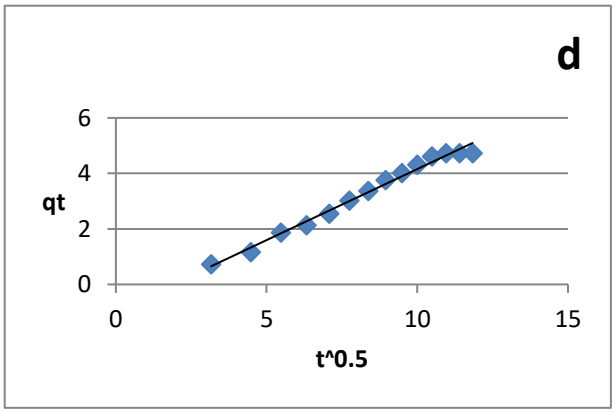


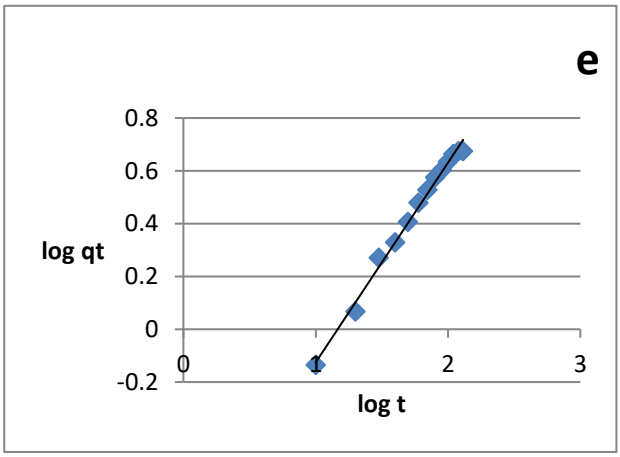


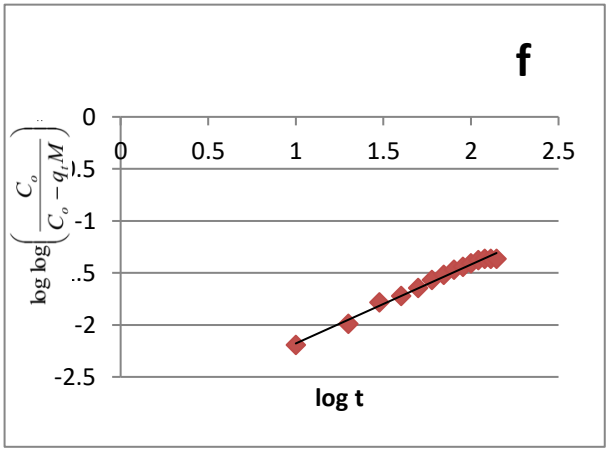

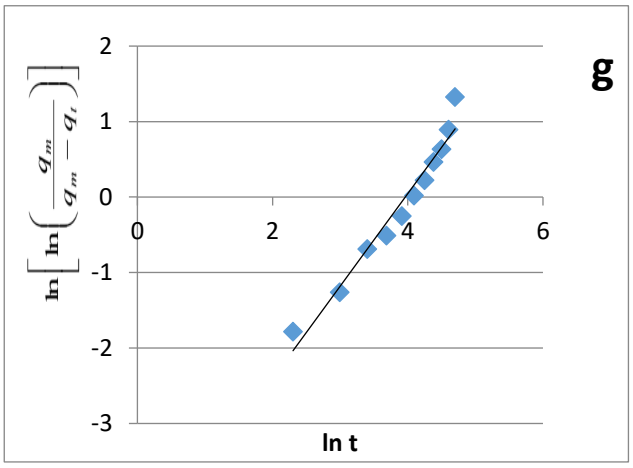


**Fig 2 (a) Pseudo-first order kinetic (b) Pseudo-second order kinetic (c) Elovich plot (d) Intraparticle diffusion plot (e) Fractional power model plot (f) Bangham's model plot (g) Avrami kinetic model plot**

**Table 2: Parameters in the linearized kinetic models for the adsorption of $Pb^{2+}$ on chitosan.**

| Kinetic Model | Parameters | Values |
|---|---|---|
| | H (g/mg min) | 0.0706 |
| **Pseudo-Second order** | $K_2$ (g/mg min) | $5.961\times10^{-4}$ |
| | qe (mg/g) | 10.88 |
| | $R^2$ | 0.9531 |
| | | |
| **Pseudo-First order** | $K_1$ ($min^{-1}$) | 0.032 |
| | qe(mg/g) | 7.909 |
| | $R^2$ | 0.8649 |
| | | |
| **Intraparticle** | $K_d$ ($mg/gmin^{1/2}$) | 0.5122 |
| | C (mg/g) | 0.964 |
| | $R^2$ | 0.9865 |
| | | |
| **Elovich** | a (mg/g min) | 0.1877 |
| | b (g/mg) | 0.5721 |
| | $R^2$ | 0.9584 |
| | | |
| **Fractional Power model** | v | 0.757 |
| | K | 0.131 |
| | $R^2$ | 0.9927 |
| | | |
| **Bangham** | $K_B$ | 0.266 |
| | b | 0.759 |
| | $R^2$ | 0.9893 |
| | | |
| | | |
| **Avrami** | $K_{AV}$ | 0.0190 |
| | $n_{AV}$ | 1.226 |
| | $R^2$ | 0.9581 |

**Proximate Analysis of Chitosan**

The proximate analysis of SSC is shown in Table 3 below. The solubility is one of the standards used to determine the quality of chitosan. The higher the solubility, the better the quality of the chitosan produced. The SSC has a solubility of 94.63%. The solubility of chitosan was examined using water and acetic acid. It was found that chitosan was no soluble in water but partially soluble in acetic acid. The Moisture content and ash content of chitosan were found to be 3.24 % and 1.21% respectively. The protein of the chitosan was 3.11%.

**Table 3: Results of Proximate Analysis of Chitosan**

| Parameters | Chitosan |
|---|---|
| Solubility (%) | 94.63 |
| Moisture Content (%) | 3.24 |
| Ash content (%) | 1.21 |
| Protein (%) | 3.11 |

**Scanning Electronic Microscopy**

The SEM images, in Fig 3 (a) and 3 (b) revealed the surface morphology of chitosan from snail shells. The morphology of the adsorbent was observed to be rough and possessed irregular shape particles capable of adsorption of metals from solution. It was observed that the SSC biopolymer possesses porous and fibril structures.

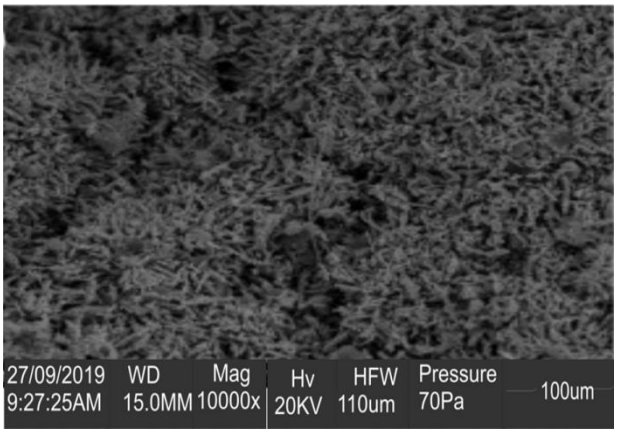


**Fig 3 a: SEM Image of Chitosan at X10000**

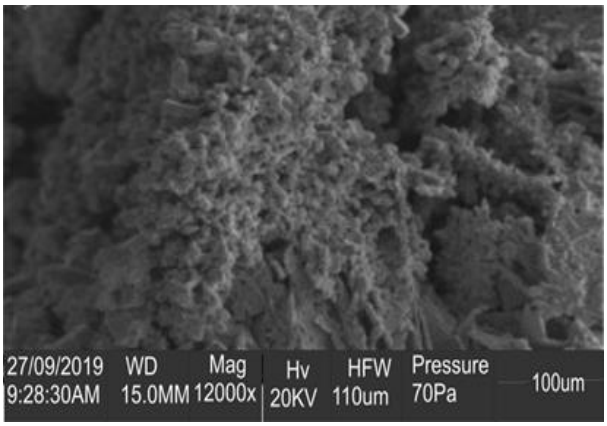


**Fig 3 b: SEM Image of Chitosan at X12000**

**EDS Analysis of Chitosan**

The result of Energy Dispersive X-ray Spectroscopy (EDS) shows the elements present in the SSC. Oxygen, Carbon, Magnesium, Calcium, and phosphorus are present in the chitosan sample as shown in Fig 4 below. Oxygen has the highest peak in the EDS spectrum followed by Carbon and calcium respectively. The EDS compositional analysis results obtained on the spectrum of the extracted chitosan from snail shells confirm a weight percent of Oxygen (45.5wt %), Carbon (25.2 wt. %), Magnesium (7.0 wt. %), Calcium (15.7 wt. %) and Phosphorus (1.2 wt. %).

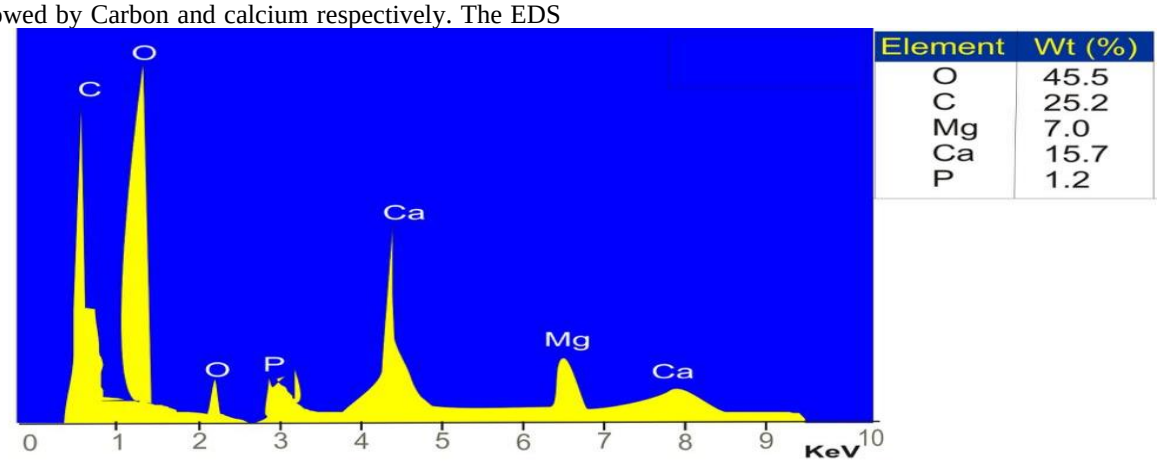


**Fig 4: EDS spectra of Chitosan.**

**Fourier-Transform Infrared (FTIR) Analysis**

The FTIR analysis of the adsorbent was determined using a Thermo Scientific Spectrometer. The corresponding spectra of the chitosan showed the wavelengths in the range 4000 to 350 $cm^{-1}$ of the different functional groups in the samples which were identified by comparison with those in the library. As shown in Table 4, The distinct band at 3445$cm^{-1}$ could be attributed to the stretching of $-NH_2$ and -OH present in primary amines and pyranose ring respectively. The band at 2927.76 $cm^{-1}$ could be attributed to $-CH_2$ in the $-CH_2OH$ group, while the observed peak at 1631.73 cm-1 was assigned to -C=O in the $-NHCOCH_3$ group (amide I band). The characteristic band at 1056.00$cm^{-1}$ was assigned to -C-O in the -OH group. Also, the band at 685.36 $cm^{-1}$ was attributed to NH out of the plane. The agreement between the characteristic band of standard chitosan and the chitosan used in this study confirmed the production of chitosan from snail shells.

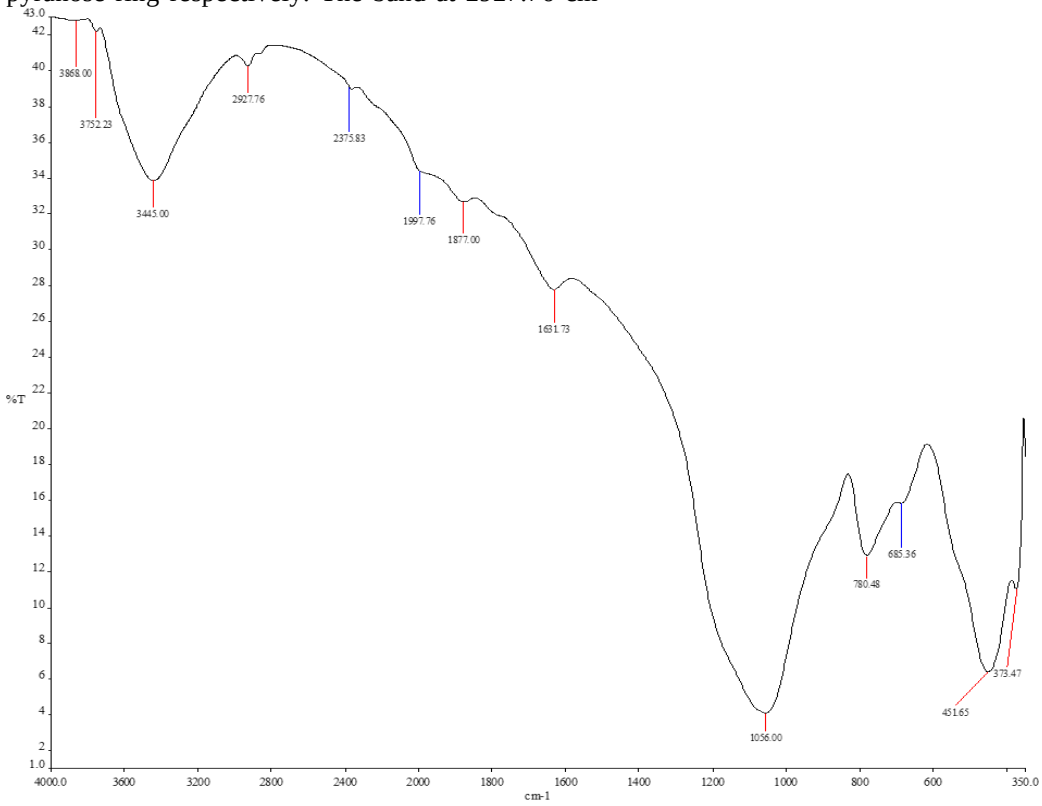


**Fig. 5: FTIR Spectra of Chitosan**

**Table 4: Comparison of FTIR spectrum with standard spectra from Sigma Aldrich**

| **Wavelength** | | | **Functional groups** |
|---|---|---|---|
| **Experimental $cm^{-1}$** | Sigma Aldrich Standard cm-1 | % error | |
| **3445.00** | 3422 | ±0.67 | υ(NH2) associated with primary amines and υ (OH) associated with pyranose ring |
| **2927.76** | 2923 | ±0.163 | υ (CH2) in CH2OH group |
| **1631.73** | 1655 | ± 1.41 | υ (C=O) in NHCOCH3 group (amide I band) |
| **1562.01** | 1554 | ± 0.51 | υ (NH2) in NHCOCH3 group (amide II band) |
| **1056.00** | 1073 | ±1.58 | υ (C–O) in secondary OH group |
| **685.36** | 662 | ±3.53 | δ (NH) out of the plane |

**Thermodynamic Study**

The thermodynamic study gives an insight into the nature of the adsorption process. As shown in Table 5, the increase in the values of $\Delta G°$ with an increase in temperature indicates that the adsorption process is less favorable at high temperatures. The negative value of $\Delta H°$ means that the adsorption process is exothermic. The small negative value of enthalpy showed that the adsorption process is physical. The enthalpy change, $\Delta H°$, and the entropy change, $\Delta S°$, for the adsorption process are -21.384 kJ/mol and 75.44 J/mol K respectively. The positive value of entropy ($\Delta S°$) showed an increased randomness of the adsorption process.

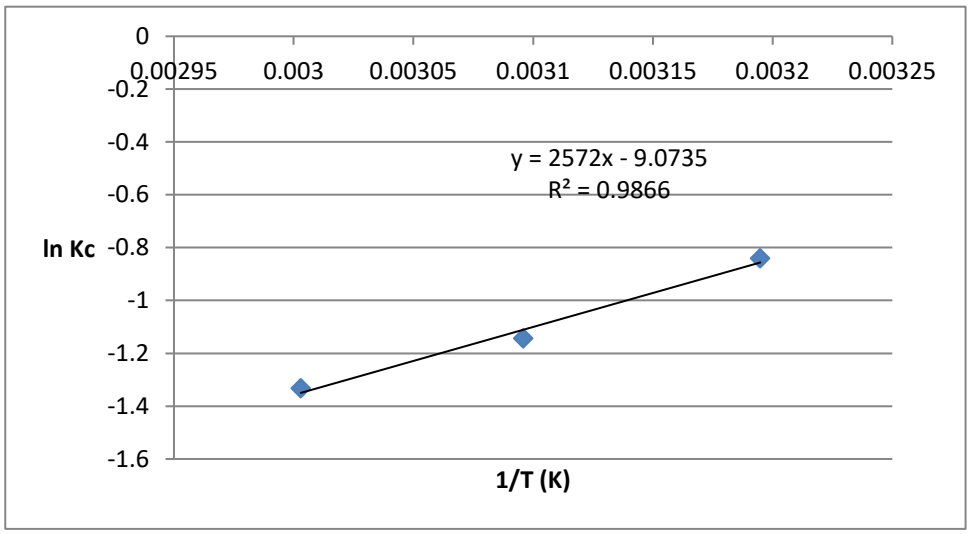


**Fig 6: Plot of ln $K_c$ versus 1/T**

**Table: 5 Thermodynamic parameters for adsorption of lead onto chitosan**

| Temperature (K) | ΔG (J/mol) | ΔS°(J/mol.K) | ΔH°(KJ/mol) |
|---|---|---|---|
| **313** | 2186.39 | **75.44** | -21.384 |
| **323** | 3071.761 | | |
| **333** | 3689.615 | | |

## 6.0 CONCLUSION

The ability of chitosan produced from snail shells as a natural adsorbent to remove $Pb^{2+}$ ions from textile wastewater was investigated in this work. The results showed that SSC is a good adsorbent for the removal of lead Pb (II) from wastewater. It was also observed that the removal of $Pb^{2+}$ increases slightly as the temperature increases. The adsorption Isotherms fitted the adsorption data of $Pb^{2+}$ into SSC.

Kinetic parameters were analyzed using the Pseudo-first order, Pseudo-second order, Intraparticle diffusion, Elovich, Fractional power, Bangham and Avrami model. All the kinetic models excellently fitted the adsorption data $Pb^{2+}$ into chitosan. Kinetic studies showed that the adsorption of $Pb^{2+}$ ions into SSC followed Elovich kinetic model. Intra particle diffusion model was used to determine the adsorption mechanism. However, Intraparticle diffusion was not the rate-determining step because the plot of $q_t$ against $t^{0.5}$ did not pass through the origin. This showed that there was some degree of boundary layer diffusion.

It can be concluded that chitosan from snail shells (SSC) offers an effective and efficient means of removing $Pb^{2+}$ from wastewater.

## ACKNOWLEDGMENTS

The author appreciates the support and materials provided by the Department of Chemical Engineering, Lagos State University Epe Campus and University of Lagos, Akoka, Yaba, Lagos, Nigeria, and the assistance of Engr. Amokun Mosunmola Khadijat during manuscript preparation.

## REFERENCES

Ahmad MA, Puad NAA, Bello OS (2014). Kinetic, equilibrium, and thermodynamic studies of synthetic dye removal using pomegranate peel-activated carbon prepared by microwave-induced KOH activation. Water Resources and Industry 6:18-35

Ajala, LO, Ali EE, (2012), Preparation and Characterization of groundnut shell-based activated charcoal. J. Appl. Sci Environ Manag. 24(12):2139-16

Babel S, Kumiawan TA (2004). Cr (VI) removal from synthetic wastewater using coconut shell charcoal and commercial activated carbon modified with oxidizing agent and/or chitosan.Chemosphere 54 (7): 951-967

Baby R, Hussein MZ, Zainal Z. ((2021) Functional activated carbon derived from palm kernel shells for the treatment of stimulated heavy metal-contaminated water. Nanometer.;11, 3133.

Daniel T Oyekunle, James A. Omoleye (2019). Effect of particle sizes on the kinetics of demineralization of snail shell for chitin synthesis using acetic acid. Heliyon 5(11):e02828.

El-Batouti, M.; Al-Harby, N. F.; Elewa, M. M. (2021) A. Review on Promising Membrane Technology Approaches for Heavy Metal Removal from Water and Wastewater to Solve Water Crisis. Water, 13, 3241–3262. DOI: 10.3390/w13223241.

Ghimire, S., Neupane, B., Pokhrel, S., Le, H. H., Lebek, W., Heinrich, G., Adhikari, R. (2011). "Conversion of chitin isolated from fresh-water prawns to chitosan and its characterization". Polymers Research Journal, 11(1), 1 15.

Ghorbani M., O. Seyedin, M. Agha Mohammad Hassan, (2020) Adsorptive removal of lead (II) ion from water and wastewater media using carbon-based nanomaterials as unique sorbents: a review, J. Environ. Manage., 109814, https://doi.org/10.1016/j.jenvman.2019.109814.

Hossain, M., Hossain, M., and Hassan, T. (2016). "Equilibrium, Thermodynamic and Mechanism Studies of Malachite". International Letters of Chemistry, Physics Astronomy, 64, 77-88.

Ho YS, Mckay G (2000). The kinetics of sorption of divalent metal ions onto sphagnum moss peat. Water Research 34(3):735-742.

Hussain, S. T.; Ali, S. A. K. (2021) Removal of Heavy Metal by Ion Exchange Using Bentonite Clay. J. Ecol. Eng, 22, 104–111. DOI: 10.12911/22998993/128865.

Iconaru, S. L.; Gu_egan, R.; Popa, C. L.; Motelica-Heino, M.;Ciobanu, C. S.; Predoi, D. Magnetite (Fe3O4) (2016) Nanoparticles as Adsorbents for as and Cu Removal. Appl. Clay Sci., 134,128–135. DOI: 10.1016/j.clay.2016.08.019

Islam S, Bhuiyan MAR, Islam MN (2017). Chitin and Chitosan: Structure, Properties and Applications in Biomedical Engineering. Journal of Polymers and the Environment 25(3):854-866.

Kalut, S.A. (2008) 'Enhancement of Degree of Deacetylation of Chitin in Chitosan Production', pp. 5-31.

Khazael, M., S. Nasseri, M.R. Ganjali, M. Khoobi and R. Nablzadeh et al., (2016). Response Surface Modeling of Lead (II) removal by grapheme oxide- Fe3O4 nanocomposite using Central composite design. J. Environ. Health Sci. Eng., Vol.14. 10.1186/s 40201-016-0243-1.

Khora, E. and Limb, L.Y. (2003) 'Implantable applications of chitin and chitosan', *Biomaterials*, pp. 2339-2349.

Kim, S.K. (2010) *Chitin, Chitosan, Oligosaccharides and Their Derivatives.*, New York: CRC Press.

Kumar, J.; Joshi, H.; Malyan, S. K. (2022) Removal of Copper, Nickel, and Zinc Ions from an Aqueous through Electrochemical and Nanofiltration Membrane Processes. Appl. Sci, 12, 1–15.

Li, M.; Hu, K.; Wang, J.9 (2021) Study on Optimal Conditions of Flocculation in Deinking Wastewater Treatment. J. Eng. Appl. Sci.35, 1–14.

Malkoc E, Nuhoglu Y (2007) Potential of tea factory waste for chromium (VI) removal from aqueous solutions: thermodynamic and kinetic studies. Sep Purif Technol 54:291–298

Moosa, A., Ridha, A., and Kadhim, N. (2016). Use of Biocomposite Adsorbents for the Removal of Methylene Blue Dye from Aqueous Solution. American Journal of Materials Science,6(5), 135-146.

Mujianto. (2012). Sintesis dan Modifikasi Kitosan dari Limbah Kulit Udang Untuk Aplikasi Enhanced Oil Recovery (Synthesis and Modification of Chitosan from Shrimp Shell Waste for Enhanced Oil Recovery Applications). Institut Teknologi Bandung (Bandung Institute of Technology

Nomanbhay S. M, Palanisamy K.; (2005) Removal of heavy metal from industrial Wastewater using chitosan coated oil palm shell charcoal. Electronic Journal of Biotechnology 8, pp.43-53.

Olafadehan OA, Amoo KO, Ajayi TO, Bello VE (2021). Extraction and characterization of chitin and chitosan from Callinectes amnicola and Penaeus notialis shell wastes. Journal of Chemical Engineering and Material Science 12(1):1-30.

Oliveira, E.A., S.F. Montanher and M.C. Rollemberg, (2011). Removal of textile dyes by sorption on low-cost sorbents. A case study: Sorption of reactive dyes onto Luffa cylibdrica. Desalin. Water Treat., 25: 54-64

Qasem, N. A. A.; Mohammed, R. H.; Lawal, D. U. (2021) Removal of Heavy Metal Ions from Wastewater: A Comprehensive and Critical Review. Npj Clean Water, 4, 1–15. DOI: 10.1038/ s41545-021-00127-0.

Rajeshwari S., Venckatesh.R and G.Sangeetha, (2010). "Activated Carbon Prepared from Eichornia Crassipes as an Adsorbent for the Removal of Dyes from Aqueous Solution". *International Journal of Engineering Science and Technology*, Vol.,2 (6), pp 2418-2427.

Shon. (2011). Effect of processing conditions on functional properties of collagen powder from skate (Raja kenojei) skins. Food Science and Biotechnology. 20(1):99-106.

Sivarajasekar N, Baskar R (2014). Adsorption of basic red onto activated carbon derived from immature cotton seeds: isotherm studies and error analysis. Desalination and Water Treatment 52(40- 42):7743-7765

Zhang Y, Y. Chen, W. Kang, H. Han, H. Song, C. Zhang, H. Wang, X. Yang, X. Gong, C. Zhai, (2020) Excellent adsorption of Zn (II) using NaP zeolite adsorbent synthesized from coal fly ash via stage treatment, J. Clean. Prod., 120736, https://doi.org/10.1016/j.jclepro.2020.120736

Zhao, Q.; Xu, T.; Song, X.; Nie, S.; Choi, S. E.; Chuanling, S. I. (2021) Preparation and Application in Water Treatment of Magnetic Biochar. Front. Bioeng. Biotechnol, 9, 2296–4185.

ylwan, I.; Thorin, E. (2021) Removal of Heavy Metals during Primary Treatment of Municipal Wastewater and Possibilities of Enhanced Removal: A Review. Water, 13, 1121. DOI: 10. 3390/w13081121.

Yoro KO, Singo M, Mulopo JL, Daramola MO (2017). Modelling and experimental study of the $CO_2$ capture. Energy Procedia 114:1643- 1664.

Zhu J, Z. Huang, F. Yang, M. Zhu, J. Cao, J. Chen, Y. Lin, S. Guo, J. Li, Z. Liu, (2021) Cadmium disturbs epigenetic modification and induces DNA damage in mouse preimplantation embryos, Ecotoxicol. Environ. Saf, 306, https://doi.org/10.1016/j.ecoenv.2021.112306.

10.51975/25400102.som
Journal of the Nigerian Society of Chemical Engineers, 40(1), 2025

# EVALUATION OF PHENOL REMOVAL FROM WASTEWATER WITH NANO-CHITOSAN AND ITS REGENERATION POTENTIAL

**[*]Abubakar Abubakar Ibrahim[1], Abdulfatai Jimoh[2], Ismail Babatunde Adefeso[3], Fatima Muhammad Abubakar[4] and Ibrahim Shaba Mohammed[5]**

*[1,3,4]Department of Chemical and Petroleum Engineering, Faculty of Engineering, Bayero University Kano, PMB 1033, Kano, Kano State, Nigeria*

*[2]Department of Chemical Engineering, Faculty of Engineering, University Abuja, PMB 117, Airport Road, Abuja, Nigeria*

*[5]Department of Agricultural and Bioresources Engineering, School of Engineering and Engineering Technology, Federal University of Technology Minna, PMB 65, Minna, Nigeria*

**Corresponding author: Tel: +2348032670719; E-Mail: aaIbrahim.cpe@buk.edu.ng*

**ABSTRACT**

*Phenol is considered to be a very toxic pollutant in refinery wastewater which poses danger to man and its environment. This study target was to establish the effective assessment of phenol removal using chitosan, nano-chitosan obtained from crab shells and their generative potentials. The crab shells were prepared and converted to chitin. The experiment conducted was at different conditions for both chitosan (CTS) and nano-chitosan (NCTS) to achieve basic polysaccharide of low molecular weight chitosan (LMWC) and low molecular weight nano-chitosan (LMWNC) for removal of phenol from the refinery wastewater. Various techniques were used to characterize both chitosan, nano-chitosan and refinery wastewater, such as Double beam UV- spectrophotometer, Fourier Transforms Infrared Spectroscopy (FTIR), X-Ray Fluorescence (XRF) and Dynamic Light Scattering (DLS). The characterization of obtained chitosan and nano-chitosan absorbents showed good surface area, high pore sizes, effective size reduction yield of over 80% with good content of macro elements and good molecular weight. The values of calcium were 6.6972%, 5.6422% for CTS and NCTS respectively. The results of interaction revealed at factors of 35% sodium hydroxide, 3 h and 75 $^{o}$C gives the degree of deacetylation (DD) to be 81.75%. The percentages of phenol removal were 87.88% and 98.77% for both CTS and NCTS respectively. The maximum regeneration obtained was 93.65 % which occurred at 50 mins. Hence, this showed that the synthesized nano-chitosan polysaccharide from white shrimp shells had the potential for phenolic compounds removal from refinery wastewater and the NCTS enhances the adsorption capacity due to higher surface areas.*

***Keywords:*** *chitosan; nano-chitosan; phenol; wastewater; refinery; regeneration.*

## 1.0 INTRODUCTION

Wastewater from industrial sources such as refinery has been reported as the nuisance of life-threatening contaminating ecosystem (Ibrahim et al., 2022a, Ibrahim et al., 2022b). Every year, about 140 billion tons of industrial and agricultural wastes are generated of which 13 billion tons are from plant biomass waste, only 3% are used for making goods (Ibrahim et al., 2022b, Apollon et al., 2024, Khader et al., 2024). The study of Mohammad et al. (2014) reported about 30 million tons/year of waste generated from the aquatic processing are thrown into the sea or remain on the land causing environmental contaminants and public health concerns, because of their high perishability and high pollution effect (Kesari et al., 2021). The contaminants are characterized by the presence of high concentrations of toxic organic hydrocarbon like phenols (Khader et al., 2024).

Phenol is among the most common organic pollutants and is present in wastewater from petroleum industries (Mohammad et al., 2014, Radha Thirumalaiarasu and Mahalakshmi, 2022). Phenol is the 11th of the 126 chemical priority pollutants by United State Environmental Protection Agency (USEPA) with odour threshold limit of 0.04 ppm (Ibrahim et al., 2022a, Panigrahy et al., 2022). The work of Soto et al. (2011) reported that as a result of toxic and inhibitory characteristics, phenols are very difficult to remove by biological processes (Panigrahy et al., 2022, Filipowicz et al., 2020). The removal of the phenol from wastewater can be achieved through several techniques such as physical, chemical, and biochemical processes (Panigrahy et al., 2022, Oliveira et al., 2021, Radha Thirumalaiarasu and Mahalakshmi, 2022).

The techniques used for phenol removal from wastewater are adsorption, which depends on adsorbents with high adsorption capacity, good mechanical resistance, and simple restoration (Khader et al., 2024, Zhou et al., 2023). Other methods used are membrane separation (Chen et al., 2019, Lee et al., 2022), electrocoagulation (Sadeghi et al., 2019), Fenton oxidation (Fu et al., 2020), and catalytic reduction (Gabris et al., 2022, Abdelfattah and Ismail, 2023, Salahuddin et al., 2020) theirs associated problems hinder the effective usage (Ibrahim et al., 2022b, Ibrahim et al., 2017). These identified challenges make

it very necessary to focus more on eco-friendly methods of getting rid of this toxic constituent of effluent before being discharged into water body (Ibrahim et al., 2022a). The needs for a more efficient method for synthesizing adsorbents containing natural polymers have received reorganization, in particular polysaccharides. Nano-chitosan, a natural biopolymer derived from chitin, has gained attention due to its biocompatibility, biodegradability, and excellent adsorption properties (Ibrahim et al., 2022a). Therefore, the major focus of this research is using more abundant aquatic waste like crab shells.

The valorization of aquatic wastes through CTS and NCTS preparation is to avoid the negative influences on human health and the environment (El Kaim Billah et al., 2023). CTS and NCTS are new polymeric materials and have demonstrated many good applications (Ibrahim et al., 2017). CTS is a semi-crystalline cationic polysaccharide that attracts positively charged molecules and enhances bonding due to the presence of the -$NH_2$ group. In addition, the -OH group is also present in the structure and helps to increase the adsorption capacity (Kou et al., 2022). Due to their large specific surface area, small size, and structures, CTS and NCTS have been proven to possess a great potential as superior adsorbents for removing many kinds of organic and inorganic contaminants from natural water and wastewater (Ibrahim et al., 2017, Sivakami et al., 2013). Also, studies have shown that this adsorbent (CTS/NCTS) is low cost which is yet to be exploited with phenol removal from refinery wastewater. This research work deems it fit to assess effectiveness of phenol removal capacity on CTS and NCTS. The main aim of the research is to evaluate the effectiveness of phenol removal capacity by CTS and NCTS.

## 2.0 MATERIALS AND METHODS

### 2.1 Chemicals and Materials

Crab shells was obtained from Dukun, Mokwa Local Government of Niger State and wastewater obtained from Kaduna Refinery, were stored in a cleaned container, put into the freezer and later transported to the laboratory for necessary analysis (Ibrahim et al., 2013). Chemical used include hydrogen sulphate ($H_2SO_4$), cupric sulphate ($CuSO_4$), sodium hydroxide (NaOH), lactic acid ($CH_3CH(OH)CO_2H$), sodium tripolyphosphate (STPP), acetone $(CH_3)_2CO$ and hydrogen peroxide ($H_2O_2$) all of which were analytical grades manufactured by Analar BDH. The apparatus and instruments used were weighing balance (Scout pro SPU), Fourier Transform Infrared spectrometer (Parkin Elmer 200). Dynamic Light Scattering (DLS) - Malvern, Double beam UV - spectrophotometer - G5-UV61PC, Shaking Water Bath - 030S and Viscometer - NDJ - 5S.

### 2.2 Deacetylation of Chitin to Chitosan

The removals of acetyl groups from chitin were done with the aid of 35% of NaOH, temperature 75 $^{\circ}$C and time 3 h. Then centrifugation was carried out for 20 mins at 2000 rpm after each washed with distilled water until the pH values reached neutral value. The supernatant was filtered and residues were oven dried at 60 $^{\circ}$C for 6 h. The obtained chitosan was ground to small particle size of 250 micrometer and stored for further analysis. Also, about 7% $H_2O_2$ was added to the obtained CTS and heated at 60 $^{\circ}$C for 1 h and filtered. The distilled water was used to neutralize it and about 5 ml of ethanol was added to the solution, for 6 h, after which it was filtered, dried and weighed (Ibrahim et al., 2017).

### 2.3 Nano-chitosan Synthesis

About 5 g of milled CTS were primed at various concentrations of 2% sodium tripolyphosphate (STPP), 2% acetic acid solution and time of 2.5 h. The STPP were added dropwise and mixed at 450 rpm. The formed nano-chitosan (NCTS) washed several times with distilled water, filtered and oven dried at 60 $^{\circ}$C (Ibrahim et al., 2022a) for 6 h (Wijesena et al., 2017, Vijayalakshmi et al., 2017). The average of particle size distribution was calculated with the aid of dynamic light scattering (DLS).

### 2.4 Characterization of Chitosan and Nano-chitosan

The surface functional groups of chitosan and nano-chitosan were determined by Fourier Transform Infrared (FTIR) spectroscopy. The regeneration capacity of nano-chitosan was obtained by Fourier Transform Infrared (FTIR) spectroscopy. The data obtained were plotted with the aid of essential Fourier Transform Infrared software (Ibrahim et al., 2022a, Ibrahim et al., 2024). The structural analysis of the samples was conducted using PAN analytical X' Pert PRO MPD X-ray diffraction system PW3040/60 machine. The average of particle size of nano-chitosan distribution was obtained with the aid of Dynamic Light Scattering (DLS)-Malvern.

### 2.5 Digestion of Refinery Wastewater

About 350 $cm^3$ of wastewater samples were distilled to obtain 300 $cm^3$ of distillate which was transferred to a separating funnel. Also, about 10 $cm^3$ of buffer solution with 2 $cm^3$ each of 4aminiantipyrine and potassium hexacyanoferrate were added to separating funnel respectively, allowed for 10 mins. The collected phenol was dried with sodium sulphate and double beam spectrophotometer (G5 - UV61PC) was used to determine concentration of phenol at wavelength of 460 nm.

#### 2.5.1 Phenol removal by both LMWC and LMWNC

Certain amounts of both low molecular weight chitosan (LMWC) and low molecular weight nano-chitosan (LMWNC) were added to different conical flasks (250 ml), filled with the same various volume of known phenol concentration in wastewater as shown in Figure 2.1. Each of the adsorbents and adsorbate (phenol), were mixed with aid of oscillating shaker.

The amounts of phenol removed from Refinery wastewater (RWW) by the adsorbents were obtained.

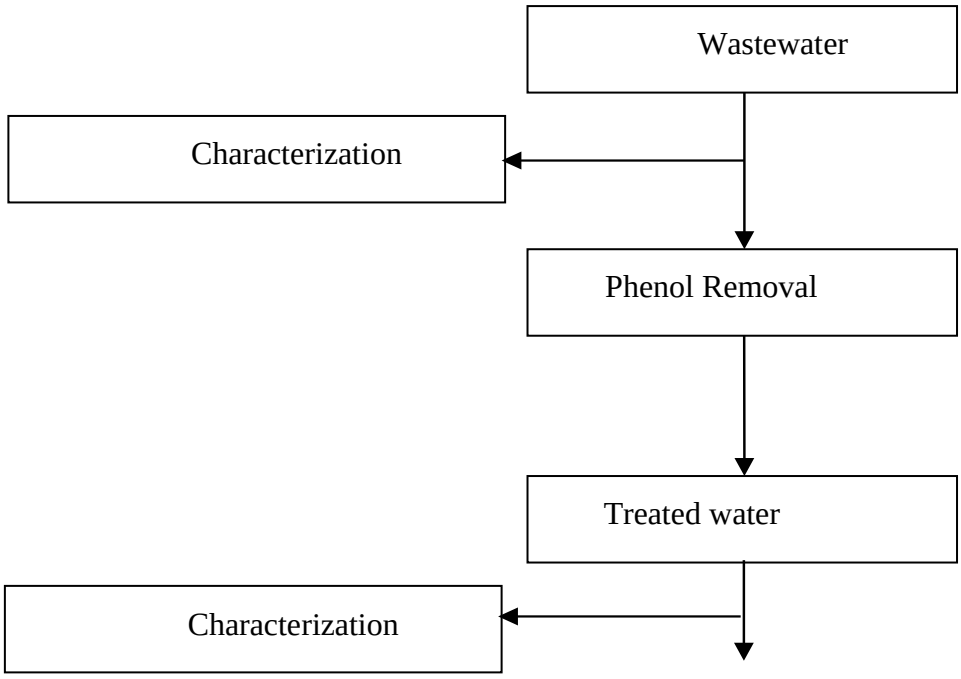


**Figure 2.1: Sketch Diagram of Phenol Removal (Ibrahim et al., 2024).**

**2.5.2 Regeneration of nano-chitosan for phenol removal**

The economy and environmental importance of adsorption depends on efficiency of regeneration. Problems associated with adsorption processes are disposal of adsorbent after usage. The regeneration can reduce the need of new adsorbent and also reduce the problem of disposal of used adsorbent. Various regeneration methods have been used with different degrees of success. These methods include washing, thermal and chemical regeneration with their respective parameters.

## 3.0 RESULTS AND DISCUSSION

### 3.1 Mineral Composition of Chitosan and Nano-chitosan

The results of mineral composition of the CTS and NCTS were shown in Table 3.1.

**Table 3.1: Mineral Composition of Chitosan and Nano-Chitosan**

| Element | CS (%) | NCS (%) |
|---|---|---|
| K | 0.0052 | 0.0034 |
| Ca | 7.4132 | 6.1321 |
| Mn | LOD | LOD |

***Note**: LOD: low detection, CS: Chitosan, NCS: Nano-chitosan*

Table 3.1 shows that the species are good sources of macro elements such as calcium, potassium while phosphorus was obtained from XRF analysis. After each stage of preparation, the values of calcium were 7.4132, 6.1321 (%) for CTS and NCTS respectively.

The decrease was due to demineralization carried out. This is supported by the findings of (Fawole, 2007) and (Abdulkarim et al., 2013). Nevertheless, the very low values recorded may be due to the fact that the aquatic animal needs the micro elements in trace amounts and perhaps the concentrations in the water body is very low (Sunday et al., 2012).

### 3.2 Chitosan and Nano-chitosan Synthesis

The results revealed at factors of 35% sodium hydroxide, 3 h and 75 $^{\circ}$C gives the degree of deacetylation (DD) to be 81.75%. These values were higher than 60.69% degree of deacetylation reported by (Abdulkarim et al., 2013). The deacetylation degree showed that the percentage of acetyl groups can be removed from the chitin to produce CTS, which play a vital role in determine the quality of produced CTS (El Knidri et al., 2020, Kou et al., 2022). From the experiment carried out, degree of deacetylation and molecular weight of CTS produced from waste crab shells were 81.76% and 74334.19 Da.

The results of interaction shows that the 2% STTP, 2.5 h and 2% Acetic acid gives 82% for the percentage size reduction.

It was observed from experiment that the particle size of NCTS was 82% yields which may be due to the accumulation of polymer molecules and intermolecular cross linking through TPP spanning (Khorram and Fallah, 2018). Surface area of the samples used plays a vital role in influencing the application and performance of the adsorbent. Increase in surface area of the samples was due to the outcome of the treatment processes such as demineralization, deproteination, deacetylation and nano sizing chitosan. The larger the surface area, the better the performance of adsorbent (Choorit et al., 2008).

### 3.3 Fourier Transform Infrared (FTIR)

The surface functional groups of the chitosan and nano-chitosan were determined by Fourier Transform Infrared (FTIR) spectroscopy. The data obtained were plotted with the aid of essential Fourier Transform Infrared Software as were presented in Figure 3.1.

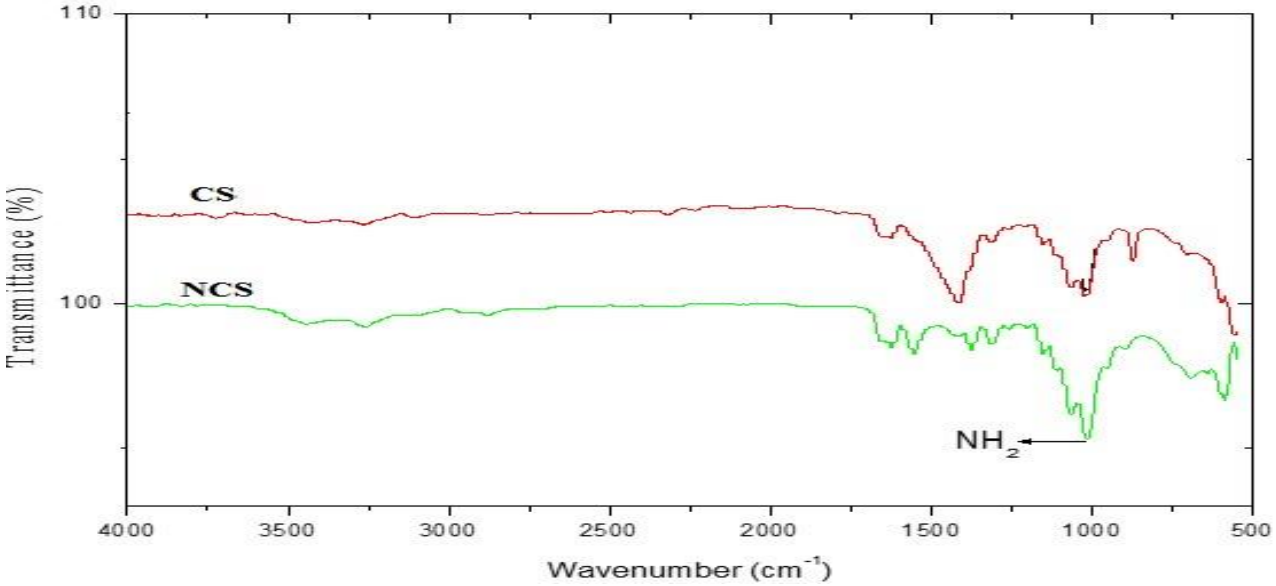


**Figure 3.1: Infrared Spectra of the Chitosan (CS) Nano-Chitosan (NCS) Obtained from Waste Crab Shells**

**Table 3.2: Functional Group and their Respective Peak Using FTIR**

| Functional Group | CS | NCS | Standard |
|---|---|---|---|
| C – O | 1009.03 | 1026.09 | 1300 – 1000 |
| N – H | 3216.03 | 3261.36 | 3500 – 3100 |
| Amide II | 1591.13 | 1620.72 | 1640 – 1550 |
| C = O | 1587.11 | 1656.86 | 1750 – 1625 |
| O – H | 2912.13 | 2934.64 | 3400 – 2400 |
| $NH_2$ | 1001.31 | 1026.09 | 1030 – 1050 |
| Amide I | 1621.15 | 1621.72 | 1670 – 1600 |
| C O | 2030.37 | 2139.30 | 2200 – 2100 |

The FTIR studies of the CTS and NCTS were compared with standard commercial species. The major absorption band represents the free amino group ($-NH_2$) at $C_2$ position of glucosamine, were observed as shown in Table 3.2. The absorption bands which represent the -C-O stretching of primary alcoholic group ($-CH_2$ - OH) were observed for CTS and NCTS. Also, the main vibration values obtained were compared with standard that indicated the N-H stretching, symmetric $CH_3$ stretching and asymmetric $CH_2$ stretching, CH stretching, C=O stretching in secondary amide (amide I) and C-N- stretching in secondary amide (amide II) confirms with their structure as shown in Table 3.2 and Figure 3.1.

The broad and weak absorption bands were due to the combined effect of $NH_2$ and OH groups. The absorption band of each sample could be attributed to the N-H secondary amine stretches. The weak absorption band in the region was due to the presence of methylene and methyl groups in each sample structure and originates due to the C-H bond. The absorption peak at 3216.03 $cm^{-1}$ and 3261.36 $cm^{-1}$ for CTS and NCTS were due to the presence of N-H of amide II bond structure in the polymer. These spectra values were within the standard for CTS and NCTS and thus are similar to vibration patterns reported by (Ibrahim et al., 2022a, Ibrahim et al., 2024, Pereira et al., 2014) with insignificant changes in the positions and intensities which were due to the differences in the method of synthesized polymer.

**3.4 Assessment of Wastewater and Treated Water**

For this study, the wastewater collected from Kaduna Refining and Petrochemical Company (KRPC) was analyzed before treated with the developed adsorbents as shown in the Table 3.3 and post analysis was also carried out.

**Table 3.3: Analyzed Wastewater and Treated Water from Kaduna Refining Plant**

| Parameter | Wastewater | NCTS | CTS | WHO |
|---|---|---|---|---|
| pH | 6.79 | 7.00 | 6.70 | 7.50 |
| Temperature ($^{o}$C) | 28.20 | 27.00 | 28.00 | <35.00 |
| Total Solids (mg/l) | 140.71 | 57.40 | 80.30 | 30.00 |
| Total Dissolved Solids (mg/l) | 380.07 | 241.23 | 310.51 | 500.00 |
| Suspended Solids (mg/l) | 89.26 | 22.51 | 48.57 | >10.00 |
| Dissolved Oxygen (mg/l) | 12.31 | 8.41 | 10.22 | 8-10.00 |
| Biochemical Oxygen Demand (mg/l) | 15.94 | 9.42 | 11.56 | 9.42 |
| Chemical Oxygen Demand (mg/l) | 208.72 | 67.28 | 124.26 | 67.28 |
| Phenol (mg/l) | 7.18 | 0.033 | 0.40 | 0.001 |
| Chloride (mg/l) | 57.89 | 25.08 | 33.06 | 250.00 |
| Sulphate | 250.00 | 125.00 | 160.00 | 400.00 |
| Ammonia (mg/l) | 10.75 | 3.25 | 6.35 | 0.20 |
| Conductivity | 733.00 | 366.00 | 424.00 | 200.00 |

Wastewater sample was collected from KRPC Ltd, Kaduna State. The wastewater sample was analyzed for general characterization and treated with both CTS and NCTS to determine the presence and level of pollutant as shown in the Table 3.3. The values of the pollutant before and after treatment with the adsorbents observed that pH of wastewater increased after treatment from 6.79 to 7.00 and 6.70 for both NCTS and CTS respectively. The electrical conductivity was observed to be reduced after treatment from 733 to 366 and 424.00 for both NCTS and CTS respectively, reduction of chemical oxygen demand was observed after treatment within the range of 208.72 to 67.28 and 124.26 mg/l for both NCTS and CTS respectively and after treatment, the biochemical oxygen demand was observed to be reduced from 15.94 to 9.42 and 11.56 mg/l for both NCTS and CTS respectively. This indicates that the low-cost adsorbent has better adsorption capacity in wastewater treatment, which could be attributed to the modified CTS. However, NCTS has higher adsorption capacity of pollutants compared to CTS. Consequently, this NCTS from waste crab shells could be employed in multi-component wastewater treatment.

**3.4.1 Influence of contact time**

The influences of contact time between adsorbate on the adsorbents (CTS and NCTS) are presented below (Figures 3.2 and 3.3) It shows that adsorption process was faster at start but get slower as time progresses. This could be as result of vacant active site on the adsorbents at first stage which later got saturated as the time progressed. Also, low mass transfer was observed at lower concentration compared to high mass transfer in the higher initial concentration. The adsorption capacity of the adsorbents increased with an increase in contact time, which paves way to the determinant factor in evaluating the adsorption capacity and percentage removal of an adsorbent as shown in Figures 3.2 and 3.3.

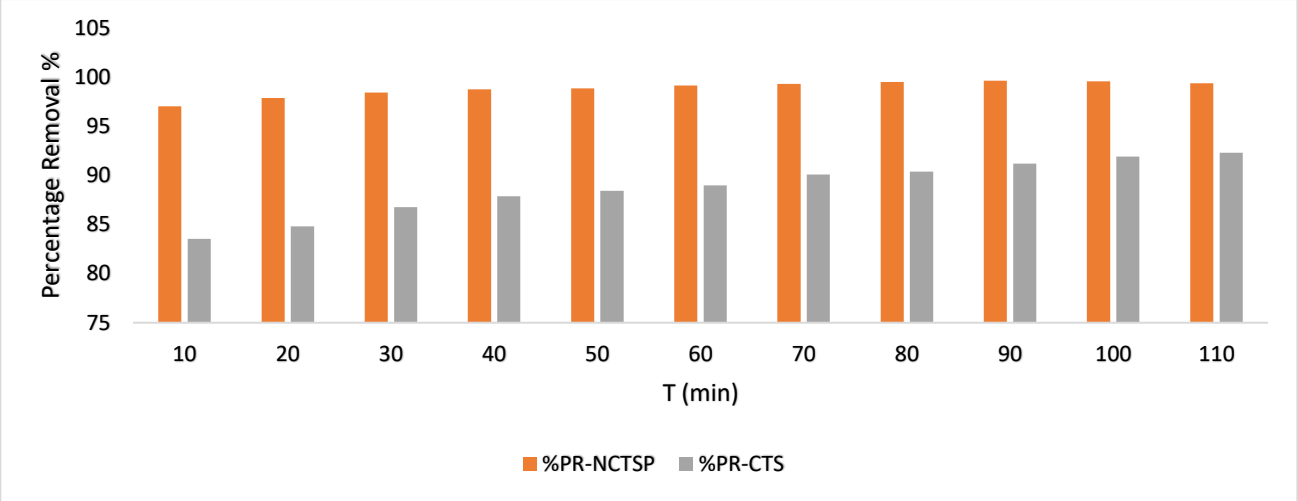


**Figure 3.2: Percentage Phenol Removal by Nano-Chitosan and Chitosan**

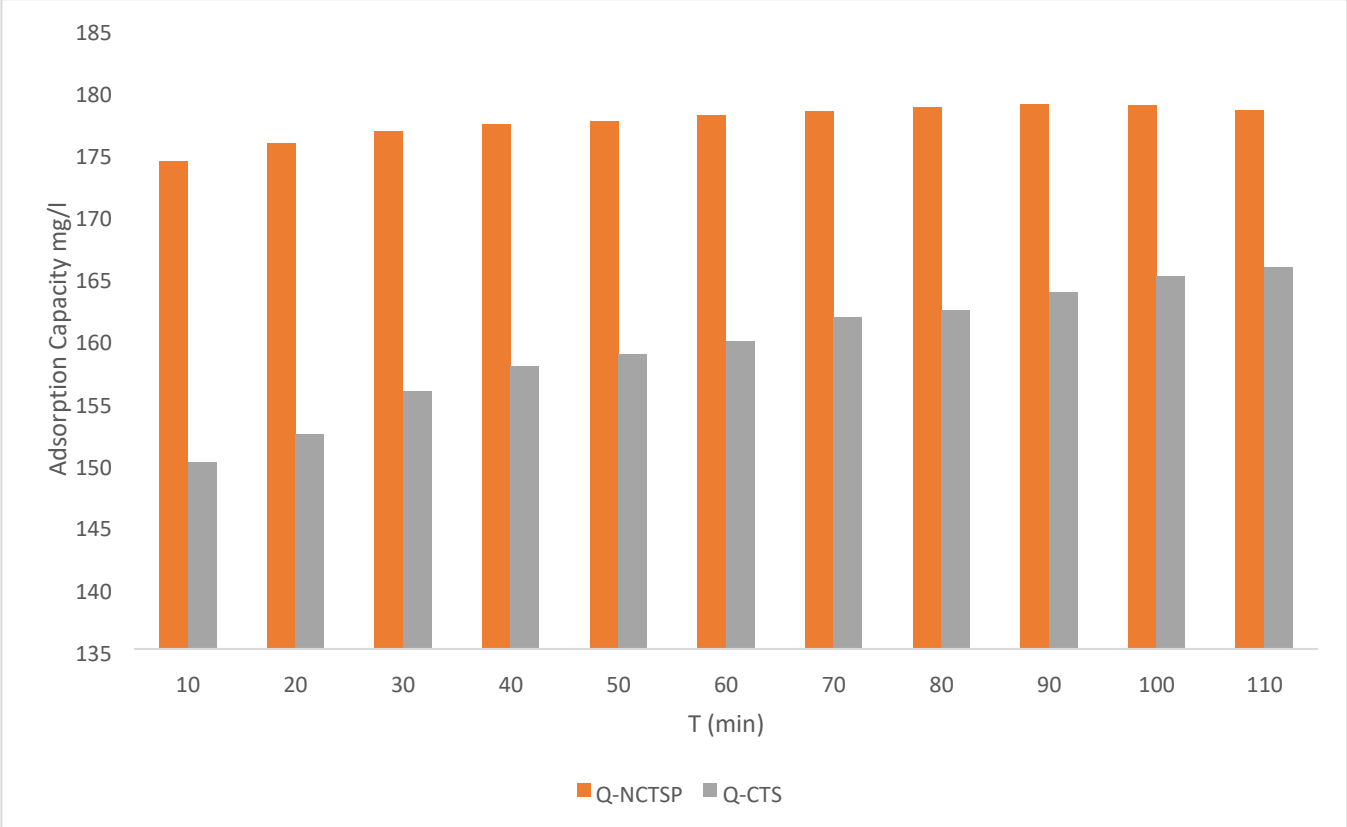


**Figure 3.3: Phenol Adsorption Capacity by Nano-Chitosan and Chitosan**

Figures 3.2 and 3.3 showed that adsorption capacity and removal efficiency of NCTS were 177.30 mg/g and 98.77% and that of CTS were 87.88 mg/g and 87.88% all within 10 to 40 mins. It was also deduced that large amount of phenol was adsorbed in the first 10 - 40 mins of contact time. This initial fast rate of adsorption may be a consequence of the availability of several binding sites for solute uptake. The large amount of phenol removal in the first few minutes of contact time between solute and adsorbent may be due to increased surface area resulting from the influence of improved surface reactivity from the influence of chemical pretreatment. Similar observation of large removal in less than 20 mins was reported by (El Jamal and Awala, 2011).

### 3.4.2 Influence of temperature

The influent of temperature on phenol adsorption on CTS and NCTS were presented as the adsorbents witnessed an increase in adsorption removal percentage and no significant change with further increase of temperature. A rapid increase in adsorption was observed within initial time at different temperatures

and then a gradual increment was observed. At higher temperatures the rate of diffusion of solute within the pores of the adsorbent increases (Ibrahim et al., 2022a).

**3.4.3 Influence of adsorbent dosage**

The influence of adsorbent dosage on adsorption of phenol using NCTS and CTS were carried out as different doses of adsorbents ranging from 1.36 - 4. 68 mg/l. The maximum percentage removal of phenol was observed as shown in Figure 3.3 and compared to the value reported by (Auta et al., 2012). The low adsorption percentage can be ascribed to the fact that all the adsorbents have a limited number of active sites that would have achieved saturation above a certain adsorbate concentration (Barkat et al., 2009). Effective utilization of synthesis NCTS cum further research to domesticate the NCTS adsorbent will contribute to SDG goals - SDG 3 (good health and wellbeing) and SDG 6 (clean water and sanitations).

**3.5 Regeneration Effectiveness of Nano-chitosan for Phenol Removal**

The following results were obtained after carried of regeneration procedure to ascertain the effectiveness of reuse of NCTS in phenol removal. However, about 20% EDTA solution was found to be effective in desorbing phenol and recovering the adsorption. From the results obtained, maximum regeneration was 93.65, 92.16, 91.49, 91.11, 90.11, 86.49 and 80.65% from first to seventh cycles which occurred at 50 min intervals as presented in Table 3.4. The results indicated that the batch gets saturated early and the regeneration efficiency increases slightly. The material was tested in seven cycles of sorption/desorption and it demonstrated reproducible performance, similar results were obtained by (Vijayalakshmi et al., 2017).

**Table 3.4: Regeneration Data of Phenol Adsorbed on Prepared NCTSP**

| S/N | Time (min) | 10 | 20 | 30 | 40 | 50 |
|---|---|---|---|---|---|---|
| | Cycles | Percentage Regenerations of Nano-chitosan % | | | | |
| 1 | Cycle 1 | 80.81 | 84.04 | 85.39 | 92.31 | 93.65 |
| 2 | Cycle 2 | 78.57 | 81.93 | 83.82 | 89.47 | 92.16 |
| 3 | Cycle 3 | 73.91 | 79.01 | 84.62 | 89.29 | 91.49 |
| 4 | Cycle 4 | 71.91 | 80.26 | 83.87 | 88.46 | 91.11 |
| 5 | Cycle 5 | 65.91 | 79.17 | 80.7 | 87.23 | 90.00 |
| 6 | Cycle 6 | 62.2 | 77.05 | 76.92 | 82.93 | 86.49 |
| 7 | Cycle 7 | 60.81 | 76.92 | 70.21 | 77.78 | 80.65 |

**3.6 Fourier transform infrared (FTIR) of Adsorbent after Regeneration**

The surface functional groups of the based adsorbent were determined by Fourier Transform Infrared (FTIR) spectroscopy. The data obtained were plotted with Origin Software as presented in Figure 3.4.

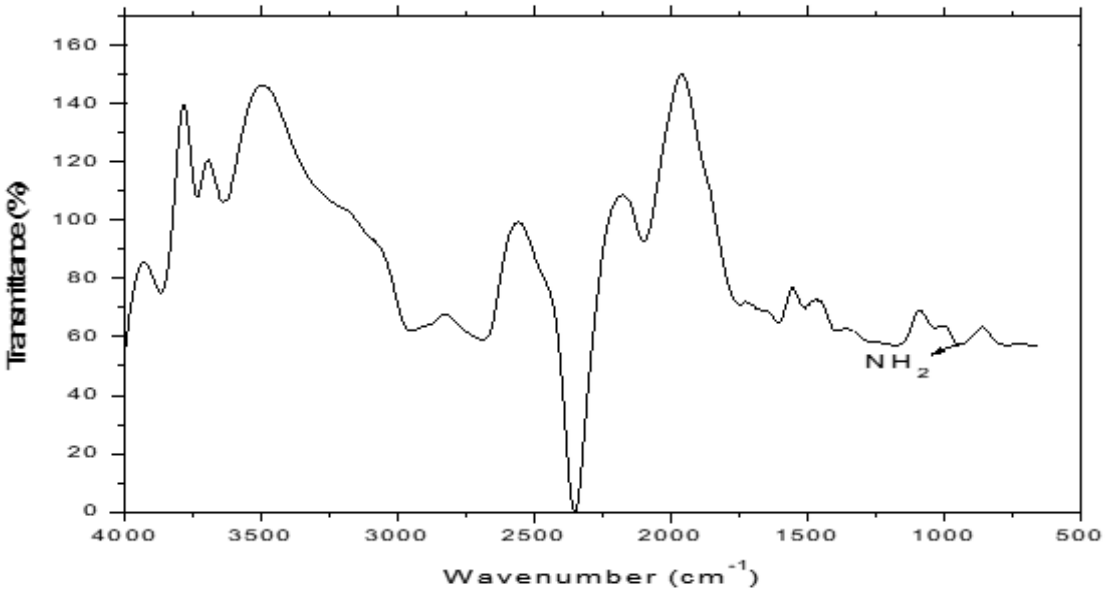


**Figure 3.4: Infrared Spectra of the Adsorbent after Adsorption**

The FTIR studies of the adsorbents were compared with standard commercial species. The broad and weak absorption bands were due to the combined effect of -$NH_2$ and -OH groups. The absorption band of each sample could be attributed to the N-H secondary amine stretches. The weak absorption band in the region were due to the presence of methylene and methyl groups in each sample structure and originates due to the C-H bond. These spectral values obtained were within the standard and are similar to vibration patterns reported by (Pereira et al., 2014) with insignificant changes in the positions and intensities which was due to the differences in the method of synthesized polymer.

## 4.0 CONCLUSION

The results of interaction revealed at factors of 35% sodium hydroxide, 3 h and 75 °C gives the DD to be 81.75%. This may be accredited to the procedures applied during the preparation. The standard quality of chitosan is also determined through molecular weight. It was observed from experiment that the particle size of NCTS was 82% yields as results of interaction of 2% STTP, 2.5 h and 2% Acetic acid. The value obtained may due to the accumulation of polymer molecules and intermolecular cross linking through TPP spanning. The percentages of phenol removal were 87.88% and 98.77% for both chitosan and nano-chitosan respectively.

**Acknowledgment**

The author would like to thank the Petroleum Technology Development Fund Nigeria.

**Declaration of competing interest**

The authors declare that they do not have any competing interest in the preparation and submission of this manuscript.

## 5.0 REFERENCES

ABDELFATTAH, I. & ISMAIL, A. A. 2023. Reduction of COD concentration and complete removal of phenol in industrial wastewater utilizing mesoporous TiO2 nanoparticles under UVA illumination. *Optical Materials,* 145**,** 114410.

ABDULKARIM, A. Y., ISA, M. T., ABDULSALAM, S., MUHAMMAD, A. & AMEH, A. O. 2013. Extraction and Characterisation of Chitin and Chitosan from Mussel Shell. *Civil and environmental research,* 3**,** 108-114.

APOLLON, W., RUSYN, I., KULESHOVA, T., LUNA-MALDONADO, A. I., PIERRE, J. F., GWENZI, W. & KUMAR, V. 2024. An overview of agro-industrial wastewater treatment using microbial fuel cells: Recent advancements. *Journal of Water Process Engineering,* 58**,** 104783.

AUTA, M., JIBRIL, M., TAMUNO, P. B. L. & AUDU, A. A. 2012. Preparation of activated carbon from oil palm fruit bunch for the adsorption of Acid Red 1 using optimized Response surface methodology. *International Journal of Engineering Research and Applications (IJERA)* 2**,** 1805 - 1815.

BARKAT, M., NIBOU, D., CHEGROUCHE, S. & MELLAH, A. 2009. Kinetics and thermodynamics studies of chromium(VI) ions adsorption onto activated carbon from aqueous solutions. *Chemical Engineering and Processing: Process Intensification,* 48**,** 38-47.

CHEN, Y., ZHANG, Z., CHEN, D., CHEN, Y., GU, Q. & LIU, H. 2019. Removal of coke powders in coking diesel distillate using recyclable chitosan-grafted Fe3O4 magnetic nanoparticles. *Fuel,* 238**,** 345-353.

CHOORIT, W., PATTHANAMANEE, W. & MANURAKCHINAKORN, S. 2008. Use of response surface method for the determination of demineralization efficiency in fermented shrimp shells. *Bioresource Technology,* 99**,** 6168-6173.

EL JAMAL, M. M. & AWALA, H. M. 2011. EQUILIBRIUM AND KINETICS STUDY OF ADSORPTION OF SOME DYES ONTO FELDSPAR. *Journal of the University of Chemical Technology and Metallurgy,* 46**,** 45-52.

EL KAIM BILLAH, R., AYOUCH, I., ABDELLAOUI, Y., KASSAB, Z., KHAN, M. A., AGUNAOU, M., SOUFIANE, A., OTERO, M. & JEON, B.-H. 2023. A Novel Chitosan/Nano-Hydroxyapatite Composite for the Adsorptive Removal of Cd(II) from Aqueous Solution. *Polymers* [Online], 15.

EL KNIDRI, H., LAAJEB, A. & LAHSINI, A. 2020. Chapter 2 - Chitin and chitosan: chemistry, solubility, fiber formation, and their potential applications. *In:* GOPI, S., THOMAS, S. & PIUS, A. (eds.) *Handbook of Chitin and Chitosan.* Elsevier.

FAWOLE. Proximate and Mineral Composition in Some Selected Fresh Water Fishes in Nigeria. 2007.

FILIPOWICZ, N., MOMOTKO, M., BOCZKAJ, G. & CIEŚLIŃSKI, H. 2020. Determination of phenol biodegradation pathways in three psychrotolerant yeasts, Candida subhashii A011, Candida oregonensis B021 and Schizoblastosporion starkeyi-henricii L012, isolated from Rucianka peatland. *Enzyme and Microbial Technology,* 141**,** 109663.

FU, C.-C., TRAN, H. N., CHEN, X.-H. & JUANG, R.-S. 2020. Preparation of polyaminated Fe3O4@chitosan core-shell magnetic nanoparticles for efficient adsorption of phosphate in aqueous solutions. *Journal of Industrial and Engineering Chemistry,* 83**,** 235-246.

GABRIS, M. A., REZANIA, S., RAFIEIZONOOZ, M., KHANKHAJE, E., DEVANESAN, S., ALSALHI, M. S., ALJAAFREH, M. J. & SHADRAVAN, A. 2022. Chitosan magnetic

graphene grafted polyaniline doped with cobalt oxide for removal of Arsenic(V) from water. *Environmental Research,* 207**,** 112209.

IBRAHIM, A. A., JIMOH, A., ADEFESO, I. B., MOHAMMED, I. S., MOHAMMED, A. & BERNARD, E. 2024. Effectiveness of Chitosan and Nano–Chitosan for Phenol Removal from Refinery Effluent. *Applied Journal of Environmental Engineering Science,* 10**,** 137 - 154.

IBRAHIM, A. A., JIMOH, A., AUTA, M. & YAHYA, D. 2017. *OPTIMIZATION AND MODELING OF CHITIN SYNTHESIS FROM FISH SCALE USING RESPONSE SURFACE METHODOLOGY (RSM).*

IBRAHIM, A. A., JIMOH, A., DIEKOLA, Y. M. & AUTA, M. 2022a. Extraction of Nano-Chitosan from Waste White Shrimp Shells for Removal of Phenol from Refinery Wastewater: Optimization of Chitosan Synthesis and Phenol Adsorption. *ABUAD Journal of Engineering Research Development (AJERD),* 5**,** 93 - 109.

IBRAHIM, A. A., JIMOH, A., DIEKOLA, Y. M. & AUTA, M. 2022b. Proximate Analysis and Characterization of some Aquatic Wastes as Potential Feedstock for Chitin/Chitosan Production. Nigeria Journal of Engineering and Applied Sciences (NJEAS). 5(1). 93 -101.

IBRAHIM, A. A., JIMOH, A., OKAFOR, J. O., ABDULKAREEM, A. S. & GIWA, A. 2013. Effect of Lead Mining Activities on Crop Plants and Water: A Case Study of Tunga Tsauni, Gurara, Niger State, Nigeria. *International Journal of Engineering Research & Technology (IJERT),* 2**,** 755 - 765.

KESARI, K. K., SONI, R., JAMAL, Q. M. S., TRIPATHI, P., LAL, J. A., JHA, N. K., SIDDIQUI, M. H., KUMAR, P., TRIPATHI, V. & RUOKOLAINEN, J. 2021. Wastewater Treatment and Reuse: a Review of its Applications and Health Implications. *Water, Air, & Soil Pollution,* 232**,** 208.

KHADER, E. H., KHUDHUR, R. H., MOHAMMED, T. J., MAHDY, O. S., SABRI, A. A., MAHMOOD, A. S. & ALBAYATI, T. M. 2024. Evaluation of adsorption treatment method for removal of phenol and acetone from industrial wastewater. *Desalination and Water Treatment,* 317**,** 100091.

KHORRAM, A. G. & FALLAH, N. 2018. Treatment of textile dyeing factory wastewater by electrocoagulation with low sludge settling time: Optimization of operating parameters by RSM. *Journal of Environmental Chemical Engineering,* 6**,** 635-642.

KOU, S., PETERS, L. & MUCALO, M. 2022. Chitosan: A review of molecular structure, bioactivities and interactions with the human body and micro-organisms. *Carbohydrate Polymers,* 282**,** 119132.

LEE, H. J., PARK, C.-G., YEO, I.-S., PARK, J. H. & MAGNONE, E. 2022. Successful removal of phenol from industrial wastewater using novel hydrophobic modified ceramic hollow fiber membrane contactors with remarkably high stability. *Journal of Industrial and Engineering Chemistry,* 114**,** 402-408.

MOHAMMAD, Y., SHAIBU-IMODAGBE, E., IGBORO, S., GIWA, A. & OKUOFU, C. 2014. Adsorption of phenol from refinery wastewater using rice husk activated carbon. *Iranica Journal of Energy & Environment,* 5.

OLIVEIRA, K. M. G. D., CARVALHO, E. H. D. S., SANTOS FILHO, R. D., SIVEK, T. W., THÁ, E. L., SOUZA, I. R. D., COELHO, L. D. D. S., PIMENTA, M. E. B., OLIVEIRA, G. A. R. D., OLIVEIRA, D. P. D., CESTARI, M. M. & LEME, D. M. 2021. Single and mixture toxicity evaluation of three phenolic compounds to the terrestrial ecosystem. *Journal of Environmental Management,* 296**,** 113226.

PANIGRAHY, N., PRIYADARSHINI, A., SAHOO, M. M., VERMA, A. K., DAVEREY, A. & SAHOO, N. K. 2022. A comprehensive review on eco-toxicity and biodegradation of phenolics: Recent progress and future outlook. *Environmental Technology & Innovation,* 27**,** 102423.

PEREIRA, A. G. B., MUNIZ, E. C. & HSIEH, Y.-L. 2014. Chitosan-sheath and chitin-core nanowhiskers. *Carbohydrate Polymers,* 107**,** 158-166.

RADHA THIRUMALAIARASU, S. & MAHALAKSHMI, G. K. 2022. Development of Various Strategies for the Removal of Phenol Pollutant. *In:* VASANTHY, M., SIVASANKAR, V. & SUNITHA, T. G. (eds.) *Organic Pollutants: Toxicity and Solutions.* Cham: Springer International Publishing.

SADEGHI, A., TASHAKKORIAN, H. & TAJBAKHSH, M. 2019. Fe3O4-TiO2/chitosan nanobiocomposite as a novel cadmium adsorbent: fabrication, characterization, equilibrium isotherms, adsorption kinetics and thermodynamics study. *DESALINATION AND WATER TREATMENT,* 142**,** 193-204.

SALAHUDDIN, N. A., EL-DALY, H. A., EL SHARKAWY, R. G. & NASR, B. T. 2020. Nano-hybrid based on polypyrrole/chitosan/grapheneoxide magnetite decoration for dual function in water remediation and its application to form fashionable colored product. *Advanced Powder Technology,* 31**,** 1587-1596.

SIVAKAMI, M. S., GOMATHI, T., VENKATESAN, J., JEONG, H.-S., KIM, S.-K. & SUDHA, P. N. 2013. Preparation and characterization of nano chitosan for treatment wastewaters. *International Journal of Biological Macromolecules,* 57**,** 204-212.

SOTO, M. L., MOURE, A., DOMÍNGUEZ, H. & PARAJÓ, J. C. 2011. Recovery, concentration and purification of phenolic compounds by adsorption: A review. *Journal of Food Engineering,* 105**,** 1-27.

SUNDAY, A., ORJIEKWE, C., EHIAGBONARE, J. & JOSIAH, S. J. 2012. Nutritional Composition of Three Different Fishes (Clarias gariepinus, Malapterurus electricus and Tilapia guineensis). *Pakistan Journal of Nutrition,* 11**,** 793-797.

VIJAYALAKSHMI, K., DEVI, B. M., LATHA, S., GOMATHI, T., SUDHA, P. N., VENKATESAN, J. & ANIL, S. 2017. Batch adsorption and desorption studies on the removal of lead (II) from aqueous solution using nanochitosan/sodium alginate/microcrystalline cellulose beads. *International Journal of Biological Macromolecules,* 104**,** 1483-1494.

WIJESENA, R. N., TISSERA, N. D., ABEYRATNE, C., BANGAMUWA, O. M., LUDOWYKE, N., DAHANAYAKE, D., GUNASEKARA, S., DE SILVA, N., DE SILVA, R. M. & DE SILVA, K. M. N. 2017. In-situ formation of supramolecular aggregates between chitin nanofibers and silver nanoparticles. *Carbohydrate Polymers,* 173**,** 295-304.

ZHOU, Y., ZHANG, X., DENG, J., LI, C., SUN, K., LUO, X. & YUAN, S. 2023. Adsorption and mechanism study for phenol removal by 10% CO2 activated bio-char after acid or alkali pretreatment. *Journal of Environmental Management,* 348**,** 119317.

# PERFORMANCE EVALUATION OF CUTTING FLUIDS MADE FROM BIO-DEGRADABLE VEGETABLE OILS IN MACHINING OF MILD STEEL

**Cyril Anosike AMAGHIONYEODIWE, Ijeoma IKECHUKWU, Ekene IGBOAYAKA, Ukemeobong JASPER. and * Anthony Iheanyichukwu OBI,**
*Department of Mechanical Engineering, Michael Okpara University of Agriculture, Umudike*
** Corresponding Author Email: toniobi2002@yahoo.co.uk*

**ABSTRACT**
*Three vegetable oils, palm oil, shea butter, and groundnut oil, were investigated for use as lubricants in the orthogonal turning of mild steel. The cutting speed was varied while the depth of cut and feed was kept constant; the surface finish was determined using a roughness checker, and the interface temperature was measured using a k-type thermocouple. Tool life and coefficient of friction were determined. Results show improved tool life and good surface finish were obtained at low and medium cutting speeds. Findings show the satisfactory performance of groundnut oil with chip compression of 0.83 at the speed of 300 rpm and that of the shear butter with a maximum temperature of 62$^o$C within the speed range. The cooling effect of the vegetable oils compared favourably with that of the standard soluble oil. The order of performance of the oils was palm oil, shear butter, and groundnut oil, which decreased in order, a performance attributed to their oiliness. The result of this work can be used to source new cutting fluids in cutting operations.*
***Keywords:*** *cutting fluid, vegetable oil, tool life, spindle speed, feed rate, chip compression, coefficient of friction*

## INTRODUCTION

Machining is a widespread metal shaping process that achieves high precision with good tolerance and surface finish. It is versatile in producing complicated free-form shapes with many features over an extensive size range, which can be made cheaply, quickly, and simply by controlling the path of a standard cutting tool. Another reason for the success of metal machining is the idea of competition to increase productivity, hold market share, and find new markets. These have led to significant changes in machining practice. The changes include machine technology, manufacturing systems, and materials technology. Chip formation is a significant outcome of machining operations, and **c**utting parameters influence the morphology of the chip. The process of chip formation gives a continuous form through crack propagation. Thus, the type and shape of the chip depend directly on the physical and mechanical properties of the machined material. For continuous chip formation, for example, once the chip thickness is known, the stresses and temperature in the work and tool, which influence tool life and quality of machined surface, can be estimated (Childs *et al.,* 2000). Notably, cutting speed, depth of cut, and feed are major parameters influencing chip formation and, hence, the quality of the machined surface. An earlier researcher (Biermann *et al.,* 2024) observed that chip thickness is influenced by lubrication, and adding a lubricant causes the chip to become thinner and reduces the friction between the chip and tool. Investigations have shown that cutting speed and feed have some influence on the cutting force. High cutting speeds increase the chip removal rate while the cutting force is decreased. Also, heat is generated at the chip-tool interface, adversely affecting chip formation mode, cutting force, tool life, and machined surface quality.

Metalworking fluids (MWFs) are used to improve productivity and the quality of machined products through cooling, lubrication, extending tool life, reducing process variability, and preventing corrosion (Lawal *et al.,* 2012); hence, the necessity for continuous search for new and improved machining lubricants to reduce to a minimum the adverse effects encountered in machining. Water is an effective cooling agent that removes heat more rapidly than oil but is a very poor lubricant when used alone and causes rusting. Some essential additives are generally added to transform water into a suitable metalworking fluid (Peterson, 2007).

Due to their advantages, the consumption of MWFs is increasing in the machining industry. Despite their widespread use, they pose significant health and environmental hazards during use, such as skin cancer and soil degradation. Various alternatives such as synthetic, solid, and vegetable-based lubricants, dry cutting, and minimum quantity lubrication (MQL) are being explored as the demand for renewable and bio-degradable lubricants increases (Ponnekanti and Savita, 2012). Cutting speed, temperature variation, and tool life are part of the criteria for orthogonal turning operations and choosing suitable machining lubricant. Machining is an effective method for evaluating metal-forming lubricants because the cutting fluid alters the forces between tool and work, cutting temperature, shear angle, wear, tool life, chip form, and surface finish (Sristi and Zaman, 2024). The cutting fluid reaches the chip/tool interface by diffusing through the distorted structure of

the metal and by capillary action. This study evaluates the performance of cutting fluids made from biodegradable vegetable oils in machining mild steel. Specifically, it comparatively assesses the lubricity effects of palm oil, shear butter, and groundnut oil on chip quality, surface finish, coefficient of friction, and tool life in the machining of mild steel. The result is part of sourcing new lubricants as alternative cutting fluids in machining.

**Theoretical Background**

The depth of cut $t_1$, existing before the formation of the chip, changes into the thickness $t_2$ after the chip has been generated. Hence, the chip thickness ratio or chip compression $\lambda$ can be computed as

$$\lambda = t_2/t_1 \qquad (1)$$

Further analysis (Obi, 1997) will show that the coefficient of friction $\mu$, occurring between chip and tool, is given by

$$\mu = \frac{\ln \lambda}{\pi/2 - \alpha} \qquad (2)$$

where

$\alpha$ = rake angle of the tool

To avoid failure by fatigue in a typical tool lifetime, tool material and geometry should be selected to maintain maximum tensile stress caused by the cutting forces, and the chosen cutting parameters, such as feeds and speeds, are within the limit of the temperature increases in the tool. Tool life prediction is important for tool management, and Taylor's tool life equation, though old, is still widely used for this work. An approximate equation due to Ojolo and Ogunkomaiya (2014), given in equation 3, is used to compute tool life.

$$T = L \times 60/Nf \qquad (3)$$

Where,

$N$ (RPM) = cutting speed in Revolutions per minute
$f$ = feed rate in Millimetre per revolution
$L$ = Length of effective cut
$T$ = Tool life in seconds

**Chip-tool Interface Temperature**

One of the goals of temperature measurement in machining is to quantitatively measure the heat energy distribution throughout the cutting region, which is difficult because of the high temperatures. Tool failure caused by fracture disrupts the machining process so suddenly that conditions are chosen to avoid this. The heat sources in machining include shear deformation and friction between the tool and workpiece and between the tool and chip.

However, measuring the average temperature at the chip/tool contact is sufficient. In this work, the average temperature was measured using a K-type thermocouple arrangement developed by Dhar and Islam (2005), as shown in Fig. 1. It was mounted on the tool-work interface junction, and the temperature was read off a calibrated digital multimeter.

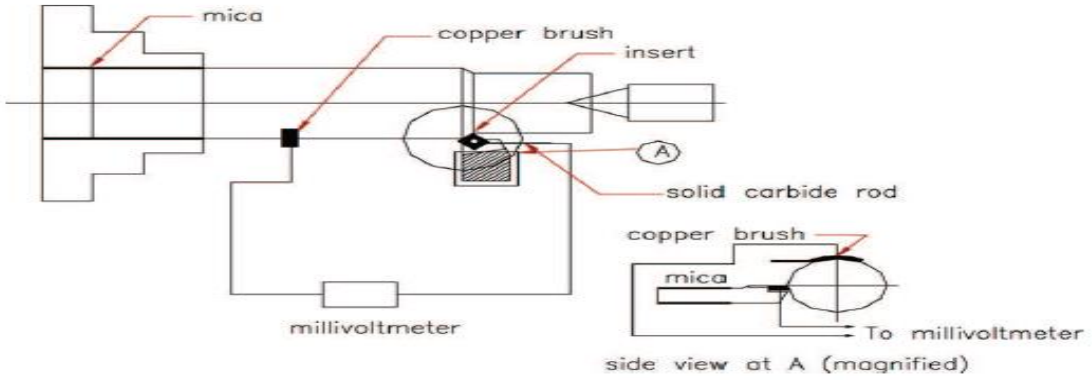


**Fig.1: K-type thermocouple for temperature Measurement (Dhar and Islam, 2005)**

It is also important to note that lubricants play a vital role in machining, such as the cooling effect to ameliorate high temperatures on the tool and workpiece, ensure the production of smooth surfaces of the work, reduce friction, and prolong tool life. A good lubricant would generate the best among these criteria. In this work, three local oils are applied separately to determine their order of acceptability as machining lubricants through their cooling effects, chip compression, coefficient of friction, and surface finish.

**MATERIALS AND METHODS**

The investigation used mild steel samples soaked in palm oil, shea butter, and groundnut oil, with soluble oil as a control. Obi *et al.* (1998) determined the trace elements of these oils, which are shown in Table 1.

**Table 1: Trace Elements in the vegetable oil samples (Obi, 2000)**

| | Trace elements in samples (µg/g) | | |
|---|---|---|---|
| **Element** | **Palm oil** | **Shea butter** | **Groundnut** |
| Al | 31.000 | 44.010 | 19.350 |

| Trace elements in samples (µg/g) | | | |
|---|---|---|---|
| **Element** | **Palm oil** | **Shea butter** | **Groundnut** |
| Ca | 80.800 | 74.750 | 29.890 |
| Ci | 29.600 | 60.350 | 11.910 |
| Cu | 1.430 | 2.011 | 1.790 |
| Mg | 28.100 | 26.890 | 7.320 |
| Mn | 0.940 | 1.690 | 0,470 |
| Na | 29.600 | 72.760 | 17.450 |
| V | 0.065 | 0.0671 | 0.039 |

The cutting tool was of tungsten carbide with a 10° rake angle, 9° clearance angle, and 1.5mm nose radius with a 10mm tool overhang. A lathe machine of Model Metalx WARSZAWA, Serial No. TUE40-9800 was used. The soluble oil was applied directly to the tool-workpiece interface, while the vegetable-based oils were applied using a small plastic can. The mild steel rod, with a diameter of 75 mm and length of 120mm, purchased from scientific equipment dealers, was used for this work. Its chemical composition is given in Table 2.

**Table 2: Elemental composition of low carbon steel (%) (Faci, 2017)**

| C | Si | Mn | P | S | Cr | Mo | Ni | Cu | Al | Mg |
|---|---|---|---|---|---|---|---|---|---|---|
| 0.215 | 3.350 | 1.316 | 0.102 | <0.100 | 0.029 | 0.015 | 0.022 | 0.012 | 0.130 | 0.014 |

The rod was mounted on the lathe and machined at a constant feed rate and depth of cut of 0.8 mm/rev and 1.5 mm, respectively, at 100, 150, 200, 250, and 300 rev/min speeds, using soluble oil as a cutting fluid. Excessively high turning speeds were avoided because, at high speeds, there is less time for the heat generated to be conducted through the workpiece. Moreover, the lubricating performance of the oils can only best be evaluated at low speeds, which helps avoid the splashing of the oils during machining and maintains uniform film over the chip-tool interface (Obi, 1997). The temperature of the work-tool interface at each speed was measured, the chips collected and their thicknesses measured with a micrometer screw gauge, the chip compression and coefficient of friction were computed using equations 1 and 2, respectively (Obi, 1997), and the tool life with equation 3. The average of four chip thickness measurements was used to compute the chip compression in each case. The surface roughness of the machined surface after each operation was determined using a roughness checker *(Taylsurf subtronic)* with a sampling length of 1cm. The process was repeated for the vegetable-based oils; the results are recorded in Table 3. The mild steel used in this work was used by Faci (2017)

## RESULTS AND DISCUSSION

Table 3 presents the results of chip thickness, temperature, surface roughness, chip compression, coefficient of friction, and tool life at varying spindle speeds.

**Table 3: Measured chip thickness, temperature, and surface roughness and computed values of compression and coefficient of friction**

| Machining Lubricant | Spindle speed (RPM) | Thickness of chip (t)(mm) | Chip compression (λ) | Chip-tool temperature (°C) | Surface Roughness (µm) | Tool Life (min) | Coefficient of friction (µ) |
|---|---|---|---|---|---|---|---|
| Palm oil | 100 | 0.42 | 9.09 | 58.3 | 2.00 | 57.7 | 0.32 |
| | 150 | 0.40 | 10.00 | 65.0 | 1.40 | 56.37 | 0.29 |
| | 200 | 0.38 | 11.00 | 63.9 | 1.20 | 41.38 | 0.28 |
| | 250 | 0.38 | 11.92 | 69.3 | 1.25 | 32.04 | 0.27 |
| | 300 | 0.40 | 10.62 | 73.9 | 1.20 | 12.65 | 0.25 |
| Soluble oil | 100 | 0.45 | 11.50 | 57.0 | 2.20 | 0.33 | 0.33 |
| | 150 | 0.44 | 12.70 | 61.0 | 1.75 | 0.30 | 0.30 |
| | 200 | 0.42 | 14.50 | 65.0 | 1.40 | 0.28 | 0.30 |
| | 250 | 0.40 | 12.50 | 70.0 | 1.40 | 0.27 | 0.28 |
| | 300 | 0.42 | 10.30 | 75.0 | 1.25 | 0.26 | 0.27 |

| Machining Lubricant | Spindle speed (RPM) | Thickness of chip (t)(mm) | Chip compression (λ) | Chip-tool temperature (°C) | Surface Roughness (µm) | Tool Life (min) | Coefficient of friction (µ) |
|---|---|---|---|---|---|---|---|
| Groundnut oil | 100 | 0.38 | 10.0 | 61.0 | 2.40 | 0.34 | 0.34 |
| | 150 | 0.37 | 11.4 | 64.0 | 2.20 | 0.32 | 0.32 |
| | 200 | 0.45 | 10.0 | 67.5 | 1.75 | 0.30 | 0.30 |
| | 250 | 0.46 | 9.50 | 70.0 | 1.40 | 0.28 | 0.28 |
| | 300 | 0.43 | 8.30 | 72.0 | 1.20 | 0.27 | 0.26 |
| Shea Butter | 100 | 0.32 | 11.4 | 53.0 | 1.40 | 105.83 | 0.35 |
| | 150 | 0.35 | 12.8 | 55.1 | 1.20 | 93.57 | 0.35 |
| | 200 | 0.34 | 14.3 | 62.0 | 1.20 | 82.36 | 0.32 |
| | 250 | 0.35 | 13.9 | 60.0 | 1.00 | 76.37 | 0.30 |
| | 300 | 0.37 | 11.8 | 58.0 | 0.60 | 68.38 | 0.28 |

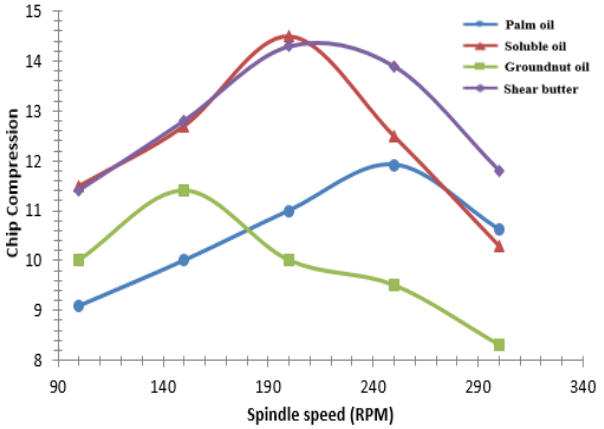


**Figure 2: Variation of chip compression with speed.**

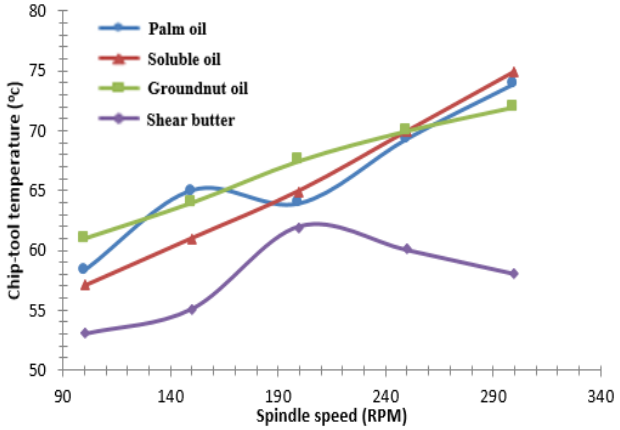


**Figure 3: Variation of chip tool interface temperature with the speed**

Fig. 2 shows the variation of chip compression with speed. The profile shows a slight rise in chip compression with speed, followed by a general drop as the speed increases. The changing values of the cutting angle, formation of built-up-edge, and variation of coefficient of friction cause the variation in chip compression. Obi (2000) has shown that with an increase in cutting speed, chip compression is first reduced to a minimum and then increased to reach a maximum, after which it drops again and varies slightly at high speeds. Another investigation (Obi, 1997) has shown that the reduction of chip compression with speed indicates a reduction of cutting force, power consumed, and reduction of temperature, which depends on the cutting fluid used. Groundnut oil performs better than the rest of the cutting fluids with chip compression of 0.83 at 300 rpm. Fig. 3 shows that the chip-tool interface temperature increases with the speed of machining. Previous authors have shown that the temperature generated was due to the primary shear of the workpiece, average temperature rise due to the rake face of the tool, and heat due to friction between the tool and the workpiece and between the chip and the tool and that this heat increases with cutting speed. At low cutting speeds, the principal factor affecting chip-tool interface temperature is the deformation at the shear zone, while at high cutting speeds, the tool-chip friction. Theoretical analysis of the plane strain deformation of metal showed that energy deformation when converted to heat, increases the temperature. The rise in temperature is due to the heat generated at the primary shear plane and friction between chip and tool and between tool and workpiece, which increases with speed. Obi (2000) has shown that cutting forces decrease with speed, and since heat is the product of force and velocity, more heat is generated with increasing speed. Among the oils investigated, shear butter performed better than the rest, with a maximum temperature of 62°C within the speed range tested. It was followed respectively by groundnut oil (70°C), palm oil (70.9°C), and soluble oil (75°C).

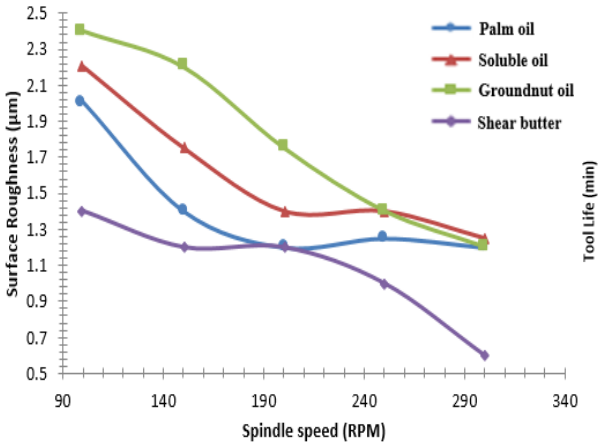


**Figure 4: Speed-Temperature Characteristics of the oils**

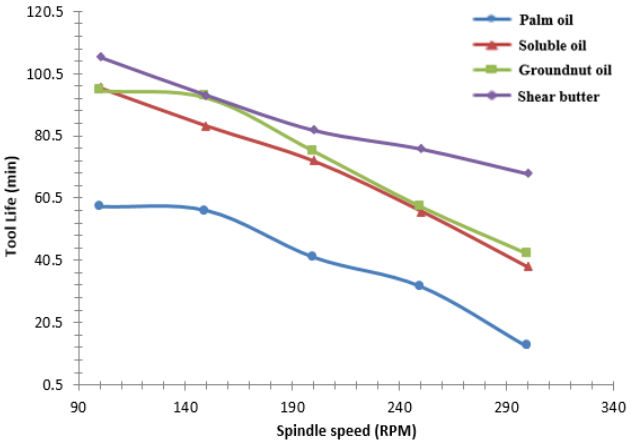


**Figure 5: Effect of cutting speeds on Tool Life using the oils**

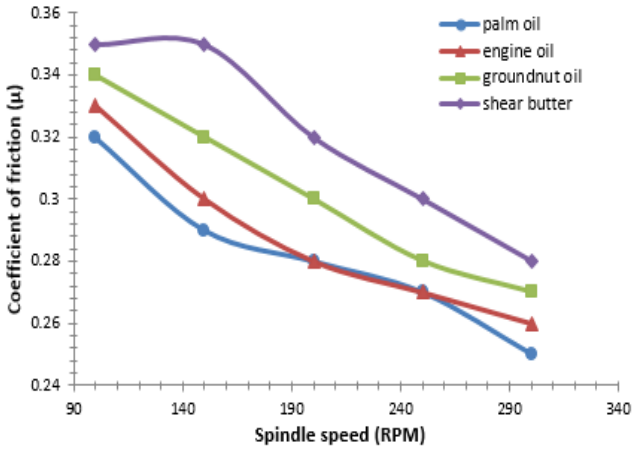


**Fig 6: Effect of cutting speeds on the coefficient of friction.**

The improvement of surface roughness with speed is shown in Fig 4. Built-up-edge (BUE) formation occurs at low speeds and offers a way of relieving some strains that occur at low speeds but at the expense of worsening the cut surface finish. The BUE reduces and disappears at higher speeds, improving the surface finish. Cutting fluid reduces the BUE to a size commensurate with the feed, reduces the contact area between tool and workpiece, and reduces the tool forces so that power consumption is reduced and temperatures lowered, resulting in improved tool life. As the cutting speed increases, a limit is reached above which the BUE is not formed. The shape of the tool changes, and the surface finish improves as the BUE disappears. There was a slight surface quality deterioration with palm oil at high cutting speeds. Previous authors summarized the reason for the lowered effectiveness of cutting fluids at high cutting speeds: the cutting fluids fly off the chip at high cutting speeds, the reaction time for the formation of a chemical compound is too short, and the time for convection of heat developed at high cutting speeds is too short. Fig. 5 is the variation of cutting speed with tool life. It is observed that tool life improves with speed. Thermal damage to tools occurs because of temperature increases. As tool damage, by wear or fracture, increases the surface roughness and the accuracy of the machined surface deteriorates, it is necessary to adopt an inflexible criterion to evaluate tool material machining capabilities, such as temperature variation with speed. Fig. 6 is the variation of speed with a coefficient of friction. The adiabatic shear band is generated during machining due to the workpiece's viscoelastic behavior, leading to the workpiece's deformation. Subsequently, chips are formed by cracking and plasticization following high-pressure stresses. With increasing cutting speed, the shearing bands become more intense, reducing the width between the segments and fragments due to localized deformation in the primary shear zone and increased temperature. Mechanical properties decrease in the cutting zone by reducing resistance to plastic deformation, which causes chip shearing. Forces decrease with increased cutting speed due to reduced friction between chip and tool, hence the shape of Fig. 6.

***Physiochemical characteristics of oil that enhance their performance***

The properties of vegetable oils that enhance their performance in machining operations include the presence of fatty acids (Ajala, 1982), which are effective as boundary lubricants due to a chemical reaction

between the polar head of the acid molecule and the surface they react with, to produce the adsorbed layer which is sufficiently thick to separate the surfaces thereby reducing friction. The presence of surface-active agents such as *stearic* acid and halogens like chlorine help to reduce the surface energy and increase its wetting power or oiliness. Ajala (1982) has shown that *shea butter* contains 35% by weight of *stearic* acid compared to groundnut and palm oil, with percentage stearic contents of 4.5% and 4%, respectively. Also, Obi (2000) has shown that *shea butter* contains 60.35 µg/g of *chlorine*, *groundnut oil* 11.91µg/g, and *palm oil* 29.60µg/g. These properties have contributed to the satisfactory performance of these vegetable oils in machining.

**Conclusion**

This study evaluates the performance of cutting fluids made from biodegradable vegetable oils in machining mild steel. It comparatively assesses the lubricity effects of palm oil, shear butter, and groundnut oil on chip quality, surface finish, coefficient of friction, and tool life in the machining of mild steel. The findings show that the cutting speed significantly affects the quality of turning of mild steel. Also, the lubricants improve the cutting tool's life, with a better surface finish for machining at low and medium cutting speeds. This implies ecology-friendly vegetable-based oils could successfully replace soluble oils as cutting fluids.

It is therefore recommended that the adoption of shea butter and groundnut oil as a metalworking fluid in metal cutting operations such as turning and other machining operations because of their high thermal conductivity and oxidative stability be encouraged; also, the oxidative stability of the vegetable oil-based cutting fluid could be improved using nature-friendly, uncomplicated and less-mineralized solution antioxidant to cater for the problem of the chlorinated, sulphured and phosphorus-based types used which are known to cause health issues to operator typical to mineral based oils.

**REFERENCES**


Ajala, A. O. (1982). Investigation of the major characteristics of some vegetable oil used in Nigeria. An Unpublished M.Sc. Thesis, Ahmadu Bello University, Zaria, Nigeria.

Biermann, D., Saelzer, J., Bergmann, B., Schenzel, J., Menze, C. J., Gerken, J. F., Wolf, T., Denkena, B., Möhring, H-C., and Zabel, A. (2024). Fundamental characterization of lubrication effects through various cooling lubricants in the chip formation zone. *Production Engineering*, 1-13.

Childs T., Maekawa K., Obikawa T., and Yamane Y., (2000). Metal Machining: Theory and Applications. First Edition. John Wiley and sons inc., New York, USA.

Dhar, N. R., S. Islam, M. Kamruzzaman, and T. Ahmed. The Calibration of Tool-Work Thermocouple in Turning Steels. National Conference on Industrial Problems on machines and mechanisms, 24th -25th February 2005.

Faci, N.D. (2017). Mechanical and Corrosion behaviour of low carbon steel in crude oil inhibited by some extracts of *Acacia nilotica (*Gum Arabic tree) plant. An unpublished M. Sc. Thesis, Ahmadu Bello University, Zaria.

Lawal, S.A., Choudhury, I. A. and Nukman, Y. (2012), Application of vegetable oil-based metalworking fluids in machining ferrous metals—A review. International Journal of Machine Tools and Manufacture, 52: 1- 12.

Mallock, A. (1881-82). The action of cutting tools. Proc. Roy. Soc. London, 33, pp. 127-139

Obi, A. I. (1997). Use of local oil as cutting fluids for aluminum and brass. Nigerian Journal 0f Technical Education, 14(2), pp. 98-111.

Obi, A. I., A.K. Oyinlola and Aku S.Y. (1998). The effect of locally produced vegetable-based oils on tool wear and thickness of chips in the drilling of mild steel. Nigeria Journal of Physics, 9, pp. 30-37

Obi, A. I. (2000). Lubricity Assessments of Vegetable-Based oils in some metal forming processes. An Unpublished Ph.D. Thesis, Ahmadu Bello University, Zaria, Nigeria.

Ojolo, S. J and Ogunkomaiya, O. (2014). A Study of Effects of Machining Parameters on Tool Life. *International Journal of Materials Science and Applications.* Vol. 3, No. 5, pp. 183-199. doi: 10.11648/j.ijmsa.20140305.19

Petterson, A. (2007), "High-Performance Base Fluids for Environmentally Adapted Lubricants". Journals of Tribology International 40: 638-645.

Ponnekanti N., and P. Savita (2012). Development of eco-friendly/biodegradable lubricants: An overview. Renewable and Sustainable Energy Reviews, 16, pp. 764-774

Sristi, N. A., and Zaman, P. B. (2024). A review of textured cutting tools' impact on machining performance from a tribological perspective. *The International Journal of Advanced Manufacturing Technology*, 1-35.

10.51975/25400104.som
Journal of the Nigerian Society of Chemical Engineers, 40(1), 2025

# OPTIMIZING LEAD IONS REMOVAL EFFICIENCY OF MELON HUSK BIO-ADSORBENT USING RESPONSE SURFACE METHODOLOGY AND PYOMO

***Azubuogu, P. U. and Loveday, I. E.**
*Department of Chemical Engineering, School of Engineering and Engineering Technology, Federal University of Technology, Owerri, Nigeria.*
*azubuogupeace1@gmail.com, nuelsloveday@gmail.com

**ABSTRACT**

*This study aims to optimize the removal efficiency of melon husk as a bio-adsorbent for lead ions in water. Response Surface Methodology (RSM) and Pyomo were employed to analyze experimental data from literature and identify optimal operating conditions. The independent variables used were dosage of melon husk and contact time. It was observed that time had a more positive influence on removal efficiency than dosage. Using the Stat-Ease 360 software, a quadratic model, exhibiting an excellent fit with an adjusted R-squared of 0.6862, was developed to describe the relationship between dosage and contact time on lead removal efficiency. RSM identified an optimal melon husk dosage of 0.64 g and a contact time of 49 minutes. However, Pyomo optimization revealed a slightly more efficient configuration with an optimal dosage of 0.63 g and a contact time of 44.8 minutes. This suggests that Pyomo may be a more effective tool for predicting the optimal conditions in this particular application.*
*Keywords: Melon husk; Water Treatment; Response Surface Methodology, Pyomo Optimization; Process Modelling.*

## 1. INTRODUCTION

Water is a vital resource needed for various human activities, including domestic and industrial purposes. Despite natural replenishment through rainfall, increasing pressure on water resources is evident due to growing demand and pollution has become a major concern (Debnath & Saha, 2020). Over the years, industrialization has significantly contributed to the pressure on and contamination of water bodies through agricultural runoffs and improper discharge of effluent water, chemical spills, etc. Take the recent incident at Walsall, where cyanide spilled into a canal, killing numerous fishes and endangering the health and lives of those that use the water for domestic purposes (Jessica, 2024). Many similar cases of chemical and oil spills have been reported in communities in Nigeria, accompanied by deaths and illnesses in those who live in the area of spillage (Chiamaka, 2024). The presence of heavy metals in concentrations above the WHO limits can pose harm to aquatic organisms and humans. One of such metals often seen in household domestic water is lead (Pb) ions. Lead ions contamination typically stems from the corrosion of lead-based plumbing systems, pipes, and fixtures, industrial discharges, mining runoff, and certain agricultural activities. Lead ions exposure can result in developmental delays, learning disabilities, and neurological problems in children, while adults may experience cardiovascular and kidney issues (Igwe, 2007). According to WHO (2006), the maximum acceptable level of lead ions in drinking water is 0.05 mg/L. Several methods have been used to treat water contaminated with heavy metals like lead, including ion exchange, reverse osmosis, chemical precipitation, adsorption, electro-dialysis, membrane filtration, etc. (Camilo *et al*., 2021; Mesut, 2021; Bhaumik & Hiren, 2022, Mohamed *et al*., 2024). Most of these methods heavily rely on chemicals like chlorine, coagulants, flocculants, which can create toxic sludge and byproducts after the treatment process (Seragadam *et al*., 2024). Among these conventional methods, adsorption is a relatively simple and inexpensive method for removing heavy metals from water. Materials used as adsorbents include carbon-based adsorbents like activated carbon and graphene, chitosan-based adsorbents, mineral adsorbents like zeolites and clay, bio-adsorbents, etc. Following the drive for more environmentally friendly solutions, there has been a growing interest in using agricultural waste materials, such as melon husk, rice husk, shea butter husk, orange peels, watermelon rind, groundnut husk, etc. as bio-adsorbents for heavy metals removal from aqueous solutions (Bernard *et al*., 2018; Kebru *et al*., 2022; Naik *et al*., 2022; Hadid *et al*., 2023). These bio-adsorbents are cheaper and readily available than the chemical alternatives. They are biodegradable and non-toxic and thus safe for use in removal of heavy metals in household water. They can also be regenerated and reused, making the whole treatment process low-cost. The removal of heavy metals like Lead from water using bio-adsorbents like melon husk has been proposed to be a physisorption process (Mustapha *et al*., 2016). Bernard & Jimoh (2021) investigated the use of melon seed husk-derived activated carbon for Cr (VI) ion removal from electroplating wastewater. The activated carbon effectively adsorbed Cr (VI) ions, with ultrasound assistance significantly enhancing the adsorption rate. The Langmuir model best described the adsorption isotherm, and the pseudo-second-order model accurately represented the adsorption kinetics. Nwankwo & Mogbo (2014) demonstrated the effectiveness of urea-activated melon husk as a low-cost adsorbent for removing Cd (II) ions from industrial effluents. The adsorption process followed pseudo-second order kinetics, and both Langmuir and Freundlich isotherm models accurately described the adsorption behaviour. Ayantola *et al*.

(2020) studied the removal of Fe (II) and Pb (IV) ions from industrial wastewater using melon husk activated carbon. They found that adsorbent dosage significantly influenced Fe (II) ions removal, with an optimal dosage point. Pb (IV) removal was less dependent on dosage, except for $H_2SO_4$ activated carbon. Adesola *et al*. (2014) investigated the biosorption of Ni (II), Cr (III), and Co (II) ions by melon seed husk. The study found that various factors, including pH, contact time, biosorbent dose, initial metal ion concentration, and temperature, influenced biosorption efficiency. Pseudo-second-order kinetics best described the biosorption process. Melon husk dosage significantly affected metal ion removal. The Freundlich isotherm model best fit the experimental data, suggesting a multilayer adsorption mechanism. The order of spontaneity for metal ion removal was Ni (II) ion > Co (II) ion > Cr (III) ion. Adelagun *et al*. (2014) modified melon seed husk with NaOH and studied its Pb (II) ion removal efficiency. The Freundlich isotherm model best described the adsorption process, indicating heterogeneous adsorption. The pseudo-second-order kinetic model suggested chemisorption as the dominant mechanism with an optimal dosage of 0.6 g. Kabir & Samson (2022) investigated the use of $H_2SO_4$ modified melon husk activated carbon for removing lead ions from electroplating wastewater. The adsorption process followed pseudo-second-order kinetics, indicating chemisorption. The Langmuir and Freundlich isotherms fit the data well, with $R^2$ values between 0.888 and 1.000. Melon husk activated carbon was more effective in adsorbing $Pb^{2+}$ than $Fe^{2+}$ from the wastewater.

While these studies have demonstrated the potential of melon husk as a low-cost, readily available bio-adsorbent for lead ion removal from water, there remains a lack of comprehensive investigations into the optimal operating conditions for maximizing removal efficiency. This study aims to evaluate the influence of key parameters (e.g., melon husk dosage and contact time) on lead ion removal from waste water using melon husk. By employing optimization methods like Response Surface Methodology and Pyomo, the optimal values of these parameters to achieve the highest possible removal efficiency is determined.

## 2. MATERIALS AND METHODS

This study employs Response Surface Methodology (RSM) and the Pyomo Python package to optimize the removal of lead ions from water using melon husk and identify the influence of key parameters (dosage and time) that maximize removal efficiency of melon husk.

### 2.1 Response Surface Methodology

Response Surface Methodology (RSM) is a statistical technique used to explore and optimize the relationship between a response variable like removal efficiency and multiple input variables (e.g., dosage and time). Typically, RSM involves designing an experiment (DoE), however due to the challenges associated with performing different runs at different conditions, it has been shown that RSM can be used on existing data, especially in this age of big data (Mochammad *et al*., 2022**).** Stat-Ease 360 was utilized for modelling and analysis of the data in Table 1 adapted from an already conducted experiment by Adelagun *et al*., (2014).

The problem consisted of two (2) factors: Dosage (A) and Time (B); and one response variable: Removal efficiency. Table 1 shows the response surface design matrix (actual) of the existing data. Tables 2 and 3 show the minimum and maximum levels of the factors and response.

**Table 1. Response Surface Methodology (RSM) Design Matrix (Actual)**

| Run | Factor 1<br>A: Dosage of melon husk (g) | Factor 2<br>B: Time (mins) | Response<br>Removal efficiency (%) |
|---|---|---|---|
| 1 | 1 | 0 | 0 |
| 2 | 0.6 | 60 | 0.965 |
| 3 | 1 | 120 | 0.989 |
| 4 | 0.2 | 120 | 0.944 |
| 5 | 0.6 | 0 | 0 |
| 6 | 1 | 10 | 0.671 |
| 7 | 0.6 | 10 | 0.656 |
| 8 | 0.2 | 60 | 0.934 |
| 9 | 0.2 | 40 | 0.913 |
| 10 | 0.2 | 0 | 0 |
| 11 | 0.6 | 20 | 0.934 |
| 12 | 0.2 | 20 | 0.212 |
| 13 | 0.6 | 60 | 0.965 |
| 14 | 0.2 | 10 | 0.48 |
| 15 | 0.6 | 40 | 0.952 |
| 16 | 0.6 | 120 | 0.983 |
| 17 | 1 | 20 | 0.983 |
| 18 | 1 | 40 | 0.985 |
| 19 | 1 | 60 | 0.987 |

**Table 2. Independent Variables used in the RSM Design**

| Factor | Name | Units | Minimum | Maximum | Coded Low | Coded High | Mean | Std. Dev. |
|---|---|---|---|---|---|---|---|---|
| A | Dosage | g | 0.2000 | 1.0000 | -1 ↔ 0.20 | +1 ↔ 1.00 | 0.6000 | 0.3266 |
| B | Time | mins | 0.0000 | 120.00 | -1 ↔ 0.00 | +1 ↔ 120.00 | 42.63 | 40.39 |

**Table 3. Dependent Variable used in the Response Surface Methodology (RSM) Design**

| Response | Name | Unit | Observations | Minimum | Maximum | Mean | Std. Dev. |
|---|---|---|---|---|---|---|---|
| R1 | Removal efficiency | % | 55.00 | 0 | 0.989 | 0.7133 | 0.3787 |

### 2.2 Pyomo Optimization

Pyomo is a Python-based modelling library specifically designed for optimization problems. It provides a flexible and powerful framework for solving mathematical optimization problems. It also employs various solvers like Interior Point Optimizer (IPOPT), Couenne, and Solving Constraint Integer Problems (SCIP) to find the optimal values of the decision variables. The model developed from Stat-Ease 360 was implemented in Pyomo as a Concrete Model. This means that all the variables, parameters, constraints, and objective function have been defined with specific values and expressions as seen in Figure 1.

```
m.T = pyo.Var(within = NonNegativeReals, bounds=(0,m.Tmax))
m.D = pyo.Var(within = NonNegativeReals, bounds=(0.2,m.Dmax))

a = -0.072368478054635
b = 0.70774472999147
c = 0.024205467565955
d = -0.0023722030981067
e = -0.31089133408641
f = -0.00013881719522709


m.obj = pyo.Objective(expr=a + b*(m.D) + c*(m.T) + d*(m.D)*(m.T) + e*(m.D)**2 + f*(m.T)**2, sense=pyo.maximize)


solver = SolverFactory('couenne')
results = solver.solve(m)
```

**Figure 1: Pyomo Concrete Model**

The Couenne solver was used to solve this optimization problem. Couenne is a powerful open-source solver for mixed-integer nonlinear programming (MINLP) problems such as the one in this study. Couenne employs global optimization techniques to ensure that it finds the globally optimal solution, rather than just a local optimum.

## 3. RESULTS AND DISCUSSION

### 3.1 Response Surface Methodology

The factors shown in Table 2 were used as independent variables and the response shown in Table 3 was used as the dependent variable to be maximized. A quadratic model was found to best fit the data. Table 4 shows the evaluation of the model terms. From the low $R^2$ values, it can be seen that there is no correlation between the terms as this would render the model a poor one. VIFs of 1.0 and close to 1.0 show that there is no multicollinearity in the design.

**Table 4: Model Terms Evaluation**

| Term | Standard Error | VIF | $R_i^2$ | Power |
|---|---|---|---|---|
| A | 0.3173 | 1.2 | 0.1724 | 82.9 % |
| B | 0.3504 | 1.0 | 0.0014 | 75.1 % |
| AB | 0.4311 | 1.2 | 0.1724 | 57.4 % |
| $A^2$ | 0.4779 | 1.0 | 0.0098 | 97.1 % |
| $B^2$ | 0.5730 | 1.0 | 0.0090 | 89.7 % |

The quadratic model developed to describe the process is shown below:

i. Final equation in terms of coded factors:

Removal efficiency = 1.107544319277 + 0.076937177280551A + 0.136744198629038B - 0.056932874354561AB + 0.049742613453826$A^2$ - 0.49974190238175$B^2$ --- *1*

ii. Final equation in terms of actual factors:

Removal efficiency = -0.072368478054635+ 0.70774472999147A + 0.024205467565955B - 0.0023722030981067AB - 0.31089133408641$A^2$ - 0.00013881719522709$B^2$ ---- *2*

where A = Dosage, B = Time

### 3.2 Fit Summary

Table 5 shows the fit summary of the RSM design. It can be seen that the quadratic model best maximises the Adjusted $R^2$ (0.6862) which is also very close to the Predicted $R^2$ (0.5576) indicating that the model is a good fit to the data provided.

**Table 5. Model Fit Summary Statistics for the Response Surface Methodology Design**

| Source | Sequential p-value | Adjusted $R^2$ | Predicted $R^2$ | |
|---|---|---|---|---|
| Linear | 0.0074 | 0.3908 | 0.2130 | |
| 2FI | 0.6696 | 0.3583 | -0.0764 | |
| **Quadratic** | **0.0038** | **0.6862** | **0.5576** | **Suggested** |
| Cubic | 0.0920 | 0.7797 | 0.5046 | **Aliased** |

### 3.3 Analysis of Variance (ANOVA)

The analysis of variance (ANOVA) for statistical significance of the quadratic model is computed on Table 6.

**Table 6. ANOVA Analysis of the Quadratic Model**

| Source | Sum of Squares | df | Mean Square | F-value | p-value | |
|---|---|---|---|---|---|---|
| **Model** | 2.00 | 5 | 0.3993 | 8.87 | 0.0008 | significant |
| A-Dosage | 0.0588 | 1 | 0.0588 | 1.31 | 0.2737 | |
| B-Time | 1.10 | 1 | 1.10 | 24.44 | 0.0003 | |
| AB | 0.0174 | 1 | 0.0174 | 0.3874 | 0.5444 | |
| $A^2$ | 0.0108 | 1 | 0.0108 | 0.2407 | 0.6319 | |
| $B^2$ | 0.7606 | 1 | 0.7606 | 16.90 | 0.0012 | |
| **Residual** | 0.5851 | 13 | 0.0450 | | | |
| Lack of Fit | 0.5851 | 12 | 0.0488 | | | |
| Pure Error | 0.0000 | 1 | 0.0000 | | | |
| **Cor Total** | 2.58 | 18 | | | | |

The F-value of 8.87 implies the model is significant and the subsequent values for the parameters show their degree of effects on the response variable, Removal Efficiency. High F-values and P-values less than 0.05 indicate model terms are significant. In this case, the Time terms (**B** and **B²**) are the most significant model terms.

### 3.4 Response Surface Design

The interaction effect of dosage and time is shown in Figures 2 and 3. It can be confirmed that time has more influence on removal efficiency than dosage. Time appears to have a positive effect on the removal efficiency until it gets to a maximum at about 81 mins when a decline starts to occur.

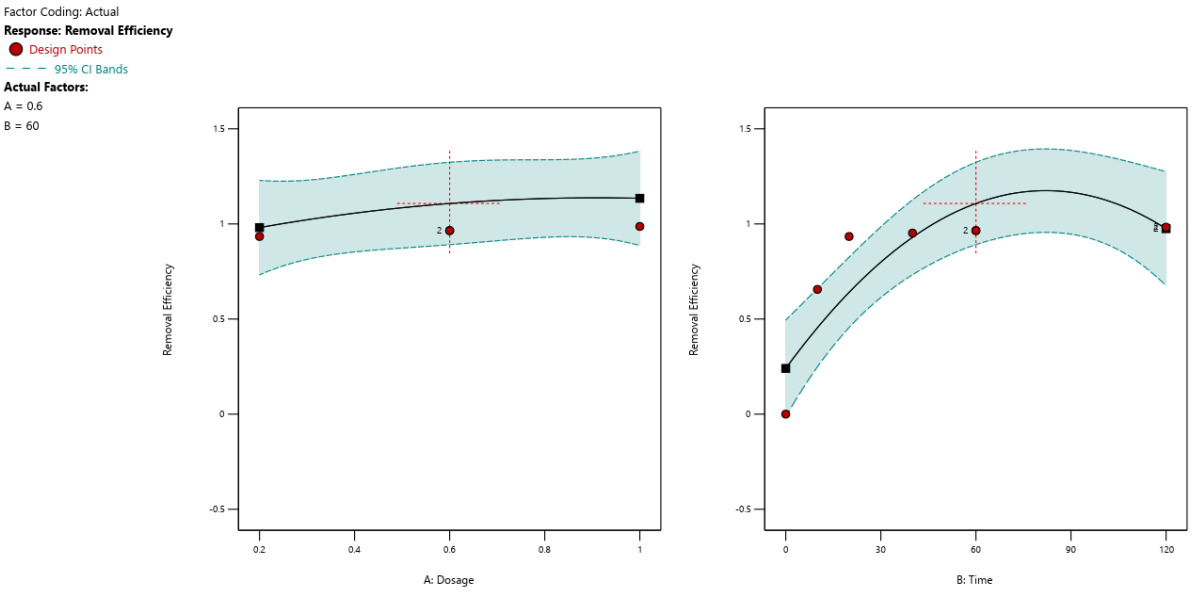


**Figure 2: Interaction effect of dosage and time on Removal Efficiency**

### 3.5 Numerical Optimization from RSM

Optimization using the Response Surface Methodology approach yielded the following optimal values for a maximum Removal Efficiency as seen in Figure 4.

**Optimum Dosage = 0.64 g, Optimum Time = 49 mins**

The optimal dosage obtained in this study is close to 0.6 g reported by Adelagun *et al*., (2014).

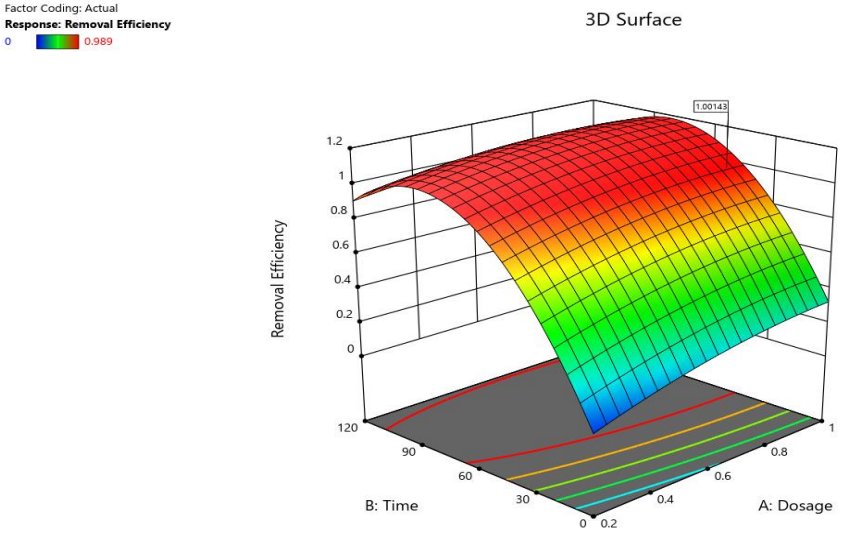


**Figure 3: 3-dimensional response surface plots showing the effects of dosage and time on Removal Efficiency**

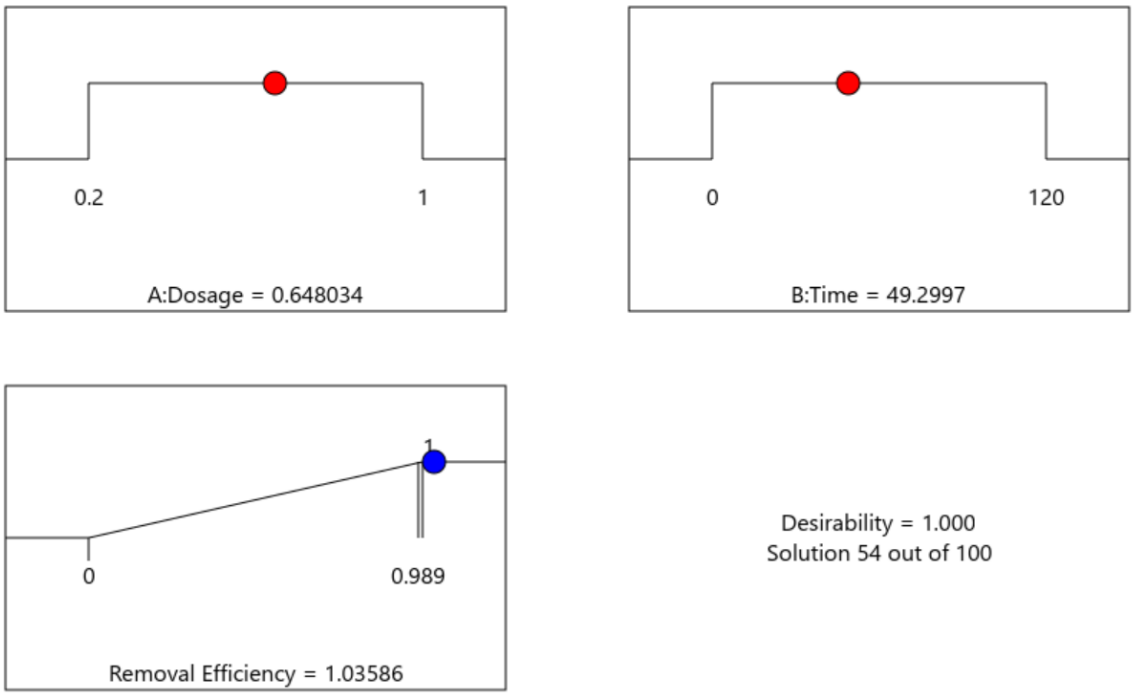


**Figure 4: Optimization Solution from Response Surface Methodology Design.**

### 3.6 Optimal Values from Pyomo

The model generated from Stat-Ease shown in equation 2 was used as the Objective Function for the Pyomo optimization problem. Optimization using the Couenne solver yielded optimal values for a maximum Removal Efficiency of 99 % as seen in Figure 5.

**Optimum Dosage = 0.63 g, Optimum Time = 44.8 mins**

This is very close to the optimum gotten from Response Surface Methodology.

```
[ ]
    value(m.obj)
0.9900000105944394

[ ] m.T.extract_values()
{None: 44.81097574261496}

[ ] m.D.extract_values()
{None: 0.6344597500315144}

    results.solver.termination_condition
<TerminationCondition.optimal: 'optimal'>
```

**Figure 5. Pyomo Optimization Results**

## 4. CONCLUSIONS

This study successfully optimized the removal efficiency of melon husk for lead ions using Response Surface Methodology (RSM) and Pyomo. A quadratic equation was determined to be the most suitable model, with an adjusted $R^2$ of 0.6862 and a predicted $R^2$ of 0.5576 indicating a good fit to the experimental data. Pyomo

optimization identified an optimal dosage of 0.63 g and RSM yielded an optimal dosage of 0.64 g, both of which are close to the experimental value of 0.6 g (Adelagun *et al*., 2014). Pyomo yielded a slightly lesser optimal time for maximized removal efficiency, suggesting its potential superiority over RSM in this case. While both methods yielded similar results, Pyomo's slightly more accurate dosage prediction and reduced computational time make it a promising tool for future optimization studies. The study also found that contact time positively affects removal efficiency, while dosage has a less pronounced impact. Future research could explore the influence of other factors, such as pH, temperature, and particle size, to further optimize the removal process.

**REFERENCES**

Adelagun R.O.A., Berezi E.P., Itodo A.U., Oko O.J., E.A. Kamba, C. Andrew and H.A. Bello (2014). Adsorption of Pb2+ from aqueous solution by modified melon (Citrullus lanatus) seed husk. Chemistry and Materials Research. www.iiste.org. ISSN 2225- 0956 (Online) Vol.6 No.2, 2014

Adesola Babarinde, Grace O. Omisore and J. Oyebamiji Babalola (2014). Kinetic, isothermal and thermodynamic parameters for the biosorption of Ni(II), Cr(III), and Co(II) onto Melon (Citrillus lanatus) seed husk. International Journal of Chemical and Biochemical Sciences (2014):18-33, (ISSN 2226-9614).

Ayantola Kabir Ajala, Oluwaseun Olatunji Otunola, Wasiu Oyebisi Oyeniyan (2020). Adsorption of Lead and Iron from Industrial Wastewater using Melon (Citrullus Colocynthis) Husk Activated Carbon. International Journal of Engineering Research & Technology (IJERT). http://www.ijert.org ISSN: 2278-0181, IJERTV9IS070658. Vol. 9 Issue 07, July-2020

BERNARD Esther and JIMOH Adulfatai (2021). Equilibrium and Kinetic of Ultrasound-Assisted Adsorption of Chromium (VI) ion from Electroplating Wastewater Using Melon Seed Husk Activated carbon. Journal of Turkish Chemical Society.

Bernard, E., Jimoh, A., Manse, A. and Yahya, M.D. (2018). Rice Husk, Melon Husk and Shea Butter Husk as Potential Adsorbent for Removal of Metal Ions from Solution: A Review. Nigerian Research Journal of Engineering and Environmental Sciences 3(2) 2018 pp. 834-842

Bhaumik Sutariya and Raval Hiren (2022). Energy and resource efficient reverse osmosis system with tunable recovery for brackish water desalination and heavy metal removal. Water and Environment Journal. 36. 10.1111/wej.12788.

Camilo Zamora-Ledezma, Daniela Negrete-Bolagay, Freddy Figueroa, Ezequiel Zamora-Ledezma, Ming Ni, Frank Alexis, Victor H. Guerrero, (2021). Heavy metal water pollution: A fresh look about hazards, novel and conventional remediation methods, Environmental Technology & Innovation, Volume 22, 2021, 101504, ISSN 2352-1864, https://doi.org/10.1016/j.eti.2021.101504

Chiamaka Ozurumba (2024). SPECIAL REPORT: Enugu community where residents rely on polluted river, deplorable PHC. Premium Times. Retrieved from [https://www.premiumtimesng.com/regional/ssouth-east/694801-special-report-enugu-community-where-residents-rely-on-polluted-river-deplorable-phc.html]

Debnath Subhradip and Saha Kaustav (2020). Next Generation Rainwater Harvesters and Smart Ground Water Replenishment. International Journal of Chemical and Environmental Sciences, Volume 1, Number 4, April 2020, pp. 30-43(14) Society for Makers, Artists, Researchers and Technologists. https://doi.org/10.15864/ijcaes.1403

Hadid Sukmana, Gergő Ballai, Tamás Gyulavári, Erzsébet Illés, Gabor Kozma, Zoltán Kónya and Cecilia Hodúrs (2023). Hungarian and Indonesian rice husk as bioadsorbents for binary biosorption of cationic dyes from aqueous solutions: A factorial design analysis. Heliyon. 9. e17154. 10.1016/j.heliyon.2023.e17154.

Igwe J. C. (2007), "A review of potentially low cost sorbents for heavy metal removal and recovery. Terrestrial and Aquatic Environmental Toxicology, vol. 1, issue 2, pp. 60-69.

Jessica Murray **(2**024). About 90 kg of dead fish removed from Walsall canal after sodium cyanide leak. The Guardian. Retrieved from [https://www.theguardian.com/uk-news/article/2024/aug/19/90kg-dead-fish-walsall-canal-sodium-cyanide-leak#:~:text=About%2090kg%20(200lbs)%20of%20dead,a%20metal%20finishing%20company%2C%20Anochrome]

Kabir A. Ajala & Samson O. Ojoawo (2022). Adsorption Thermodynamics of Fe2+ and Pb2+ in Industrial Wastewater Treatment using Melon Husk Activated Carbon. Mediterranean Journal of Basic and Applied Sciences (MJBAS) Volume 6, Issue 1, Pages 64-74, January-March 2022 ISSN: 2581-5059 www.mjbas.com

Kebru Tegegn, Zekeria Yusuf, Sasikumar J. and Kefelegn Gorfu (2022). Biosorbent Efficacy of Groundnut Husk for the Elimination of Chromium from the Effluent of Mojo Tannery Industry, Ethiopia.

International Journal of Biomaterials. 2022. 1-7. 10.1155/2022/9997348.

Mesut YlmazoÄŸlu (2021). Organic-Inorganic Ion Exchange Materials for Heavy Metal Removal from Water. 10.1007/978-3-030-80334-6_7.

Mochammad Arbi Hadiyat, Bertha Maya Sopha, Budhi Sholeh Wibowo (2022). Response surface methodology using observational data: a systematic literature review. Applied Sciences 12 (20), 10663. 10.3390/app122010663

Mohamed Dawam, Hussein Oraby and Mohamed Gobara (2024). A Review on: Advances in Membrane Technologies for Heavy Metal Removal from contaminated Water A Review on: Advances in Membrane Technologies for Heavy Metal Removal from contaminated Water. Journal of Physics: Conference Series. 2830. 10.1088/1742-6596/2830/1/012004.

Mustapha S, Ndamitso NM, Mohammed UM, Adeosun NO, Idris M (2016). Study on activated from melon (Citrullus lanatus) husk as natural adsorbent for removal of hardness in water. Advances in Analytical Chemistry 6 (1), 1-9, 2016

Naik Ramavathu Lakshmana, Kumar M. and Narsaiah, T. (2022). Removal of heavy metals (Cu & Ni) from wastewater using rice husk and orange peel as adsorbents. Materials Today: Proceedings. 72. 10.1016/j.matpr.2022.06.112.

Nwankwo Ogonna Daniel, Ewuim Sylvanus Chima, Mogbo Tochukwu Chinedu (2014). Comparative study of the Bioadsorbtion of Cadmium and lead from industrial waste water using melon (citrullus colocynthis) husk activated with sulphuric acid. American Journal of Environmental Protection 2014; 1(1): 1-8 Published online May 30, 2014 (http://www.sciencepublishinggroup.com/j/ajep) doi: 10.11648/j.ajep.s.20140101.11

Seragadam Padma, Samaroha Ghosh, Badri Srinivas, Kartik Ghanta and Susmita Dutta (2024). Bioremediation of Heavy Metals—Its Pros and Cons. 10.1007/978-3-031-53688-5_10.

World Health Organization (2006). Guidelines for Drinking Water Quality. In: Chemical Fact Sheet. World Health Organization. Geneva

10.51975/25400105.som
Journal of the Nigerian Society of Chemical Engineers, 40(1), 2025

# RESPONSE SURFACE OPTIMISATION OF COTTON FIBRE ACETYLATION FOR OIL SORPTION USING CENTRAL COMPOSITE DESIGN

**Momoh O. J.[*1,2], Olawale, A. S.[1], Ajayi O. A.[1] and Olakunle M. S.[1]**
[1]*Chemical Engineering Department, Ahmadu Bello University Zaria, Nigeria*
[2]*Chemical Engineering Department, Confluence University of Science and Technology, Osara, Kogi State.*
**Email: ojamesmomoh@gmail.com*

**ABSTRACT**

*Acetylation enhances the hydrophobicity of lignocellulosic biomasses by replacing their dominant hydrophilic hydroxyl groups with hydrophobic acetyl groups, thereby increasing their suitability for oil sorption. This modification typically results in weight gain due to the higher molecular mass of the introduced functional groups. This study employed the Central Composite Design (CCD) Response Surface Methodology (RSM) to optimise cotton fibre acetylation to enhance its weight percent gain (WPG) and improve its suitability for oil sorption. Reaction time, temperature, and the fibre mass-to-volume ratio of acetic anhydride were investigated, with WPG as the response parameter. Among the 20 experimental runs, the highest weight gain of 4.782% was achieved at 2 hours, 137°C, and a mass-to-volume ratio of 0.011 (0.550 g/50 ml). However, optimisation of the experimental conditions yielded a predicted WPG of 4.950% at 2.584 hours, 129.964°C, and 0.258 g of fibre per 50 ml of acetic anhydride. Validation of the predicted optimum response resulted in an experimental WPG of 4.896%, closely matching the predicted value of 4.950%. The minimal deviation of 0.054 demonstrated the model's high accuracy and reliability. Additionally, the desirability score of 1.000 indicated that the optimised conditions perfectly aligned with the study's objectives. Successful acetylation was confirmed through FTIR analysis, which provided evidence of the introduction and enhancement of peaks associated with acetylated products.*

***Keywords**: Cotton, Acetylation, Response Surface and Optimisation.*

## 1. INTRODUCTION

Cotton fibre is a promising natural alternative to synthetic sorbents for oil spill cleanup (Silva, *et al*., 2023; Nguyen, *et al*., 2023; Luo *et al*., 2013; Adebajo and Frost, 2004; Agida, *et al*., 2017). They are primarily composed of cellulose (82-96%), hemicellulose (2-6.4%), lignin (0-5%), and pectin (<1-7%) (Tu, *et al*., 2024; Bahlool and Kamel 2023), cotton exhibits a robust cellular structure due to rigid cellulose chains and extensive intermolecular and intramolecular hydrogen-bonding (Fang, *et al*., 2024; Hsieh, 2007). This structure enhances its durability compared to fibre-like kapok. However, cotton's hydrophilic nature limits its oil sorption capacity, necessitating modifications by substitution of hydroxyl functional group with hydrophobic moieties. Previous studies of cotton, kapok, rice husk, corn cob, banana and orange peel and lignocellulose biomass in their natural form show low oil sorption capacity compared to the synthetic sorbent (Olawale and Saidu, 2010; Saidu 2011; Olawale *et al*., 2022a; 2022b). **Acetylation is one of the methods for enhancing the oil-absorbing properties of lignocellulosic biomass,** transforming it into a hydrophobic, oil-absorbing material suitable for oil spill cleanup. This process involves replacing the hydrophilic hydroxyl groups in the biomass with hydrophobic acetyl groups, as represented in Equation 1. Since acetyl groups have higher molecular mass than the hydroxyl groups, acetylation typically increases the biomass weight, hence the use of weight gain to ascertain the level of acetylation (Heo *et al*., 2024; Teli and Terega, 2022)

$$\underset{\text{Lignocellulose}}{LC-OH} + \underset{\text{Acetic anhydride}}{R_2(C=O)_2O} \rightarrow \underset{\text{Acetylated LC}}{LC-(C=O)R} + \underset{\text{Acetic acid}}{RCOOH} \quad (1)$$

Acetylation of some lignocellulose biomass for oil spill clean-up has been reported in the literature (Fasanya, *et al*., 2020; Mahmoud, 2020; Nwadiogbu, *et al*., 2016; Onwuka, *et al*., 2019; Teli and Valia, 2013a, 2013b; Chung, *et al*., 2011; Sun, *et al*., 2004; Agida, *et al*., 2017; Adebayo and Frost 2003; Luo, *et al*., 2013). Whereas, previous studies employed the one-factor-at-a-time (OFAT) approach, which is limited in capturing factors interaction and identifying optimum conditions, this study aimed at utilising the response surface methodology (RSM) central composite design CCD, considered more robust, for process optimisation, accounting for factors interactions, optimal experimental conditions, deeper

understanding of process conditions to enhance performance. Luo *et al*., 2013 have successfully proposed the kinetic model for cotton linter pulp acetylation catalysed by sulfuric acid. Adebayo and Frost (2004) reports have shown successful acetylation of cotton fibre by reaction with acetic anhydride in the presence of DMAP catalyst as indicated by both FTIR and NMR. However, acetylating temperature, time and ratio of the mass of the biomass to the volume of the acetylating agent are factors which could significantly affect the extent of acetylation based on a particular biomass structural configuration. The combined effect of these factors on the weight per cent gain and extent of acetylation using response surface methodology (RSM) are not deeply established in the previous studies. Hence, this study is aimed at enhancing the acetylation of cotton fibre for crude oil sorption using design expert software response surface methodology, having been established as a reliable tool for process optimisation. In addition, to establish the significance of acetylating temperature, time and ratio of cotton fibre to the volume of the acetylating agent on the acetylation of cotton fibre.

## 2. MATERIALS AND METHODS

### 2.1 Material Collection and Preparation

The cotton fibre (SAMCOT-9 variety) was sourced from the Fibre Unit of the Institute of Agricultural Research, Ahmadu Bello University Zaria, the seed was harvested in the 2022/2023 season and manually ginned to remove the cotton fibres, and debris was carefully removed from the fibre, it was air dried and subsequently oven dried at 60 $^0$C for 8 hours to remove moisture content.

### 2.2 Experimental Design

Design Expert Version 13 software (Stat-Ease, Inc.) was employed in the study using the Central Composite Design (CCD) as an optimisation tool within Response Surface Methodology (RSM) to investigate how the variables influence the acetylation process, based on its efficiency in model complex relationships between variables (Mourabet *et al*, 2017; Bayuo, 2020). It was used to develop predictive equations and identify optimal process conditions for the acetylation process. CCD can be implemented as circumscribed (CCC), inscribed (CCI), or face-centred (CCF) designs. CCC was selected for this study due to its larger experimental region compared to CCI and CCF (Bhattacharya, 2021).

To enhance the cotton fibre acetylation, three independent variables were considered: reaction time, temperature, and sorbent mass/acetic anhydride ratio. Prior research conducted by Luo et al. (2013) investigated the acetylation of cotton linter pulp utilising the One Factor at a Time (OFAT) approach, specifically focusing on reaction time, temperature, and mass-to-volume ratio at 0.5-2 hours, 30-45 °C, and 2g/80ml (0.025) respectively. Similarly, Mahmoud (2020) investigated the acetylation of flax fibre, which was undertaken precisely at 1 hour and 65 °C with a mass-to-volume ratio of 5g/100ml (0.05). While, Fasanya et al. (2020) examined the reaction time, temperature, and mass-to-volume ratio for *Sansevieria liberica* acetylation, specifically at 3 hours, 70 °C, and 2g/60ml (0.033) respectively.

Based on the previous studies (Fasanya et al. 2020; Mahmoud 2020; Luo et al., 2013), a wider range of reaction time, temperature, and mass-to-volume ratio were selected for this study as shown in Table 1, using the response surface methodology due to its efficacy in elucidating the significance of process parameters, their interactions, and its capacity to ascertain optimal conditions.

**Table 1: Experimental Build Information**

| Factor | Name | Unit | Min | Max | Coded Low | Coded High | Mean | Std. Dev |
|---|---|---|---|---|---|---|---|---|
| A | Time | hr | 0.2000 | 3.80 | -1 ↔ 0.50 | +1 ↔ 3.50 | 2.00 | 1.14 |
| B | Temperature | $^0$C | 53.00 | 137.00 | -1 ↔ 60.00 | +1 ↔ 130.00 | 95.00 | 26.49 |
| C | Solid/ Liquid | g/50 ml | 0.0100 | 1.09 | -1 ↔ 0.10 | +1 ↔ 1.00 | 0.5500 | 0.3405 |

### 2.2 Fibre acetylation

A mixture of the oven-dried fibre and acetic anhydride in the range of experimental variables (Table 1) with NBS catalyst (2 % of the acetic anhydride) was heated between 53 – 137 $^0$C under reflux in a 250 ml round-bottom flask fitted with a condenser for a duration of 0.2 hour – 3.8 hours. At the end of the reaction time, the hot reagent was decanted off and the acetylated cotton was thoroughly washed with ethanol and acetone to remove the unreacted acetic anhydride and the acetic acid product.

Furthermore, drying of the acetylated fibre in an oven at 60 $^0$C for 16 hours, after which the weight gain was determined by Shimadzu ATX224 digital weighing balance (0.0001 g) and subsequently stored in a desiccator at room temperature as carried out in previous studies (Adebayo and Fost, 2004; Sun, *et al.,* 2004; Onwuka *et al.*, 2018; Nwadiogbu *et al.,* 2016; Fasanya, *et al*., 2020).

### 2.3 Fourier transform infrared (FTIR) Analysis

The FTIR was performed using Shimadzu-8400S Fourier transform infrared (FTIR) spectrophotometer within the spectra range of 4000–500 cm$^{-1}$. The IR spectra were analysed using spectroscopic software Win-IR Pro (Version 3.0). 2 mg of fibre was mashed, mixed with 200

mg KBr, and then pressed into 1 mm-thick disks, the sample was placed in the FTIR spectrometer and its beam directed at the sample to measure how much of the beam and at which frequencies the sample absorbs the infrared light to identify the molecular identity of the fibres.

### 2.4 Optimisation of Experimental Conditions for WPG Enhancement and its Validation

The desirability function was used to predict the best conditions, maximizing the response variable while considering desired constraints. The selection of optima conditions from CCD was based on the highest desirability of 1 to maximum predicted response (highest fibre weight gain). The optimised conditions were applied in a real experiment and the actual response measured and compared with the predicted response followed by error analysis. The percentage variation between predicted and actual values was calculated to assess model accuracy as shown in Equation 2.

$$\% \text{ Error} = \frac{\text{Predicted} - \text{Experimental}}{\text{Predicted}} \times 100 \qquad (2)$$

## 3. RESULTS AND DISCUSSION

### 3.1 Response surface analysis of cotton weight per cent gain after acetylation

The introduction of acetyl moieties into the cotton fibre consequently results in to increase in the mass of the acetylated fibre due to the higher molecular mass of the hydrophobic acetyl (Heo *et al*., 2024). However, the weight gain varied correspondingly under different combinations of reaction time, temperature and fibre-to-acetic anhydride ratio (solid/liquid) as shown in Table 1 indicating the influence of the investigated parameters on the responses.

**Table 1: CCD Experimental Design Template and Corresponding Experimental Responses**

| | Factor 1 | Factor 2 | Factor 3 | Response 1 |
|---|---|---|---|---|
| Run | A: Time | B: Temperature | C: Solid/Liquid | WPG |
| | h | $^0$C | g/50 ml | % |
| 1 | 2 | 53.0 | 0.55 | 0.164 |
| 2 | 0.2 | 95.0 | 0.55 | 0.218 |
| 3 | 2 | 95.0 | 0.55 | 3.673 |
| 4 | 2 | 95.0 | 0.55 | 3.691 |
| 5 | 3.5 | 130.0 | 0.10 | 4.700 |
| 6 | 0.5 | 60.0 | 1.00 | 0.120 |
| 7 | 2 | 95.0 | 0.55 | 3.201 |
| 8 | 2 | 95.0 | 0.55 | 3.691 |
| 9 | 0.5 | 130.0 | 1.00 | 1.350 |
| 10 | 2 | 95.0 | 0.01 | 4.000 |
| 11 | 2 | 137.0 | 0.55 | 4.782 |
| 12 | 2 | 95.0 | 1.09 | 3.679 |
| 13 | 3.5 | 60.0 | 1.00 | 0.430 |
| 14 | 3.5 | 60.0 | 0.10 | 0.400 |
| 15 | 0.5 | 130.0 | 0.10 | 1.500 |
| 16 | 2 | 95.0 | 0.55 | 3.891 |
| 17 | 2 | 95.0 | 0.55 | 3.691 |
| 18 | 3.8 | 95.0 | 0.55 | 3.255 |
| 19 | 3.5 | 130.0 | 1.00 | 4.750 |
| 20 | 0.5 | 60.0 | 0.10 | 0.100 |

In Table 2, analysis of the experimental data based on weight per cent gain shows a preferable fit to the quadratic model compared to the linear and two-factor interaction (2FI) with cubic models being aliased within the range of the investigated parameters. The preference for the quadratic model over the cubic model is attributed to the significance of only two out of the three investigated factors. While the factors' interaction may be described by the cubic model, the quadratic may offer better fits where all factors are not significant within the

range of investigations (Iro, *et al*., 2024 Kousha *et al*., 2015; Das, 2017). Therefore, the quadratic model offers a good balance between capturing essential response surface features and keeping the model interpretable and manageable. The appropriateness of the model is further confirmed by the analysis of variance (Table 3), which shows a significant model with an F-value of 57.10 and a p-value less than 0.0001. In CCD analysis of variance, a p-value greater than 0.05 and an F-value less than 0.05 typically confirm the significance of the model and its terms (Oladipo, *et al*., 2018; Eletta, *et al*., 2016). The analysis of variance reveals that the most significant model terms are acetylating temperature (A) and time (B), followed by the interacting terms AB, $A^2$ and $B^2$. However, the data suggests that the fibre-to-acetylating agent ratio (C) is the least significant independent variable, particularly at elevated temperatures. Implying that solid-to-liquid ratio is less critical compared to other reaction parameters in the acetylation of cotton.

**Table 2: WPG Fit Summary for Cotton Fibre Acetylation**

| Source | Sequential p-value | Lack of Fit p-value | Adjusted $R^2$ | Predicted $R^2$ | |
|---|---|---|---|---|---|
| Linear | 0.0015 | 0.0004 | 0.5352 | 0.3309 | |
| 2FI | 0.4168 | 0.0003 | 0.5367 | -0.4932 | |
| **Quadratic** | **< 0.0001** | **0.1049** | **0.9637** | **0.8791** | **Suggested** |
| Cubic | 0.0402 | 0.9286 | 0.9861 | 0.9896 | Aliased |

While solid-to-liquid ratio generally affects most processes as a component moves from the solid to the liquid phase and vice versa for efficient mass transfer, however, the significance of the solid-to-liquid ratio may depend on the specific process with other factors having a stronger influence on the response variable as in this process. Furthermore, unlike most reactions where reactants are fully dissolved, cotton acetylation is a heterogeneous process with the cotton and acetic anhydride/acetylating agent in different phases and reaction occurring at the interface between the solid cotton fibres and the liquid acetic anhydride, thereby suppressing the solid to liquid ratio effects. In addition, the acetylation was carried out in a solvent-free state with a high concentration of acetylating agent in the liquid phase may have enhanced effective collisions with cellulose molecules at high temperature, thereby limiting the solid-to-liquid ratio effects on the responses compared to reaction time and temperature which directly influence the rate and extent of acetylation within the cellulose fibre. However, minimum amount of liquid is still necessary to ensure the proper distribution of reactants and efficient mass transfer throughout the reaction mixture while maintaining the fibrous structure.

**Table 3: Weight Percent Gain Analysis of Variance (ANOVA)**

| Source | Sum of Squares | df | Mean Square | F-value | p-value | |
|---|---|---|---|---|---|---|
| Model | 59.25 | 9 | 6.58 | 57.10 | < 0.0001 | significant |
| A-Time | 10.83 | 1 | 10.83 | 93.93 | < 0.0001 | |
| B-Temperature | 25.92 | 1 | 25.92 | 224.79 | < 0.0001 | |
| C-Solid/Liquid | 0.0174 | 1 | 0.0174 | 0.1510 | 0.7057 | |
| AB | 4.49 | 1 | 4.49 | 38.90 | < 0.0001 | |
| AC | 0.0055 | 1 | 0.0055 | 0.0478 | 0.8313 | |
| BC | 0.0028 | 1 | 0.0028 | 0.0244 | 0.8790 | |
| $A^2$ | 8.95 | 1 | 8.95 | 77.65 | < 0.0001 | |
| $B^2$ | 3.34 | 1 | 3.34 | 28.96 | 0.0003 | |
| $C^2$ | 0.1114 | 1 | 0.1114 | 0.9660 | 0.3489 | |
| Residual | 1.15 | 10 | 0.1153 | | | |
| Lack of Fit | 0.8883 | 5 | 0.1777 | 3.36 | 0.1049 | not significant |
| Pure Error | 0.2646 | 5 | 0.0529 | | | |
| Cor Total | 60.40 | 19 | | | | |

To further verify the model fitness, a residual error (pure error) or variability of 0.2646 in Table 3 was obtained in the weight per cent gain response analysis, this represents an unexplained variability by the experimental factors, value this low indicates higher precision in the experiment. Signifying that the model is a good fit for the data with most of the variability in the response variable explained by the experimental factors (Kousha, *et al*., 2015). In addition, a value of 0.2646 suggests the chosen model captures a very high proportion of the variation observed in the response variable. Similarly, a mean square error (MSE) of 0.0529, which is an average of the squared pure errors, representing the average variability in the response variable that is not explained by the model was obtained, also confirming the model fitness. The lack of fit (f-value) of 0.1049 also confirms the significance of

the chosen model, implying that the lack of fit is not significant relative to the pure error. In addition, the adjusted $R^2$ of 0.9637 is in reasonable agreement with the predicted $R^2$ of 0.8791 with a difference of 0.0846, which is less than 0.2 as shown in Table 4. An adequate precision of 21.5000 which is greater than 4 was obtained, this affirms the ability of the model to navigate the design space.

**Table 4: Weight Percent Gain Fit Statistics**

| | | | |
|---|---|---|---|
| Std. Dev. | 0.3395 | $R^2$ | 0.9809 |
| Mean | 2.56 | Adjusted $R^2$ | 0.9637 |
| C.V. % | 13.24 | Predicted $R^2$ | 0.8791 |
| | | Adeq Precision | 21.5000 |

$$WPG = 3.63584 + 0.997647A + 1.54335B - 0.04C + 0.74875AB + 0.02625AC - 0.01875BC - 1.31387A^2 - 0.802413B^2 + 0.146545C^2 \quad (2)$$

Equation 2 is the predictive empirical model expression in terms of the coded factors for the weight per cent gain response which indicates the relative impact of the factors by comparing the factor coefficients. In Figure 1, the closeness of the experimental value to the predicted value indicates that the responses obtained from the experimental results properly fit within an acceptable variance range when compared to the predicted values from the empirical model, this is an indication of the high $R^2$ value of 0.9809 obtained in Table 4, as seen in Figure 1 with most of the points distributed relatively near the 45-degree diagonal line with no much outliers. This points to the adequacy of the model for predicting the response parameter within the range of the investigated variables.

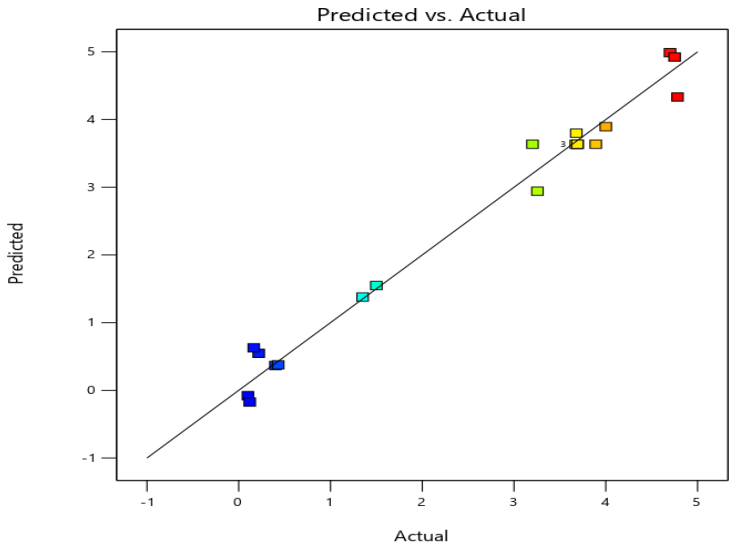


**Figure 1: Correlation Between Predicted and WPG Actual Experimental Data**

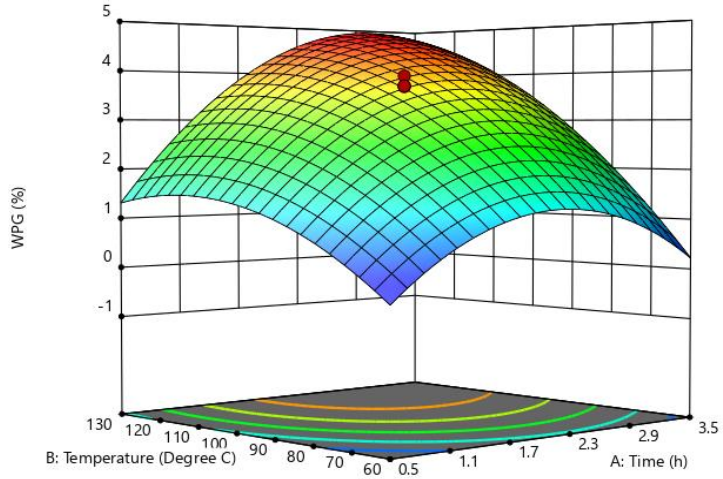


**Figure 2: 3D Response Surface Plot for the Variables Effects on Cotton Weight Percent Gain**

Figure 2 represents the resultant effect of the independent variables on the weight per cent gain response, indicating that an increase in acetylating temperature and reaction time leads to an increase in the cotton fibre weight per cent gain to an optimum point of about 4.782 weight gain. However, the weight gain was not significant at a reaction time of 0.5 minutes and temperature of 60 $^0$C, suggesting the requirement of a higher reaction time and temperature for successful acetylation. This is in agreement with Sun *et al*., 2004 and Chung et *al*., 2011 which reported visible acetylation after 1 hour and above 100$^0$C for Sugarcane bagasse. However, for cotton, acetylation became more substantial at 2 hours and a temperature of 95 $^0$C with an increase in weight per cent gain to above 3.60.

### 3.2 FT-IR results analysis

Using FTIR spectroscopy, the successful acetylation of the fibre was verified based on functional group transformation after acetylation, to identify the absence or presence of peaks associated with acetylated products. Typically, these peaks are visible at 1745 cm$^{-1}$, 1376 cm$^{-1}$ and 1234 cm$^{-1}$ representing carbonyl stretching of ester, C-H in -O(C=O)-$CH_3$ and C-O peak of acetyl group. The FT-IR spectra of the acetylated fibre are shown in Figure 3-8. In Figure 3 the spectral of the cotton fibres acetylated at 0.5 hour, 60 $^0$C, shows no significant transformation at fibre to the volume of acetic anhydride ratio of 0.1g/50ml and 1g/50ml. However, at 0.20 hour, 95$^0$ (Figure 4) and 0.5 hour, 130 $^0$C (Figure 5) a more visible appearance of peak at 1745 cm$^{-1}$ was observed, similarly at 2 hours and 95 $^0$C (Figure 6) the carbonyl stretching of ester at 1745 cm$^{-1}$ became distinctly visible, implying the dependence of successful acetylation on reaction time and temperature and not singly on each of the factor, this is also a confirmation of the significant of these factors in the weight gain analysis of variance (Table 3) and corresponding model equation (Equation 2).

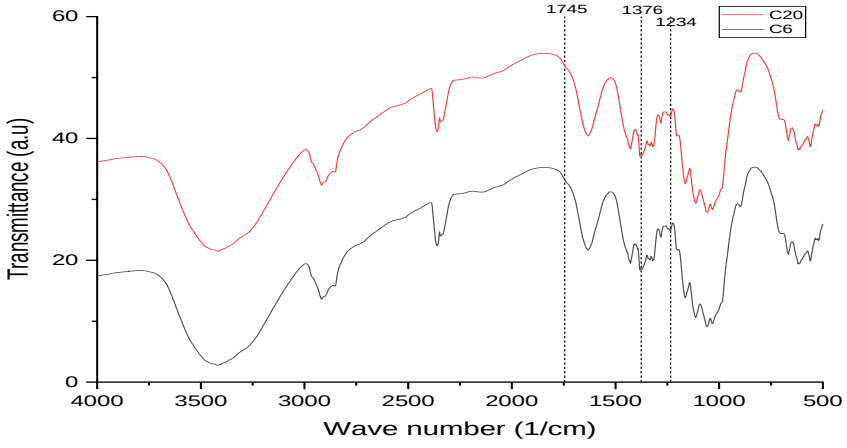


**Figure 3: FT-IR spectral of acetylated cotton fibre at 0.5 hour, 60 $^0$C, 1 g cotton fibre/50ml acetic anhydride ($C_{20}$) and 0.5 hour, 60 $^0$C, 0.1 g cotton fibre/50ml acetic anhydride ($C_6$)**

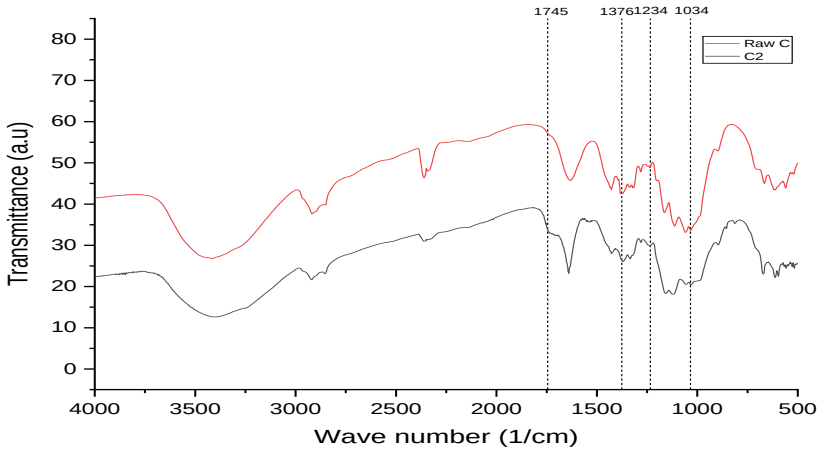


**Figure 4: FT-IR spectral for acetylated cotton fibre at 0.2 hour, 95 $^0$C, 0.55 g cotton fibre/50ml acetic anhydride**

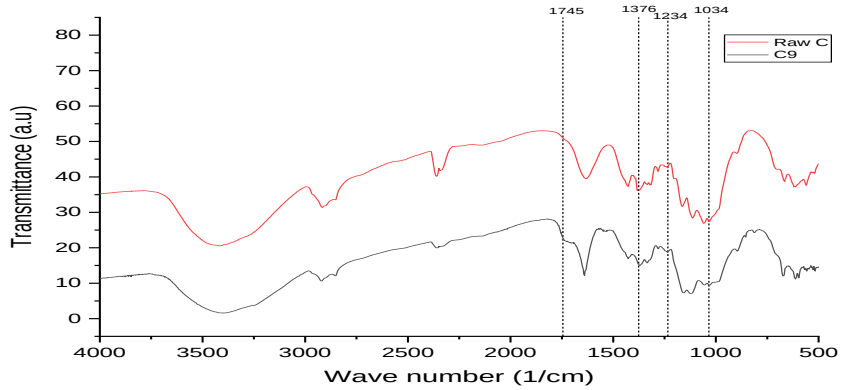


**Figure 5: FT-IR spectral for acetylated cotton fibre at 0.5 hour, 130$^0$C, 1 g cotton fibre/50ml acetic anhydride**

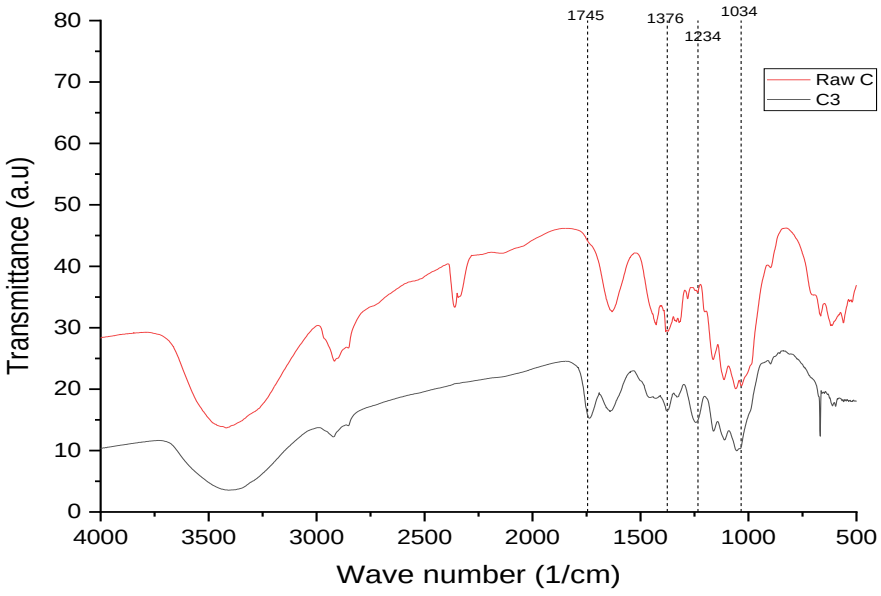

**Figure 6: FT-IR spectral of acetylated cotton fibre at 2 hour, 95$^0$C, 0.55 g cotton fibre/50ml acetic anhydride**

A comparison of the FT-IR spectral of unmodified cotton fibre (Raw C) with acetylated cotton fibre at 3.5 hour, 130 $^0$C, 1 g cotton fibre/50ml acetic anhydride and 3.5 hour, 130 $^0$C, 0.1 g cotton fibre/50ml acetic anhydride (Figure 7) shows very significant transformation with visible appearance of peaks at 1745 cm$^{-1}$, 1376 cm$^{-1}$ and 1234 cm$^{-1}$ representing carbonyl stretching of ester, C-H in -O(C=O)-$CH_3$ and C-O peak of acetyl group respectively. However, the typical characteristic peaks associated with raw cotton fibres remain present at 1376 cm$^{-1}$, 2922 cm$^{-1}$ and 3420 cm$^{-1}$, representing the bending vibration of C–H, the stretching vibration of C-H, and the stretching vibration of O-H bond respectively.

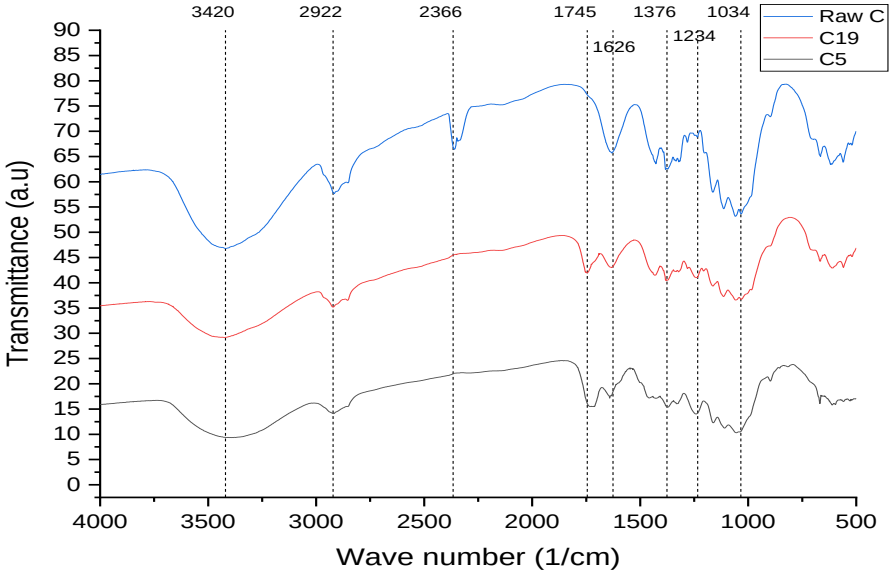


**Figure 7: FT-IR spectral of unmodified cotton fibre (Raw C) and acetylated cotton fibre at 3.5 hour, 130 $^0$C, 1 g cotton fibre/50ml acetic anhydride ($C_{19}$) and at 3.5 hour, 130 $^0$C, 0.1 g cotton fibre/50ml anhydride ($C_5$)**

Cotton fibre is about 90 % cellulose and typically hydrophilic due to the predominance of the O-H band associated with highly cellulosic biomass. The decrease in the intensity of the O-H stretching at 3420 cm$^{-1}$ in the modified cotton fibre is evidence of the successful replacement of the hydrophilic O-H bond with the enhancement of the hydrophobic acetyl groups (Chung *et al*., 2011); this was further confirmed by the decrease in the intensity of the H-O-H bending peak at 1626 cm$^{-1}$(Onwuka et al., 2016). The strong absorbance band at 1034.04 cm$^{-1}$ is ascribed to the C–O and O–H stretching vibration of the polysaccharide in cellulose (Olawale *et al*., 2020a). The FTIR bands of the raw and modified cotton fibres also conform with previous reports on cotton fibre acetylation (Lv, *et al*., 2018; Bello *et al*., 2016; Adebajo & Frost, 2004). From the experimental data, a maximum weight gain of 4.782% was observed under conditions of 137 °C for 2 hours with a fibre-to-acetic anhydride ratio of 0.55 g/50 ml, this finding aligns with the FT-IR spectra presented in Figure 8. A comparison of the unmodified cotton (Raw C) spectrum to that obtained under these optimal conditions reveals a significant reduction in the hydroxyl band at 3420 cm$^{-1}$, indicating extensive O-H substitution. No peak was observed in the region of 1840–1760 cm$^{-1}$ in the spectra of all the acetylated cotton samples indicating that the acetylated products are free of unreacted acetic anhydride (Sun *et al*., 2004).

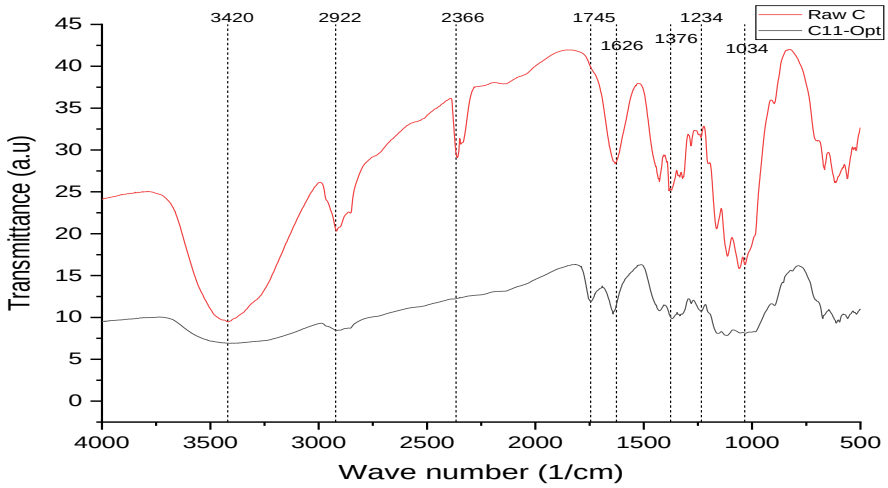


**Figure 8: Comparison of the FT-IR spectral of the unmodified cotton (Raw C) and optimum extent of acetylation cotton (2 hours, 137 $^0$C, 0.55 g cotton fibre/50ml acetic anhydride) ($C_{11}$)**

Similarly, the absence of a peak at 1700 $cm^{-1}$ for a carboxylic group in all the spectra of the acetylated samples also indicates that the acetylated products are free of the acetic acid by-product (Chung *et al*., 2011; Sun *et al*., 2004), these confirms the thorough rinsing of the acetylated products with acetone and ethanol after acetylation as shown in Plate 4.1, in addition the reliability of weight gain as basis for establishing extent of acetylation.

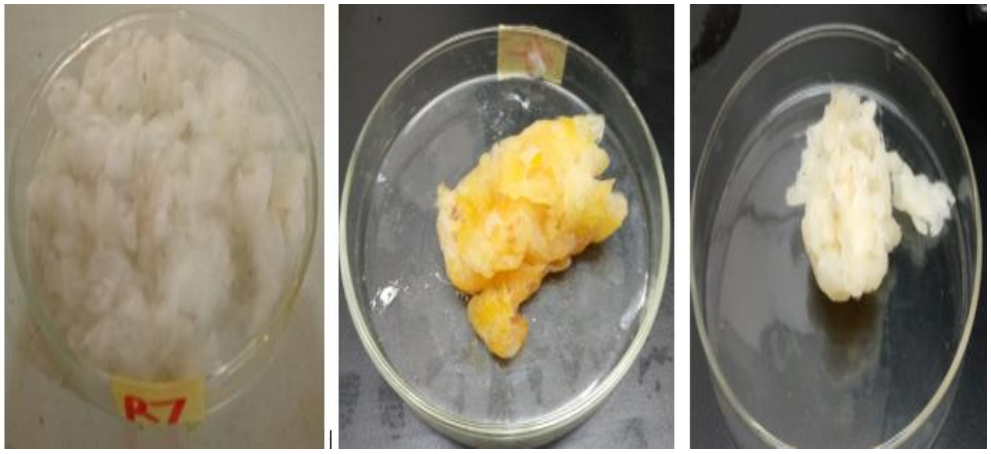

**Plate 1 (a): Raw cotton fibre (b): Fibre after acetylation (c) Rinsed acetylated product**

### 3.3 Optimisation of Acetylated Cotton Fibre Weight Gain

Optimizing experimental conditions helps to achieve the desired optimum response in response surface methodology (Uzochukwu et al., 2024). A study by Adebayo and Frost (2004) reported weight gain as a reliable index for determining the extent of acetylation in cotton fibre. Therefore, an attempt was made to enhance cotton fibre weight gain by considering experimental conditions within the range of investigated parameters in the optimisation constraints, as shown in Table 5. Several optimised solutions were generated, as shown in Table 6. Solution Number 1 presents the predicted optimal conditions of 2.584 hours, 129.964°C, and 0.258 g of fibre per 50 mL of acetic anhydride.

**Table 5: Weight Gain Optimisation Constraints**

| Name | Goal | Lower Limit | Upper Limit | Lower Weight | Upper Weight | Importance |
|---|---|---|---|---|---|---|
| **A: Time** | is in range | 0.5 | 3.5 | 1 | 1 | 3 |
| **B: Temperature** | is in range | 60 | 130 | 1 | 1 | 3 |
| **C: Solid/Liquid** | is in range | 0.1 | 1 | 1 | 1 | 3 |

| | | | | | | |
|---|---|---|---|---|---|---|
| **WPG** | maximize | 0.1 | 4.782 | 1 | 1 | 3 |
| **Oil Sorption Capacity** | maximize | 32.5 | 47.01 | 1 | 1 | 3 |

**Table 6: Weight Gain Optimisation Solutions**

| Number | Time | Temperature | Solid/Liquid | WPG | Desirability | |
|---|---|---|---|---|---|---|
| **1** | **2.584** | **129.964** | **0.258** | **4.950** | **1.000** | **Selected** |
| **2** | 3.261 | 129.137 | 0.530 | 4.904 | 1.000 | |
| **3** | 2.605 | 129.403 | 0.118 | 5.044 | 1.000 | |
| **4** | 3.500 | 130.000 | 0.100 | 4.988 | 1.000 | |
| **5** | 2.611 | 128.856 | 0.293 | 4.936 | 1.000 | |

**Table 7: Validation of Optimal Conditions for Weight Gain**

| Number | Time (h) | Temperature $^0$C | Solid/Liquid (g/50ml) | WPG | Desirability |
|---|---|---|---|---|---|
| **Optima (Predicted)** | 2.584 | 129.964 | 0.258 | 4.950 | 1.000 |
| **Validated** | 2.584 | 130 | 0.258 | 4.896 | 1.000 |

An actual experiment was conducted using the optimized (predicted) conditions from Solution Number 1, with the temperature rounded to 130°C. The experimental result yielded a WPG of 4.896 as shown in Table 7 which closely matched the predicted WPG of 4.950. The difference between the predicted and actual results was only 1.09 %, demonstrating the model's high accuracy and reliability. The desirability score of 1.000 indicates that the optimised conditions perfectly align with the study's objectives, confirming that the selected conditions are ideal for maximizing cotton fibre weight gain. The small error margin in the validation results further supports the model's reliability.

## 3. CONCLUSION

An examination of cotton fibre acetylation under varying reaction conditions— temperature, time, and fibre-to-acetic anhydride ratio revealed that reaction time and temperature are critical factors influencing the process. This finding was validated by FT-IR analysis. Acetylation was limited at 2 hours and 53 °C, 0.2 hours and 95 °C, and 0.5 hours and 130 °C, as evidenced by weight gain and FT-IR spectra. However, acetylation significantly improved at 2 hours and 95 °C, with minimal influence from the fibre-to-acetic anhydride ratio. Under the condition of 2 hours, 137 °C, and a fibre-to-acetic anhydride ratio of 0.011 (0.550 g/50 mL) the highest WPG was obtained amongst the 20 experimental runs. However, the CCD-based optimisation approach successfully identified reaction time of 2.584 hours, 129.964°C, and 0.258 g of fibre per 50 ml of acetic anhydride as the optima conditions with predicted WPG value of 4.950 %. Validation of the predicted optimum response resulted in an experimental WPG of 4.896 %, closely matching the predicted value of 4.950 %. The minimal variation in the validation results confirmed the effectiveness of the optimisation model.

**REFERENCES**


Adebajo, M. O., and R. L. Frost. 2004. Acetylation of raw cotton for oil spill cleanup application: An FTIR and 13C MAS NMR spectroscopic investigation. Spectrochimica Acta Part A: *Molecular and Biomolecular Spectroscopy* 60 (10):2315–21. doi: 10.1016/j.saa.2003.12.005.

Agida I. R., Olawale A. S. and Isah, M. T. (2017). Prospects of Biosorbents Development for Oil Spill Cleanup in Nigeria: A Review. *Proceedings of Materials Science and Technology Society of Nigeria (MSN) Kaduna State* Chapter. pp 7 – 13. Zaria, 2017.

Ansell, M.P. & Mwaikambo, Leonard. (2009). The structure of cotton and other plant fibres. *Handbook of Textile Fibre Structure*. 2. 62-94. 10.1533/9781845697310.1.62.

Bahlool, S. O. and Kamel, S. A. (2023). Utilization of Egyptian cotton waste fibres for production of Carboxymethyl cellulose (CMC). *Journal of Textiles, Coloration and Polymer Science*, *20*(1), 83-90.

Bayuo, J., Abukari, M.A., Pelig-Ba1. K. B. (2020). Optimisation using central composite design (CCD) of response surface methodology (RSM) for biosorption of hexavalent chromium from aqueous media. *Applied Water Science* (2020) 10:135. https://doi.org/10.1007/s13201-020-01213-3.

Bello, A., Isah M.T, Aderemi, B.O and Mukhtar, B. (2016). Acetylation of Cotton Stalk for Cellulose Acetate Production. *American Scientific Research Journal for Engineering, Technology, and Sciences* (ASRJETS) (2016) Volume 15, No 1, pp 137-150.

Bhattacharya S. (2021). Central composite Design for Response Surface Methodology and its Application in pharmacy. In: *Response Surface Methodology in Engineering Science*. London,

UK: IntechOpen; 2021. DOI: 10.5772/INTECHOPEN.95835.

Chung, S., Suidan, M.T., and Venosa, A. D (2011)., Partially Acetylated Sugarcane Bagasse for Wicking Oil from Contaminated Wetlands. *U.S. Environmental Protection Agency Papers*. 118. https://digitalcommons.unl.edu/usepapapers/118.

Eletta, O.A.., Ajayi, O.A., Ogunleye, O.O., Akpan, I.C 92016). Adsorption of cyanide from aqueous solution using calcinated eggshells: Equilibrium and optimisation studies, *Journal of Environmental Chemical Engineering* http://dx.doi.org/10.1016/j.jece.2016.01.020

Fasanya, O.O., Adesina, O.B., Okoduwa, U.J., Abdulkadir, J., Winful, E., Obidah, T.Y., Adamun, S. I, Audu., E.A.., Zar Myint, M.T., Olabimtan, O.H, and Barminas, J.T. (2020). Characterization of Sansevieria Liberica & Urena Lobata Fibres as Potential Sorbent Materials for Crude Oil Clean Up. *Journal Of Natural Fibres* https://doi.org/10.1080/15440478.2020.1788486.

Luo, P., Cao, C., Liang, Y., Ma, X., Xin., C., Jiao, Z., Cao, J., Zhang, J. (2013). Kinetics Study of the Acetylation of Cotton Linter Pulp. *BioResources* 8(2), 2708-2718.

Lv, N., Wang, Luo, S.P and Zhou, R (2018). Superhydrophobic/superoleophilic cotton-oil absorbent: preparation and its application in oil/ water separation. *The Royal Society of Chemistry*. RSC Adv., 8, 30257–30264.

Mahmoud, M.A (2020). Oil spill cleanup by raw flax fibre: Modification effect, sorption isotherm, kinetics and thermodynamics. *Arabian Journal of Chemistry* (2020) 13, 5553–5563.

Mourabet, M., El Rhilassi A., El Boujaady H., Bennani-Ziatni M., Taitai A. (2017) Use of response surface methodology for optimisation of fluoride adsorption in an aqueous solution by Brushite. *Arab J Chem*, 10:S3292–S3302. https://doi.org/10.1016/j.arabj c.2013.12.028

Nguyen, T. T., Loc, N. D., & Van Nam, T. (2023). Modified methods of oil cleanup with cellulose–based adsorbents: a review. *VN J. Hydrometeorol.*, *14*, 96-120.

Nwadiogbu, J. O., Okoye, P. A. C., Ajiwe, V. I., & Nnaji, N. J. N. (2014). Hydrophobic treatment of corn cob by acetylation: kinetics and thermodynamics studies. *Journal of Environmental Chemical Engineering*, 2, 1699–1704.

Nwadiogbu, J. O., V. I. E. Ajiwe, and P. A. C. Okoye. (2016). Removal of crude oil from aqueous medium by sorption on hydrophobic corncobs: Equilibrium and kinetic studies. *Journal of Taibah University for Science* 10 (1):56–63. doi:10.1016/j.jtusci.2015.03.014.

Oladipo, A.S., Ajayi, O.A., Oladipo, A.A., Azarmi, S.L., Nurudeen, Y., Atta, A.Y. and Ogunyemi, S.S. (2018). Magnetic recyclable eggshell-based mesoporous catalyst for biodiesel production from crude neem oil: Process optimisation by central composite design and artificial neural network, *Comptes Rendus Chimie* (2018), https://doi.org/10.1016/j.crci.2018.03.011

Olawale A. S. Ajayi O. A. and Olakunle M. S. (2022a). Assessment of Soya Bean Husk for Crude Oil Spill Cleanup. *Journal of the Nigerian Society of Chemical Engineers*, 35(1), 2020.

Olawale A. S. Ajayi O. A. and Olakunle M. S. (2022b). Study of Corn Husk as Sorbent for Oil Spill Cleanup. *Journal of the Nigerian Society of Chemical Engineers*, 35(1), 2020.

Olawale A. S. and B. B. Saidu (2010). Oil sorption change characteristics of lignocellulosic particulates. *3rd International Conference on Engineering Research and Development: Advances in Engineering Science and Technology*. Pp 63, 10184.

Onwuka, J. C., E. B. Agbaji, V. O. Ajibola, and F. G. J. A. W. Okibe. 2018. Treatment of crude oil-contaminated water with chemically modified natural fibre. *Applied Water Science* 8 (3):86. doi:10.1007/s13201-018-0727-5.

Onwuka, J. C., E. B. Agbaji, V. O. Ajibola, and F. G. Okibe. 2019. Thermodynamic pathway of lignocellulosic acetylation process. *BMC Chemistry* 13 (1):79. doi:10.1186/s13065-019-0593-8.

Silva, M. S., Frety, R., & Vidal, R. R. L. (2023). Cotton linter as biosorbent: removal study of highly diluted crude oil-in-saline water emulsion. *International Journal of Environmental Science and Technology*, *20*(2), 2111-2126.

Sun, X.F., Sun, R.C. and Sun, J.X. (2004). Acetylation of sugarcane bagasse using NBS as a catalyst under mild reaction conditions for the production of oil sorption-active materials. *Bioresource Technology* 95 (2004) 343–350.

Teli, M. D., and S. P. Valia. 2013a. Acetylation of banana fibre to improve oil absorbency. *Carbohydrate Polymers* 92 (1):328–33. doi:10.1016/j.carbpol.2012.09.019.

Teli, M. D., and S. P. Valia. 2013b. Acetylation of jute fibre to improve oil absorbency. *Fibres and Polymers* 14 (6):915–19. doi:10.1007/s12221-013-0915-8.

Tu, Q., Gao, W., Zhou, J., Wu, J., Zeng, J., Wang, B., & Xu, J. (2024). Characteristics of Dialdehyde

Cellulose Nanofibrils Derived from Cotton Linter Fibres and Wood Fibres. *Molecules*, *29*(7), 1664.

Uzochukwu, M.I., Momoh, O.J., Adebisi, A.A. et al. (2024). Evaluation of the Mechanical Properties of Natural Rubber/Baobab (Adansonia Digitata) Fibre Nanocomposite Using Response Surface Methodology: A Pedagogical Approach. *Chemistry Africa* (Springer Nature). https://doi.org/10.1007/s42250-024-00957-8

10.51975/25400106.som
Journal of the Nigerian Society of Chemical Engineers, 40(1), 2025

# THERMOGRAVIMETRIC AND DIFFERENTIAL THERMAL ANALYSIS STUDY OF INTERLOCKING COMPRESSED STABILIZED EARTH BLOCK AND ITS MICROSCOPIC CHARACTERIZATION

***Hamidu, L. A. J[1]. and Adamu, A. Y[1].**
*[1]Nigerian Building and Road Research Institute,*
*10 NBRRI Way/I.T. Igbani Street, off Awolowo Way, Jabi, Abuja, Nigeria*
*Corresponding author: lucadohamidu@yahoo.com*, kiddogimba@yahoo.com*

**ABSTRACT**

*The search for alternative building and road construction material in a strained economic situation is critical for socio-economic activities to thrive. The Nigerian Building and Road Research Institute (NBRRI) has keyed into the technology of making interlocking compressed stabilized earth block (ICSEB), as an alternative building materials. Nevertheless, parameters such as decomposition process and its microscopic properties have not been studied for the user comfort as friendly building material. This paper, examine "the time dependency thermogravimetric and differential thermal analysis (TGA-DTA), scanning electron microscope (SEM) and Fourier transform infrared (FTIR) of the already made ICSEB" based on the 95% laterite and not less than 5% cementing stabilization, with compaction pressure of 3 KN/mm$^2$. Results revealed that, the ICSEB TGA takes 41.45 minutes, 33.33 minutes and 29.58 minutes to decompose at 10 $^oC$/min, 15 $^oC$/min and 20 $^oC$/min heating rates and the combined TGA-DTA is endothermic process decomposition. SEM morphology showed heterogeneous phase formation with visible cracks, EDX detected 15 elements at 537 µm, having 41.37% carbon, 24.06% silicon, 21.35% aluminium, 5.14% Iron, 3.04% calcium, while others are in traces. These results imply that low aluminium and silicon content with greater carbon was responsible for early decomposition of the block in less than 1 hour heating. This therefore, suggests that the block has low-bearing capacity which requires optimization for its sustainability being an affordable and economical material within the reach of low-income earners.*

*KEYWORDS: Breakthrough, Mechanism, Optimization, Stabilization, Time Dependency*

## 1. INTRODUCTION

The search for alternative building materials either as a partial replacement or total replacement of Portland cement has become a subject of intense research in the recent times, which has led to the exploration of earth soil potentials. Earth soil over the years has been the major component used in the building and road construction, it is therefore desirous that everyone should own a befitting and comfortable shelter for successful running of day-to-day activities for a living. However; owning a house had been a major challenge to the low income earners especially in developing country such as Nigeria, due to high cost of building materials amidst the economic hardship occasion by divers' factors (rural-urban migration, security, social amenities, good roads, health care services e.t.c). These factors have caused a high demand for research into locally sourced, eco-friendly and affordable building materials. According to (Hamidu and Adamu, 2024), "the high cost of building materials is worrisome to low-income earners which are not only applicable to developing countries, but to also the developed countries".

Some research works carried out on the Nigerian Building and Road Research Institute compressed stabilized earth blocks (NBRRI-CSEBs) for the user comfort, includes thermal conductivity (Bakam et al, 2020a), fire resistance (Bakam et al, 2020b), and thermal decomposition as a function of temperature (Hamidu and Adamu, 2024), all reported that the blocks could not withstand temperature above 500 $^oC$ of firing, thus; making it a low-bearing material that requires surface coverage for longevity of the block. Similarly, studies on CSEBs by other authors on the acoustical properties which analyzed the effect of compaction pressure, water hyacinth ash and lime found out that the properties of CSEBs can be steered using binder concentration and compaction in a controlled manner (Ouma et al, 2023). Acoustics of compressed earth blocks bound using sugarcane bagasse ash and water hyacinth were also studied (Ongwen and Alruqi, 2023).

In related development, (Lyambo, 2012) study on the durability of CSEB reported that the durability is controlled by three factors: block strength, deterioration mechanism and the design of the building. These mechanisms were based on the assumption using masonry standards (Eurocode, BS, SANS, ASTM) which

is ranging between 1.2 and 2.1 MPa (Delgado and Guerrero, 2007). The durability in terms of exposure to wetting-drying (WD) cycles and high temperature was carried out (Nshimiyimana et al, 2022), their finding revealed that the stabilization of CEBs with lime-rich binder is more resilient to the WD cycles than cement, which also shows that the cement stabilized CEBs would at least retain their strength after exposure to high temperature. (Nurul et al, 2020) did a study on the compressive strength of cement-stabilized CEBs; they reported that the CEBs gained the highest compressive strength of 3.4 N/mm$^2$ when stabilized with 10% of cement content over a curing period of 28 days. (Muhwezi and Achanit, 2019) conducted a study on the effect of sand on the properties of compressed soil-cement stabilized block reported the quality depends on the mechanical and physical properties of the soil test.

Building collapses has been a reoccurring phenomenon in Nigeria, which had led to loss of human lives, properties and materials. It is therefore imperative to determine critical mechanisms such as the rate of decomposition and kinetic of the ICSEBs produced by NBRRI to understand the durability of such vital building material from the abundant natural resources. (Fernandez-Caliani et al, 2004) reported on the use of TGA/DTA usage for determining the pattern of energy transition in clays and clay material properties. Decomposition rate and kinetic study which is seldom investigated is usually carried out using specialized process such as thermogravimetric analysis (TGA) or thermogravimetric (TG) and differential thermal analysis (DTA) (Al-Gawari, 2022). While phase formations of the matrices is analyzed via: scanning electron microscope (SEM) in conjunction with energy dispersive X-ray (EDX) for their morphological and elemental compositions (Hamidu et al, 2019). Furthermore; the vibrational frequencies of the active functional group for the elements responsible for the chemical and physical properties of material is best studied using Fourier transform infrared (FTIR) (Tinti et al, 2015). This was also reported by (Kamwa et al, 2023) on their study on "effect of Curing Temperature on Properties of Compressed Lateritic Earth Bricks Stabilized with Natural Pozzolan-Based Geopolymer Binders Synthesized in Acidic and Alkaline Media" using both the FTIR and SEM/EDX for the analysis where curing temperatures above 45 °C for the acidic-stabilized CEBs and 55 °C for the alkaline-stabilized CEBs, were studied. In this study, the use of thermogravimetric (TGA) and differential thermal analysis (DTA) instrumentation study to investigate the decomposition of NBRRI-ICSEB based on American Society for Testing and Materials (ASTM) standards as function of time and to further examine the morphological composition via scanning electron microscope (SEM-EDX) and Fourier transfer infrared (FTIR) spectroscope for proper understanding of the elemental composition is sort.

## 2. MATERIALS AND METHODS

### 2.1 Materials

The material used in this work, was the already made interlocking compressed stabilized earth blocks (ICSEBs) by the Nigerian Building and Road Research Institute (NBRRI), which had composition of not less than 5% cement to not more than 95% laterite stabilization compacted at 3 KN/mm$^2$ (Bakam et al, 2020a). The ICSEB characterization was performed using combination of several methods which includes; thermogravimetric and differential thermal analyses, scanning electron microscope/energy dispersive X-ray spectroscope (SEM/EDX) and Fourier transform infrared spectroscope (FTIR).

### 2.2 Methods

The ICSEB sample was crushed and ground using laboratory mortar and pestle to smaller sizes of 1 mm (Hamidu and Adamu, 2024). This was followed by the TGA-DTA experimentation, where 50 mg of the sample was weighed and put into the sample holder, and placed in the analysis chamber, covered on the cheallar and allowed to cool to 15 $^o$C. It was further connected to the desk top computer to obtain all information about the sample degas in a static Nitrogen atmosphere with a purge rate of 20 mL/minute using TGA 4000 PerkinElmer model. The heating began at 0 minute to 90 minutes for each sample at 10 $^o$C/min, 15 $^o$C/min and 20 $^o$C/min heating rates until stabilization. At the end of each run, data with TGA and combine TGA-DTA curves were generated.

The SEM study was carried out in conjunction with energy dispersive X-ray spectroscopy (EDX) on the NBRRI-ICSEB for morphological and elemental compositions, using SEM machine model sputter coater Q150T by Quorum UK. The sample was first placed on a stub; thereafter it was placed in a sputter coater followed by deposition into the SEM machine column for analysis at different magnifications, 30, 80, 100 µm and full count detection at 537 µm. while the quantitative elemental compositions were obtained by linking the EDX analyzer coupled to the microscope for the periodic table. Fourier transform infrared model FT-IR-8400S, Schmazdu and Sputter Coater Q150T UK model was used for the FTIR spectroscopic was recorded in the range of 400 – 4000 cm$^{-1}$ wavelength using the pressed pellets containing 5 mg of ICSEB and 95 mg Kbr (Hamidu et al, 2019).

## 3. RESULTS AND DISCUSSION

### 3.1 Thermogravimetric Analysis of NBRRI-ICSEB

The results from the TGA heating at different heating rates of 10, 15 and 20 $^o$C/min is presented on Figure 1, with time (min) on the abscissa (X-axis) and weight percentage (%) on the ordinate (Y-axis).

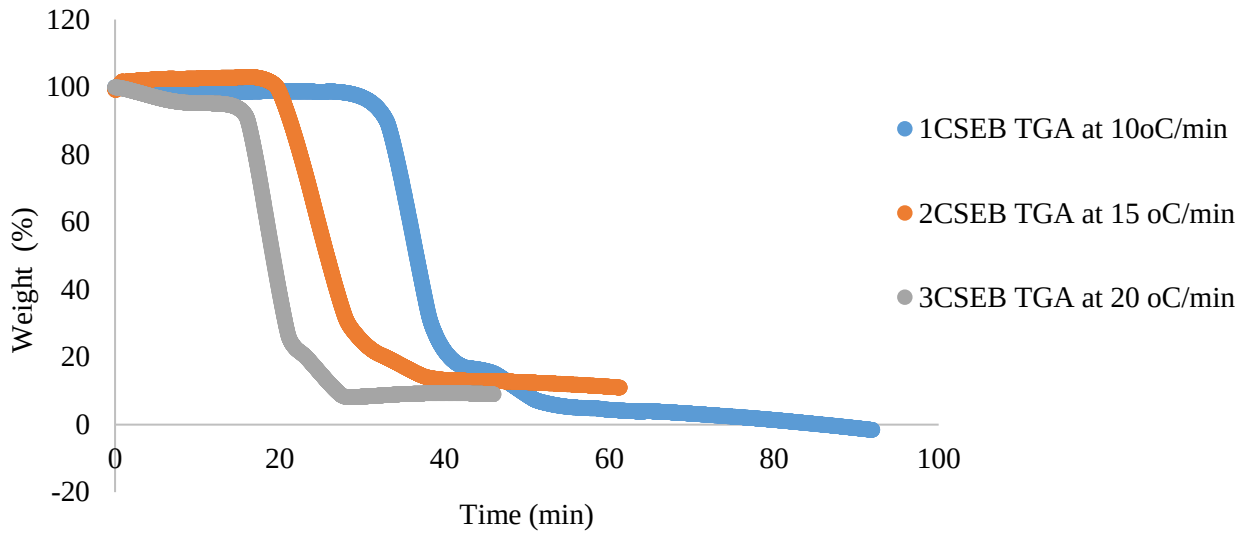


**Figure 1: NBRRI Interlocking Compressed Stabilized Earth Block Thermogravimetric Curves**

From Figure 1, the blue line (1CSEB TGA at 10 ºC/min) shows the time dependency at 10 ºC/minute decomposition process. The horizontal region became stable showing no change in mass of the ICSEB between 0.54 min and 31.15 min with a weight loss of 4.504 %. This implies the ICSEB thermal stability and removal of water of hydroxylation. At the second phase, the mass loss begins from (31.15 min) 95.458 weight (%) and stabilized in between (41.35 min) 18.464 weight (%) implying the removal of carbonic compound and organic matters as the main stage taking about 81.53% of the total initial weight, while the residual 18.47% being the pure component of the materials in the ICSEB. According to Dilnesa (2020), the removal of water of hydroxylation using TGA occurs in the range of 400 to 500 ºC, while above 600 ºC is the decarbonization of the material. This short time loss in the properties of the compressed stabilized earth block produced by NBRRI at 10 ºC/min heating rate supports the findings of (Hamidu and Adamu, 2024) and (Bakam et al, 2020a) that the NBRRI-ICSEB cannot withstand heating at temperature above 500ºC (41.35 minutes). The second stage investigation of the heating rate at 15 ºC/min is indicated by the brown line (2CSEB TGA at 15 ºC/min), the heating began at (0.8 min) until the process became stable at 18.83 min. The second phase of the decomposition of organic material and other volatile components began at 18.83 min progressively to 34.48 min taking 82.28% of the material ICSEB, being the volatile carbon and organic matters present in the ICSEB, while the residual being the pure component material used in the production of ICSEB is 17.72%. And the third phase of the TGA was the investigation of the heating rate at 20 ºC/min as indicated by the gray line (3CSEB TGA at 20 ºC/min). The removal of moisture began 0.6 min until stabilization stage on the horizontal region of the curve at 15.08 min. While complete decomposition reached steady state at 29.92

min taking 91.70% weight of the material being carbon content and other volatile organic matters, while the 8.30% residual being the pure component that makes up the ICSEB. The thermal process of the phase transition is described by the combined thermograph curves for both TGA-DTA which outline the process of energy pattern by the NBRRI-ICSEB and its stability.

### 3.2 Combined Thermogravimetric and Differential Thermal Analysis of NBRRI-ICSEB

The combined TGA/DTA decomposition process shown in Figure 2 illustrates the thermal decomposition of a typical material.

Figures (2a, b and c) presents and describe the complete process of time dependency of the ICSEB's removal of water of hydroxylation and transition (phase change) to final decarbonization of the material resulting to the residual as the pure material component that is present the matrices.

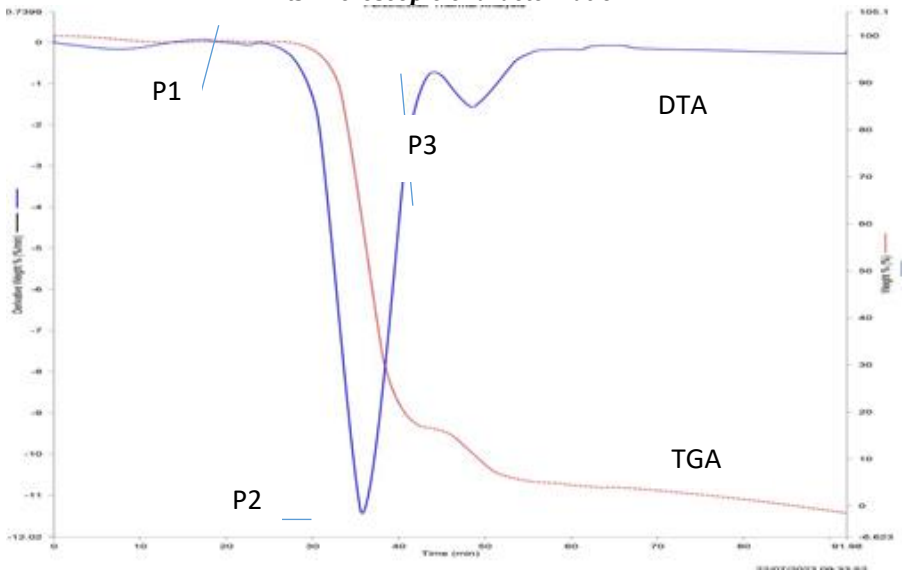


**Figure 2a: NBRRI-ICSEB TGA-DTA at 10 ºC/min**

Figure 2a, describe the transition stages (P1, P2 and P3) for NBRRI-ICSEB curve at 10 ºC/min. P1 is attributed to removal of water of hydroxylation adsorbed in the ICSEB, between P1 and P2, endothermic process was observed in 35 minutes, depicting the oxidization and removal of volatile compound containing in the ICSEB. As the heating process continued from P2 to P3, all carbonaceous materials were removed and complete decomposition attained in 54 minutes with endothermic process taking place, as the ICSEB absorbed more heat. This process could be related to the similar work by Fernandez-Caliani et al. (2004) reported in the journal of clays and clay materials.

Figure 2b; present the combined TGA-DTA of NBRRI-ICSEB decomposition at 15 ºC/min heating rate.

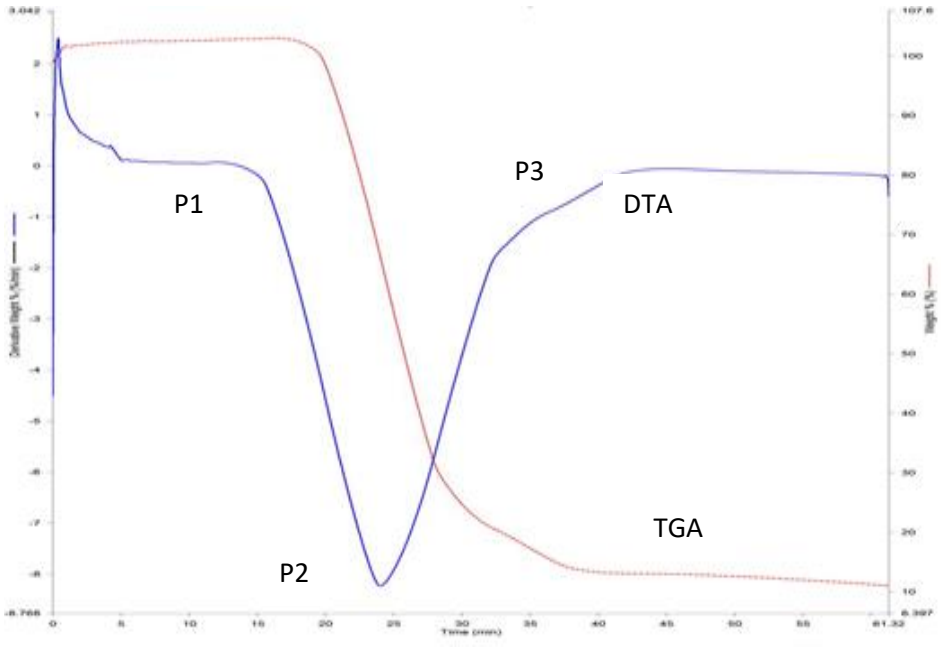


**Figure 2b: NBRRI-ICSEB Combine TGA-DTA at 15ºC/min**

This Figure shows the thermal decomposition of the ICSEB at heating rate of 15 ºC/min. Point P1 is attributed to the removal of adsorbed water in ICSEB known as the water of hydroxylation within 16 minutes of heating time (Hamidu and Adamu, 2024). Between P1 and P2 as heating progressed, endothermic process

was observed with heat being absorbed by the ICSEB (25 minute), thereafter, from P2 to P3 is the complete decomposition process removing all carbonaceous

material with the residual as pure components that sustained the ICSEB in 43 minutes. This process is similar to the work reported by (Hamidu and Adamu, 2024) and (Fernandez-Caliani et al, 2004) on TGA-DTA processes in material characterization.

Figure 2c; present the combined TGA-DTA of NBRRI-ICSEB thermal decomposition at 20 ºC/min heating rate.

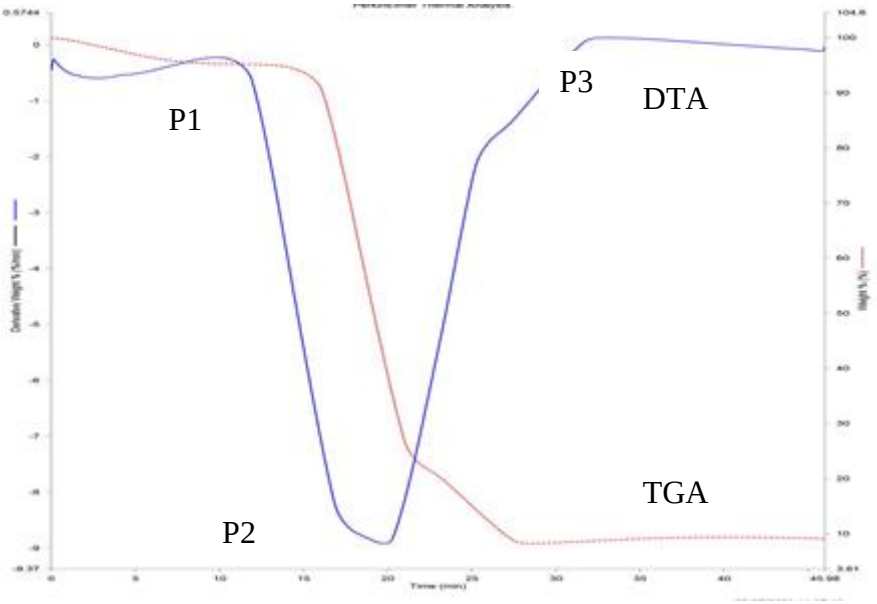


**Figure 2c: NBRRI-ICSEB Combine TGA-DTA at 20 ºC/min**

Point P1 in Figure 2c is attributed to the removal of adsorbed water in the ICSEB known as dihydroxylation process which is removed within 12 minutes of heating, as heating progressed, between P1 and P2, an endothermic process of decomposition where observed with heat being absorbed by the NBRRI-ICSEB and complete removal and oxidization of volatile compounds in 20 minutes of heating. Between P2 and P3 is the removal of the carbonaceous material in the NBRRI-ICSEB within 32 minutes of heating time and the residual is pure material sustaining the ICSEB as also reported in temperature dependency thermogravimetric and differential thermal analysis of NBRRI-ICSEB (Hamidu and Adamu, 2024).

The entire decomposition processes from the TGA results in Figure 1 and combined TGA-DTA in Figure 2 results, revealed that the NBRRI-ICSEB made from laterite of not more than 95% and not less than 5% cement stabilization has shown it absorb more heat which is referred to as endothermic process of decomposition. Based on results from this finding, it implies that the NBRRI-ICSEB is a low bearing material and has short duration of heating time of less than 1 hour. This fast decomposition of the NBRRI-ICSEB could be due to the high content of the combustible materials in the earth soil that forms major component in making the interlocking compressed stabilized earth block.

### 3.3 Scanning Electron Microscope and Energy Dispersive Spectroscope of NBRRI-ICSEB

The scanning electron microscope (SEM) and energy dispersive x-ray (EDX) spectroscope shows the

morphological and elemental compositions of NBRRI-ICSEB. The results for SEM-EDX is shown on Figure 3 (a to d), and Table 1 for the elemental compositions. The SEM images were taken at 30, 80 and 100 µm to study the visibilities of the phase's formation, while complete image detection alongside with the EDX was obtained at 537 µm running at 15 keV.

Figure 3a show the SEM image at 30 µm, with visible cracks within the matrix. In this image, silver like shining silicates and alumina are heterogeneously appearing with pore at the center implies non-homogeneity in the matrix.

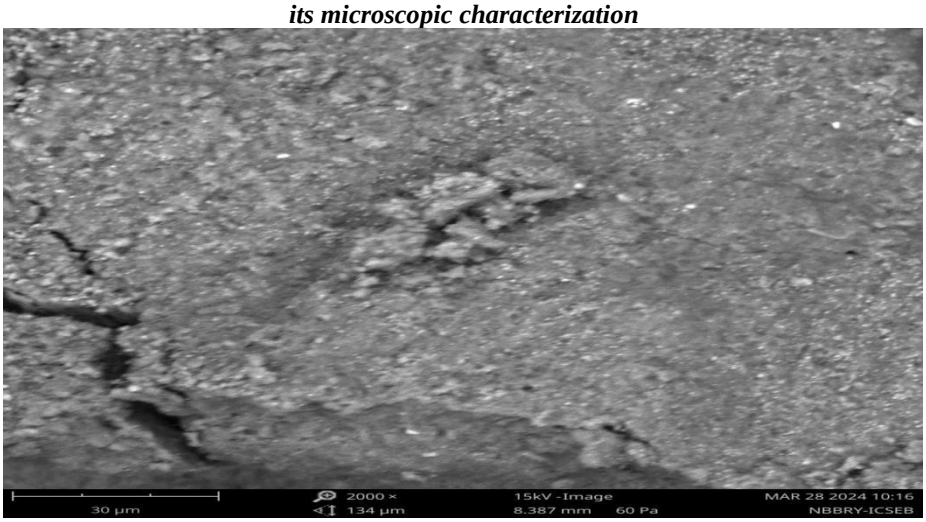


**Figure 3a: NBRRI-ICSEB Scanning Electron Microscopy Image at 30µm**

Figure 3b is the SEM image at 80 µm detection.

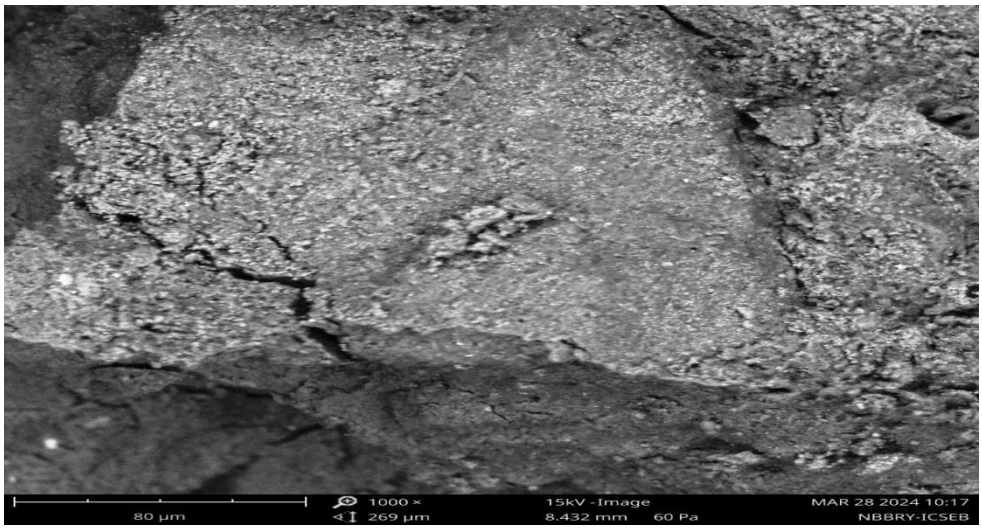


**Figure 3b: NBRRI-ICSEB Scanning Electron Microscopy Image at 80 µm**

At 80 µm, all the phases are separated by visible cracks and pore formations with colour black implying the presence of carbon as dominant elements, with embedded silicates and aluminum materials. This separation is an indication of the quality of materials used in NBRRI-ICSEB production. These cracks could create permeability for water penetration into the block leading to its deterioration. The carbon dominance could be the reason for early decomposition as reported (Hamidu and Adamu, 2024), (Bakam et al, 2020a) on the thermal stability of NBRRI-ICSEB.

Figure 3c is the NBRRI-ICSEB SEM image at 100 µm detection.

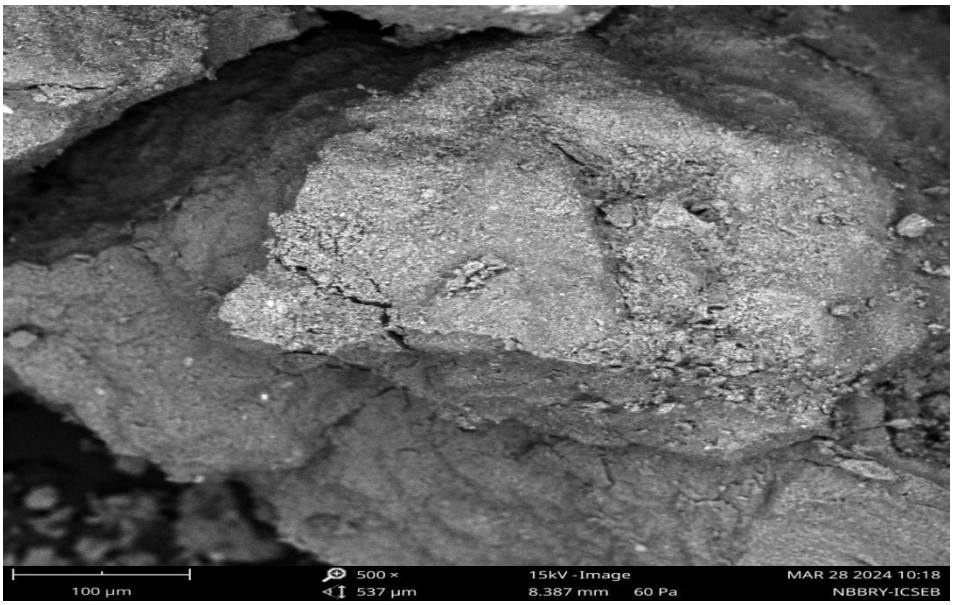


**Figure 3c: NBRRI-ICSEB Scanning Electron Microscopy Image at 100 µm**

At 100 µm, the Carbon, Silicon, Aluminium and Silver phases are clearly visible with cracks within the regions. The result also indicates that, the matrix is not homogenous and thus creating visible phase's separations. At full image detection shown on Figure 3d all elements were detected.


**Figure 3d: NBRRI-ICSEB Full Detection Scanning Electron Microscopy Image at 537 µm**

The EDX analysis of NBRRI-ICSEB (Table 1) revealed the elemental compositions present in the block, the presence of Si, Al, Fe, Ca, and Na above 1% with others in traces of less than 1% confirms the formation alumino-silicon-carbonates binder in the matrix.

**Table 1: EDX Analysis of NBRRI-ICSEB Compositions**

| Element Number | Element Symbol | Element Name | Atomic Conc. |
|---|---|---|---|
| 14 | Si | Silicon | 24.06 |
| 13 | Al | Aluminium | 21.35 |
| 6 | C | Carbon | 41.37 |
| 26 | Fe | Iron | 5.14 |
| 20 | Ca | Calcium | 3.04 |
| 47 | Ag | Silver | 0.40 |
| 30 | Zn | Zinc | 0.55 |
| 11 | Na | Sodium | 1.06 |
| 12 | Mg | Magnesium | 0.85 |
| 15 | P | Phosphorus | 0.58 |
| 17 | Cl | Chlorine | 0.46 |
| 22 | Ti | Titanium | 0.34 |
| 16 | S | Sulfur | 0.47 |
| 19 | K | Potassium | 0.35 |
| 23 | V | Vanadium | 0.00 |
| | | | 100.00 |

From the EDX (Table 1), the weight percentage shows that carbonaceous material is predominant followed by silicone and Aluminium. The carbon dominance in the EDX was responsible to the rapid decomposition of the NBRRI-ICSEB as shown in Figure 1 and continued reaction (combustion) leads to more energy is absorbed (endothermic process) and weakening the properties of the materials sustaining the block.

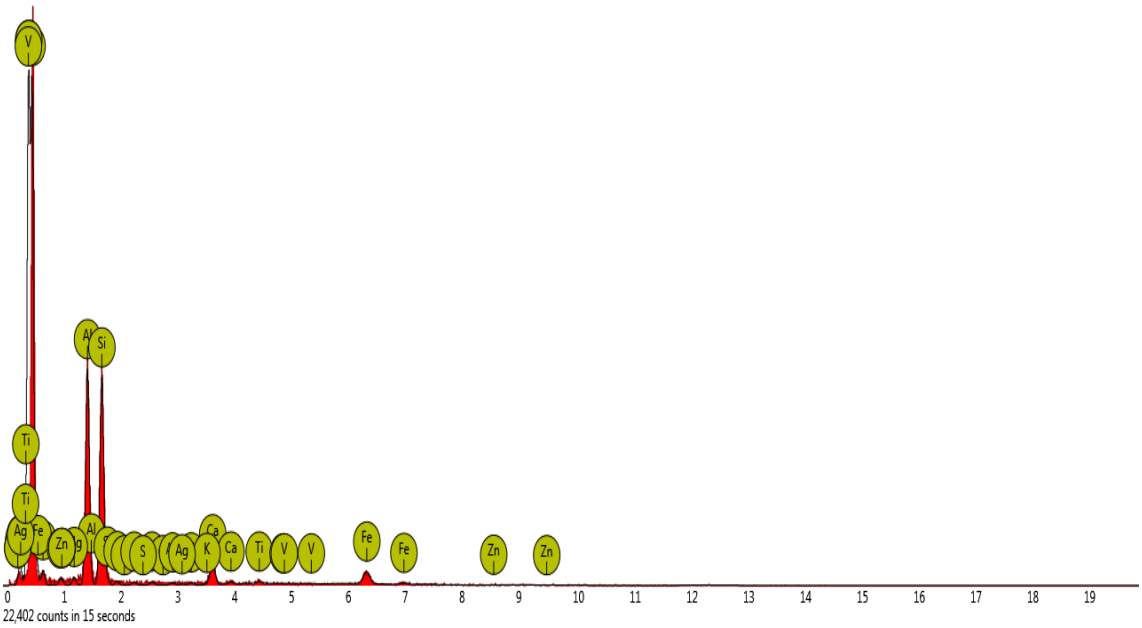


**Figure 4: NBRRI-ICSEB Energy Dispersive X-ray Spectra**

### 3.4 Vibrational Frequencies of NBRRI-ICSEB

The vibrational frequencies of the Nigerian Building and Road Research Institute-Interlocking Compressed Stabilized Earth Block (NBRRI-ICSEB) showing the key components influencing the chemical and physical properties of the material is presented in Figure 5.

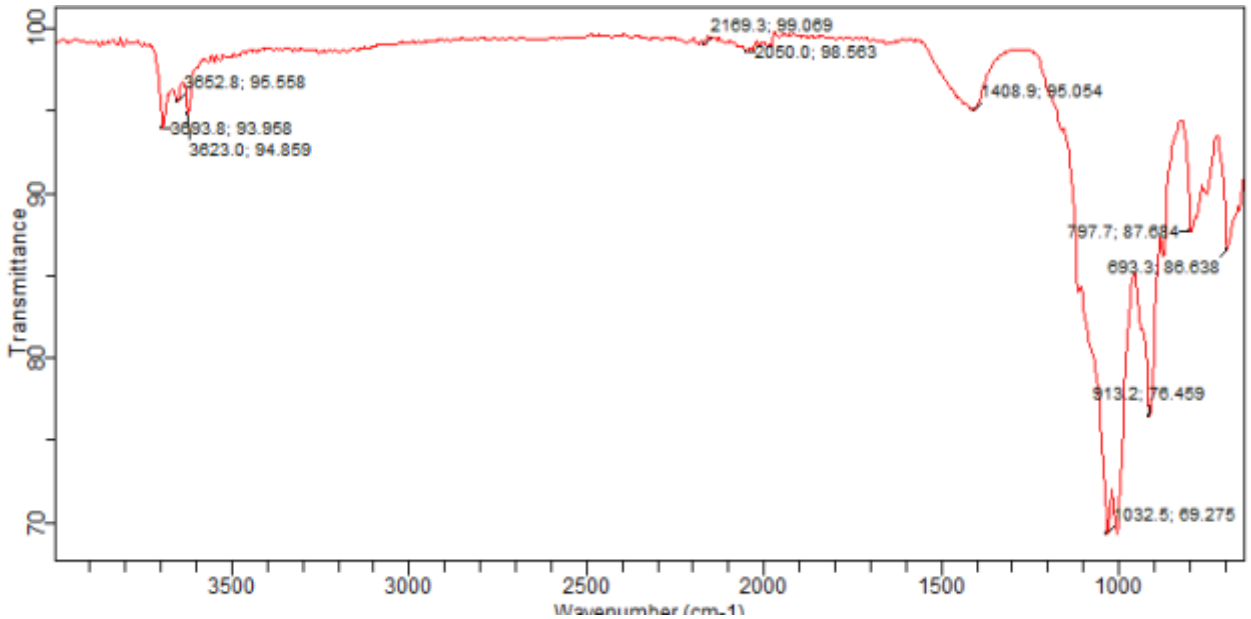


**Figure 5: NBRRI-ICSEB Fourier Transform Infrared Spectrum**

The structure is characterized by broad spectra and overlapping bands of Si-O-H vibration assigned to clays, kaolinite and iron oxides at 3693.8 $cm^{-1}$ are attributed to minerals presence for the NBRRI-ICSEB (Kaze et al, 2018). Accordingly, the hydroxyl (O-H) stretching which occurs between 3719 – 3685 $cm^{-1}$ and Si-O bending at 1032.5 $cm^{-1}$ stretching between 1136 and 1070 $cm^{-1}$ show silicates containing double layers of $O-Si-O$, implies that the material is a composition of hydroxyl silicate principally identified as phyllosilicate (Encyclopedia, 2017). Furthermore; the silicate layer vibrational frequency occurring in the absorbance range 3682 $cm^{-1}$ – 3577 $cm^{-1}$ reflects the internal OH groups between the tetrahedral and octahedral sheets at 3652.8 $cm^{-1}$ depicting internal H-bonding between the octahedral surface. In the ranges of 1478 – 1408 $cm^{-1}$ vibrational frequency is assigned to carbonates, in this range, the absorbance peak occurred at 1408.9 $cm^{-1}$ could be due to the component of cements material used in the stabilization of the NBRRI-ICSEB. The FTIR results revealed that most component of ICSEB produced had silicates and carbonates as dominating the functional group which also supported the EDX elemental composition in Table 1 where carbon had the highest percentage followed by silicon and Aluminium. According to (Bruckman and Wriessnig, 2013) and (Grinard et al, 2012), carbonate is a key component influencing both chemical and physical soil properties as accurately established using FTIR. The carbonaceous material is a material that support combustion when burning, thus results into more heat accumulation (absorb in by the block) thereby weakening the residual properties of the components that made up the NBRRI-ICSEB. This also supports the combined TGA/DTA results in 3.2 as endothermic process of decomposition.

## 4.0 CONCLUSION

Time dependency thermogravimetric and differential thermal analysis, scanning electron microscope and Fourier transform infrared studies of the Nigerian Building and Road Research Institute Interlocking Compressed Stabilized Earth Block (NBRRI-ICSEB) was examined. The following conclusions are drawn; that the NBRRI-ICSEB has low bearing capacity to withstand heating more than 1 hour at 10 $^oC$/min, 15 $^oC$/min and 20 $^oC$/min heating rates to decompose. The combined TGA/DTA results shows the NBRRI-ICSEB absorbs in heat energy which could be described as endothermic process of decomposition as carbonaceous materials continue to combust. The SEM and EDX micrograph, revealed the inhomogeneity formation (heterogeneous formation) with visible cracks in the regions of 30 µm, 80 µm and 100 µm. The EDX revealed 15 elements existing in the formulated NBRRI-ICSEB with carbon dominance, which is responsible to influencing the chemical and physical properties of the produced block. The FTIR spectrum revealed the presence of carbonaceous material as the major functional group, which could also aid combustibility of the ICSEB. We therefore recommend NBRRI-ICSEB for optimization to meet up with the demand for usage as environmentally friendly material for user comfort in building.

**Declaration of competing interest**

The authors declare that there is no competing financial interest or personal relationships that could have influenced the work reported in this paper.

**Acknowledgement**

We sincerely appreciate Engr. Prof. Samson Duna, Director General/Chief Executive Office of the Nigerian Building and Road Research Institute for his financial support and the use of NBRRI-ICSEB., Engr. Abdulrahman Mohammed, Chemical Engineering Department Federal University of Technology Minna, Niger State where the Thermogravimetric and Differential Thermal Analysis was conducted, Engr. Isa Yakubu, Chemical Engineering Department for the SEM-EDX and FTIR at Umar Musa Yar'Adua University, Katsina State, Nigeria. This work is undertaken by the authors and did not receive any sponsorship. All references cited and materials used is duly acknowledged and referenced.

**Data Availability**

All data generated or analyzed during this study are included in this article for the SEM-EDX, and while TGA-DTA can be made available on request from the corresponding author.

**REFERENCES**

Al-Gawari, Z. S. (2022). The Principle of Thermogravimetric Analysis and Its Applications, https://orcid.org/0000-0003-3816-2876.

Bakam, V. A., Mbishida, M. A., Danjuma, T., Zingfat, M. J., Hamidu, L. A. J. and Pyendang, Z. S. (2020a). Determination of Thermal Conductivity of Interlocking Compressed Stabilized Earth Block (CSEB), *International Journal of Recent Engineering Research and Development*, Vol. **5, (**1), pp. 01-08.

Bakam, V. A., Mbishida, M. A., Danjuma, T., Zingfat, M. J., Hamidu, L. A. J. and Pyendang, Z. S. (2020b). Effect of Firing Temperature on Abrasive and Compressive Strengths of an Interlocking Compressed Stabilized Earth Block (CSEB), *International Journal of Recent Engineering Science* (IJRES), Vol. **7**(3), pp.49 – 52.

Bruckman, V. J. and Wriessnig, K. (2013) Improved soil carbonate determination by FT-IR and X-ray analysis. *Environmental Chemistry Letters*, Vol. **11**(1), pp. 65-70.

Delgado M. C. J. and Guerrero I. J. (2007), the Selection of Soils for Unstabilised Earth Building: A Normative Review, *Construction and Building Materials*, Vol. **21**, (2007), pp. 237 – 251.

Dilnesa, B. Z. (2020). Application of Thermogravimetric Method in Cement Science, Materials Science and Technology.

Encyclopedia of Spectroscopy and Spectrometry, third Edition, Vol. **2**(2017), pp. 448 – 454.

Fernândez-Caliani, J. C,. Crespos, E., Rodas, M., Barrenechea, J. F. and Luque, F. J. (2004). Formation of Nontronite from Oxidative Dissolution of Pyrite Disseminated in Precambrian Felsic Metavolcanics of the Southern Iberian Massif (Spain), journal of Clays and clay Minerals, Vol. 52(1), pp. 106 – 114, doi:10.1346/CCMN.2004.052010.

Grinand, C., Barthes, B. G., Brunet, D., Kouakoua, E., Arrouays, D., Jolivet, C., Caria, G. and Bernoux, M. (2012) Prediction of soil organic and inorganic carbon contents at a national scale (France) using mid-infrared reflectance spectroscopy (MIRS). *European Journal of Soil Science*, Vol. **63**(2), pp. 141-151.

Hamidu, L. A. J. and Adamu, Y. A. (2024). Thermogravimetric and Thermal Differential Analysis Instrumental Study of Nigerian Building and Road Research Institute Compressed Stabilized Earth Block Decomposition on Temperature Basis; *Global Science Journal*, Vol. **12**(1), pp. 2853 – 2866.

Hamidu, L. A. J., Aroke, U. O., Osha, O. A. and Muhammad, I. M. (2019). Fourier Transform Infrared Spectroscopy and Scanning Electron Microscopy Characterization of Adhesive Produced from Polystyrene Waste, *Path of Science*, Vol. **5**(12), pp. 3001 – 3008, DOI: 10.22178/pos.53-4.

Kamwa, R. A. T., Tome, S., · Nemaleu, J. G. D., Noumbissie, L. T., · Tommes, B., Eguekeng, I., Woschko, A. S. D., Chongouang, J., Janiak, C. and Etoh, M. (2023). Effect of Curing Temperature on Properties of Compressed Lateritic Earth Bricks Stabilized with Natural Pozzolan-Based Geopolymer Binders Synthesized in Acidic and Alkaline Media. *Arabian Journal for Science and Engineering* https://doi.org/10.1007/s13369-023-08069-0.

Kaze, R. C., Myllyam, L., Moungam, B., Cannio, M., Rosa, R., Kamseu, E., Melo, U.C. and Leonelli, C. (2018). Microstructure and engineering properties of $Fe_2O_3$(FeO)–$Al_2O_3$–$SiO_2$ based geopolymer composites. Journal of Clean Production Vol. **199**, July 2018, pp. 849–859. https://doi.org/ 10.1016/j.jclepro.2018.07.171.

Lyambo Lisias Linge (2012). Durability of Compressed Stabilised Earth Blocks, Master of Civil Engineering Dissertation, School of Civil and Environmental Engineering, University of the Witwatersrand.

Muhwezi, L. and Achanit, S. E. (2019). Effect of Sand on the Properties of Compressed Soil-Cement Stabilized Blocks. *Colloid and Surface Science.* Vol. 4, April, 2019 (1), pp. 1-6. Doi: 10.11648/j.css.20190401.11.

Nshimiyimana, P., Hema, C., Sore, S. O., Zoungrana, O., Messan, A. and Courard, L. (2022). Durability Performances of Compressed Earth Blocks

Exposed To Wetting–Drying Cycles and High Temperature, WIT Transactions on the Built Environment, 210, © 2022 WIT Press.

Nurul, A. I., Thamendran, M., Muhammad, I. S. and Nur'Ain, M. Y. (2020). Sustainable Use of Laterite Soil as Compressed Cement Stabilized Earth Block For Low Cost Housing Construction, IOP Conference Series: Materials Science and Engineering Vol. 849 (2020) 012027. Doi: 10.1088/1757-899X/849/1/012027.

Ongwen, N.O. and Alruqi, A.B. Acoustics of Compressed Earth Blocks Bound Using Sugarcane Bagasse Ash and Water Hyacinth Ash. Appl. Sci. Vol. 2023, 13, 8223. https://doi.org/10.3390/app13148223.

Ouma, J., Ongwen, N., Ogam, E., Auma, M., Fellah, Z. E. A., Mageto, M., Mansour, M. B. and Oduor, A. (2023). Acoustical properties of compressed earth blocks: Effect of compaction pressure, water hyacinth ash and lime, *Case Studies in Construction Materials* Vol. 18(2023) e01828.

Sauerbrunn, S. and Gill, P. (n. d). Decomposition Kinetics Using TGA Ta Instruments 109 Lukens Drive New Castle, De 19720.

Tinti, A., Tugnoli, V., Bonora, S. and Francioso, O. (2015). Recent Applications of Vibrational Mid-Infrared (Ir) Spectroscopy for Studying Soil Components: A Review, *Journal of Central European Agriculture*, Vol. **16**(1), pp. 1 – 22; doi:10.5513/JCEA01/16.1.1535.

10.51975/25400107.som
Journal of the Nigerian Society of Chemical Engineers, 40(1), 2025

# THE USE OF BANANA STEM EXTRACT AS GREEN INHIBITOR TO MITIGATE CORROSION IN ACIDIC ENVIRONMENT: OPTIMIZATION APPROACH

**Olamide OLAWALE [1,2] ; Oluwatobiloba Enoch FAKOLA[1,2] ; Temitope Alaba OSHIN [1,2,*]**

*1. SGD9: Industry, Innovation and Infrastructure*
*2. Chemical Engineering Department, College of Engineering, Landmark University, Omu-Aran, Kwara State, Nigeria.*
** Corresponding Author: oshin.temitope@lmu.edu.ng, +2349066597165*

**ABSTRACT**

*Organic corrosion inhibitors, which are commonly used in the petroleum, refinery, pipeline, and automobile applications, are toxic and have negative environmental consequences. A cost-effective green inhibitor is undoubtedly a better option. The aim of this study is to use banana stem extract as a viable green inhibitor to mitigate corrosion in marine environment using an optimization approach. The extract was phytochemically analyzed to find out if it contained any bioactive constituents capable of preventing metal corrosion. Box-Behnken design was used to investigate the effects of process variables: temperature (30°-60°C), immersion time (3-9 days), extract amount (0.2-0.8 g/l). Scanning Electron Microscope (SEM) and Energy Dispersive Spectroscopy (EDS) were employed for characterization. The extract was found to be a good inhibitor because it contains alkaloids, phenols, tannins, saponins, terpenoids, steroids and flavonoids, according to the results of the phytochemical analysis. The experimental design's optimal process levels were found to be 45°C, 6 days of immersion, and 0.5 g/l of inhibitor. It was observed that more white patches were present on the SEM and EDS results of the mild steel from validated experiment via adsorption. It confirmed that banana stem extract is a good inhibitor in 0.1M $H_2SO_4$ solution.*

***Keywords:*** *Corrosion, Optimization, Phytochemical Analysis, Energy Dispersive Spectroscopy*

## 1. INTRODUCTION

Green corrosion inhibitors are free of hazardous substances, biodegradable materials, and heavy metals (Alimohammadi et al., 2023), and have been reported to be the best technique for mitigating corrosion challenges. It has been found that the presence of organic compounds such as flavonoids, steroids, tannins and alkaloids make some of these plant-biowastes to have inhibitory effects. Several researchers claim that inhibitor molecules adhere to metal surfaces and stop corrosion in corrosive solutions (Qiang et al., 2023).

Some of the plant extracts that had been used as corrosion inhibitor are: Bitter kola (Anadebe et al., 2018); Polyphenol extract (Chami et al., 2023); maple leaves extract (Wang et al., 2023); waste feverfew root (Zhou et al., 2023); *Pisum sativum L* leaves extract (Chen et al., 2023); *Glebionis coronaria* plant extract (Kellal et al., 2023); *Convolvulus microphyllus* extract (Hladhar et al., 2023); Tulsi and green tea extracts (Chowdhury et al., 2023); *Chromolaena odorata* leaves extract (Liao et al., 2023); Papaya leaves extract (Tan et al., 2021); *Medicago sative* plant (Al-Turkustani et al, 2011); *Moringa oleifera* and *Jatropha curcas* leaves extracts (Ikubnani et al., 2023); essential oil extracted from the leaves (El Aatiaoui et al., 2023); walnut green husk extract (Li et al., 2023*), Stylosanthes gracilis* extract (Ofuyekpone etal., 2021); Methyl-5-benzoyl-2-benzimidazole Carbamate (Mebendazole) (Edoziuno et al., 2020); extract of *Centrosema pubescens* (Ofuyekpone et al., 2023); Anthelmintic Drug (Edoziuno et al., 2024). There are large numbers of

inhibitors reported in corrosion science but no work had been reported on the use of Banana stem extract as a corrosion inhibitor in 0.1 M $H_2SO_4$ environment with optimization and optimization studies as at when this research was conducted. This study investigated the use of banana stem extract as green inhibitor to mitigate corrosion in acidic environment via optimization approach.

## 2. MATERIALS AND METHODS

### 2.1 Preparation of Banana Stem Extract (BSE)

The Landmark University teaching and research farm provided the banana stem which was air-dried for 4 days to remove moisture and retain the bioactive components. 35 grams of the powdered banana stem was weighed and extracted using 350 ml of ethanol as solvent at a temperature of 78 $^oC$ for 4 hours through a Soxhlet extraction process. The entire process was repeated and 500ml of banana extract was gotten which was used for the research. Thereafter, the extract was kept in the refrigerator for further use.

### 2.2 Preparation of mild steel

Mild steel was cut into 2.2 cm by 1.9 cm coupons with a centrally punched hole measuring 0.1 cm. Emery paper was used to scrub mild steel in order to remove any dirt from the metal surfaces of the samples. Prior to being air-

dried and weighed, the samples were washed in distilled water and cleaned with acetone.

**2.3 Design of Experiment**

Box-Behnken Design was used to study the interactions of process variables. The variables considered were: Inhibitor concentration (0.2 g/l-0.8g /l), Temperature (30 $^{o}$C-60 $^{o}$C) and Time (3 days-9 days) which generated 17 experimental runs. This methodology was adapted from Oyewole et al. (2022) and Oyewole et al. (2023b). Table 1 shows the variables that were tested and levels. Box-Behnken Design for the interaction of variables for the 17 experimental runs that were generated is in Table 2.

**Table 1: Variables with different levels**

| Variables | Unit | Levels | |
|---|---|---|---|
| | | Low | High |
| **Time of immersion** | Days | 3 | 9 |
| **Temperature** | $^{0}$C | 30 | 60 |
| **Inhibitor concentration** | g/l | 0.2 | 0.8 |

**Table 2: Box-Behnken Design for interaction of variables**

| | Variable 1 | Variable 2 | Variable 3 |
|---|---|---|---|
| Run | A: Temperature (°C) | B: Inhibitor Concentration (g/l) | C: Time (days) |
| 1 | 45 | 0.5 | 6 |
| 2 | 45 | 0.5 | 6 |
| 3 | 45 | 0.8 | 3 |
| 4 | 60 | 0.5 | 3 |
| 5 | 45 | 0.2 | 3 |
| 6 | 45 | 0.8 | 9 |
| 7 | 45 | 0.2 | 9 |
| 8 | 45 | 0.5 | 6 |
| 9 | 45 | 0.5 | 6 |
| 10 | 30 | 0.5 | 3 |
| 11 | 60 | 0.2 | 6 |
| 12 | 30 | 0.8 | 6 |
| 13 | 30 | 0.5 | 9 |
| 14 | 60 | 0.5 | 9 |
| 15 | 60 | 0.8 | 6 |
| 16 | 45 | 0.5 | 6 |
| 17 | 30 | 0.2 | 6 |

**2.4 Phytochemical Analysis**

The phytochemical analysis of the banana stem extract was performed to determine the presence of bioactive constituents.

**2.4.1 Test for Tannins**

In a water bath containing 30 $cm^3$ of water, 0.30 g of (Banana Stem Extract) BSE was weighed and boiled for 10 minutes. Filtration was carried out after boiling using Whatman filter paper (125 mm). Three drops of 0.1 % ferric chloride were applied to 5 $cm^3$ of the filtrate. This methodology was adopted from Ejikeme et al. (2014).

**2.4.2 Test for Saponins**

Water bath with a volume of 30 cm3 of water, 0.30 g of BSE was boiled for 10 minutes and filtered using Whatman filter paper (125 mm). A mixture of 5 cm3 of distilled water with 10 cm3 of filtrate was centrifuged for a stable persistent froth. This analysis was adopted from Ejikeme et al. (2014).

**2.4.3 Test for Terpenoids**

To 0.5 ml of BSE, 1 ml of trichloroacetic acid was added. The appearance of red colouration indicated the presence of terpenoids as adopted from (Ahmed et al., 2022; Kancherla et al., 2019).

**2.4.4 Test for Flavonoids**

BSE (0.30 g) was weighed and transferred into a beaker. The BSE was extracted with 30 cm3 of distilled water at room temperature, for 2 hours and filtered with Whatman filter paper (125 mm). 10 cm3 of the aqueous filtrate of the BSE was added to 5 cm3 of 1.0 M of dilute ammonia solution, thereafter; 5 cm3 of concentrated tetraoxosulphate (VI) acid was added. This method was adopted from Ezeonu and Ejikeme (2016).

**2.4.5 Test for Alkaloids**
Diluted HCl was added to 2 g of BSE, then mixed evenly and filtered. Mayer reagent was added to 2-3 ml of the filtrate and Mayer's test was conducted. The formation of a yellow precipitate showed Alkaloid was present. This method was adopted from (Parbuntari et al., 2018).

**2.4.6 Test for Steroids**
2 ml of chloroform was added to 2 ml of BSE and 1 ml of concentrated $H_2SO_4$ was added by the side of the test tube. After shaking, the formation of red colouration in the upper layer and a greenish-yellow fluorescence in the acid layer indicates the presence of steroids.

**2.5 Weight Loss Analysis**
The weight loss was calculated using the experimental runs generated by the software.
The weight loss was calculated using equation (1)

$$\Delta W = Wp - Wf \quad (1)$$

where ΔW is the weight loss (g),
Wp is the weight before immersion (g);
Wf is the weight after immersion (g).
The corrosion rate in the absence and presence of inhibitors was calculated using equation 2.;

$$CR = \frac{\Delta W}{At} \quad (2)$$

t is time of exposure in days
A is area of the specimen ($cm^2$)
CR is the corrosion rate at each exposure time.

**2.6 Scanning Electron Microscopy (SEM) and Energy Dispersive Spectroscopy (EDS) Characterization**
SEM-EDS were used to characterize and determine the surface morphology and elemental compositions for mild steel of: optimal process level (validated); blank and maximum inhibition efficiency. The type of SEM-EDS used was JCOL-model JSM-6390 at Covenant University, Ota, Nigeria.

## 3. RESULTS AND DISCUSSION

**3.1 Result of Phytochemical Analysis**
Table 3 displayed the findings of phytochemical analyses conducted on banana stem extract. This demonstrated the presence of alkaloids, terpenoids, flavonoids, phenols, tannins, and saponins. These components were reported to be components of a good inhibitor in a number of green inhibitors made from plant biomass, supporting the research result of (Oyewole et al., 2023a).

**Table 3: Phytochemical Analysis**

| S/N | Phytochemical constituents | Result |
|---|---|---|
| 1 | Tannnis | + |
| 2 | Saponins | + |
| 3 | Steroids | + |
| 4 | Terpenoids | + |
| 5 | Flavonoids | + |
| 6 | Alkaloids | + |

+ indicated presence of phytochemicals
- indicated absence of phytochemicals

**3.2 Result of Weight Loss Measurements**
The tests were performed under total immersion. The results of the third experimental run showed the lowest corrosion rate. Table 4 displays the weight loss analysis results, while Table 5 displays the inhibition efficiency results. The conditions of 45 ºC, 6 days, and 0.5 g/l of inhibitor concentration resulted in highest level of inhibition efficiency.

**Table 4: Result from Weight Loss Measurement**

| | | Variable 1 | Variable 2 | Variable 3 | Response 2 | Response 3 |
|---|---|---|---|---|---|---|
| **Std** | **Run** | **A: Temperature (°C)** | **B: Inhibitor Concentration (g/l)** | **C: Time (days)** | **Corrosion Rate (g/days.cm²)** | **Weight Loss (grams)** |
| **8** | 1 | 60 | 0.5 | 9 | 0.0130 | 0.4890 |
| **3** | 2 | 30 | 0.8 | 6 | 0.0061 | 0.1530 |
| **11** | 3 | 45 | 0.2 | 9 | 0.0022 | 0.0840 |
| **9** | 4 | 45 | 0.2 | 3 | 0.0136 | 0.1700 |
| **10** | 5 | 45 | 0.8 | 3 | 0.0200 | 0.2590 |
| **2** | 6 | 60 | 0.2 | 6 | 0.0046 | 0.1160 |
| **14** | 7 | 45 | 0.5 | 6 | 0.0024 | 0.0600 |
| **7** | 8 | 30 | 0.5 | 9 | 0.0037 | 0.1380 |
| **1** | 9 | 30 | 0.2 | 6 | 0.0082 | 0.2060 |
| **5** | 10 | 30 | 0.5 | 3 | 0.0152 | 0.1900 |
| **6** | 11 | 60 | 0.5 | 3 | 0.0093 | 0.1170 |
| **17** | 12 | 45 | 0.5 | 6 | 0.0024 | 0.0600 |

| | | Variable 1 | Variable 2 | Variable 3 | Response 2 | Response 3 |
|---|---|---|---|---|---|---|
| **Std** | **Run** | **A: Temperature (°C)** | **B: Inhibitor Concentration (g/l)** | **C: Time (days)** | **Corrosion Rate (g/days.cm$^2$)** | **Weight Loss (grams)** |
| **16** | 13 | 45 | 0.5 | 6 | 0.0024 | 0.0600 |
| **13** | 14 | 45 | 0.5 | 6 | 0.0024 | 0.0600 |
| **12** | 15 | 45 | 0.8 | 9 | 0.0041 | 0.1530 |
| **4** | 16 | 60 | 0.8 | 6 | 0.0051 | 0.1270 |
| **15** | 17 | 45 | 0.5 | 6 | 0.0024 | 0.0600 |

**Table 5: Result of Inhibition efficiency**

| | | Variable 1 | Variable 2 | Variable 3 | Response 1 |
|---|---|---|---|---|---|
| **Std** | Run | A: Temperature (°C) | B: Inhibitor Concentration (g/l) | C: Time (days) | Inhibitor Efficiency |
| **8** | 1 | 60 | 0.5 | 9 | 92.9058 |
| **3** | 2 | 30 | 0.8 | 6 | 97.7638 |
| **11** | 3 | 45 | 0.2 | 9 | 98.2989 |
| **9** | 4 | 45 | 0.2 | 3 | 83.0000 |
| **10** | 5 | 45 | 0.8 | 3 | 96.2590 |
| **2** | 6 | 60 | 0.2 | 6 | 98.1220 |
| **14** | 7 | 45 | 0.5 | 6 | 98.5667 |
| **7** | 8 | 30 | 0.5 | 9 | 98.0069 |
| **1** | 9 | 30 | 0.2 | 6 | 97.0115 |
| **5** | 10 | 30 | 0.5 | 3 | 95.6640 |
| **6** | 11 | 60 | 0.5 | 3 | 98.1798 |
| **17** | 12 | 45 | 0.5 | 6 | 98.5667 |
| **16** | 13 | 45 | 0.5 | 6 | 98.5667 |
| **13** | 14 | 45 | 0.5 | 6 | 98.5667 |
| **12** | 15 | 45 | 0.8 | 9 | 97.8011 |
| **4** | 16 | 60 | 0.8 | 6 | 98.2380 |
| **15** | 17 | 45 | 0.5 | 6 | 98.5667 |

**3.3 Result of ANOVA for the Corrosion Rate, CR**

The model is significant, according to the model's F-value of 4.70. The probability that an F-value this large could be the result of noise is only 2.67%. **P-values** less than 0.0500 indicate model terms which are significant. In this case **C²** and AC are the significant term. The Adjusted $R^2$ of 0.6757 and coefficient of regression $R^2$ was 0.8581 were observed from the ANOVA as shown in Table 6. Regression equations generated in terms of coded terms is in equation 3 respectively. The result of ANOVA is in Table 6.

**Regression Equation**

$$\text{Corrosion rate} = 0.0024 - 0.001A + 0.0008B - 0.0044C - 0.0006AB + 0.0038AC - 0.0012BC + 0.0020A^2 + 0.0016B^2 + 0.0059C^2 \quad (3)$$

**Table 6: ANOVA**

| Source | Sum of Squares | df | Mean Square | F-value | p-value | |
|---|---|---|---|---|---|---|
| **Model** | 0.0004 | 9 | 0.0000 | 4.70 | 0.0267 | significant |
| **A-temperature** | 1.554 | 1 | 1.554 | 0.0159 | 0.9031 | |
| **B-inhibitor concentration** | 5.532 | 1 | 5.532 | 0.5672 | 0.4759 | |
| **C-Time** | 0.0002 | 1 | 0.0002 | 15.81 | 0.0054 | |
| **AB** | 1.629 | 1 | 1.629 | 0.1670 | 0.6950 | |
| **AC** | 0.0001 | 1 | 0.0001 | 5.88 | 0.0451 | |
| **BC** | 5.428 | 1 | 5.428 | 0.5565 | 0.4800 | |
| **A²** | 0.0000 | 1 | 0.0000 | 1.66 | 0.2390 | |

| | | | | | |
|---|---|---|---|---|---|
| **$B^2$** | 0.0000 | 1 | 0.0000 | 1.17 | 0.3144 |
| **$C^2$** | 0.0001 | 1 | 0.0001 | 15.21 | 0.0059 |
| **Residual** | 0.0001 | 7 | 9.753 | | |
| **Lack of Fit** | 0.0001 | 3 | 0.0000 | | |
| **Pure Error** | 0.0000 | 4 | 0.0000 | | |
| **Cor Total** | 0.0005 | | | | |
| | | **Adj $R^2$** 0.6757 | $R^2$ | 0.8581 | |

### 3.4 Surface Response Plots

The 3D interactive effect of process variables on corrosion rate are shown in Figures 1–3. These showed relationship between the variables and corrosion rate response.

### 3.5 Experimental Validation

The design of experiment predicted variables optimal process level as Time: 7.03 days, Temp: 55.3ºC and Conc: 0.62g/l. This has been validated, and an inhibition efficiency of 96.935% was obtained.

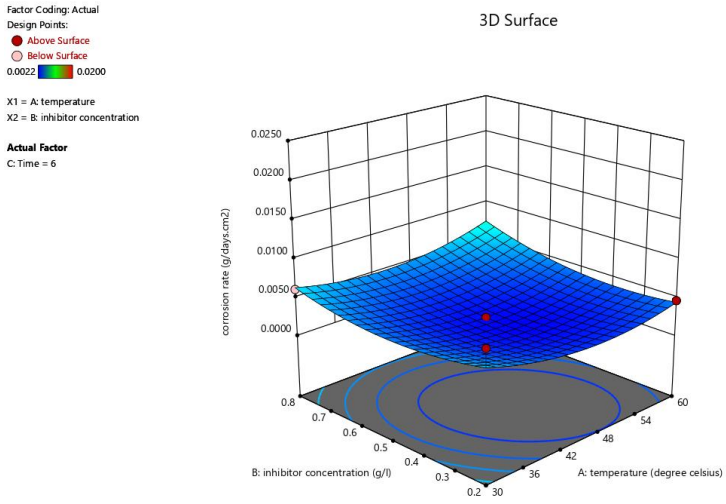


**Figure 1: 3-D Response Surface Plot for the interaction of Temperature and Inhibition Conc**

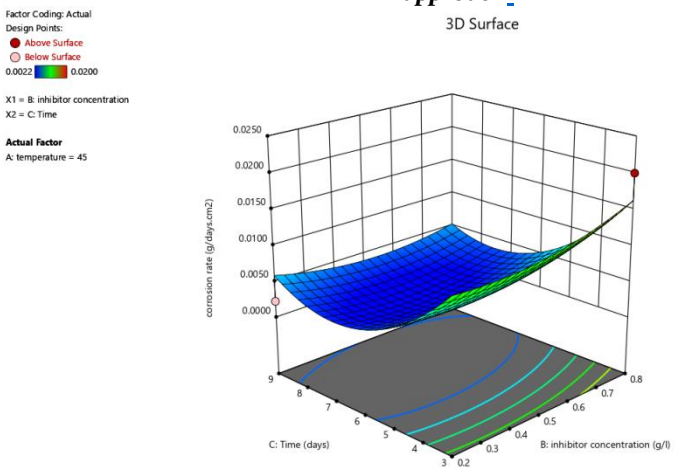


**Figure 2: 3-D Response Surface Plot for the interaction of Time and Inhibition Conc**

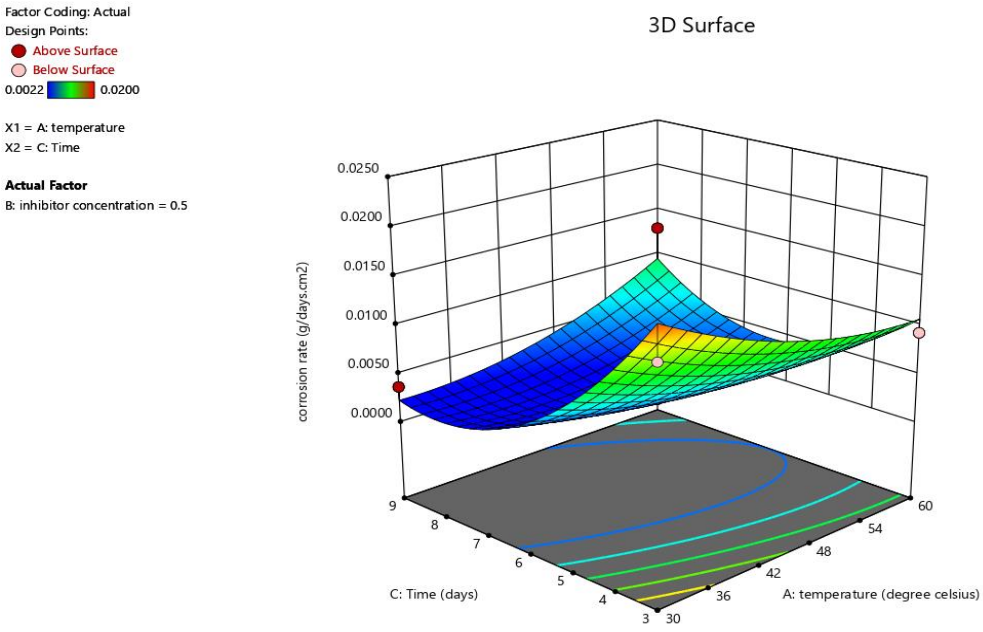


**Figure 3: 3-D Response Surface Plot for the interaction of Temperature and Time**

### 3.6 Results of Scanning Electron Microscope (SEM) Analysis

The acidic medium caused the blank surface to be severely damaged, as shown in Figure4a, with significant cracks and serrated edges. In contrast, Figure 4b, showed less damage and smoother surface, due to inhibitor present. In addition, Figure 4c demonstrated a more protective bio-film which was caused by interaction of bioactive constituents on the outer layer of mild steel at the optimal process level (validated).


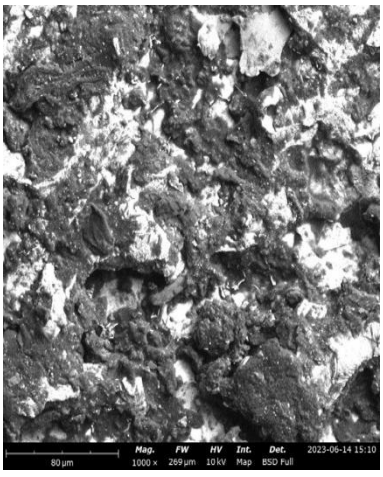


**4a** **4b** **4c**

**Figure 4a: Blank surface morphology**
**Figure 4b: Mild steel with highest inhibition efficiency, morphology**
**Figure 4c: Mild steel of validated experiment surface morphology.**

### 3.7 Results of EDS Analysis

EDS was used to examine the elemental compositions of mild steel blank, mild steel with the highest inhibition efficiency, and mild steel with optimal process variables (validated), as illustrated in Figures 5a-c. The elemental composition of the blank showed presence of O, Fe, N, and C; in Figure 5a. O, Fe, higher amount of O which is a heteroatom was seen in Figure 5b. There is decrease in amount of O while amount of Fe increased as seen in Figure 4c, which supported the findings of (Alimohammadi et al., 2023; Oyewole et al., 2023b, Abaei, et al., 2023). Furthermore, in the validated experiment, interphase functioned as a physical barrier to further impede corrosion in the mild steel. H2 + BSE was the van der Waals interaction, and the extract adsorbed $SO4^-$ ion. As a concentrated oxide hydroxide inhibition component, the corrosion and proactive types' active site was blocked.

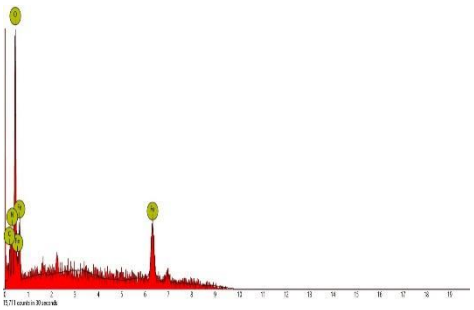

| | Element symbol | Element name | Atomic conc % | Weig % |
|---|---|---|---|---|
| | O | Oxygen | 54.57 | 29.05 |
| | Fe | Iron | 35.85 | 66.61 |
| | N | Nitrogen | 7.75 | 3.61 |
| | C | Carbon | 1.83 | 0.73 |

**Figure 5a: EDS spectra of the mild steel of the Blan**

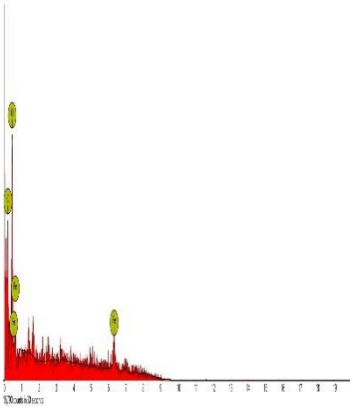

| | Element symbol | Element name | Atomic conc % | Weight conc % |
|---|---|---|---|---|
| | O | Oxygen | 63.89 | 39.83 |
| | Fe | Iron | 25.33 | 55.12 |
| | C | Carbon | 10.78 | 5.05 |

**Figure 5b: EDS spectra of mild steel obtained via highest inhibition efficiency**

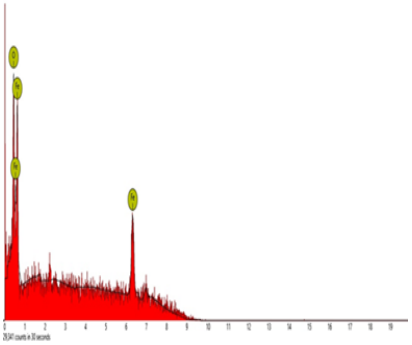

| Element symbol | Element name | Atomic conc % | Weight conc % |
|---|---|---|---|
| O | Oxygen | 40.21 | 16.15 |
| Fe | Iron | 59.79 | 83.85 |

**Figure 5c: EDS spectra of mild steel of optimal process level**

## 4. CONCLUSIONS

The presence of saponins, flavonoids, tannins, phenols, steroids, terpenoids, and alkaloids was revealed by the phytochemical analysis, confirming the effectiveness of banana stem extract as a corrosion inhibitor. The validated experiment was carried out at an optimal process level of 7.03 days, 55.33 $^{o}$C and 0.62 g/l inhibitor concentration. The result of SEM and EDS showed that more protective film was formed on the surface of the mild steel. This confirmed that more adsorption was responsible for the blockage of corrosion on mild steel of validated experiment than from highest inhibition efficiency. It can be concluded that Banana stem is a good inhibitor for the corrosion of mild steel in 0.1M $H_2S0_4$. This research can be replicated to solve corrosion problems in petroleum, oil and service

industries because it is cost effective and also an eco-friendly approach.

## REFERENCES


Abaei, M., Rahimipour, M. R., Farvizi, M., & Eshraghi, M. J. (2023). Microstructure and Corrosion Behavior of Al-Cu-Fe Quasi-crystalline Coated Ti-6Al-4V Alloy. International Journal of Engineering, 36(10), 1880-1891.

Ahmed, Z. (2023). Analysis of Phytochemical Potentiality and In Vitro Antimicrobial Properties of Jute Leaf Extracts. Environmental Science, 2(2), 122.

Alimohammadi, M., Ghaderi, M., Ramazani SA, A., & Mahdavian, M. (2023). Falcaria vulgaris leaves extract as an eco-friendly corrosion inhibitor for mild steel in hydrochloric acid media. Scientific Reports, 13(1), 3737.

Al-Turkustani, A. M., Arab, S. T., & Al-Qarni, L. S. S. (2011). Medicago Sative plant as safe inhibitor on the corrosion of steel in 2.0 M H2SO4 solution. Journal of Saudi Chemical Society, 15(1), 73-82.

Chami, A., Benabbou, R., Taleb, M., Rais, Z., & El Haji, M. (2023). Inhibition of corrosion of steel in 1 M HCl solution by polyphenol extract: Application for Steel used in the automotive industry in Morocco. Moroccan Journal of Chemistry, 11(3).

Chen, J., Wu, Y., Guo, L., Li, W., Tan, B., & Brahmia, A. (2023). Insight into the anti-corrosion mechanism of Pisum sativum L leaves extract as the degradable inhibitor for Q235 steel in sulfuric acid medium. Journal of the Taiwan Institute of Chemical Engineers, 143, 104664.

Chowdhury, M. A., Ahmed, M. M. S., Hossain, N., Islam, M. A., Islam, S., & Rana, M. M. (2023). Tulsi and green tea extracts as efficient green corrosion inhibitor for the corrosion of aluminum alloy in acidic medium. Results in Engineering, 17, 100996.

Edoziuno, F. O., Adediran, A. A., Odoni, B. U., Oki, M., & Adesina, O. S. (2020). Comparative analysis of corrosion inhibition effects of mebendazole (MBZ) on mild steel in three different sulphuric acid concentrations. International Journal of Corrosion and Scale Inhibition, 9(3), 1049-1058.

Edoziuno, F.O., Odoni, B.U., Adediran, A.A., Byadi, S., Barhoumi, A., Nwaeju, C.C., Modebe, L.U. and Okeniyi, J.O., 2024. Surface corrosion inhibition of mild steel in an acidic environment by an anthelmintic drug: experimental, RSM, DFT and MD simulation studies. Port Electrochima Acta, 42, pp.1-29

Ejikeme, C., Ezeonu, C. S., & Eboatu, A. N. (2014). Determination of Physical and Phytochemical Constituents of some Tropical Timbers Indigenous to nigerdelta area of nigeria. European Scientific Journal, 10(18), 247-270.

El Aatiaoui, A., Daoudi, W., El Badri, A., Salhi, A., El Massaoudi, M., El Boutaybi, A., ... & Loutou, M. (2023). Anticorrosive potential of essential oil extracted from the leaves of Calamintha plant for mild steel in 1 M HCl medium. Journal of Adhesion Science and Technology, 37(7), 1191-1214.

Ezeh, E. M., & Chinedu, A. P. (2023). Assessment of the corrosion inhibitory potentials of Chromolaena Odorata leaf extract on mild steel in hydrogen chloride acid environment. Moroccan Journal of Chemistry, 11(1), 11-1.

Ezeonu, C. S., & Ejikeme, C. M. (2016). Qualitative and quantitative determination of phytochemical contents of indigenous Nigerian softwoods. New journal of Science, 2016(1), 5601327.

Haldhar, R., Vanaraj, R., Dagdag, O., Berisha, A., & Kim, S. C. (2023). Convolvulus microphyllus extract as a green, effective, and affordable corrosion inhibitor: theoretical calculations and experimental studies. Coatings, 13(5), 860.

Ikubanni, P. P., Adeleke, A. A., Odusote, J. K., Adegoke, H., Oki, M., & Okolie, J. A. (2023). Corrosion control of AISI 1007 steel using hybrid inhibitors of plant extracts. Chemistry Africa, 6(6), 3161-3171.

Kancherla, N., Dhakshinamoothi, A., Chitra, K., & Komaram, R. B. (2019). Preliminary analysis of phytoconstituents and evaluation of anthelminthic property of Cayratia auriculata (in vitro). Maedica, 14(4), 350.

Kellal, R., Left, D. B., Azzi, M., & Zertoubi, M. (2023). Insight on the corrosion inhibition performance of Glebionis coronaria plant extract in various acidic mediums. Journal of Applied Electrochemistry, 53(4), 811-832.

Li, X., Xin, X., & Deng, S. (2023). Synergism between walnut green husk extract and sodium dodecyl benzene sulfonate on cold rolled steel in 1.0 mol/L H2SO4 solution. Corrosion Communications, 9, 1-12.

Ofuyekpone, O. D., Utu, O. G., Onyekpe, B. O., Adediran, A. A., & Oki, M. (2021). Data on corrosion inhibition effect of Stylosanthes gracilis extract on UNS S30403 austenitic stainless steel in dilute acid solution. Chemical Data Collections, 35, 100763.

Ofuyekpone, O. D., Utu, O. G., Onyekpe, B. O., Unueroh, U. G., & Adediran, A. A. (2023). Corrosion Inhibition of Chloride-Induced Attack on AISI 304L Using Novel Corrosion Inhibitor: A Case Study of Extract of Centrosema pubescens. Chemistry Africa, 6(1), 459-476.

Oyewole, O., Abayomi, T. S., Oreofe, T. A., & Oshin, T. A. (2022). Anti-corrosion using rice straw extract for mild steel in 1.5 M H2SO4 solution. Results in Engineering, 16, 100684.

Oyewole, O., Adeoye, J. B., Udoh, V. C., & Oshin, T. A. (2023a). Optimization and corrosion inhibition of Palm kernel leaves on mild steel in oil and gas applications. Egyptian Journal of Petroleum, 32(1), 41-46.

Oyewole, O., David, A., Seun, A. O., & Bello, O. S. (2023b). Optimization and inhibitive effects of Sweet Potato Leaf Extract (SPLE) on mild steel. Chemical Data Collections, 45, 101015.

Parbuntari, H., Etika, S. B., & Delvia, E. (2021). Molecular encapsulation of bioactive molecules of Ruku-Ruku leaves (Ocimum tenuiflorum Linnen) as a preliminary stability study. In Journal of Physics: Conference Series (Vol. 1788, No. 1, p. 012002). IOP Publishing.

Qiang, Y., Ran, B., Li, M., Xu, Q., & Peng, J. (2023). GO-functionalized MXene towards superior anti-corrosion coating. Journal of Colloid and Interface Science, 642, 595-603.

Tan, B., Xiang, B., Zhang, S., Qiang, Y., Xu, L., Chen, S., & He, J. (2021). Papaya leaves extract as a novel eco-friendly corrosion inhibitor for Cu in H2SO4 medium. Journal of colloid and interface science, 582, 918-931.

Wang, Y., Qiang, Y., Zhi, H., Ran, B., & Zhang, D. (2023). Evaluating the synergistic effect of maple leaves extract and iodide ions on corrosion inhibition of Q235 steel in H2SO4 solution. Journal of Industrial and Engineering Chemistry, 117, 422-433.

Zhou, Z., Min, X., Wan, S., Liu, J., Liao, B., & Guo, X. (2023). A novel green corrosion inhibitor extracted from waste feverfew root for carbon steel in H2SO4 solution. Results in Engineering, 17, 100971.

10.51975/25400108.som
Journal of the Nigerian Society of Chemical Engineers, 40(1), 2025

# ENHANCING CARBON (IV) OXIDE ADSORPTION FROM FLUE GAS MIXTURE AT ELEVATED TEMPERATURE USING COMPOSITE OF NANOPARTICLES

**[*]Ojong, O. E[1]; Osha, O. A[1]; Abam, F. I[2]; and Samuel, S. S[1]**

[1]*Department of Chemical Engineering, Faculty of Engineering and Technology, University of Calabar, Calabar, Cross River State, Nigeria,*

[2]*Department of Mechanical Engineering, Faculty of Engineering and Technology, University of Calabar, Calabar, Cross River State, Nigeria*

[1*]*ojong.ojong@unical.edu.ng; [1]odeyosha@unical.edu.ng; [2]fidelisabam@unical.edu.ng; [1]silas.samuel@unical.edu.ng*

[*]*Corresponding Author: ojong.ojong@unical.edu.ng*

**ABSTRACT**

*Chitosan/clay materials from periwinkle shells and clay soil at a 50:50 ratio was made adsorbent and characterized, used for the adsorption of $CO_2$ from flue gas at elevated temperatures (50 $^oC$ – 500 $^oC$) in a fixed bed column (length 1.5m, and internal diameter 0.02m). Flue gas with composition of Methane (0.003), Ethane (0.002), Hydrogen (0.05), $CO_2$ (0.15), Water Vapour (0.02), and Nitrogen (0.76), of pressure 49KPa, temperature of 500 $^oC$, and flow rate of 75min/L from the exhaust tank; enters the fixed bed column for the adsorption process where the adsorbent is already placed. The results of the characterization of the adsorbent showed that 5.283nm, 2.64nm, 434.7$m^2$/g, 704.2$m^2$/g, 0.202cc/g, and 56.73% were best the values for the adsorbent' pore width, pore diameter, microspore surface area, pore volume, and porosity, obtained using Dubinin-Raduskevich (DR), density functional theory (DFT), hydraulic diameter (DH), Langmuir, DH, and scanning electron microscope (SEM) analysing techniques respectively. The Fourier transform infrared (FTIR) Spectrum showed the presence of halogen (C-Cl), $2^0$ alcohol (C-O), Nitro (N-O), and amine (N-H) compounds in the nanoparticles, revealing a strong affinity for $CO_2$ particles in the flue gas. Another analysis showed the presence of elements (Ca, Si, Al, and Sr) in high compositions (0.470, 0.202, 0.186, and 0.092, respectively), revealing that the adsorbent is resistant to high temperatures. X-ray diffraction (XRD) analysis of the adsorbent gave Ca $(OH)_2$, $CaCO_3$, and $TiO_2$ with compositions of 0.78, 0.19, and 0.026, respectively which revealed the strong affinity of the adsorbent for $CO_2$. The Surface morphology of the adsorbent revealed that the surface was very rough and contains variety of pores or holes with wide capacities, indicating that more $CO_2$ was captured and accommodated within the surface. Thermal analysis using the Barrett-Joyner-Halenda (BJH) method revealed that the adsorbent could withstand high temperatures up to $900^0C$, at this temperature, the adsorbent is only about 18% of the amount that enters the fixed-bed column for adsorption, but 100% of it can remain in the process for temperatures ranging from 0 $^oC$ – 300 $^oC$. Finally, it was revealed that 95% of $CO_2$ was adsorbed at the maximum value for the temperature (50 $^oC$ – 350 $^oC$), time (0.5 - 5hr), and bed height (1 - 6cm).*

***Keywords:*** *Adsorption, $CO_2$, flue gas mixture, elevated temperature, chitosan/clay nanoparticles.*

## 1. INTRODUCTION

Carbon nanotubes and activated carbon have been studied to promote pollutants adsorption, but there are some limitations on their use as adsorbents (Dadet *et al*., 2024), since the choice of its usage is dependent on the exceptional adsorption efficiency and the technique applied, especially locally sourced materials that are converted to adsorbent(s). Adsorption process using activated carbon from neat chitosan is relatively expensive, and microporous, although efficient, but limited, because of the relatively large size of some molecules, weak mechanical properties, low specific gravity, swells and floats when dissolved in water, and has low stability in acidic media (Breck, 2018). Similar to activated carbon and carbon nanotubes, chitosan/clay nanoparticles contain zeolites that are easily obtained from the environment because they are locally sourced from soil (Ruthven, 2012) and the zeolites adsorbent can easily be regenerated and the solute can be separated from the gaseous solution after the adsorption process is completed (Younas *et al*., 2016). Nanoparticles are discrete particles or clusters with dimension between 10-100 nm, but metallic nanoparticles exhibit size-and-shape-dependent properties that are of interest for applications ranging from catalyst and sensing to optics, antibacterial activity, and data storage (Thambimuthu *et al*., 2019). The particle size, shape, and morphology of nanoparticles are checked and controlled; because the catalytic activity of nanoparticles is dependent on their size, structure, shape, size distribution, and chemico-physical environment (Kanniche *et al*., 2021). A nanocomposite is made up of a blend of two or more materials in which at least one of the components is nanosized (Yang *et al*., 2018), comprises of different physicochemical properties and apparent interface, advantageous to individual components, including higher toughness, higher stiffness, high specific strength, gas

barrier characteristics, flame retardancy, corrosion, and resistance (Wang *et al*., 2021). Nanocomposites have diverse applications in the biological sciences, drug delivery systems, and wastewater treatment, for instance, nanocomposite materials are incorporated into functional materials like carbon nanotubes, activated carbon, reduced graphene oxide, and different polymeric matrices for numerous applications, including the efficient handling of water pollutants and removal of other gases from gas mixtures (Bonenfant *et al*., 2018). Polymer-clay nanocomposite materials have attracted great interest owing to their improved properties such as elasticity, strength, hardness, flame retardancy, dimensional stability, electrical conductivity, solubility, heat resistance, wettability, and dyeability, depending on the type and content of the material used for the catalytic adsorption of gases such as carbon dioxide (Montalvo *et al*., 2021). Chitosan-based composites have also been reported for their improved mechanical, thermal, and adsorption properties, and have received a great deal of attention in recent years, with several studies conducted on the development of composite materials as adsorbents for non-ionic and anionic pollutants, organic pollutants, and herbicides (Triebe, 2017). For Carbon capture systems (CCS) to be implemented on a global industrial scale, it is of paramount importance that more suitable capture technologies, such as adsorption, that are both cost-effective and efficient are developed, and CCS will only gain public acceptance and implementation in industry once it has been confirmed to be economically viable. Many factors affect the economic viability of CCS, and one of these factors is the lack of inexpensive technology and high-performance materials for selective removal of $CO_2$ from flue gas. Therefore, various novel materials for post-combustion $CO_2$ capture have been developed and studied (Khelifa *et al*., 2021; IEA, 2016).

Several studies conducted in this area of research have been revisited, and it was found that the most recent and established technologies for $CO_2$ capture are chemical absorption using liquid amine-based solvents using monoethanolamine (Dadet *et al*., 2024), which can pose health risks when released into air from $CO_2$ capture plants, as well as an efficiency penalty, and the huge costs associated with the regeneration of spent amine based liquid solvents. Activated carbon produced from agricultural waste via chemical or physical activation, has gained wide attention as a brilliant adsorbent for the removal of pollutants owing to its high surface area, stability, array of functional groups and excellent pore structures (Afshin *et al*., 2019). Chemical activation enhances its specific surface area and porosity (Piriya *et al*., 2021) and (Silva, 2015) explored the use of activated char obtained from the pyrolysis of a mixture of non-recyclable plastics for the adsorption of $CO_2$ in fixed-bed columns in which 15 $^oC$ – 45 $^oC$, 10% - 40% by volume, and 1g - 2g of adsorbent loaded in the bed, were the input temperature, and amount of $CO_2$ and adsorbent, respectively. (Schumann *et al*., 2021) applied a type 4A zeolite produced from clay mineral as an adsorbent to adsorb $CO_2$ from flue gas present in power-fuelled plants, and the synthesized materials were characterized by X-ray diffraction (XRD), Fourier Transform Infrared Spectroscopy (FTIR), $N_2$ adsorption–desorption at 196 $^oC$ and $CO_2$ adsorption at $60^0C$ (up to 10 bar) isotherms, and Nuclear Magnetic Resonance (NMR). In addition, the adsorption capacity of $CO_2$ was evaluated using $CO_2$ adsorption–desorption isotherms at 25 $^oC$ up to atmospheric pressure, with the synthesized zeolite 4A successfully prepared from natural kaolinite (via meta kaolinization) at 100 $^oC$ for 48h under alkaline conditions, revealing the physicochemical properties similar to those of the commercial 4A zeolite. It has been reported that $CO_2$ was captured successfully at low temperatures with locally sourced adsorbents, such as zeolite types made from activated basolites/clay, palm shell immersed in chitosan solution, biochar synthesized from chitosan at 50:50 material ratios (Ruthven, 2012; Ho *et al*., 2017; Pham *et al*., 2018), and synthetic adsorbents such as ethanolamine base solution and amine modified and moisture- swing nanoparticles (Dadet *et al*., 2024; Hudson *et al*., 2017).

Limited or no studies have been reported on the use of locally sourced adsorbents to capture $CO_2$ from flue gas at elevated temperatures. Therefore, this study is the first attempt to formulate and characterize composites of chitosan (periwinkle shells) and clay materials (clay soil), combined at a 50:50 ratio, to serve as an adsorbent for the removal of $CO_2$ from flue gas at elevated temperatures.

## 2. MATERIALS AND METHOD

### 2.1 Materials

Periwinkle shells and clay soil were obtained from Creek town (Obio Oko), located in Odukpani local Government Area of Cross River of Nigeria (Nair, 1977), situated about 8miles Northeast from Duke town (Hallett, 1964), and is one of the city-states that comprise of old Calabar region (Aye, 2000; Daniell, 1848). Flue gas from cracked natural gas with composition of methane (0.3%), ethane (0.7%), hydrogen (5%), $CO_2$ (15%), water vapour (2%), $N_2$ (78%) (IEC & FL, 2016), and distilled water (Chemical/Petrochemical Engineering laboratory, Port Harcourt). Instruments used are analytical balance (Scout Pro, Ohaus, London, UK), pH meter (pH ep® pocket-sized pH meter, Hanna Instruments, Inc., United States of America (USA), grinding mill (Biocotek, China), shaker (Ro-tap, England), stop watch (Quartz, China), Thermometer (Pyrex Technico, England), Fourier transform infrared (FTIR) spectrometer (Thermo Scientific, Nicolet ISI 10, USA), scanning electron microscope (SEM)/ energy dispersive analysis of x-ray (EDX) spectrophotometer (Karl Zeiss, Germany), Brunauer-Emmett-Teller (BET) surfer machine (Thermo Scientific, USA), thermogravimetric analyzer (Orton Simultaneous DTG/TGA, USA), UV-Vis spectrophotometer (Angstrom Advanced Inc, model 752,

Massachusetts, USA) A multi-gas detector/analyser, and muffle furnace (TT-EF-12, Techmel, USA).

### 2.2 Method

Chitosan was extracted and composite nanoparticles was prepared from chitosan and clay materials.

#### 2.2.1 Extraction of Chitosan

Periwinkle shells were washed and dried in an electric air-drying oven for 6h at 105 ℃. The completely dried shells were ground using a mechanical grinding machine and then sieved through a 100µm mesh size. Deproteinization was conducted by heating approximately 300g of grounded periwinkle shell powder, add 1000 ml 2M NaOH placed to a water bath set to a constant temperature of 70 ˚C for 4 h. The product was neutralized by washing with tap water until the pH reaches 7. The solid was collected, washed again with distilled water, and the solid product dried in an air-dry vacuum oven. The dried product underwent demineralization through treatment with 1000 ml solution of 3.25M HCl at an ambient temperature of approximately (30±3) ℃. The mixture was stirred intermittently at 30-minute intervals for 4 h and the solid product was collected and rinsed with distilled water until it reached a pH of 7, after which it was dried. The demineralized sample was subjected to deacetylation by treating it with a 500 ml solution of 8.75M NaOH. The sample was then placed on a constant temperature magnetic stirrer and heated at 100 ℃ for 12 h. Subsequently, the sample was deacetylated, filtered, and washed with distilled water and it was subsequently dried in a vacuum oven, and the dried powder was sieved through 0.45µm mesh size and kept as nanosized particles in an air-tight container until use.

#### 2.2.2 Preparation of Clay Soil for nanoparticles/Composite

Clay soil collected from Calabar creek was filtered and the filtrate was placed in a beaker, where it was calcinated into nanoparticles after extraction of the clay sample at 800 ºC.

#### 2.2.3 Characterization of chitosan/clay adsorbent

The surface functional groups of the chitosan/clay mixture of the 50:50 ratio nanoparticle adsorbent samples were determined using an FTIR analyzer in the wavenumber range 4000-500 $cm^{-1}$. Textural properties were measured using a surface area analyzer (Thermo Scientific, USA), and SEM images of the adsorbent surface and texture were obtained using a Karl Zeiss instrument (Germany). Thermal decomposition of the adsorbent sample was determined using a standard Orton simultaneous DTG/TGA analyzer. The elemental composition of the adsorbent was obtained using EDX, as the individual fluorescent energies detected were specific to the elements were present in the sample.

#### 2.2.4 Adsorption Experiment

The $CO_2$ adsorption was conducted in a fixed bed comprising a cylindrical column made of Pyrex glass with a total length of 150cm and an internal diameter of 2.01cm. The column was packed at various heights of adsorbents between 1cm and 6cm and placed within a high-temperature chamber with dimensions of 30cm x 40cm which helped to maintain a temperature range of 50 – 250°C. Flue gas of Pressure 0.5kg/$cm^2$.G, flow rate of 75L/min and temperature of $185^0$C enters the adsorber where the chitosan/clay nanoparticles were placed inside the column for the adsorption process.

## 3. RESULTS AND DISCUSSION

**3.1. Result of Characterization of the Chitosan/Clay Composite Nanoparticles** Chitosan/clay nanoparticles prepared from locally sourced periwinkle shells and clay soil were characterized using a gas chromatography (GC) analyzer to obtain the results presented in Table 1. Characterization of the nanoparticles from chitosan/clay showed that it is a weakly acidic material with high porosity and large surface and micropore areas. This indicates that the chitosan/clay material is a good adsorbent for the adsorption of pollutants ($CO_2$) from flue gas. The large surface and micropore areas proved this reason, as these are properties that determine the adsorbent performance. A larger pore volume allows more adsorption of $CO_2$ particles onto the surface of the adsorbent and with nanosized particles, indicating that the adsorbent material is a nanoparticle and composite, which is specific and targeted for its functionality. Different methods were used for the characterization of the adsorbent, among them, DR gave the best pore width of the adsorbent of 5.283nm and best pore surface area value of 400.6$m^2$/g, pore size determination (DA) analysis gave the best result of pore diameter value of 2.64nm, hydraulic diameter (DH) method of cumulative adsorption pore volume analysis gave the best value of pore volume of 0.2015cc/g, and finally, the Langmuir surface area gave the best value of surface are as 704.2$m^2$/g.

**Table 1: Characterization of Adsorbent**

| Property | Value |
|---|---|
| Bulk density (g/$cm^3$) | 1.473 |
| Ph | 6.74 |
| Porosity (%) | 56.73 |
| Surface area ($m^2$/g) | 704.2 |
| Micropore area ($m^2$/g) | 400.6 |
| Pore volume (cc/g) | 0.2015 |

| | |
|---|---|
| Pore width (nm) | 5.283 |
| Pore diameter (nm) | 2.64 |

### 3.1.2 Result for the Physiochemical Analysis of the Adsorbent

The chitosan/clay composite particles (adsorbent) were determined based on the different analyses performed. functional group present (see Figure 1). The analysis showed the presence of an olefin alkene functional group (C-double bond), indicating a strong affinity for the addition reaction process, such that the attraction of the pollutant to the adsorbent is very strong, and hence a good adsorbent. In addition, the halogen compound (C-Cl), $2^0$ alcohol compounds (C-O), nitro compound (N-O), and $1^0$ amine compounds (N-H), with their functional groups having excess lone pairs of electrons at the surface, are capable of undergoing the reaction process, indicating that there is a strong energy within the adsorbent pores and surface areas that are created to have a very strong affinity for capturing $CO_2$ from the flue gas.

The FTIR method was the best method to determine the functional group present in the adsorbent, as shown in Table 2, depicts FTIR analysis result showing the wave number, nature of frequency, bond type and the type of

**Table 2: Functional Group Analysis of Adsorbent with FTIR**

| Wavenumber ($cm^{-1}$) | Nature of frequency | Assignment | Comment |
|---|---|---|---|
| 712.65 | Strong | C=C bending | Alkene disubstituted (cis) |
| 856.57 | Strong | C-Cl stretching | halo compound |
| 1095.60 | Strong | C-O stretching | Secondary Alcohol |
| 1500.73 | Strong | N-O stretching | nitro compound |
| 3436.29 | medium | (N-H stretching) | Primary amine |

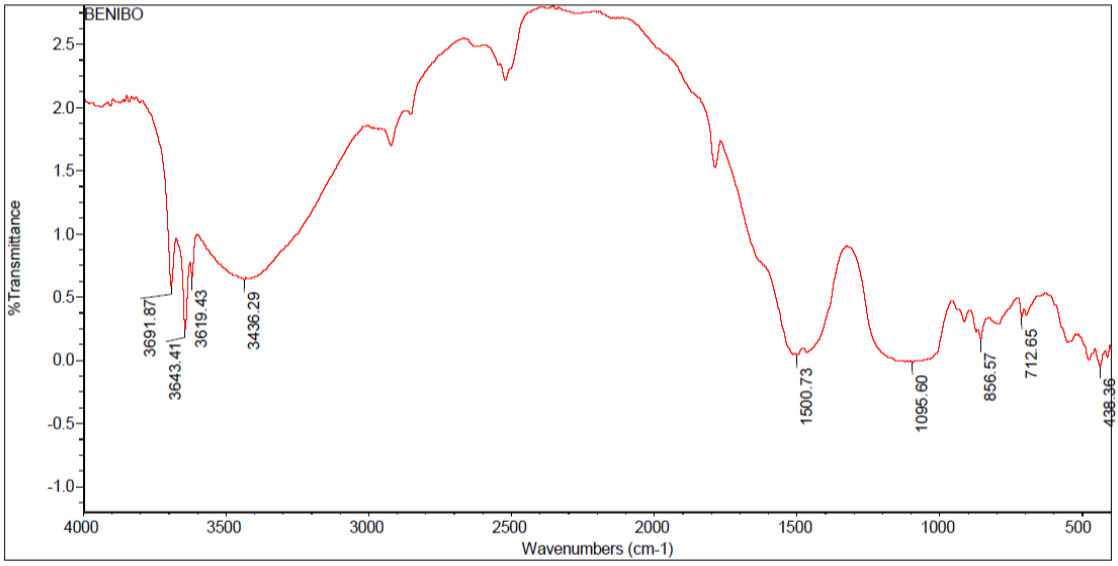


**Figure 1 Functional Group Analysis of Adsorbent with FTIR**

### 3.1.3 Elemental Composition of the Adsorbent

The chitosan/clay nanoparticles were also characterized to determine their elemental composition as shown in Table 3. The elemental analysis of the adsorbent, as shown in Table 3, indicates that Ca, Si, Al, and Sr have higher concentrations by weight, meaning that the adsorbent is electron affinity or electrovalent in nature. The presence of these elements proved that the adsorbent could withstand high-temperature applications. Other elements, such as Ti, Mg, Sb, and K, were present at very low concentrations by weight. This adsorbent is very rich, as it may have diverse applications in chemical engineering, with the lowest concentration by weight being Pb, a very good indication of the essentiality of the nanoparticle because Pb is poisonous at high concentrations (see Figure 2 for more clarification).

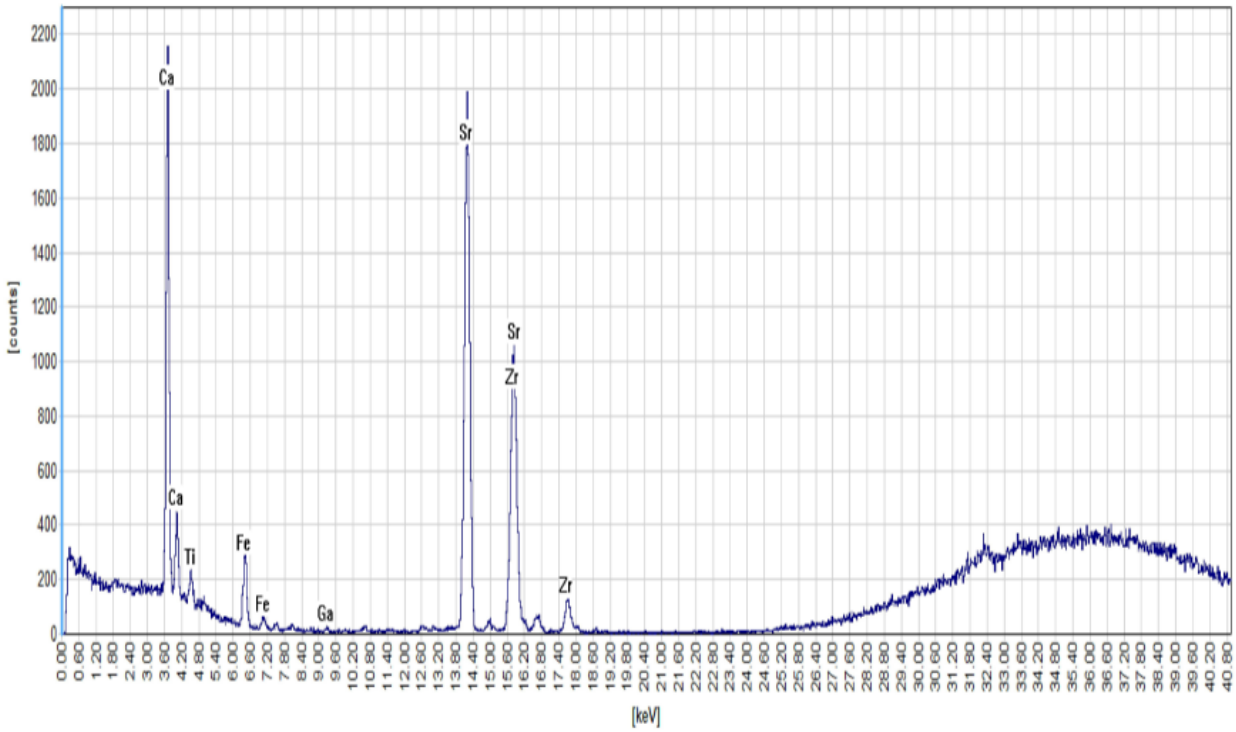


**Figure 2 Elemental Composition of the Adsorbent**

**Table 3: Elemental Analysis of the Adsorbent**

| Element | Concentration (wt%) |
|---|---|
| Calcium (Ca) | 47.0388 |
| Silicon (Si) | 20.2151 |
| Aluminum (Al) | 18.5732 |
| Strontium (Sr) | 9.17707 |
| Titanium (Ti) | 1.08093 |
| Magnesium (Mg) | 1.51206 |
| Antimony (Sb) | 0.88979 |
| Potassium (K) | 0.54609 |
| Iron (Fe) | 0.42161 |
| Niobium (Nb) | 0.18649 |
| Zirconium (Zr) | 0.08452 |
| Sulphur (S) | 0.08219 |
| Phosphorus (P) | 0.07948 |
| Chlorine (Cl) | 0.02590 |
| Manganese (Mn) | 0.02125 |
| Vanadium (V) | 0.01812 |
| Lead (Pb) | 0.01584 |

Based on the compound made up of the adsorbent using XRD analysis, it showed from the pie-chart of Fig. 3 that slake lime have the highest presence in the adsorbent with 78%, followed by limestone of 19% and oxide of Ti with 2.62%.

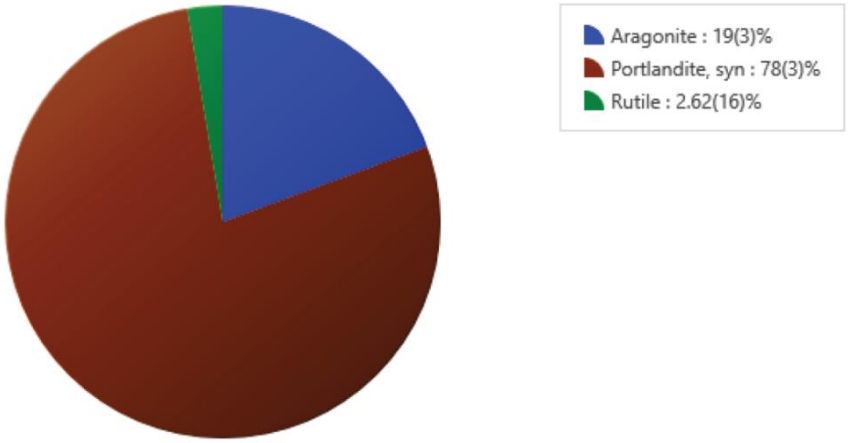


**Figure 3 The Composition of the Compounds Present in the Adsorbent using XRD Analysis**

Figure 3 depicts the compounds present in the adsorbent and its percentage spread within the make up of the adsorbent. Ca $(OH)_2$, $CaCO_3$ and $TiO_2$ were present after XRD analysis. Their compositions were 78%, 19% and 2.62% respectively. The presence of slake lime, which has a strong affinity to react with $CO_2$ showed selective adsorption of the adsorbent to attract $CO_2$ from the stream of flue gas; hence, maximum removal of the pollutant from the mixture was achieved. Ca can retain heat; hence, at elevated temperatures, the adsorbent can still perform adsorption without denaturation.

### 3.1.4 Results of XED-EDS Analysis

The XED and energy dispersion X-ray spectrometry (EDS) analysis of the adsorbent provided the elemental composition of the make-up of the nanoparticles, and the surface analysis results are presented in Table 4 and Figure 4. The elemental composition of the adsorbent, as discussed earlier in Table 4, indicates the presence of Ca, Al, and Si with the highest weight concentrations of 42.98%, 23.91%, and 22.04% respectively, whereas, Na, Ti, Mg, P, Fe, K, S, and Cl have low weight concentrations of 3.51%, 1.95%, 1.35%, 1.21%, 1.03%, 0.92%, 0.56%, and 0.52%, respectively, and the atomic concentration by percentage is also in the same order. As shown in Table 4, the presence of these elements is indicative of the ability of the adsorbent to withstand high-temperature adsorption of the pollutant from the flue gas mixture.

**Table 4: Elemental Composition of the Adsorbent showing Atomic and Weight Concentration in %**

| Element Number | Element Symbol | Element Name | Atomic Concentration | Weight Concentration |
|---|---|---|---|---|
| 20 | Ca | Calcium | 34.53 | 42.98 |
| 13 | Al | Aluminum | 28.53 | 23.91 |
| 14 | Si | Silicon | 25.27 | 22.04 |
| 11 | Na | Sodium | 4.92 | 3.51 |
| 22 | Ti | Titanium | 1.31 | 1.95 |
| 12 | Mg | Magnesium | 1.80 | 1.36 |
| 15 | P | Phosphorus | 1.26 | 1.21 |
| 26 | Fe | Iron | 0.59 | 1.03 |
| 19 | K | Potassium | 0.75 | 0.92 |
| 16 | S | Sulfur | 0.56 | 0.56 |
| 17 | Cl | Chlorine | 0.47 | 0.52 |

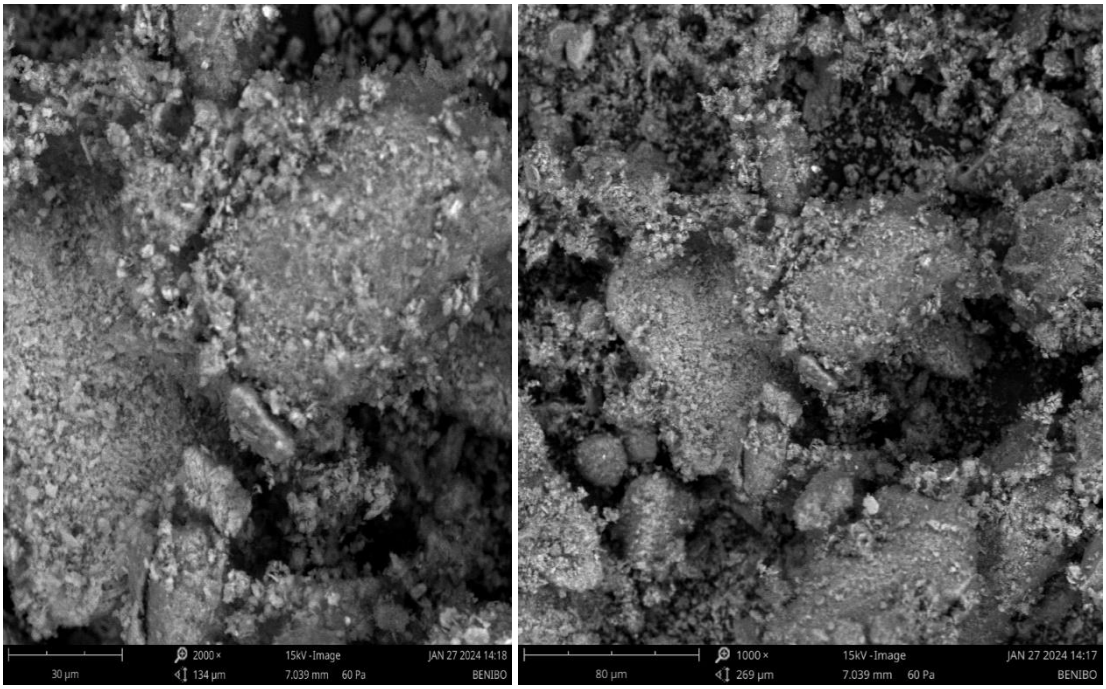


**(a)** **(b)**

**Figure 4 Surface Morphology of the Adsorbent at: (a) 2000X Magnification, and (b) 1000X magnification**

Figure 4 shows the surface morphology of the chitosan/clay nanoparticles used as adsorbent for the adsorption of $CO_2$ from flue gas, which is very rough with pores, indicating that the adsorbent is very good for the adsorption of pollutants, as many active sites are present on the surface for the attraction of the pollutant or $CO_2$ onto the surface, which can accommodate more pollutants for efficiency. The image scanned produce 15kV of dimension 7.039mm and pressure of 60Pa.

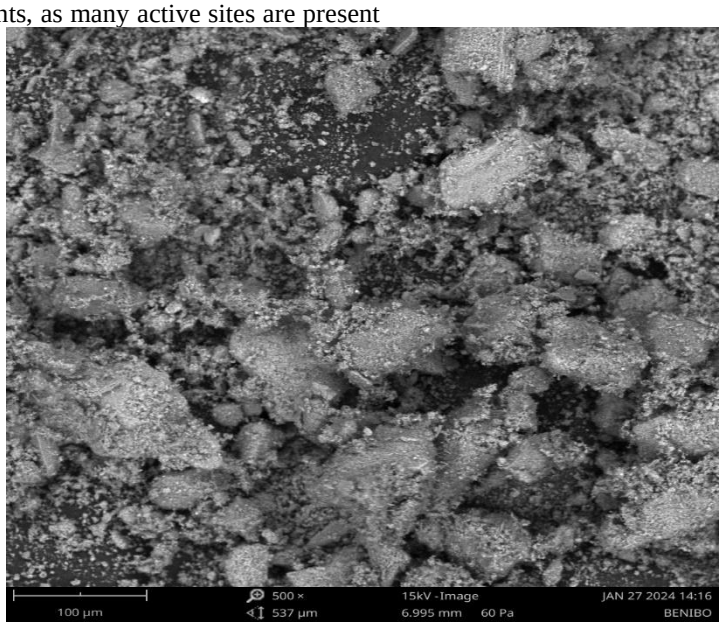


**Figure 4c Surface Morphology of the Adsorbent at 500X Magnification**

Figure 4c shows the surface morphology of the chitosan/clay nanoparticles used as adsorbents for the adsorption of $CO_2$ from flue gas, with lengths and diameter of the adsorbent sampled for analysis as 100µm and 537µm respectively. The surface morphology showed that it is very rough with pores, indicating that the adsorbent is very good for the adsorption of pollutants as many active sites are present on the surface for attraction of the pollutant or $CO_2$ into the surface. This surface can accommodate more of the pollutants into it for efficiency, with the scanned image produce 15kV of dimension 6.995mm and pressure of 60Pa.

### 3.1.5 Thermal Analysis of the Adsorbent

Thermal analysis of the adsorbent determined the temperature range in which the adsorbent could withstand adsorption without destruction. PerkinElmer thermal analysis and the BJH method were the best methods to check the adsorbent capacity as shown in Figure 6.

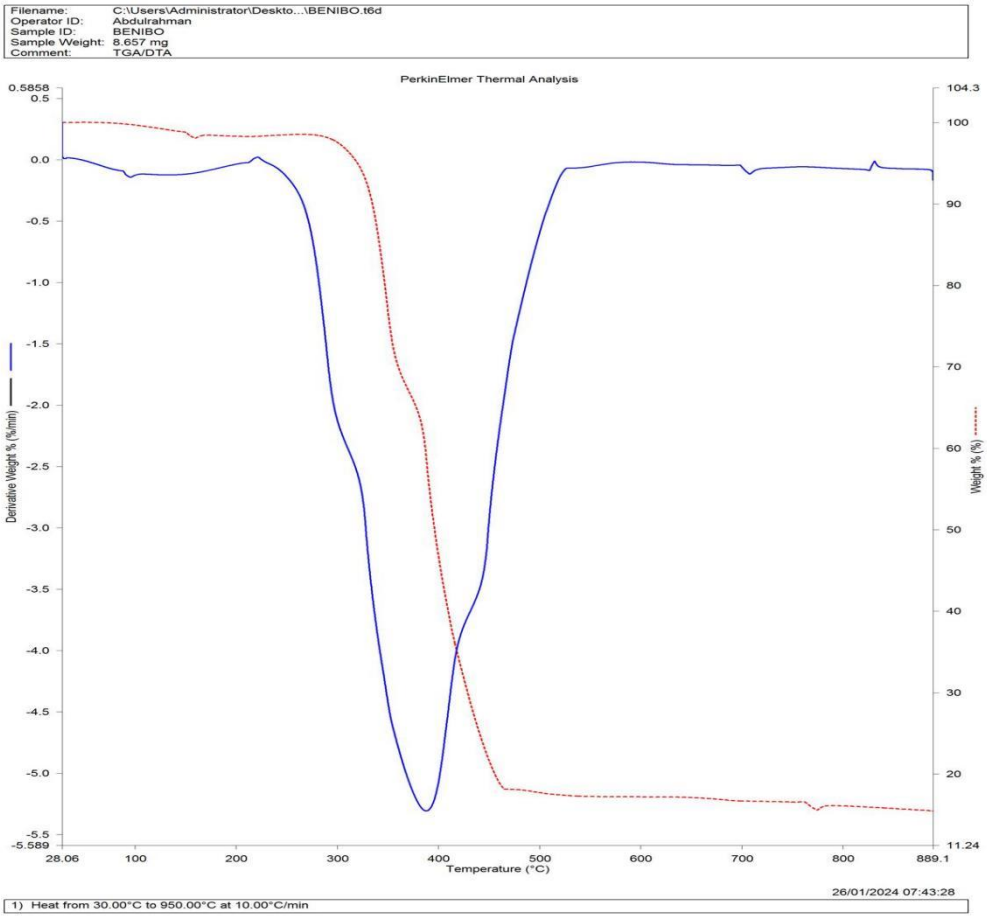


**Figure 5 Effect of Temperature on the Weight and Derivative Weight of the Chitosan/Clay Nanoparticles**

The adsorbent produced from chitosan/clay materials, as shown in Figure 5, is very effective and capacitated in the sense that it can withstand temperatures up to 800 $^{o}$C and above, but without destruction, the adsorbent can withstand 100% temperature upto 400 $^{o}$C, meaning that, at this temperature, the amount of adsorbent present remains intact without reducing, but as the temperature further increases above 400 $^{o}$C, the 100% by weight of adsorbent in the absorber column drops to approximately 20% by weight of the absorbent and until its weight drops further to approximately 18% at a temperature of approximately 850 $^{o}$C. This indicates that the adsorbent made up of chitosan/clay materials is useful for adsorption at elevated temperatures, as it proved that the choice of adsorption of $CO_2$ from the stream of flue gas at elevated temperatures is successful, as upto 95% of $CO_2$ is captured from the flue gas at such temperatures.

## 4. CONCLUSION

Chitosan/clay nanoparticles were successfully produced as adsorbents than can resist thermal degradation up to 400$^{0}$C as it was noticed in the BJH analysis of the adsorbent, where 100% of the adsorbent was maintained in the temperature range of (0 $^{o}$C to 300 $^{o}$C) and 18% of the adsorbent from 100% was able to withstand high temperatures up to 900$^{0}$C. Chitosan/clay nanoparticles are highly effective and efficient for the removal of $CO_2$ from flue gas at elevated temperatures. The 95% $CO_2$ captured at the surface of the particles is evidence, and the presence of pores, large surface areas, and rough surfaces of the adsorbent proved this claim.

**Funding Statement**
This study was not supported by any grant from the University or NGO or Federal Government.

**Ethical Compliance**
All procedures performed in studies involving human participants were in accordance with the ethical standards of the University of Calabar.

**Data Access Statement**
Research data supporting this publication are confidential and only available on request

**Conflict of Interest Declaration**: The authors declare that they have NO affiliations with or involving in any organization or entity with any financial interest in the subject matter or materials discussed in this manuscript.

**Author Contributions**
Ojong, O.E. conceived the original concept and the writing of the manuscript, Osha, O.A. contributed to the design and implementation of the research, Abam, F.I. edited and supervised the project, S.S. Shamaye conducted the experiment and the analysis of the results.

**REFERENCES**

Afshin, S., Rashtbari, Y., Shirmardi, M., Vosoughi, M. & Hamzehzadeh, A. (2019). Adsorption of basic violet 16 dye from aqueous solution onto mucilaginous seeds of Salvia sclarea: kinetics and isotherms studies. *Desalination and Water Treatment*, 161: 365–375.

Aye, E.U. (2000). The Efik people, Calabar, Glad Tidings press Ltd, ISBN 978-30541-3-9.

Bonenfant, D., Kharoune, M., Niquette, P., Mimeault, M. & Hausler, R. (2018). Advances in principal factors influencing carbon dioxide adsorption on zeolites. *Science Technology of Advance Material*, 9: 7–13.

Breck, D.W. (2018). Zeolite Molecular Sieves, 172st ed., John Wiley & Sons, New York.

Dadet, W., Ojong, O. E. & Dagde, K. K. (2024). The design and energy simulation of $CO_2$ capture process (CCP) for a liquefied natural gas (LNG) Plant. *Advances in Science and Technology*, 142: 181-192.

Daniell, W.F. (1848). On the natives of old Callebar, West Coast of Africa. *Journal of the Ethnological Society of London* (1848-1856), 1: 210-227.

Hallett, R. ed. (1964). Records of the African Association (1788-1831), New York: T. Nelson, London.

Ho, T.H., Howes, T. & Bhandari, B.R. (2017). Encapsulation of gases in powder solid matrices and their applications. *Powder Technology*, 59, 87–108.

Hudson, M.R., Queen, W.L., Mason, J.A., Fickel, D.W., Lobo, R.F. & Brown, C.M. (2017). Unconventional, highly selective $CO_2$ adsorption in zeolite SSZ-13. *Journal of American Chemical Society*, 134:1970–1973.

International Energy Agency (IEA) (2016). World Energy Outlook, Paris Cedex, France, 1- 667.

Kanniche, M. (2021). Pre-combustion, Post-combustion and Oxy-combustion in thermal power plant for CO capture. *Applied Thermal Engineering*, *Elsevier*, 30(1), 53.

Khelifa, A., Benchehida, L. & Derriche, Z. (2021). Adsorption of carbon dioxide by X zeolites exchanged with $Ni^{2+}$ and $Cr^{3+}$: isotherms and isosteric heat. *Journal of Colloid and Interface Science*, 278(1), 9-17.

Montalvo, S., Guerrero, L. & Borja, R. (2021). Application of natural zeolites in anaerobic digestion process. *Applied Clay Science*, 58 (1), 125-133.

Nair, K.K. (1977). King and Missionary in Efik politics (1846-1858). *Journal of African Studies*, 4 (3), 243-280.

Pham, T.D., Xiong, R., Sandler, S.I. & Lobo, R.F. (2018). Experimental and computational studies on the adsorption of $CO_2$ and $N_2$ on pure silica zeolites. *Microporous Material*, 185, 157–166.

Piriya, R.S., Jayabalakrishnan, R.M., Maheswari, M., Boomiraj, K. & Oumabady, S. (2021). Coconut shell derived $ZnCl_2$ activated carbon for malachite green dye removal. *Water Science & Technology in press*, 1-16

Ruthven, D.M. (2012). Principles of Adsorption and Adsorption Processes, 1st ed., John Wiley & Sons, New York.

Schumann, K., Unger, B., Brandt, A. & Scheffler, F. (2021). Investigation on the pore structure of binderless zeolite 13X shapes. *Microporous Mesoporous Mater*, 154, 119-123.

Silva, J.A.C. (2015). Adsorption Equilibrium and Dynamics of Fixed Bed Adsorption of $CH_4/N_2$ in Binder-free Beads of 5A Zeolite. *Industrial Engineering of Chemical Resource*, 54: 6390−6399.

Thambimuthu, K., Soltanieh, M. & Abanades, J.C. (2019). Carbon dioxide Capture and Storage. Cambridge University Press, Cambridge, 109.

Triebe, R. (2017). Separation and Purification of Gases with Molecular Sieves. *A Master Dissertation*, University of Ottawa.

Wang, Q., Luo, J., Zhong, Z. & Borgna, A. (2021). $CO_2$ capture by solid adsorbents and their applications: current status and new trends. *Energy and Environmental Science*, 4(1), 42–55.

Yang, H., Xu, Z., Fan, M., Gupta, R., Slimane, R.B., Bland, A.E. & Wright, I. (2018). Progress in carbon dioxide separation and capture. *Journal of Environmental Science*, 20(1), 14-27.

Younas, M., Sohail, M., Leong, L.K., Bashir, M.J.K. & Sumanthi, S. (2016). Feasibility of $CO_2$ adsorption by solid adsorbents: a review on low-temperature systems. *International Journal of Environment of Science and Technology*, 13:1839-1860

10.51975/25400109.som
Journal of the Nigerian Society of Chemical Engineers, 40(1), 2025

# INVESTIGATING THE IMPACT OF FEED RATE ON THE SPRAY DRYING PROCESS OF ACHA (*DIGITARIA EXILIS*) SOURDOUGH

***Zambiri, S[1], Afolabi, E.A.[2], Kovo, A. S.[2], and Abdulkadir, M.[2]**

[1]*Department of Chemical Engineering Technology, Federal Polytechnic Nasarawa, Nigeria*
[2]*Department of Chemical Engineering, Federal University of Technology, Minna, Nigeria*
[*]Email of the corresponding author: zambiri1965@gmail.com

**ABSTRACT**

*Acha (Digitaria exilis) is a cereal crop, rich in carbohydrates, dietary fibre, minerals, and amino acids. Acha sourdough in powder form has several advantages including longer shelf life, constant product quality, and low cost of maintenance and transportation. This study aims to investigate the impact of feed rate on the spray drying process of acha (Digitaria exilis) sourdough into powder form. A fresh acha sourdough was prepared and spray-dried into powder at different feed pump rates (3, 3.5. 4, 4.5, and 5 Hz). Performance indicators of the process were analyzed. The spray dryer exit air temperature ranged from 70 ℃ to 55℃, while the relative humidity varied from 7% to 21%. The thermal efficiency and evaporation rate ranged from about 67% to 79% and 4.5 g/min to 13.0 g/min respectively. Powder yield and moisture, respectively varied from 45% to 50% and 8 % to 5%. The maximum powder yield of 50% was achieved at a feed pump rate of 4Hz. The viability of Lactic acid bacteria and yeast ranged from about 4.9 log (CFU/g) to 6 log (CFU/g) and 4.6 log (CFU/g) to 5.8 log (CFU/g) respectively. The total titrable acid ranges from 1.5 ml to 1.6 ml, while the pH varied from 4.3 to 4.2. The bulk density varied from about 4.6 g/ml to 6.0 g/ml. The results showed that the spray-drying approach produced stable sourdough powder with standard functional properties for production of gluten-free baked foods.*

Keywords: *Acha; feed rate; ; impact; sourdough; and spray-drying***1.**

## INTRODUCTION

Sourdough is a mixture of flour and water, fermented by a microbial consortium of lactic acid bacteria (LAB) and yeast (Calvert *et al*., 2021; De Vuyst *et al*., 2017; De Vuyst *et al*., 2021; De Vuyst *et al*., 2023). Research on the application of biotechnology to develop sourdough-based food has increased due to its health benefits (Olojede *et al*., 2023). Besides, due to whole grain fermentation with LAB and yeasts, sourdough is rich in bioactive compounds such as phenolic acids and bioactive peptides (Luti *et al*., 2020). The total titratable acids (TTA), and pH of the sourdough are an indicator of the quality of the sourdough fermentation. The TTA is the total acidity of the sourdough, including both organic and inorganic acids, while the pH reflects the concentration of hydrogen ions. The pH and TTA can also indirectly indicate the level of microbial activity in the sourdough. A lower pH and higher TTA indicate higher acidity. Most sourdoughs are wheat-based. Recently attention has shifted towards gluten-free cereals such as acha (*Digitaria exilis*) whole grain, due to its enhanced nutritional and health benefits compared with wheat flour (Babatuyi *et al*., 2023).

The application of sourdough in baked foods is challenging due to the difficulties and costs of maintaining a live microbial culture. To mitigate this issue, sourdough is dried to stabilize the microbes (Albagli, *et al*., 2019; Caglar *et al*, 202, Montemurro *et al*., 2019; Reale *et al*., 2021). Different drying approaches such as freeze-drying, spray drying, drum drying, oven drying, and fluidized bed drying have been used to dehydrate sourdough (Brandt, 2019). Reale *et al.* (2019) suggested that a stabled sourdough requires moisture content to be less than 7%, because high moisture content can trigger unwanted biochemical and microbiological processes in the dried powder. Tan *et al*. (2018) stated that dried sourdough is easy to store, transport, and market, but drying at high temperatures may reduce the survival of yeast and LAB cells due to heat stress during dehydration. Huang *et al*. (2017) relate the cell viability during drying, to the applied method, process parameters, and the use or absence of protectant compounds. In literature, freeze-drying offers greater cell viability but is expensive and time-consuming. In contrast, spray drying is a cheaper method, a continuous process, and is good for a large-scale production (Caglar *et al*., 2021). Besides,

spray-drying has a reasonable rate of cell survival but requires a comprehensive study of drying conditions, equipment configurations, vis-a-vis feed material, powder yield, and powder quality (Peighambardoust *et al*., 2011). The spray drying process comprises three phases: atomization, droplet-to-particle conversion, and particle collection (Moreira *et al*., 2021). In the atomization stage, the atomizer converts the feed into fine droplets. These droplets dried, on contact with the hot air in the drying chamber. The dried particles separate from the drying medium through a cyclone, and are collected in a container (Santos *et al*., 2018). A high cell survival rate in spray drying is accomplished based on the optimization of drying parameters and the use of cell-protective agents (Mantzourani *et al*., 2019; Mohd Roby *et al*., 2020; Peighambardoust *et al*., 2011; Stefanello *et al*., 2019). Studies on the spray drying of sourdough have been reported in the literature (Caglar *et al*., 2021; Ilha *et al*., 2015; Reale et al., 2019; Rozylo *et al*., 2015; Tafton et al., 2013a; Tafti *et al*., 2013b). To the best of author's knowledge, no work related to spray drying of acha sourdough is found in the open literature. This study aims to investigate the impact of feed rate on the spray drying process of acha (*Digitaria exilis*) sourdough.

## 2. MATERIAL AND METHODS

### 2.1 Production of Sourdough and its Spray Drying

Dehulled acha (Digitaria exilis) was sourced from Kenyi, Kagarko local Government Area of Kaduna state. The acha was thoroughly washed with potable water, to remove adhering dust on the grains and reduce microbial load. Sedimentation technique was used to separate sand particles from the acha grains, and then the grains were oven-dried. The dried grains were milled into flour using a sterile laboratory-sized ball mill. The milled product was sieved through a 63-mμ sieve.

Acha sourdough was prepared following the approach of Edema *et al*. (2013) but with modification. The acha flour was mixed with tap water in a ratio, of 1:1.5 in a sterile 3L transparent container, and stirred thoroughly until no dry spot was noticed. The container was covered with a clean cloth, and the mixture was allowed to spontaneously ferment at room temperature. The process was propagated by back-slopping (feeding) every 24 h, adding 50 % of the previous sourdough to a fresh mixture of acha flour and water for 6 days. Lactic acid bacteria count, yeast count, pH, and total titratable acid (TTA) of the sourdough were determined.

The fresh sourdough was diluted to 10% solid, and drying was made using a pilot plant concurrent flow spray dryer (Armfield FT 80). The sourdough was pumped into the drying chamber using a progressive cavity pump and atomization was performed using a two-fluid nozzle (nozzle inside diameter 1 mm). To study the effect of feed pump rate, experiments were performed at different feed pump rates (3, 3.5, 4, 4.5, and 5Hz). In all experiments, inlet air temperature, inlet air fan rate, exit air fan rate, atomizing air pressure, and sample size were kept constant at 170℃, 35 Hz, 40Hz, 3bar and 500 ml respectively. The sourdough powder samples obtained were collected in an air-tight-capped plastic containers and kept in the dark at room temperature, for further analysis.

### 2.2 Evaluation of the spray drying process

#### 2.2.1 Exit air temperature

Process parameters including outlet temperature influence considerably the physicochemical properties of the produced powders (Jain *et al*., 2012). At each inlet air temperature, the exit air temperature was taken from the display on the control panel**.**

#### 2.2.2 Exit air humidity

The outlet air relative humidity at each inlet air temperature was gotten from the reading display on the control panel.

#### 2.2.3 Powder yield

Powder yield (PY) was determined according to Equation (1) (Tontul *et al.*, 2017):

$$PY = \frac{weight\ of\ powder\ obtained}{Weight\ of\ total\ solid\ in\ feed} \times 100 \qquad (1)$$

#### 2.2.4 Efficiency of spray dryer

The efficiency of the spray dryer was described in terms of the overall thermal efficiency of the spray dryer (TE), approximated by Equation (2) (Cheng *et al.*, 2023):

$$TE = \frac{T_{inlet} - T_{outlet}}{T_{inlet} - T_{atm}} \qquad (2)$$

Where: TE = Thermal efficiency (%)

$T_{inlet}$ = Inlet air temperature (℃),

$T_{outlet}$ = Outlet air temperature (℃),

$T_{atm}$ = the atmospheric temperature (℃).

#### 2.2.5 Evaporation rate

The evaporation rate (ER) was determined according to Equation (3) (Bahnasawy *et al*., 2010):

$$ER = \frac{FR \times (\%TS_{Powder} - \%TS_{feed})}{\%TS_{feed}} \qquad (3)$$

Where: ER = Evaporation rate (g/min),

FR = Feed rate (g/min),

$TS_{powder}$ = Total solids in powder,

$TS_{feed}$ = Total solids in the feed.

#### 2.2.6 Moisture content (MC)

The moisture content of the powder was determined following the official methods of analysis of the Association of Analytical Chemists (AOAC, 2000). About 5g of the sample in an aluminum plate was placed in a drying oven, dried at 103℃ until constant weight. Percentage moisture content was calculated using Equation (4):

$$MC = \frac{W_2 - W_3}{W_2 - W_1} \times 100 \qquad (4)$$

Where: $MC = Moisture\ content\ (\%)$,

$W_1 = Weight\ of\ empty\ dish$ ,

$W_2$ = Weight of dish with sample before drying,

$W_3$ = Weight of dish with sample after drying.

**2.2.7 Total titratable acid (TTA) and pH**

About 1 g of the sourdough was mixed with 9 ml of distilled water. The pH of the mixture was carried out using a pH that had been standardized using buffer solutions. Readings (in triplicates) were taken on the pH meter scale.

Measurement of titratable acid (TTA) produced in the sourdoughs was done according to AOAC (2000). Sourdough and distilled water were mixed in a ratio of 1:9 and 3 drops of phenolphthalein indicator were added. The mixture was titrated against 0.1 M NaOH solution, and the TTA was expressed TTA as the amount (ml) of 0.1 M NaOH necessary to achieve pH of 8.3.

**2.2.8 Microbial enumeration**

About 1 g of the sourdough was suspended in a 9 ml saline solution (0.85% (w/v) sodium chloride). The mixture was serially diluted. From appropriate tenfold dilutions, the microbial enumeration was made by pour plate technique using plates with 30–300 colonies. The LAB was enumerated on MRS agar (Merck, Darmstadt, Germany) and incubated anaerobically for 48 h at 35 °C while the yeast enumeration was determined on potato dextrose agar (PDA) (HiMedia, Mumbai, India) and incubated for 72 h at 27 °C.

**2.2.9 Bulk density**

An empty graduated cylinder of volume (25 ml) was weighed, ($W_1$). The cylinder was filled with the powder sample up to the 25ml mark gently, tapped several times on a laboratory bench, and more powder sample was added until there is no space for more. The filled cylinder was weighed, ( $W_2$) . Finally, the bulk density was calculated as:

$$Bulk\ density = \frac{(W_2 - W_1)g}{25ml} \qquad (5)$$

## 3 RESULTS AND DISCUSSIONS

### 3.1 Effect of feed Pump Rate on Exit Air Temperature (EAT) and Relative Humidity (RH)

The influence of the feed pump rate (FPR) on exit air temperature (EAT) and relative humidity (RH) is shown in Figure 1. The EAT and the RH varied from about 71℃ to 55℃ and 7% to 21% respectively. The EAT

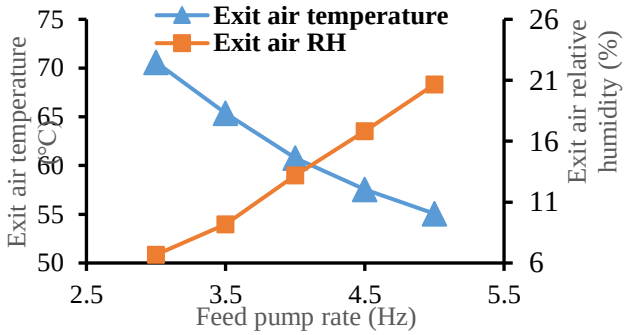


**Figure 1. Effect of Feed Pump Rate on exit air temperature and relative humidity**

reduces, with an increase in the FPR, while the RH increases, with an increase in the FPR. These trends occurred because an increase in FPR increases the cooling effect of evaporation. An increase in FPR also leads to more liquid flow and bigger droplets into the air stream (Pinon-Balderrama *et al.*, 2020). These droplets absorb more heat from the air, widening the difference between the temperatures of the inlet air and the exit air. Furthermore, the air gains more water vapour, leading to an increase in its relative humidity. Tan *et al.* (2011) earlier reported a similar trend of results.

### 3.2 Effect of Feed Pump Rate on Thermal Efficiency (TE) and Evaporation Rate (ER)

The variation of thermal energy (TE) and evaporation rate (ER) due to feed pump rate (FPR) is shown in Figure 2. The TE and DR increase, with an increase in the FPR. The TE and ER ranged from 67 to 79 % and 4.5 to 13.0 g/min respectively.

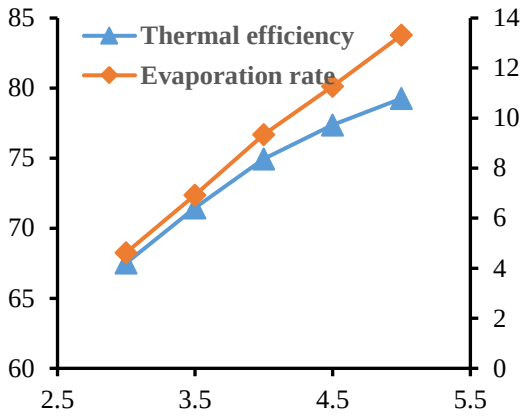


Figure 2. Effect of Feed Pump Rate on Thermal Efficiency and Evaporating Rate

The TE of the spray dryer increases with an increase in the FPR because an increase in FPR, increases liquid available to the hot air for evaporation. With more liquid available to the hot air, heat utilization is increased, and reflected as an increase in TE. An increase heat utilization also mean an increase moisture removal from the material, which appears as an increase in ER. Golman and Julklang (2014) evaluated the performance of a spray dryer and reported that the thermal energy efficiency of the spray dryer increased, with an increase in the feed flow rate.

### 3.3Effect of Feed Pump Rate on Powder Yield (PY) and Moisture Content (MC)

The quantity of powder obtained in the spray drying process via cyclone separation is influenced by the drying air flow and local velocities, the spatial geometry of the cyclone separator, and the interaction of the particles with the cyclone walls (Behboudi-Jobbehdar *et al*., 2013). In this study, the airflow was kept constant. Therefore, parameters that affect the surface stickiness of the microparticles such as the hygroscopicity, glass transition temperature, moisture, and temperature of the droplets in the drying chamber detect the powder recovery. The influence of FPR on PY and MC is shown in Figure 3.

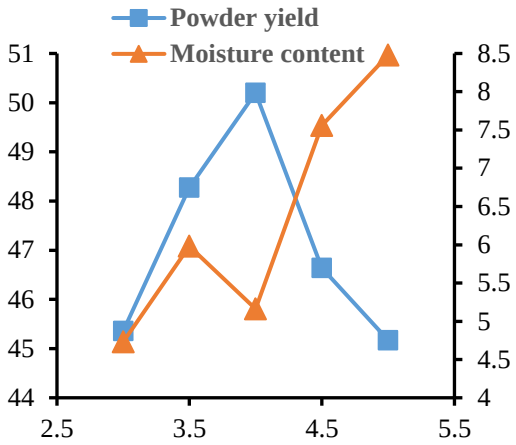


**Figure 3. Effect of Feed Pump Rate on Powder Yield and Moisture Content**

The PY increased, with an increase in FPR but later decreased with an increase in the FPR. The maximum PY attained was about 50 % at an FPR of 4Hz. The moisture content (MC) continues to increase, with an increase in the FPR. The MC varied from 4.7 to 8.5%. Authors including Chegini and Ghobadian (2005), Jain *et al.* (2017), and Hong *et al.* (2021), reported similar pattern of results. The possible explanation to these scenarios is that an increase in FPR shortens the contact time of the feed droplets with the hot air, hence lessening evaporation. A reduction in evaporation increases the MC and density of the powder. An increase in density can increase the powder yield due to an increment in weight per unit volume. However, beyond FPR of 4Hz, the MC of the powder might have increased to the level of causing powder particles to stick to dryer walls, reducing the PY.

### 3.4 Effect of Feed Pump Rate on Lactic Acid Bacteria (LAB) and Yeast Viability

When a Sourdough is spray-dried, the viability of LAB and yeast cells is reduced (Caglar *et al*., 2021). During spray drying, the LAB and yeast cells suffer mechanical, thermal, osmotic, and oxidative stresses which reduced their viability (Khemetal *et al*., 2015; Liu et al., 2018; Schutyser *et al*., 2019).

Figure 4 shows the effect of FPR on the viability of LAB and yeast. The viability of LAB and yeast varied from about 4.1 to 5.00 and 3.9 to 4.5 log (CFU/g) respectively.

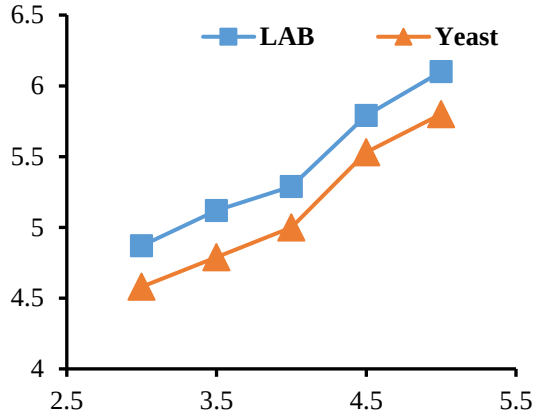


**Figure 4. Effect of Feed Pump Rate on Viability of Lactic Acid Bacteria and Yeast**

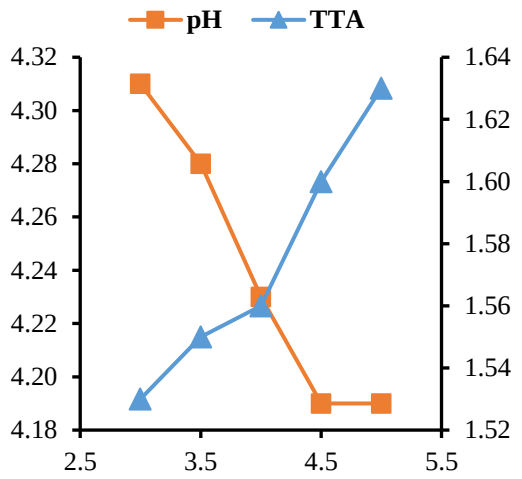


**Figure 5. Effect of Feed Pump Rate on pH and TTA**

The viability of LAB and yeast increases with an increase in FPR. This is because an increase in the FPR increases the feed flow rate. An increase in the feed flow rate reduces the residence time of the particles in the dryer chamber, likewise the EAT. A reduction in particle residence time, and EAT lowers thermal stress on the microbes, favouring their survival. This agrees with the findings of Atalar and Dervisoglu (2015) who investigated the effect of spray drying parameters on kefir powder. These authors reported that a high feed pump rate and low exit air temperature favoured the survival rate of lactococci. The microbial count of the spray-dried sourdoughs obtained in this study, satisfied the minimum requirement set by FAO/WHO of 6.27 log CFU/g of live organisms in sourdoughs (Olojede *et al*.2023).

### 3.5 Effect of Feed Pump Rate on Total Titratable Acid (TTA) and pH

Spray drying of sourdough can lead to a slight increase in pH due to the loss of acidic compounds. The variation of the TTA and the pH of the spray-dried sourdough due to an increment in FPR is shown in Figure 5.

From Figure 5, an increase in FPR reduces the pH, but an increase for TTA. Even though the changes in pH and TTA were small, it did show that an increase in FPR might have reduced the severity of the drying air temperature, which reduced the disintegration of the acidic compounds present in the sourdough. The pH and the TTA ranged from about 4.3 to 4. 19 and 1.5 to 1.6 ml respectively. Caglar *et al*. (2021) reported similar results in pH from their investigation of a sourdough spray drying. Reidzane *et al*. (2021) stated that the pH of a well-developed sourdough is from 3.5 to 4.3. The pH range obtained in this study is within this range.

### 3.6 Effect of Feed Pump Rate on Bulk Density

The effect of flow rate on bulk density is shown in Figure 6. It can be seen in Figure 6 that the bulk density increases, with an increase in the feed pump rate (FPR). Chegini and Ghobadian (2005), and Padma *et al.* (2022) reported similar observation. The increase in the feed pump rate caused inadequate drying of the sourdough powder, which increased the moisture content of the powder and hence the bulk density (Jain *et al.*, 2017).

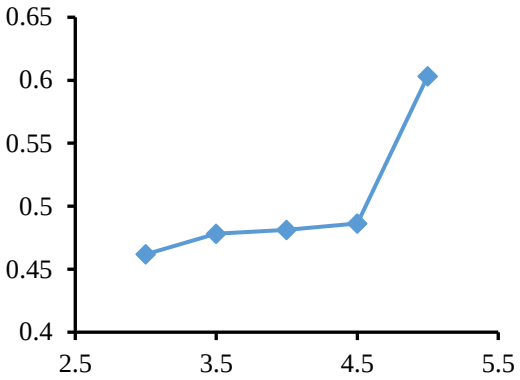


Figure 6. Effect of Feed Pump Rate on Bulk Density

In Figure 6, the bulk density of spray-dried sourdough varied from about .0.46 to 0.60 g/ml. A bulk density of 450 to 700 kg/ $m^3$ for spray-dried sourdough, was reported by Caglar *et al*.(2021).

## 4. CONCLUSIONS

Dehydration of sourdough into powder form has several advantages including longer shelf life, constant product quality, and lower transportation cost. The effect of feed pump rate on the spray drying of acha sourdough was investigated. Results of evaluation of the response parameters showed that the feed pump rate was a critical process parameter in the spray drying of the acha sourdough. The highest powder yield was 50% at a feed pump rate of 4 Hz. Beyond this feed pump rate, the powder yield reduces. The exit air temperature and pH responded negatively, with an increase in feed pump rate. The thermal efficiency, evaporation rate, moisture content, microbial counts, and bulk density, varied positively with an increase in feed pump rate.

From the analyses results of moisture content, pH, total titratable acid, and microbial counts, the spray drying process produced dehydrated acha sourdoughs with standard functional properties. These show that spray drying feed rate can be manipulated to produce acha sourdough for the production of gluten-free baked foods. Nevertheless, a holistic investigation is needed to optimize the entire process parameters, for a tradeoff for low moisture content and high powder yield.

## 5. ACKNOWLEDGMENT

The authors wish to acknowledge, the assistance of Prof B. El-Yakub and the laboratory staff of the Department of Chemical Engineering, Ahmadu Bello University, Zaria.

## NOTATION

CFU = Colony forming unit
FPR = Feed pump rate (%)
EAT = Exit air temperature (℃)
RH = Evaporation rate (%)
TE = Thermal efficiency (%)
ER = Evaporation rate (g/min)
PY = Powder yield (%)
MC = Moisture content (%)

## 6. REFERENCES

Albagli, G., Schwartz, I. M., Amaral, P. F. F., Ferreira, T. F. and Finotelli, P. V. (2021). How dried Sourdough Starters can Enable and Spread the Use of Sourdough Bread. *LWT- Food Science and Technology*, 149,111888.

Association of Official Analytical Chemists (AOAC) (2000). Official Methods of Analysis of the Association of Official Analytical Chemists, seventeenth edn. Gaithersburg, MD: Association of Official Analytical Chemists

Atalar, I. and Dervisoglu, M. (2014). Optimization of Spray Drying Process Parameters for Kefir Powder Using Response Surface Methodology. LWT- Food Science and Technology, 60(2): 751-757

Babatuyi, C. Y., Adisa, A. M., Temitope, C. I. and Enujiugha, V. N. (2023). The Variations in Chemical Composition, Antioxidant Capacity, and Pasting Properties of Fonio Sourdoughs. DYSONA– Applied Science, 4: 51-6.

Behboudi-Jobbehdar, S., Soukoulis, C., Yonekura, I. and Fisk, I. (2013). Optimization of Spray-Drying Process Conditions for the Production of Maximally Viable Microencapsulated L. acidophilus. *Drying Technology*, 31(11): 1274-1283,

Caglar, N., Ermis, E. and Durak, M.Z. (2021). Spray-dried and Freeze-dried Sourdough Powders: Properties and Evaluation of their Use in Breadmaking. *Journal of Food Engineering*, 292: 110355.

Calvert, M.D.; Madden, A.A.; Nichols, L.M.; Haddad, N.M.; Lahne, J.; Dunn, R.R. and McKenney, E.A. (2021). A Review of Sourdough Starters: Ecology, Practices, and Sensory Quality with Applications for Baking and Recommendations for Future Research. *PeerJ*, 9: e11389.

Chegini, G.R. and Ghobadian, B. (2005). Effect of Spray-drying Conditions on Physical Properties of Orange Juice Powder. *Drying Technology*, 23 (3): 657–668.

De Vuyst, L., S. Van Kerrebroeck, S. and Leroy, F. (2017). Microbial Ecology and Process Technology of Sourdough Fermentation.

*Advances in Applied Microbiology*, 100: 49–160.

De vuyst. L., Comasio, A. and Van Kerrebroeck, S. (2021). Sourdough Production: Fermentation Strategies, Microbial Ecology, and Use of Non-flour Ingredients. *Critical Reviews in Food Science and Nutrition*, 63(15): 2447-2479.

De Vuyst, L., Comasio, A. and Van Kerrebroeck, S. (2023). Sourdough Production: Fermentation Strategies, Microbial Ecology, and Use of Non-flour Ingredients. *Critial Reviews in Food Science and Nutrition*, 63(15): 2447–2479.

Edema, M. O., Emmambux, M. N. and Taylor, J. R. N. (2013). Improvement of Fonio Dough Properties Through Starch Modification by Sourdough Fermentation. *Starch/Starke*, 00: 1-8.

Golman, B. and Julklang, W. (2014). Simulation of Exhaust Gas Heat Recovery from a Spray Dryer. *Applied Thermal Engineering*, 73(1): 899–913.

Hong, P.V.C., Tan, H.D., Thanh, P.T.T., Cang, M.H., Don, D.L and Thien, L.T. (2021). Spray Drying Conditions for Protein Hydrolysate of Crocodile Meat. *Food Research*, 5 (1): 140– 148.

Huang, S., Vignolles, M. L., Chen, X. D., Le Loir, Y., Jan, G., Schuck, P. and Jeantet, R. (2017). Spray Drying of Probiotics and Other Food Grade Bacteria: a Review. *Trends in Food Science & Technology*, 63: 1-17.

Ilha, E. C., Da Silva, T., Lorenz, J. G., De Oliveira Rocha, G. and Sant'Anna, E. S. (2015). *Lactobacillus paracasei* Isolated from Grape Sourdough: Acid, Bile, Salt, and Heat Tolerance after Spray Drying with Skim Milk and Cheese Whey. *European Food Research and Technology*, 240(5): 977–984.

Jain, M. S., Lohare, G. B., Bari, M M., Chavan, R. B., Barhate, S.D. and Shah, C. B. (2012). Spray Drying in Pharmaceutical Industry: a Review. Research Journal of Pharmaceutical Dosage Forms and Technology, 4(2): 74-79.

Jain, P., Gupta, A.K., Pathak, M. K. and Khanna, N. (2017). Effect of Process Conditions on the Physicochemical Properties of Fermented Beet Root Juice Powder Produced by Spray Drying. *International Journal of Current Microbiology and Applied Sciences*, 6(12): 4209-4216.

Khem, S., Woo, M.W., Small, D.M., Chen, X.D. and May, B.K. (2015). Agent Selection and Protective Effects During Single Droplet Drying Of Bacteria. *Food Chemistry*, 166: 206–214.

Liu, B., Fu, N., Woo, M. W. and Chen, X. D. (2018). Heat Stability of *Lactobacillus Rhamnosus* GG and its Cellular Membrane during Droplet Drying and Heat Treatment. *Food Research International*, 112: 56–65.

Luti, S., Mazzoli, L., Ramazzotti, M., Galli, V., Venturi, M., Marino, G., Lihman, M., Guerrini, S., Granchi, L., Paolo, P. and Pazzagli, L. (2020). Antioxidant and Anti-Inflammatory Properties of Sourdoughs Containing Selected *Lactobacilli* Strains are retained in Breads. *Food Chemistry*, 322: 126710.

Mohd Roby, B. H., Muhialdin, B. J., Abadl, M. M. T., Mat Nor, N. A., Marzlan, A. A., lim, S. A. H., Mustapha, N. A. and Meor Hussin, A. S. (2020). Physical Properties, Storage Stability, and Consumer Acceptability for Sourdough Bread Produced Using Encapsulated Kombucha Sourdough Starter Culture. *Journal of Food Science*, 85(8): 2286-2295.

Mantzourani, I., Terpou, A., Alexopoulos, A., Bezirtzoglou, E. and Plessas, S. (2019). Assessment of Ready-To-Use Freeze-Dried Immobilized Biocatalysts as Innovative Starter Cultures In Sourdough Bread Making. *Foods*, 8(1): 40.

Moreira, M. T. C., Martins, E., Perrone, I. T., De Freitas, R., Queiroz, L.S. and De Carvalho, A. F. (2021). Challenges associated with Spray Drying of Lactic Acid Bacteria: Understanding Cell Viability Loss. *Comprehensive Reviews in Food Science and Food Safety*, 20: 3267–3283.

Olojede, A. O., Oahimire, I. O., Gbande, J.I., Osondu-Igbokwe, A. D., Thomas, R. M., Olojede., D.S. and Banwo, K., (2023). Evaluation of Acha Flour in the Production of Gluten-Free Sourdough Cookies. *International Journal of Food Science and Technology*, 58: 3244–32501.

Padma, M., Jagannadha Rao, P. V. K., Edukondalu, L., Aparna, K. and Ravi Bab, G. (2022). The Effects of Spray Drying Conditions on Moisture Content, Water Activity, Bulk Density, and Tapped Density of Rice Milk Powder. *International Journal of Environment and Climate Change*, 12(11): 3575-3590.

Peighambardoust, S. H., Golshan, T. A., and Hesari, J. (2011). Application of Spray Drying for

Preservation of Lactic Acid Starter Cultures: a Review. *Trends in Food Science & Technology*, 22(5): 215-224.

Pinon-Balderrama, C., Leyva-Porras, C., Espinosa-Solís, V., Terán-Figueroa, Y., Álvarez-Salas, C. and Saavedra-Leos, M. Z. (2020). Encapsulation of Active Ingredients in Food Industry by Spray-Drying and Nano Spray-drying Technologies. *Processes*, 8(8): 889

Reale, A., Di Renzo, T., Preziuso, M., Panfili, G., Cipriano, L. and Messia, M.C. (2019). Stabilization of Sourdough Starter by Spray Drying Technique: New Breadmaking Perspective. *Lebensmittel-LWT- Food Science and Technology*, 99: 468–475.

Reidzane, S., Kruma, Z., Kazantseva, J., Traksmaa, A. and Klava, D. (2021). Determination of Technological Parameters and Characterization of Microbiota of the Spontaneous Sourdough Fermentation of Hull-Less Barley. *Foods*, 10: 2253.

Santos, D., Maurício, A. C., Sencadas, V., Santos, J. D., Fernandes, M. H. and Gomes, P. S. (2018). Spray drying: An overview. In Biomaterials - physics and chemistry (New Edition). InTech.

Schutyser, M. A. I., Both, E. M., Siemons, I., Vaessen, E. M. J. and Zhang, L. (2019). Gaining Insight on Spray Drying Behavior of Goods Via Single Droplet Drying Analyses. *Drying Technology*, 37(5): 525-534.

Stefanello, R. F., Nabeshima, E. H., Lamanaka, B. T., Ludwig, A., Fries, L. L. M., Bernardi, A. O. and Copetti, M. V. (2019). Survival and stability of *Lactobacillus Fermentum* and *Wickerhamomyces Anomalus* strains upon Lyophilisation with Different Cryoprotectant Agents. *Food Research International*, 115: 90-94.

Tafti, A. G., Peighardoust, S. H., Behnam, F., Bahrami, A., Aghagholizadeh, R., Ghamari, M. and Rafat, S. A. (2013a). Effects of Spray-Dried Sourdough on Flour Characteristics and Rheological Properties of Dough. *Czech Journal of Food Sciences*, 31(4): 361 367.

Tafti, a. G., Peighambardoust, S. H., Hesari, J., Bahrami, A. and Bonab, E. S. (2013b). Physico-Chemical and Functional Properties of Spray-Dried Sourdough in Breadmaking. *Food Science & Technology International*, 19(3): 271-278.

Tan, L. W., Ibrahim, M. N., Kamil, R. and Taip, F. S. (2011). Empirical Modeling for Spray Drying Process of Sticky and Non-Sticky Products. *Procedia Food Science*, 1: 690 – 69.

Tan, D. T., Poh, P. E. and Chin, S. K. (2018). Microorganism Preservation By Convective Air-Drying: a Review. *Drying Technology*, 36(7): 764-779.

10.51975/254001010.som
Journal of the Nigerian Society of Chemical Engineers, 40(1), 2025

# ASSESSMENT OF NIGERIAN LAUMONTITE ZEOLITE IN THE ADSORPTION OF ACID RED 27 AND BRILLIANT GREEN DYE IN SYNTHETIC WASTEWATER

**Kovo A.S*. Faridat J., Hawa Manko and Eluwa V.**
*Department of Chemical Engineering, Federal University of Technology, Minna*
**kovo@futminna.edu.ng, 07013377258*

**ABSTRACT**

*This study dwell on the removal of color of two different dye types namely Acid Red-27 (AA27) and Brilliant Green (BG) in a simulated waste dye water. An adsorption process in which the parameters were optimized with response surface methodology was adopted. Numerical optimization was determined at optimum conditions for BG and AA27, respectively and was used in carrying out a batch equilibrium studies while studying the effect of contact time, initial concentration and adsorbent dosage. The outcome of the experimentation indicate that the adsorbent dosage of the dye solution had a significant impact on adsorption. The result also showed that Freundlich isotherm fit the isotherm model for AA27, and Langmuir isotherm fit that of BG. The overall experimental data indicate a maximum removal of 96.24 % and 83.10 % was found for Brilliant Green and Acid Red 27 respectively while the maximum dye adsorption capacity of BG and AA27 was obtained at 68.02 and 3.43 mg/g, respectively. Activated Nigerian Laumontite zeolite has capability for adsorption and hence can be used for effective removal of dyes from wastewater.*

***Keywords:*** *Laumontite zeolite; Brilliant green dye; Acid red 27; Adsorption; Laumontite*

## 1. INTRODUCTION

The production of numerous pollutants due to industrialization and modernization has negatively impacted the environment (Bushra *et al.,* 2021). The use of water by many different process industries and its attendant effects through discharges pose an enormous challenge environmentally. Brilliant green is currently used in industry worldwide for a variety of tasks, including dying paper, leather, wool, and silk. Veterinary care, dermatological products, biological stains. Acid red 27 is useful as a food dye . It is also used in cosmetics, natural and synthetic fibers, leather, paper, and phenol-formaldehyde resin. This usefulness in the mentioned processes entails they are present in the wastewater released by several process industries, including textile industry (Zafar *et al.,* 2020). The level of Water pollution beyond the threshold limit is directly related to the general effects such as gastrointestinal tract which can lead to other secondary effect including nausea, vomiting, and diarrhea, and even coughing and shortness of breath.

There are several technologies available that are used for the removal of organic contaminants. These include oxidation method (Pathania *et al.,* 2016), treatment using biotic processes (Santos and Boaventura, 2015), the use of membrane process [Lau and Ismail, 2009], coagulation/flocculation, and adsorption (Wu *et al.,* 2017). Adsorption processes are the most widely used treatment techniques for eliminating organic contaminants (Mahmoud *et al.,* 2020) because of its simplicity and effectiveness as well as economical advantage over other processes (Albadarin *et al.,* 2017). There are several adsorbents well known to possess good adsorption properties such as activated carbon, fly ash, clay minerals and zeolites. Zeolite is an aluminosilicate material (both synthetic and natural) with a polyhedral three-dimensional structure made up of $[SiO]^{4-}$ and

$[AIO]^{5-}$ complexes. These compounds have a specific chemistry and qualities that make it possible for them to adsorb various environmental pollutants (Alakhras *et al.,* 2020). Laumontite natural zeolites which have been studied extensively used as adsorbents was recently discovered in part of Nigeria and they are known to have good surface area, porous structure, and ion-exchange capabilities. This study is therefore aim to assess the efficacy of this new natural zeolite (NZ) sourced from Adamawa , Nigeria as an adsorbent for wastewater treatment by removing Acid Red 27 and Brilliant Green dye.

## 2. MATERIALS AND METHODS

### 2.1. Materials

Natural laumontite zeolite (NLZ) was sourced from Ganki, Fufore LGA in Adamawa State, Nigeria. All chemical used in this work were of analytical grade.

### 2.2. Purification and Modification of the Adsorbent material

First, 100 g of NLZ was crushed and sieved using 300 μm mesh, this was then followed by washing of the sieved NLZ with large quantity of deionized water to remove impurities and finally dried in oven for 6 h at 110 °C. The activation of the natural zeolite was carried with the aid of NaCl. The activation process to convert LAU-NZ in Na-form was prepared according to previous procedures described in the literature (Hasan, 2023). 28.89 g of NLZ was added to 1M NaCl solution which was stirred for 20 h at 50 rpm. The material was decanted, and was washed

four times with deionized water to remove excess sodium chloride and finally dried in the oven at 110 °C for 9 h.

**2.3. Characterization of natural Laumontite zeolite**

The analysis of NLZ and activated NLZ before and after the adsorption of brilliant green and acid red 27 was carried out using by Fourier transform infrared spectroscopy (FT-IR) for it functional groups, the microstructure/morphology was performed by a scanning electron microscope (SEM), the X-ray fluorescence was used to determine a material's oxide composition, and the crystallographic structural properties was determined by X-ray powder diffraction (XRD) (Model: EMPYREAN from Netherlands) in the $2\theta$ range of 5-70.

**2.4 Empirical optimization design**

Box-Behnken (BBD) was employed to evaluate the impact of process factors on the removal efficiency of BG AND AA27 on NLZ. The selected variables were initial concentration (40 – 200 mg/l), Contact time (30 – 240 min) and adsorbate dosage (0.05 -0.3 g). 17 experiment runs were generated using Design Expert software (Ver.13.0).

**Table 1 Independent factors and their chosen level of the experimental design**

| Name | Symbol | Low | High |
|---|---|---|---|
| Contact time (min) | A | 30 | 240 |
| Adsorbent dosage (g) | B | 0.05 | 0.3 |
| Intial concentration (mg/l) | C | 40 | 200 |

**Table 2 Full BBD Experimental Design Table**

| | **Factor 1** | **Factor 2** | **Factor 3** |
|---|---|---|---|
| Runs | A: Initial concentration (mg/l) | B: Contact time (min) | C: Adsorbent dosage (g) |
| 1 | 40 | 30 | 0.175 |
| 2 | 120 | 240 | 0.05 |
| 3 | 40 | 135 | 0.05 |
| 4 | 120 | 135 | 0.175 |
| 5 | 40 | 135 | 0.3 |
| 6 | 200 | 30 | 0.175 |
| 7 | 120 | 30 | 0.3 |
| 8 | 120 | 135 | 0.175 |
| 9 | 120 | 135 | 0.175 |
| 10 | 120 | 135 | 0.175 |
| 11 | 200 | 135 | 0.3 |
| 12 | 120 | 30 | 0.05 |
| 13 | 40 | 240 | 0.175 |
| 14 | 200 | 135 | 0.05 |
| 15 | 120 | 135 | 0.175 |
| 16 | 200 | 240 | 0.175 |
| 17 | 120 | 240 | 0.3 |

Diagnostic plots and analysis of Variance (ANOVA) were utilized in the statistical study to evaluate the statistical significance of the regression coefficient of the suggested models and optimum conditions for the adsorption process.

**2.5 Numerical Optimization**

Numerical optimizations were performed using the 'optimization' selection on Design Expert v13.0. Maximizing removal efficiency within the parameters and keeping all process variables within them were the objectives of the numerical optimization, subject to a few carefully considered constraints (Bader *et al.*, 2018; Cui *et al.*, 2019).

**2.6 Adsorption experiment**

The adsorption of BG and AA27 on activated NLZ was carried out by batch method. This was done by shaking 50 ml of a known initial dye concentration with known amount the adsorbent NLZ in 250 mL and the solution was stirred at 210 rpm according to the experimental variables obtained from the design factors as given by the BBD experimental design. The solution of the adsorbent and adsorbate were separated using a filter paper and the filtrate was tested for the absorbance using a UV-visible spectrophotometer. All samples were filtered before the residual acid red 27 and brilliant green quantity were quantified using UV spectroscopy at 519.50 nm and 624.50 nm respectively.

The amount of dye adsorbed at equilibrium $q_e$ (mg/g) was calculated at equilibrium condition using Eq. (1):

$$Q_e = \frac{C_0 - C_e}{w} * V \quad (1)$$

Where $C_0$ and $C_t$ are the initial concentration and final concentration of Acid red 27 and Brillant green in the solution (mg/L); V is the volume of Acid red 27 (L); W is the weight of adsorbent (g).

The removal efficiency was calculated using equation 2:

$$R = \frac{C_0 - C_t}{C_0} \times 100\% \quad (2)$$

Where $C_0$ and $C_t$ are the initial concentration and final concentration of Acid red 27 and Brillant green in the solution (mg/L).

**2.6.1 Adsorption isotherms**

The experimental data was analyzed using Langmuir and Freundlich isotherms, and the molecular distribution of adsorbate on the adsorbent surface was done for [Jahan et al., 2023] acid red 27 and brilliant green (Zafar *et al.*, 2020; Mansour *et al.*, 2020) for their adsorption characteristic.

Equation 3 represents the linear Langmuir model:

$$\frac{c_e}{q_e} = \frac{c_e}{q_{max}} + \frac{1}{q\,max\,k_L} \quad (3)$$

where $q_e$ is the equilibrium adsorption, and $q_{max}$ is the maximum adsorption capacity (mg/g), $C_e$ is the

equilibrium concentration (mg/L) related, and $k_L$ is the Langmuir isotherm constant (L/mg) related to the affinity of the binding sites to the adsorbate

Equation 4 represents the linear Freundlich model:

$$\text{Log } q_e = \log K_f + \frac{1}{n} \log C_e \quad (4)$$

The parameter in equation 3 are describe as follows, $q_e$ is the equilibrium adsorption (mg/g), $C_e$ is the equilibrium concentration (mg/L), $k_F$ is the Freundlich isotherm constant (mg/g), and 1/n is dimensionless representing the heterogeneity of the adsorbent sites and also indicates the affinity between adsorbate and adsorbent.

## 3. RESULTS AND DISCUSSION

### 3.1. Zeolite Analysis

The first five 2-theta peaks in the diffractogram clearly match the pattern of typical peaks for NLZ as described in the literature, which displays all of the peaks that are characteristic for Laumontite (Treacy and Higgins, 2007). The X-ray diffractograms of NLZ in (Fig.2a) show that the main diffraction peaks at 2θ angles, major peak values for the first five 2-theta of the samples are seen at around 7.5°, 12.5°, 25.0°, and 28.5° corresponding to hkl plains of (110), (200), (-112), and (330), respectively. The SEM images of NLZ as shown in fig 2b micrograph displayed a large plate-like structure, suggesting that the silica and alumina are sliding over one another, and the SEM micrograph revealed a uniform particle size of the sample with a regular shape when compared with literature (Hosaka *et al.*, 1995).

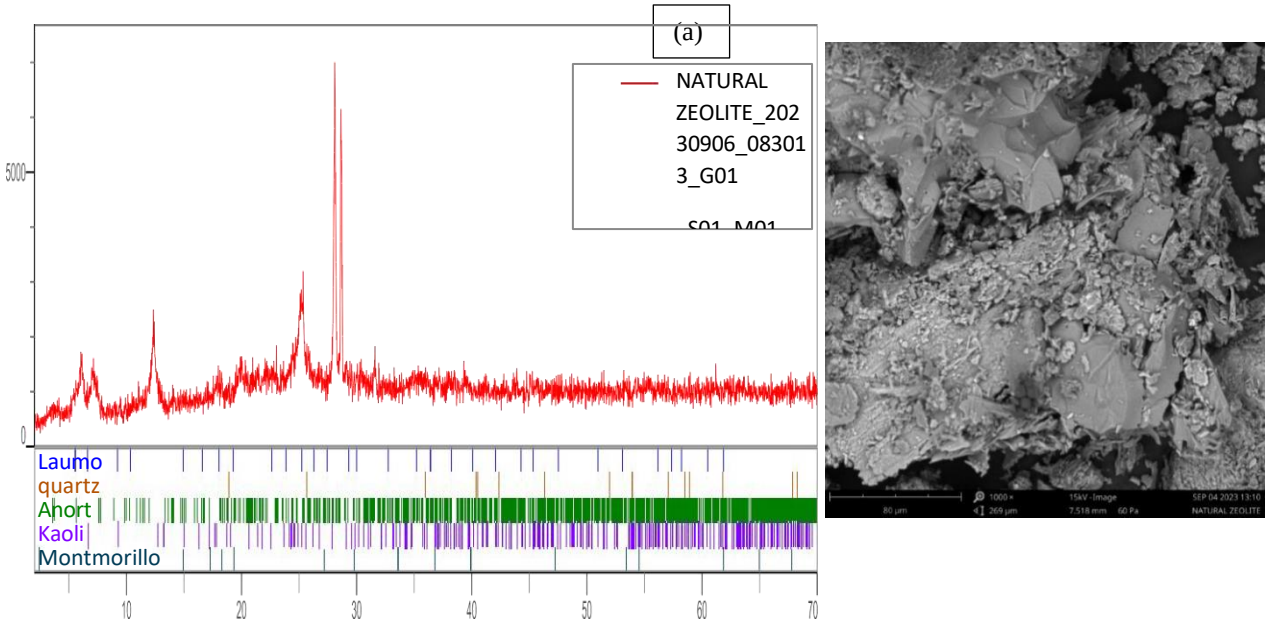


**Figure 2. (a) X-ray diffractogram of LAU-NZ and (b) SEM image of LAU-NZ**

The XRF analysis result as shown in Table 3 was used to determine the oxides and elemental compositions of the NLZ. The result as shown in table 3 present results from the X-ray Fluorescence analysis clearly indicate the preponderance of various oxide composition of the natural material

**Table 3 shows the oxides, elements, and percentage weight concentrations of LAU-NZ.**

| OXIDES | CONCENTRATION WT.% | ELEMENT | CONCENTRATION WT.% |
|---|---|---|---|
| $SiO_2$ | 46.524 | O | 45.545 |
| $V_2O_5$ | 0.068 | Al | 11.194 |
| $Cr_2O_3$ | 0.150 | Si | 21.747 |
| MnO | 0.135 | S | 2.036 |
| $Fe_2O_3$ | 15.170 | Cl | 0.487 |

| OXIDES | CONCENTRATION WT.% | ELEMENT | CONCENTRATION WT.% |
|---|---|---|---|
| $Co_3 O_4$ | 0.051 | K | 1.348 |
| NiO | 0.041 | Ca | 6.021 |
| CuO | 0.040 | Ti | 0.538 |
| $Nb_2O_3$ | 0.015 | V | 0.038 |
| $MoO_3$ | 0.023 | Cr | 0.103 |
| $SO_3$ | 5.085 | Mn | 0.104 |
| CaO | 8.424 | Fe | 0.611 |
| $K_2O$ | 1.624 | Co | 0.037 |
| BaO | 0.073 | Ni | 0.032 |
| $Al_2O_3$ | 21.150 | Cu | 0.032 |
| $Ta_2O_5$ | 0.004 | Zn | 0.015 |
| $TiO_5$ | 0.897 | Zr | 0.016 |
| ZnO | 0.019 | Nb | 0.012 |
| $ZrO_2$ | 0.022 | Ba | 0.066 |

The sample has Si/Al ratio greater than one (1.942 as shown in Table 3). Given that the minimal Si/Al ratio should be 1 and 1.3 – 3.3. the outcome appears to be in line with Breck DW and Loewenstein's rule for aluminum in four-fold coordination respectively (Soscún *et al.*, 2001).

FTIR spectra of activated NLZ, adsorbed AA27, and adsorbed BG in Fig.3 shows the band (4000 - 2500 $cm^{-1}$) is the stretching vibrations of Si-OH and Si-OH-Al, the band at (2500 - 2000 $cm^{-1}$) are attributed to the bending vibrations of water molecules H-O-H, (2000 - 1500 $cm^{-1}$) is due to asymmetric stretching vibrations of (C=O), and (1500 -400 $cm^{-1}$) asymmetric and symmetric stretching vibration of internal (Kumar, 2019). In Fig.3c, distinct absorption peaks at (1192.7 -1,786.5 $cm^{-1}$) are attributed to the asymmetric stretching vibration of internal T-O(T) bonds and symmetric stretching vibration of internal T-O(T) bonds (Hasan, 2023) and Fig.3b, The minimal shift of the T-O bond and C=O bands after loading the dye is due to the strong intensities surface complexation of the dye substance with these functional groups.

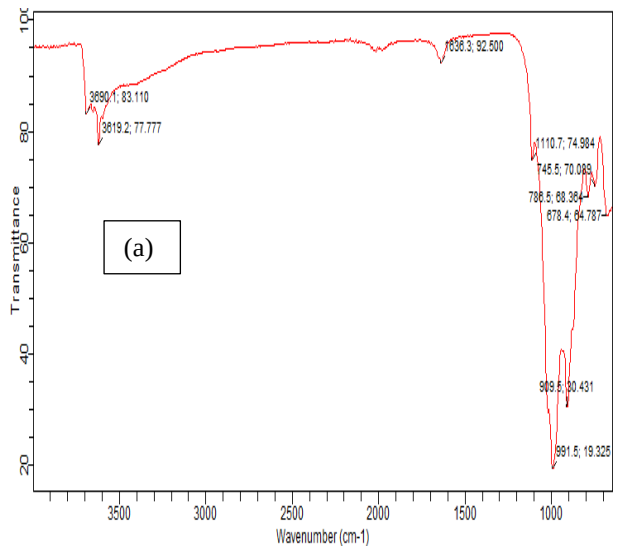


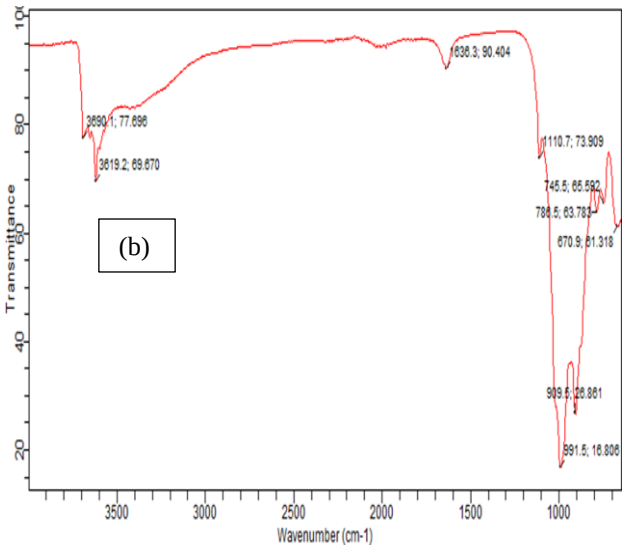

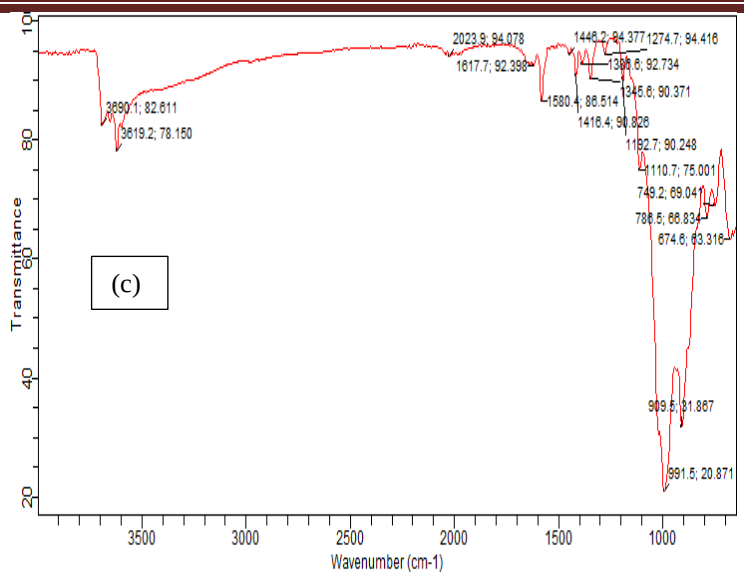


**Figure 3. FTIR analysis on (a)Activated zeolite, (b)Adsorbed AA 27, and (c)Adsorbed BG**

### 3.2 ANOVA and Diagnostic model

The results of the ANOVA demonstrated that the relationships between each response and the important factors were accurately reflected by the equations. According to the model, A, B, C, $AB^2$, $AC^2$, $BC^2$, $A^2$, $B^2$, and $C^2$ were significant model terms. Additionally, lack of fit became critical because of certain systematic fluctuations that this model was unable to account for. Equations (5) and (6) of the software's model showed how the independent parameters taken into account and % removal of BG and AA27 are related.

$$\% \text{ Removal} = +91.5231 + 4.51816\,A - 0.159446\,B + 0.478342\,C + 0.440712\,AB - 0.167962\,AC + 0.795563\,BC - 3.72207A^2 - 0.12296\,B^2 + 0.347415\,C^2 \quad (5)$$

$$\% \text{ Removal} = +99.40 + 0.9539\,A - 0.0380\,B + 0.1481\,C - 0.2492\,AB - 0.6224\,AC + 0.4053\,BC - 0.9194\,A^2 + 0.0669\,B^2 - 0.4996\,C^2 \quad (6)$$

An increase or decrease in response resulting from independent and interaction factors is indicated by a positive or negative sign in the equation. The adsorption yield is greatly influenced by all three of the parameters, according to the ANOVA analysis. In contrast, for both dyes, the adsorption yield is positively impacted by the dye concentration and adsorbate dosage in solution; the activated zeolite contact time has a negative impact according to the correlation coefficients

The preparation conditions and experimental results for the studied responses are shown in Table 4. Values of adsorption capacities varied between 9.50 and 184.95 mg/g for AA27 and between 6.52 and 198.78 mg/g for BG. The highest values of 184.95 and 198.78 mg/g were obtained for the activated zeolite of 0.05 g.

**Table 4: Box-Behnken design actual values and experimental results responses**

| Run | Actual values | | | Qe (mg/g) | | %Removal | |
|---|---|---|---|---|---|---|---|
| | Contact time (min) | Adsorbate dosage (g) | Dye Concentration (mg/g) | AA27 | BG | AA27 | BG |
| 1 | 30 | 0.175 | 40 | 9.50 | 11.12 | 83.14 | 97.31 |
| 2 | 240 | 0.05 | 120 | 109.42 | 117.99 | 91.18 | 98.33 |
| 3 | 135 | 0.05 | 40 | 33.65 | 38.50 | 84.13 | 96.24 |
| 4 | 135 | 0.175 | 120 | 31.33 | 34.04 | 91.38 | 99.30 |
| 5 | 135 | 0.3 | 40 | 5.47 | 6.52 | 81.10 | 97.82 |
| 6 | 30 | 0.175 | 200 | 52.75 | 56.98 | 92.32 | 99.72 |
| 7 | 30 | 0.3 | 120 | 18.14 | 19.76 | 90.72 | 98.81 |

| Run | Actual values | | | Qe (mg/g) | | %Removal | |
|---|---|---|---|---|---|---|---|
| | Contact time (min) | Adsorbate dosage (g) | Dye Concentration (mg/g) | AA27 | BG | AA27 | BG |
| 8 | 135 | 0.175 | 120 | 31.52 | 34.10 | 91.92 | 99.47 |
| 9 | 135 | 0.175 | 120 | 31.10 | 34.12 | 90.70 | 99.51 |
| 10 | 135 | 0.175 | 120 | 31.30 | 34.08 | 91.29 | 99.39 |
| 11 | 135 | 0.3 | 200 | 30.70 | 33.16 | 92.11 | 99.48 |
| 12 | 30 | 0.05 | 120 | 110.04 | 119.23 | 92.70 | 99.36 |
| 13 | 240 | 0.175 | 40 | 9.64 | 11.19 | 84.31 | 97.88 |
| 14 | 135 | 0.05 | 200 | 184.95 | 198.78 | 92.48 | 99.39 |
| 15 | 135 | 0.175 | 120 | 31.66 | 34.06 | 92.33 | 99.35 |
| 16 | 240 | 0.175 | 200 | 53.04 | 56.74 | 92.81 | 99.30 |
| 17 | 240 | 0.3 | 120 | 18.68 | 19.88 | 93.39 | 99.39 |

**Table 5: Analysis of variance for AA27 model**

| Source | Sum of Squares | df | Mean Square | F-value | p- value | |
|---|---|---|---|---|---|---|
| **Model** | 227.60 | 9 | 25.29 | 52.20 | < 0.0001 | significant |
| A-Initial concentration | 163.31 | 1 | 163.31 | 337.06 | < 0.0001 | |
| B-Adsorbate dosage | 0.2034 | 1 | 0.2034 | 0.4198 | 0.5377 | |
| C-Contact time | 1.83 | 1 | 1.83 | 3.78 | 0.0930 | |
| AB | 0.7769 | 1 | 0.7769 | 1.60 | 0.2459 | |
| AC | 0.1128 | 1 | 0.1128 | 0.2329 | 0.6441 | |
| BC | 2.53 | 1 | 2.53 | 5.23 | 0.0561 | |
| $A^2$ | 58.33 | 1 | 58.33 | 120.39 | < 0.0001 | |
| $B^2$ | 0.0637 | 1 | 0.0637 | 0.1314 | 0.7277 | |
| $C^2$ | 0.5082 | 1 | 0.5082 | 1.05 | 0.3398 | |
| Residual | 3.39 | 7 | 0.4845 | | | |
| Lack of Fit | 1.83 | 3 | 0.6095 | 1.56 | 0.3305 | not significant |
| Pure Error | 1.56 | 4 | 0.3908 | | | |
| Cor Total | 230.99 | 16 | | | | |

**Table 6: Analysis of variance for BG model**

| Source | Sum of Squares | df | Mean Square | F-value | p-value | |
|---|---|---|---|---|---|---|
| **Model** | 14.75 | 9 | 1.64 | 148.95 | < 0.0001 | significant |
| A-Initial concentration | 7.28 | 1 | 7.28 | 661.60 | < 0.0001 | |
| B-Contact time | 0.0115 | 1 | 0.0115 | 1.05 | 0.3401 | |
| C-Adsorbate dosage | 0.1755 | 1 | 0.1755 | 15.95 | 0.0052 | |
| AB | 0.2484 | 1 | 0.2484 | 22.57 | 0.0021 | |
| AC | 1.55 | 1 | 1.55 | 140.82 | < 0.0001 | |
| BC | 0.6572 | 1 | 0.6572 | 59.73 | 0.0001 | |
| $A^2$ | 3.56 | 1 | 3.56 | 323.48 | < 0.0001 | |
| $B^2$ | 0.0189 | 1 | 0.0189 | 1.71 | 0.2319 | |
| $C^2$ | 1.05 | 1 | 1.05 | 95.54 | < 0.0001 | |

| | | | | | | |
|---|---|---|---|---|---|---|
| **Residual** | 0.0770 | 7 | 0.0110 | | | |
| Lack of Fit | 0.0467 | 3 | 0.0156 | 2.06 | 0.2488 | not significant |
| Pure Error | 0.0303 | 4 | 0.0076 | | | |
| **Cor Total** | 14.83 | 16 | | | | |

Fig. 4, provides statistical actual and predicted values to test the significant effects of regression coefficients for the proposed models. In Fig. 4a, which showed the distribution of BG adsorption data points close to the straight line, while AA27 data in Fig. 4b deviated from the straight line. Consequently, there was a reasonable agreement between the "$R^2$" and the "$R^2_{adj}$". Additionally, "$R^2$" was higher than "$R^2_{adj}$". It is evident that over 90% of these reactions are accurately anticipated by these models, suggesting that the terms taken into account in the suggested models were important enough to produce predictions that could be accepted (Tounsadi, *et al.*, 2016).

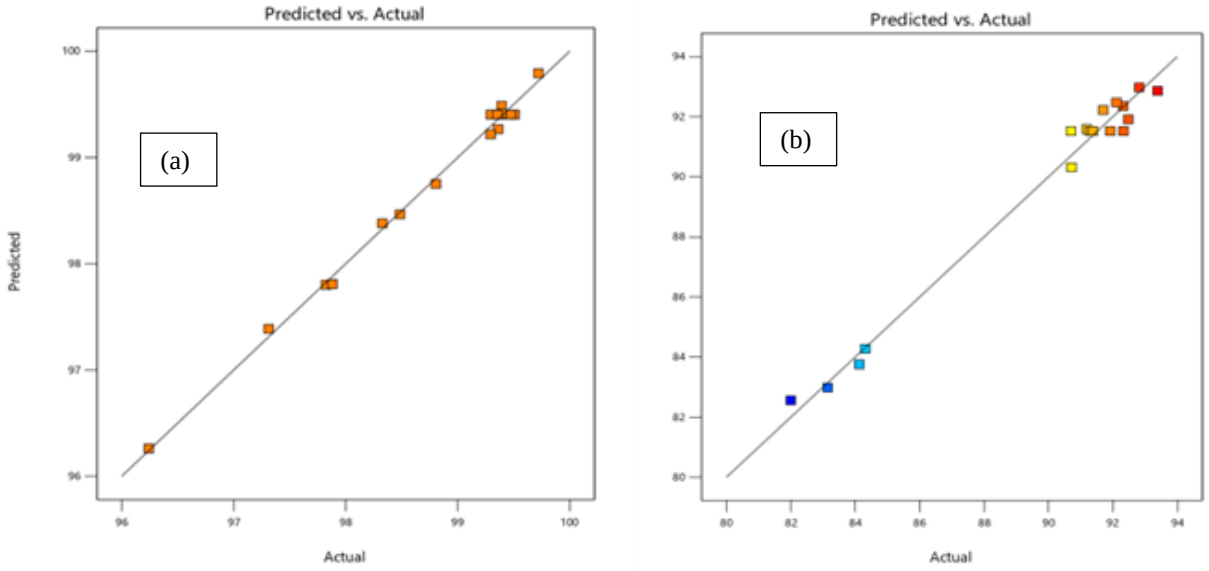


**Figure 4: Predicted values vs. actual values for (a) BG, and (b) AA27**

### 3.3 Numerical Optimization

Maximizing removal efficiency within the parameters and keeping all process variables within them were the objectives of the numerical optimization, subject to a few carefully considered constraints (Bader et al., 2018; Cui et al., 2019). These constraints are presented in Table 7 and 8 for the dyes below.

**Table 7: Factor and response constraints on the numerical optimization for BG**

| Name | Goal | Lower Limit | Upper Limit | Lower Weight | Upper Weight | Importance |
|---|---|---|---|---|---|---|
| A: Initial concentration | is in range | 40 | 200 | 1 | 1 | 3 |
| B: Contact time | is in range | 30 | 240 | 1 | 1 | 3 |
| C: Adsorbate dosage | is in range | 0.05 | 0.3 | 1 | 1 | 3 |
| Removal | maximize | 96.2417 | 99.721 | 1 | 1 | 3 |

**Table 8: Factor and response constraints on the numerical optimization for AA27**

| Name | Goal | Lower Limit | Upper Limit | Lower Weight | Upper Weight | Importance |
|---|---|---|---|---|---|---|
| A: Initial concentration | is in range | 40 | 200 | 1 | 1 | 3 |
| B: Adsorbate dosage | is in range | 0.05 | 0.3 | 1 | 1 | 3 |
| C: Contact time | is in range | 30 | 240 | 1 | 1 | 3 |
| % Removal | maximize | 81.9975 | 93.387 | 1 | 1 | 3 |

Table 6 and 7, shows the maximum removal efficiencies were observed to be 96.24% and 81.10% for BG and AA27 dyes, respectively. The optimum condition for BG is at initial concentration of 190.428 mg/l, adsorbent dosage of 0.159 g, and contact time of 69 min and that of AA27 at initial concentration of 166.649 mg/l, adsorbent dosage of 0.274 g, and contact time of 210 min The desirability values of these parameters which is a show of the ideal and desired values were observed to be 1.000 (unity) for the two dyes. The result indicate the acceptance of the predicted adsorption removal efficiencies and the applicationn of the model for the dyes removals .

### 3.4 Batch adsorption experiment

#### 3.4.1. Effect of initial concentration

A plot of removal efficiency of the BG dye is shown in Figure. 5a, while keeping other factors constant (adsorbent dosage = 0.159 g, contact time = 69 min). It can be observed that the number of active sites on the surface of the adsorbent is more available at low initial dye concentrations than it is at high initial dye concentrations. The removal efficiency of BG rises proportionally with the initial concentration (Alene *et al.*, 2020). In Fig. 5b, while keeping other factors constant (adsorbent dosage = 0.274 g, contact time = 210 min), the removal efficiency of AA27 increases inversely with the initial concentration. The number of effective adsorption sites on the adsorbents exceeds the number of competent AMD molecules at lower starting concentrations. Because of this, a greater percentage of AA 27 molecules exhibit increased adsorption effectiveness when they are bound to the adsorbent surface (Rahaman *et al.*, 2022). This show that these process favors at higher concentration.

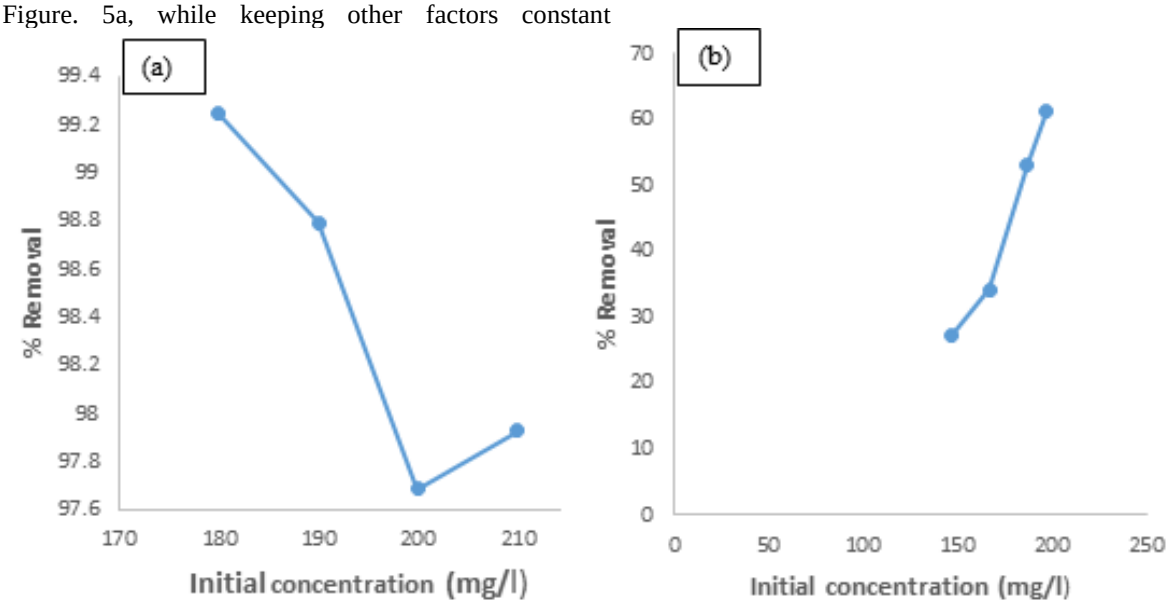


**Figure 1: Effect of initial concentration on adsorption of (a)BG dye, and (b) AA27 onto AZ**

#### 3.4.2 Effect of adsorbent dosage

The plot of removal efficiency against adsorbent dosage as presented in Figure. 6 shows that adsorbent dosage is one of the independent variables that can alter the dye. removal efficiency. The study was at constant conditions of initial concentration = 190 mg/l and contact time=69 min for BG and initial concentration = 167 mg/l and contact time= 210 min for AA27, respectively. Between the two dyes, the removal efficiency of BG is greater than that of AA27 as shown in the plot with changes in the activated zeolite dosage which is due to the amount of more adsorbent active sites and more adsorbent specific surface area become available, leading to an increase in the removal percentage of both dyes onto activated zeolite (AZ) (Alene *et al.*, 2020).

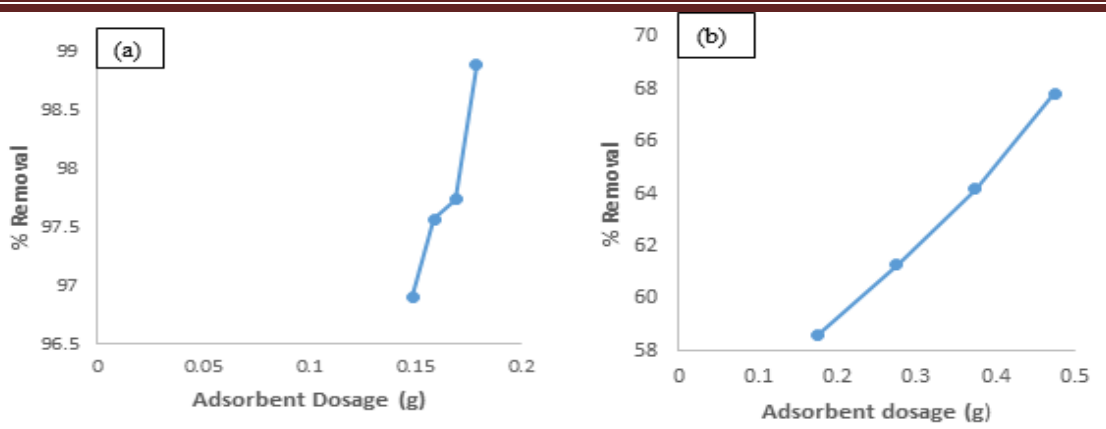


**Figure 2: Effect of adsorbent dosage on adsorption of (a)BG dye, and (b)AA27 onto AZ**

### 3.4.3 Effect of contact time

The effect of removal efficiency on contact time was studied at constant conditions of (Adsorbent dosage = 0.159 g and initial concentration = 190 mg/L) for BG and that of AA27 (Adsorbent dosage = 0.274 g and initial concentration = 167 mg/L) efficiencies of both dyes were affected by contact time as observed from Fig. 7. From the plot, it was noticed that the removal efficiency for the dyes increased with longer time of contact between the activated LAU-NZ and adsorbate. In Fig. 7a, It is evident that the dye's initial removal efficiency increased during the first 59 minutes, and that this was followed by a slow removal rate until the 89-minute mark. However, as equilibrium takes longer to reach, the number of surface sites that remain will decrease and it will become more difficult to occupy these ions (Samaka, 2021) whereas, in Fig. 7b, it was observed that there was a steep increase in the amount of dye adsorbed from 210 - 230 minutes which follows by a steady increase. Due to the unavailability of the active adsorption sites on the adsorbent surface, the adsorption effectiveness falls as the contact time increases (Munagapati *et al.*, 2021).

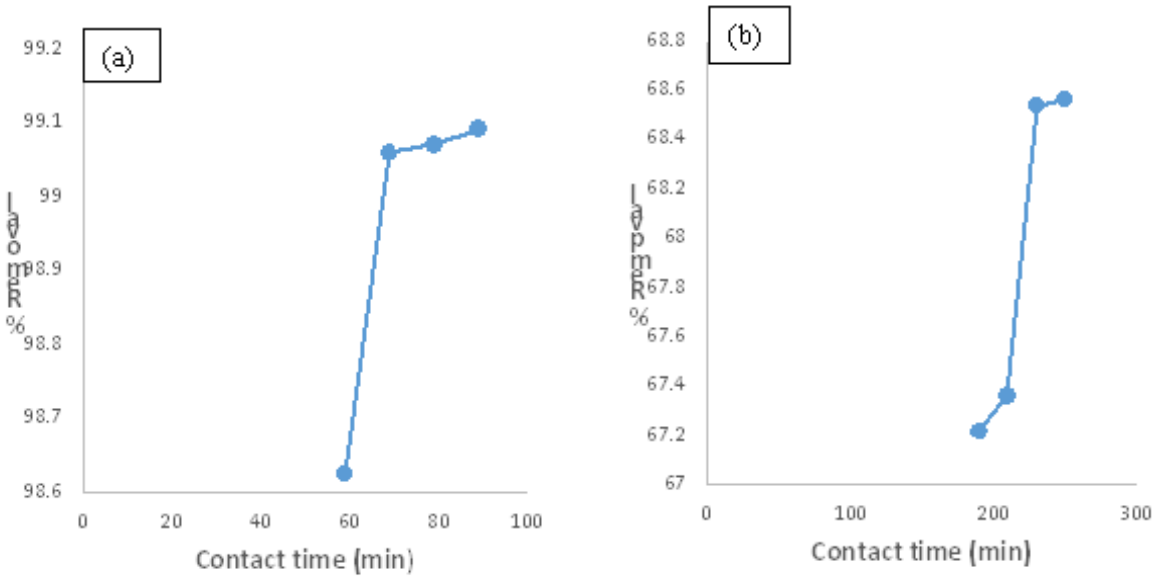


**Figure.3: Effect of contact time on adsorption of (a)BG dye, and (b) AA27 onto AZ**

### 3.5 Adsorption isotherm

Fig.8a and 8b represented the Langmuir isotherm plots of BG and AA27 respectively. Table 9 shows the adsorption parameters in the adsorption on activated LAU-NZ**,** along with the correlation coefficient $R^2$ of nearly 1. In Fig 8, the maximum adsorption capacities ($q_{max}$) of the AZ were

found to be 68.02 mg/g, and 3.43 mg/g for BG and AA27.Therfore, the adsorption of BG on activated LAU-NZ was best described using this model which showed single monolayer adsorption of BG on the surface of activated LAU-NZ as compared to AA27.

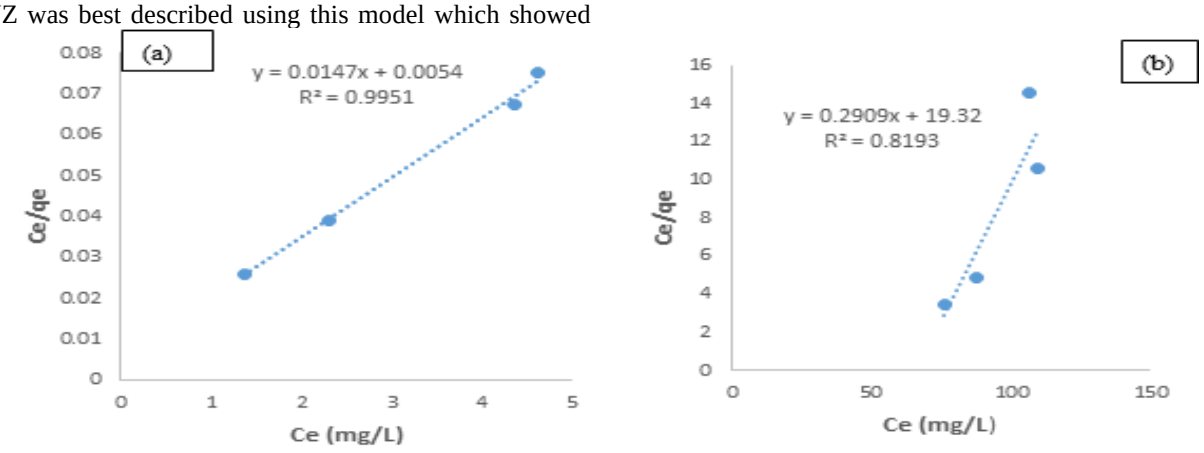


**Figure4: Langmuir isotherm plots of (a) BG and (b) AA27 27 onto AZ**

The Freundlich isotherm shows the plot of log $C_e$ vs. log $q_e$ as shown in Fig. 9a for BG and Fig.9b for AA27, respectively and both the values of 1/n and $K_f$ can be calculated from the slope and intercept. It is considered good adsorption if the n value is (0> n <1) (Munagapati *et al.*, 2021). In this study, the n value obtained from Freundlich model for BG and AA 27 was found to be 10.47 and 0.37, respectively, indicating the adsorption of BG is unfavorable and that of AA27 is favorable. This indicate that this isotherm is a better representation model for Acid red 27 dye.

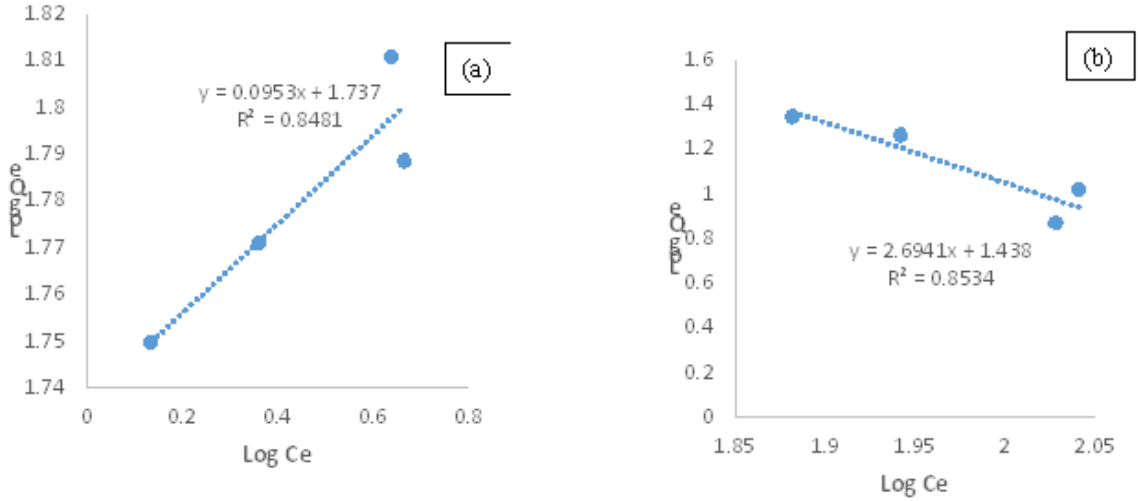


**Figure 5: Freundlich isotherm plots of (a) BG, and (b) AA27 onto AZ**

**Table 9: The adsorption isotherms parameters for Langmuir and Freundlich model**

| Adsorption parameters | Brilliant Green | Acid Red 27 |
|---|---|---|
| **Langmuir isotherm** | | |
| $K_L$ (L/mg) | 2.72 | 5.62 |
| $q_{max}$ (mg/g) | 68.02 | 3.43 |
| $R^2$ | 0.9951 | 0.8193 |
| $R_L$ | 0.0017 | 0.0015 |
| **Freundlich isotherm** | | |
| $K_f$ (mg/g) | 54.58 | 27.42 |
| 1/n | 0.0953 | 2.6941 |
| $R^2$ | 0.8421 | 0.8534 |

## 4. CONCLUSION

The removal efficiency and maximum adsorption capacities of BG and AA27 were 68.02 and 3.43 mg/g respectively with optimum removal efficacy of 96.24% and 83.14%. Characterization on the LAU-NZ by SEM, XRD and XRF. FTIR analysis was done on the activated and after adsorption. The optimal experimental conditions for the removal of the maximum dye were determined on contact time, initial concentration, and adsorbent dosage. From ANOVA, it showed that the BBD model was statically significant. It was observed that the independent variables were all significant which implies that all factors variable studied had specific impact on its removal efficiency. Numerical optimization (unity) was found to be the desirability values of these parameters, which represent the ideal and desired values. Isotherms models of Langmuir and Freundlich were applied to study adsorption of BG and AA27 on activated natural zeolite. The adsorption behavior of Langmuir was best represented ($R^2$ = 0.9951) for BG with maximum adsorption capacity of 68.02 mg/L and AA27 is described by Freundlich isotherm ($R^2$ = 0.8534). The current investigation reveals that the activated Laumontite zeolite that has been made using inexpensive method was effectively used in the removal Acid Red 27 and Brilliant Green, from simulated dye wastewater that and the results prove very successful.

**ACKNOWLEDGMENT**

This research was funded with the support of TETFUND National Research Fund with grant number TETF/ES/DR&D-CE/NRF2023/SETI/ARS/0039/VOL-1.

**REFERENCES**

Albadarin, A. B., Collins, M. N., Naushad, M., Shirazian, S., Walker, G., & Mangwandi, C. (2017). Activated lignin-chitosan extruded blends for efficient adsorption of methylene blue. *Chemical Engineering Journal*, *307*, 264–272. https://doi.org/10.1016/j.cej.2016.08.089

Alakhras, F., Alhajri, E., Haounati, R., Ouachtak, H., Addi, A. A., & Saleh, T. A. (2020). A comparative study of photocatalytic degradation of Rhodamine B using natural-based zeolite composites. *Surfaces and Interfaces*, *20*(May). https://doi.org/10.1016/j.surfin.2020.100611

Alene, A. N., Abate, G. Y., & Habte, A. T. (2020). Bioadsorption of Basic Blue Dye from Aqueous Solution onto Raw and Modified Waste Ash as Economical Alternative Bioadsorbent. *Journal of Chemistry*, *2020*. https://doi.org/10.1155/2020/8746035

Bader, A., Hartwich, M., Richter, A., & Meyer, B. (2018). Numerical and experimental study of heavy oil gasification in an entrained-flow reactor and the impact of the burner concept. *Fuel Processing Technology*, *169*(September 2017), 58–70. https://doi.org/10.1016/j.fuproc.2017.09.003

Bushra, R., Mohamad, S., Alias, Y., Jin, Y., & Ahmad, M. (2021). Current approaches and methodologies to explore the perceptive adsorption mechanism of dyes on low-cost agricultural waste: A review. *Microporous and Mesoporous Materials*, *319*(December 2020), 111040. https://doi.org/10.1016/j.micromeso.2021.111040

Cui, C., Chen, A., Pan, Z., & Ma, R. (2019). Two-dimensional numerical model and fast estimation method for calculating crevice corrosion of cross-sea bridges. *Construction and Building Materials*, *206*, 683–693. https://doi.org/10.1016/j.conbuildmat.2019.02.103

Hasan, F. (2023). *Synthesis Of Zeolite Granules From NaCl Activated- Nano Zeolite Ore To Remove Calcium Ions From Groundwater*. 0–14.

Lau, W. J., & Ismail, A. F. (2009). Polymeric nanofiltration membranes for textile dye wastewater treatment: Preparation, performance evaluation, transport modelling, and fouling control - a review. *Desalination*, *245*(1–3), 321–348. https://doi.org/10.1016/j.desal.2007.12.058

Hosaka, H., Itao, K., & Kuroda, S. (1995). Damping characteristics of beam-shaped micro-oscillators. In *"Sensors and Actuators, A: Physical"* (Vol. 49, Issues 1–2, pp. 87–95). https://doi.org/10.1016/0924-4247(95)01003-J

Jahan, R. A., Hassan, M., Rana, A. A., & Karim, M. M. (2023). *Adsorption of Anionic and Cationic Dyes from Textile Effluents by Activated Carbon Prepared from Sawdust and Fish Scale*. 189–202. https://doi.org/10.4236/aces.2023.133014

Kumar, B. V. S. (2019). *Characterization of zeolites by infrared spectroscopy*. *August*.

Mahmoud, A. S., Farag, R. S., & Elshfai, M. M. (2020). Reduction of organic matter from municipal wastewater at low cost using green synthesis nano iron extracted from black tea: Artificial intelligence with regression analysis. *Egyptian Journal of Petroleum*, *29*(1), 9–20. https://doi.org/10.1016/j.ejpe.2019.09.001

Mansour, R. A., Shahawy, A. El, Attia, A., & Beheary, M. S. (2020). *Brilliant Green Dye Biosorption Using Activated Carbon Derived from Guava Tree Wood*. *2020*.

Munagapati, V. S., Wen, H., Vijaya, Y., Wen, J., Tian, Z., Reddy, G. M., & Raul, J. (2021). Removal of anionic ( Acid Yellow 17 and Amaranth ) dyes using aminated avocado ( Persea americana ) seed powder : adsorption / desorption , kinetics , isotherms , thermodynamics , and recycling studies. *International Journal of Phytoremediation*, *0*(0), 1–13. https://doi.org/10.1080/15226514.2020.1866491

Pathania, D., Gupta, D., Al-Muhtaseb, A. H., Sharma,

G., Kumar, A., Naushad, M., Ahamad, T., & Alshehri, S. M. (2016). Photocatalytic degradation of highly toxic dyes using chitosan-g-poly(acrylamide)/ZnS in presence of solar irradiation. *Journal of Photochemistry and Photobiology A: Chemistry*, *329*, 61–68. https://doi.org/10.1016/j.jphotochem.2016.06.019

Rahaman, A., Rashed, M. A., Rahaman, M. A., Tozammel, M., & Sumon, H. (2022). A comparative study of the adsorptive removal of toxic amaranth dye from aqueous solution using low cost bio-adsorbents. *International Journal of Chemical Studies*, *10*(1).

Samaka, I. A. S. (2021). Using Agricultural Waste as Biosorbent for Hazardous Brilliant Green Dye Removal from Aqueous Solutions. *16*(4), 3435–3454.

Santos, S. C. R., & Boaventura, R. A. R. (2015). Treatment of a simulated textile wastewater in a sequencing batch reactor (SBR) with addition of a low-cost adsorbent. *Journal of Hazardous Materials*, *291*, 74–82. https://doi.org/10.1016/j.jhazmat.2015.02.074

Soscún, H., Castellano, O., Hernández, J., & Hinchliffe, A. (2001). Acidity of the Brönsted acid sites of zeolites. *International Journal of Quantum Chemistry*, *82*(3), 143–150. https://doi.org/10.1002/1097-461X(2001)82:3<143::AID-QUA1014>3.0.CO;2-O

Tounsadi, H., Khalidi, A., Machrouhi, A., Farnane, M., Elmoubarki, R., Elhalil, A., Sadiq, M., & Barka, N. (2016). Highly efficient activated carbon from Glebionis coronaria L. biomass: Optimization of preparation conditions and heavy metals removal using experimental design approach. *Journal of Environmental Chemical Engineering*, *4*(4), 4549–4564. https://doi.org/10.1016/j.jece.2016.10.020

Treacy, M. M., & Higgins, J. B. (2007). *Collection of simulated XRD powder patterns for zeolites fifth (5th) revised edition*. Elsevier.

Wu, J., Wang, G., Li, Z., Yu, E., Xie, J., & Zheng, Z. (2017). Extraction of flocculants from a strain of Bacillus thuringiensis and analysis of their properties. *Aquaculture and Fisheries*, *2*(4), 179–184. https://doi.org/10.1016/j.aaf.2017.06.003

Zafar, M. N., Ghafoor, S., Tabassum, M., Zubair, M., Nazar, M. F., & Ashfaq, M. (2020). Utilization of peanut (Arachis hypogaea) hull based activated carbon for the removal of amaranth dye from aqueous solutions. *Iranian Journal of Chemistry and Chemical Engineering*, *39*(4), 183–191. https://doi.org/10.30492/ijcce.2019.34951

# JOURNAL OF THE NIGERIAN SOCIETY OF CHEMICAL ENGINEERS INSTRUCTION TO AUTHORS

## 1. TYPES OF PUBLICATION

The Journal of the Nigerian Society of Chemical Engineers will publish articles on the original research on the science and technology of Chemical Engineering. Preference will be given to articles on new processes or innovative adaptation of existing processes. Critical reviews on current topics of Chemical Engineering are encouraged and may be solicited by the Editorial Board. The following types of articles will be considered for publication:

a. Full length **articles or review papers**.
b. **Communication** – a preliminary report on research findings.
c. **Note** – a short paper describing a research finding not sufficiently completed to warrant a full article.
d. **Letter to the Editor** – comments or remarks by readers and/or authors on previously published materials.

The authors are entirely responsible for the accuracy of data and statements. It is also the responsibility of authors to seek ethical clearance and written permission from persons or agencies concerned, whenever copyrighted material is used.

For now the journal is published twice in a year, March/April and September/October.

## 2. MANUSCRIPT REQUIREMENTS

a. The **Manuscript** should be written in clear and concise English and typed (single column) in Microsoft Word using double spacing on A4-size paper, Times New Romans font and 12 point. A full length article or review should not exceed 15 pages. Margin should be Normal (i.e. 2.54cm for Top, Bottom, Left & Right margins).
b. The **Manuscript** should be prepared in the following format: Abstract, Introduction, Materials and Methods, Results, Discussion, Conclusion, Acknowledgements, and References..
c. The **Manuscript** must contain the full names, address and emails of the authors. In the case of multiple authorship, the person to whom correspondence should be addressed must be indicated with functional email address. As an examples, authors' names should be in this format:
**Momoh, S. O., Adisa, A. A.** and **Abubakar, A. S.**
If the addresses of authors are different, use the following format:
***Momoh, S. O.[1], Adisa, A. A.[2]** and **Abubakar, A. S.[3]**
Use star * to indicate the corresponding author.
d. **Symbols** should conform to America Standard Association. An abridged set of acceptable symbols is available in the fourth edition of Perry's Chemical Engineering Handbook. Greek letters, subscripts and superscripts should be carefully typed. A list of all symbols used in the paper should be included after the main text as **Nomenclature**.
e. All **Units** must be in the SI units (kg, m, s, N, etc).
f. The **Abstract** should be in English and should not be more than 200 words. The Abstract should state briefly the purpose of the research, methodology, results, major findings and major conclusions. Abstracts are not required for Communications, Notes or Letters.
g. **Citation** must be in the Harvard Format i.e. (Author, Date). Examples are (Smith, 1990) or (Jones et al, 2011). (Kemp, 2000) demonstrated that …..; (Mbuk, 1985; Boma, 1999; Sani, 2000) if more than two authors. (Telma, 2001a), (Telma, 2001b); etc if the citation have the same author and year of publication.
For more information on Harvard Referencing:
Guide visit
http://www.citethisforme.com/harvard-referencing
h. **References** must also be in the Harvard Format i.e. (Author, Date, Title, Publication Information). References are listed in alphabetical order. Examples are shown below:
Haghi, A. K. and Ghanadzadeh, H. (2005). A Study of Thermal Drying Process. *Indian Journal of Chemical Technology*, Vol. 12, November 2005, pp. 654-663
Kemp, I.C., Fyhr, C. B., Laurent, S., Roques, M. A., Groenewold, C. E., Tsotsas, E., Sereno, A. A., Bonazzi, C. B., Bimbernet, J. J. and Kind M.(2001). Methods for Processing Experimental Drying Kinetic Data. *Drying Technology*, 19: 15-34.
i. **Tables** should contain a minimum of descriptive materials. Tables should be numbered serially throughout the manuscript in Arabic numerals (1, 2, 3, etc), and should be placed at the referenced point with captions (centralised) placed at the top of the table.
j. **Figures**, charts, graphs and all illustrations should be placed at the referenced point, numbered serially throughout the manuscript in Arabic numerals (1, 2, 3, etc) and incorporated in the text. Caption for

Figures should be placed at the bottom of the Figure (centralised). Lettering set or symbols should be used for all labels on the figures, graphs, charts, photographs even when drawn in colours. (Note that figures drawn in colours may be unreadable if printed in black and white).

k. **Equations** should be typed using MS Word Equation Editor and should be centred and numbered serially throughout the manuscript (in Arabic numeral) at the right margin.
l. Wherever possible, **Fractions** should be shown using the oblique slash. E.g. x/y
m. **Footnotes** should not be incorporated in the text.
n. **Acknowledgements** should appear at the end of the paper, before the list of references.

**3. SUBMISSION OF MANUSCRIPTS**

Manuscripts should be submitted by sending a Microsoft Word document (taking into account the Manuscript Requirements described in section 2 above) to the following email address: nschejournal@yahoo.com and copy stevmomoh@yahoo.com**.**

All correspondences are directed to the Editor-in-Chief using the submission emails addresses: nschejournal@yahoo.com and copy stevmomoh@yahoo.com. Meanwhile the online submission of articles on the journal website will soon be ready.

Authors should note that:

a. All authors listed in the manuscript have significantly contributed to the research.
b. All authors are obliged to provide retractions or corrections of mistakes.
c. All references cited are listed and financial support acknowledged.
d. It is forbidden to publish same research in more than one journal.

The fee charged for paper review and publication will be borne by the authors as follows:

**a.** Manuscript Review charges = N6,500 payable by both Members and Non-Member. Overseas is $30.00.
**b.** Publication Charges = N10,000 payable by Non-Members and Members who are not financially up-to-date. Overseas is $40.00.
**c.** Members would only get one (1) Journal free and buy the other if they so wish.
**d.** Corresponding Author whose paper is published on a particular edition would get one (1) free copy on behalf of all the co-authors. Other co-authors will buy if they so wish.

All fees are paid after the paper had been accepted for publication. These charges may be reviewed from time to time by the Governing Board of Directors of the Society.

**4. ACCEPTED PAPERS**

On acceptance, authors will be required to submit a copy of their manuscripts using Microsoft Word by emails to nschejournal@yahoo.com and copy stevmomoh@yahoo.com.

The following additional information should be observed for accepted papers: (i) Typed in Microsoft Word using 1.15 spacing on A4-size paper, Times New Romans font and 10 point; (ii) Margin should be 2.54cm for Top & Bottom; 2.20cm for Left & Right margins; (iii) The abstract should be one column document while the body of the manuscript should be double columns with 0.5cm gutter spacing except some tables and figures that may have to go in for one column document.

**5. PUBLICATION**

Full NSChE Journal edition in hard copy will be published twice annually – March/April Edition and September/October Edition.

**6. REPRINT**

Reprints are available on request at a moderate fee per page. Orders must be placed before the paper appears in Print.

**7. READER'S INFORMATION**

The papers are wholly the view of their author(s) and therefore the publisher and the editors bear no responsibility for such views.

**8. SUBSCRIPTION INFORMATION**

The subscription price per volume is as follows:

a. Individual Reader - N3,000.00
b. Institutions, Libraries, etc.- N5,000.00
c. Overseas Subscription - $100.00

Request for information or subscription should be sent to the Editor-in-Chief through the following emails addresses: nschejournal@yahoo.com and copy stevmomoh@yahoo.com.

**9. COPYRIGHT NOTICE**

By submitting your manuscript to the Journal, you have agreed that the copyright of the published material belongs to the journal.

**10. PRIVACY STATEMENT**

The names and email addresses entered in this journal site will be used exclusively for the stated purposes of this journal and will not be made available for any other purpose or to any other party.

## THE PUBLICATION CHARGES

1. The publication charges totaling Sixteen Thousand Five Hundred Naira (₦16,500) only shall be payable to the following account per an article.

   **Name of account: Nigerian Society of Chemical Engineers**

   **UBA account No:1001730178**
   **or**
   **GTB account No 0139519728**

2. The narration on the slip should be "**Journal Publication Charges**"

3. Make your payments and send a proof to the email of the Chairman/Editor-in-Chief, stevmomoh@yahoo.com at a specified date

MATRIX PETRO-CHEM LIMITED

# *Providing Continuous Value and Quality Products & Services For our Esteemed Customers*

- **OIL & GAS SERVICES**
  - Chemical Services
  - Pipeline Services
- **LUBTICANTS &**
  - PETROLEUM PRODUCTS


MATRIX PETRO-CHEM LIMITED
1, Wilmer Street,
Off Town Planning Way, Ilupeju,
P.O. Box 5652, Ikeja, Lagos, Nigeria.
Tel: 01-4936873, 4822948, Fax: 01-4936873
info@matrixpetrochem.com

PORT-HACOURT
Plot 3c, Trans Amadi,
Rumuobiokani,
Port-Hacourt.
084-794615